Shear Capacity of Concrete Beams Reinforced with Basalt Fibre-Reinforced Polymer Stirrups

A comparative study

S.B. Teeuwen

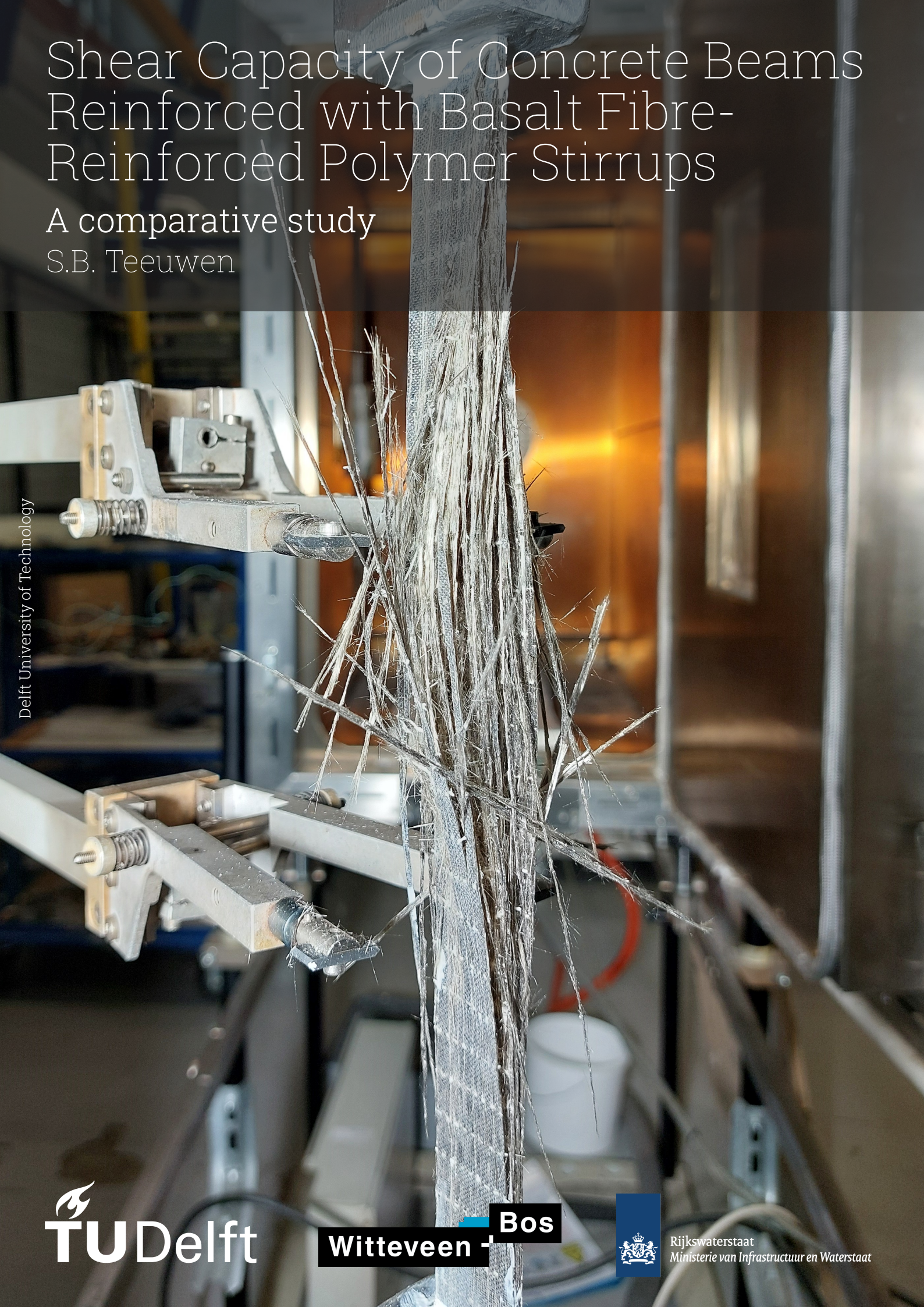

Delft University of Technology

TU Delft
Witteveen + Bos
Rijkswaterstaat
Ministerie van Infrastructuur en Waterstaat

Shear Capacity of Concrete Beams Reinforced with Basalt Fibre- Reinforced Polymer Stirrups

A comparative study

by

S.B. Teeuwen

to obtain the degree of Master of Science
at Delft University of Technology,
to be defended publicly on Friday, August 30, 2024, at 3PM
in Lecture Hall E at the Faculty of Civil Engineering and Geosciences,
Stevinweg 1, 2628 CN Delft.

Student number:	4397347	
Project duration:	May 2023 – August 2024	
Faculty:	Civil Engineering and Geosciences, Delft University of Technology	
Thesis committee:	Dr.ir. M. Luković (chair),	TU Delft, Concrete Structures
	Prof.dr.ir. M.A.N. Hendriks,	TU Delft, Concrete Structures
	Ir. H.J. Bezemer,	TU Delft, Concrete Structures
	Dr.ir. M. Pavlović,	TU Delft, Steel and Composite Structures
	Ir. P. Schoutens,	Witteveen+Bos
Advisory committee:	Dr. ir. S.A.A.M. Fennis,	Rijkswaterstaat
	Dr. ir. C.B.M. Blom,	TU Delft / Municipality of Rotterdam

TU Delft

Witteveen + Bos

Rijkswaterstaat
Ministerie van Infrastructuur en Waterstaat

Preface

This report marks the completion of my graduation project for my MSc in Building Engineering at the Faculty of Civil Engineering and Geosciences, Delft University of Technology. This research was performed in close collaboration with Witteveen+Bos, a leading engineering and consultancy firm providing sustainable solutions in infrastructure, water, environment, and construction globally. The experimental work presented in this thesis was generously financed by Rijkswaterstaat, the executive agency of the Ministry of Infrastructure and Water Management in The Netherlands.

This specific topic was chosen for my Master's thesis because it offered an opportunity to explore and contribute to an emerging field in civil engineering that integrates innovation, sustainability, and advanced materials. The research allowed me to merge theoretical knowledge with practical laboratory experiments, aiming to contribute to the understanding of Basalt Fibre Reinforced Polymer (BFRP) as a viable reinforcement option for concrete structures. I hope that this work will pave the way for more environmentally friendly construction materials and practices in the future.

This thesis is intended for a diverse audience, including researchers, engineers, and professionals in the field of civil engineering, particularly those interested in innovative materials and sustainable construction practices. The report provides comprehensive insights into the use of BFRP as reinforcement in concrete structures, combining both theoretical analysis and validation by experimental results. Readers can use this document as a guide to understanding the potential applications and benefits of BFRP in enhancing the shear capacity of concrete structures.

I would like to extend my heartfelt gratitude to the members of my assessment and advisory committee for their unwavering support, guidance, and expertise throughout this research project. Their insights and feedback were invaluable in shaping the direction and quality of my work.

I would also like to express my appreciation to the following organizations and individuals for their invaluable support and contributions:

- Rijkswaterstaat, for generously funding the experiments conducted for this research;
- Stevin 2 Laboratory staff, in particular Albert Bosman and Ake Blom, for their help;
- Dream Hall Composites Manufacturing Laboratory staff, in particular Martijn Kanger, for his help in the design and production of the laminated BFRP samples;
- Delft Aerospace Structures and Materials Laboratory (DASML) staff, in particular Dave Ruijtenbeek for his help and guidance in performing the uniaxial tensile tests;
- Model Making and Machine Lab (PMB) staff, for providing the CNC-milled Styrofoam molds for the production of BFRP strip stirrups and for access to their machinery;
- Thoenes Solutions and Deutsche Basalt Faser GmbH, in particular Peter Schneider and Georgi Gogoladze, for supplying the braided basalt FRP rods and stirrups;
- Basaltex, in particular Wouter Verbouwe, for supplying the UD-woven basalt fibre fabric;
- BetonijzerBuigCentrale, in particular Paula Kraaijeveld for her help and the company visit;
- My fellow students, in particular Kevin van der Lingen for sharing his practical experience;
- Ascem B.V., in particular Abdulkadir Eraslan for sharing his knowledge and experience;
- Vulkan Europe and Hans de Wit for supplying me with basalt fibre materials and contacts;

Finally, I would like to thank my family and friends for their help and support throughout this journey. Thank you all for your support and contributions, without which this thesis would not have been possible.

S.B. Teeuwen
The Hague, August 2024

Abstract

Steel reinforcement is widely used in concrete structures, enhancing strength, ductility, and durability, thereby preventing excessive cracking and sudden failure. However, the significant environmental impact of steel production, marked by high energy consumption, greenhouse gas emissions, and the material's susceptibility to corrosion, coupled with the associated high refurbishment costs, has driven the search for alternative materials. Basalt Fibre-Reinforced Polymer (BFRP) has emerged as a promising sustainable alternative to steel reinforcement, offering higher tensile strength and superior corrosion resistance. Despite these advantages, the application of BFRP in shear reinforcement, particularly in the form of pultruded BFRP, has been limited. Challenges such as kinked fibres in corner sections and resulting stress concentrations reduce tensile capacity and increase the risk of structural failure at these critical points. This study investigates alternative forms and production methods for BFRP stirrups, assessing their viability as shear reinforcement in reinforced concrete structures.

Two alternative BFRP stirrup designs were examined: braided BFRP rods and laminated unidirectional (UD) BFRP strips. The cross-sectional and material properties of these stirrups were characterized using detailed assessments and uniaxial tensile testing. Subsequently, six reinforced concrete beams with shear span-to-effective-depth ratios of 3.2 and varying stirrup configurations were subjected to displacement-controlled three-point bending tests to assess their shear capacity and failure mechanisms. Two beams were used as reference samples: one without stirrups and one reinforced with four steel stirrups. For direct comparison with the steel-reinforced beam, two beams were reinforced with four braided BFRP stirrups and four laminated BFRP UD-strip stirrups, respectively. Additionally, the number of BFRP stirrups was doubled in two further beams to explore the effects of increased reinforcement. The experimental results were then compared with predictions derived from analytical models to evaluate the accuracy of these models.

Uniaxial tensile tests indicated that both braided BFRP rods and laminated BFRP UD strips demonstrated lower strength and stiffness than pultruded BFRP bars. This reduction is attributed to the lower fibre volume fraction (54% and 53%, respectively, compared to 61% for pultruded bars) and the angled orientation of fibres in the braids and strips, which leads to waviness, unlike the parallel alignment in pultruded bars. Nevertheless, BFRP still demonstrated a tensile strength superior to that of steel, though with reduced stiffness of around 40 GPa instead of 200 GPa. Unlike steel, which can yield, BFRP behaves in a nearly linear elastic manner up to failure.
Experimental results and model predictions consistently indicate that while increasing the amount of BFRP shear reinforcement enhances the shear capacity of concrete beams, it still does not achieve the performance level of steel stirrups. Steel stirrups, through their ability to yield, facilitate force redistribution between the stirrups, leading to a more uniform contribution to shear capacity. In contrast, BFRP stirrups, which do not exhibit yielding behavior, show an uneven distribution of shear loads. This is particularly evident in strain data obtained via Distributed Fibre Optic Sensing (DFOS), where peak strains are observed at the intersections of shear cracks and stirrups and at corner sections. Moreover, the reduced stiffness of BFRP further intensifies this issue by leading to wider shear cracks, which in turn weakens internal shear transfer mechanisms within the concrete, such as aggregate interlock. Consequently, beams reinforced with BFRP stirrups tend to reach their shear capacity limit before the stirrups' uniaxial tensile strength is fully utilized. After reaching the beam its peak load, stress redistribution occurs, shifting from the concrete's contribution to the residual tensile capacity of the BFRP stirrups, thereby introducing a degree of ductility that provides load-bearing capacity beyond the beam its peak capacity. Ultimately, failure in beams reinforced with BFRP stirrups is triggered by rupture at stirrup its corner section.
The efficiency of basalt FRP stirrups, quantified as the additional shear capacity per unit of shear reinforcement ratio compared to the beam without stirrups and normalized against the performance of steel stirrups, was found to be 0.37 and 0.34 for beams reinforced with 4 and 8 braided stirrups, respectively. For beams with 4 and 8 laminated strip stirrups, the relative efficiency values were 0.42

and 0.29, respectively. When this relative efficiency is further normalized by the density of the stirrup material, with steel as the reference, the basalt FRP stirrups exhibit relative efficiency by weight values ranging from 1.24 to 1.79. These findings indicate that basalt FRP stirrups could offer potential advantages in environmental costs compared to steel, although this finding requires further investigation to be validated.
While the results for beams with braided BFRP stirrups were consistent, greater variability in efficiency was observed for laminated strip stirrups. This variability is attributed to the presence of out-of-plane wrinkles—a defect arising from the production process. This finding underscores the necessity of refining manufacturing techniques, such as the adoption of filament winding, to eliminate such imperfections and achieve more consistent quality and performance in BFRP stirrups.

The comparison of analytical predictions from Eurocode 2 (EC2) with the experimental results revealed that the EC2 design approach significantly underestimates the shear capacity for the reference beams with(out) steel stirrups, as it prioritizes safety and neglects the concrete's contribution in the presence of stirrups. Other methods, such as the General Shear Design Method (GSDM), were explored and proved to be more accurate for the beam sample without stirrups. For predicting the BFRP stirrup contribution to the total shear capacity, the strain approach was employed, which limits the strain in the stirrups to 0.45%. This limitation effectively controls cracking and allows for full mobilization of the shear-resisting mechanisms from both concrete and shear reinforcement, thereby enabling their contributions to be summed. By employing a combination of these methods, including a variable concrete strut angle approach with θ = 24° for the strain approach, the predicted shear capacity closely matched the experimental results, ranging from 89% to 102%. This suggests the potential reliability of these analytical models in designing BFRP-reinforced structures, although conservative assumptions remain necessary to ensure structural safety.

In conclusion, alternative BFRP stirrup designs exhibit lower uniaxial tensile strength and stiffness compared to pultruded BFRP rods. Nonetheless, these forms maintain a superior uniaxial tensile strength relative to steel. The beam sample without stirrups exhibited the lowest shear capacity, followed by beams with 4 or 8 BFRP stirrups, and finally, the beam with 4 steel stirrups, which demonstrated the highest capacity. Increasing the number of stirrups leads to an improvement in shear capacity. Current models, such as the strain approach, are accurate as they represent stirrup contributions within a realistic range.
Although this research highlights the potential of BFRP as shear reinforcement in concrete structures, it is essential to recognize that this study did not consider long-term effects or other dynamic load combinations. The absence of these factors may lead to different findings under varying conditions. Thus, further research is necessary to develop a comprehensive understanding of the long-term sustainability and performance of BFRP as a viable alternative to traditional steel reinforcement in concrete structures.

Contents

List of Figures

List of Tables

1

Introduction

1.1. Background and relevance

Reinforcement in concrete structures improves strength, ductility, and durability, while preventing excessive cracking behaviour and sudden failure. This synergy, known as reinforced concrete, ensures stability and longevity in buildings, bridges, and other infrastructure. However, the environmental impact of steel production, including high energy consumption and greenhouse gas emissions, along with susceptibility to corrosion and high refurbishment costs, has prompted the exploration of alternative materials. Consequently, the engineering community is increasingly adopting innovative materials and technologies to achieve sustainable construction without compromising structural integrity.

The urgency to address environmental challenges and promote sustainable development is underscored by ambitious targets set by governments worldwide (Paris Agreement, 2015). Moreover, the Dutch government has set an ambitious target of establishing a fully circular construction industry by the year 2050 (Rijksoverheid, 2022). This concept aims to minimize waste and resource consumption by promoting the reuse, recycling and regeneration of materials and products. Such initiatives highlight the imperative for the engineering community to embrace sustainable practices and innovative solutions in construction practices.

Basalt Fibre-Reinforced Polymer (Basalt FRP, or BFRP) reinforcement emerges as a promising alternative to steel reinforcement in addressing these sustainability challenges. FRP is a composite material consisting of a polymer matrix reinforced with fibres. The fibres provide strength and stiffness in the direction of their orientation, while the polymer matrix binds the fibres together, protects them from the environment, helps distribute loads between fibres evenly and it transmits forces from the surrounding concrete to the fibres. The production of basalt fibres, derived from natural volcanic rock, requires less energy and goes without addition of any additives (Fiore et al., 2015). This makes it more environmentally friendly than glass or carbon fibres (Ma et al., 2022). Furthermore, basalt fibres offer several advantages over steel, including environmental sustainability, higher tensile strength, and better durability in terms of alkaline resistance (Fiore et al., 2015). Furthermore, BFRP is significantly lighter than steel, which makes it easier and more cost-effective to transport. However, it requires more careful handling because it is more susceptible to damage from impacts and abrasion (Li et al., 2011). This sensitivity necessitates proper packaging and handling procedures to ensure the material maintains its integrity during transportation and installation. The nonmagnetic and non-conductive characteristics of FRP make it highly suitable for reinforcing concrete structures in facilities that contain sensitive electromagnetic equipment, such as hospitals equipped with MRI scanners (Sagar & Sivakumar, 2021). Unlike steel, which is vulnerable to corrosion in aggressive environments, basalt FRP does not undergo rusting. Therefore, it presents a promising option for structural reinforcement in corrosive environments, such as marine and industrial facilities.

Despite the potential advantages of BFRP reinforcement, its widespread implementation in engineering practice requires a thorough understanding of its mechanical and structural behaviour and performance

under various loading conditions. Experimental research on BFRP reinforcement in concrete structures remains relatively limited, particularly in its application as shear reinforcement. Shear reinforcement is typically positioned close to the concrete surface, making it particularly vulnerable to external environmental factors such as moisture, temperature fluctuations, and chemical exposure. Therefore, replacing steel with BFRP in shear reinforcement could offer significant benefits by potentially enhancing the durability and longevity of concrete structures.

This research aims to fill the knowledge gap by conducting a systematic experimental study to assess the mechanical and structural performance of BFRP shear reinforcement in concrete structures. Through the verification of basalt fibre properties, fabrication of BFRP reinforced concrete specimens, and subjecting them to mechanical testing, this study seeks to provide analytical and empirical evidence regarding the viability of BFRP reinforcement for structural applications. By analyzing the analytical and experimental results, this research strives to contribute to the advancement of sustainable development practices.

1.2. Problem statement

Pultrusion is the most common production method for FRP reinforcement. It is an efficient process for producing straight FRP rebar, because it neatly packs down parallel fibres resulting in a generally high fibre volume fraction. However, challenges arise when these pultruded FRP rods include bent sections, as commonly needed for shear reinforcement in concrete structures. These challenges originate from several factors:

- **Kinked fibres in corner sections:** The bending process of pultruded FRP rebar inherently disrupts the alignment of the reinforcing fibres, which is critical for preserving their full tensile capacity (Lee et al., 2010). During the formation of stirrups, where these rebars are bent, the fibres situated on the inner side of the corner sections are prone to kinking. This kinking phenomenon occurs due to the sharp curvature required in these sections, leading to misalignment and localized buckling of the fibres. This is depicted in Figure 1.1 (a). As a result, the tensile strength of the rebar at these bend locations is significantly compromised, since only the fibres that remain un-kinked are effectively engaged when the material is subjected to tensile forces (Ahmed et al., 2010). The reduction in tensile capacity due to fibre kinking poses a considerable challenge in the structural application of bent FRP rebars, as it limits their effectiveness in load-bearing scenarios where tensile forces are critical.
- **Stress concentrations:** The corner sections of FRP stirrups experience significant stress concentrations as a result of the confinement effects imposed by the surrounding concrete. These concentrated stresses act perpendicular to the longitudinal axis of the stirrup, where the matrix material predominantly influences the behavior of the reinforcement. This orientation induces additional shear stresses along the reinforcement in the corner sections. This is illustrated in Figure 1.1 (b). The interplay of tensile and shear stresses at these locations is particularly problematic for FRP materials, as their tensile strength is substantially reduced under combined stress conditions. Consequently, the presence of high stress concentrations in the corners of the stirrups increases the likelihood of structural failure at these critical points (fib, 2007).

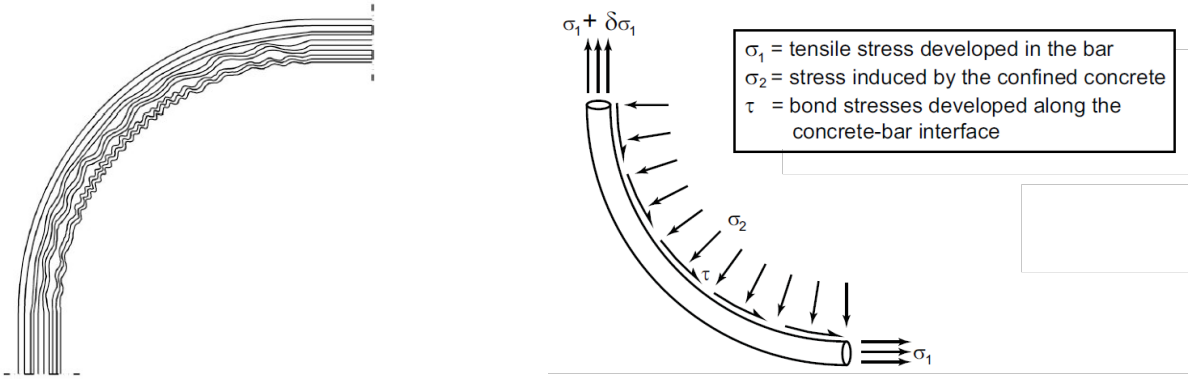

(a) Kinked fibres in corner sections (Ahmed et al., 2010) **(b)** Bent FRP rebar embedded in concrete (fib, 2007)

Figure 1.1: Strength reducing factors bent FRP reinforcement

These stress concentrations, as illustrated in Figure 1.1 (b), would also occur in structures with steel reinforcement. However, they appear different from BFRP due to their different material characteristics: steel is a homogeneous material that has the ability to yield, which allows for stress redistribution. However, in FRP reinforcement, the lack of yielding behaviour induces stress concentrations, leading to potential structural weaknesses. The reduced tensile strength at bends, due to kinked fibres and stress concentrations, limits the effectiveness and viability of traditional pultruded FRP rods in the application of shear reinforcement. The severity of these issues depends on factors such as FRP rod diameter and bend radius, with larger diameters and tighter bends worsening kinking and stress concentration issues.

Morphy et al. (1997) and Shehata et al. (2000) recommend accounting for only 40%-50% of the uniaxial tensile strength in corners for CFRP and GFRP stirrups. This significant reduction in tensile capacity highlights the inherent limitations of conventional pultruded BFRP reinforcement bars when used for shear reinforcement in concrete structures. As a result, current BFRP technology does not provide a viable alternative to steel rebar in these applications. However, alternative forms of BFRP may offer greater potential in addressing these limitations. While these alternative forms could improve the performance of BFRP in shear reinforcement, further research is necessary to validate their effectiveness and to develop suitable design methodologies for their application.

1.3. Scope

This research aims to investigate the applicability of Basalt Fibre-Reinforced Polymer (BFRP) shear reinforcement in concrete structures. The focus is on beam samples due to their universal applicability and practical feasibility in laboratory testing. Additionally, the experimental testing of reinforced concrete beam samples is well-documented in existing literature, providing a rich source of reference material.

To isolate the effectiveness of BFRP stirrups in resisting shear, steel longitudinal reinforcement will be used in all beams, preventing adverse interactions with FRP longitudinal reinforcement.

The research will concentrate solely on internal reinforcement, excluding the strengthening or wrapping of existing concrete structures, to ensure a focused investigation into BFRP shear reinforcement performance within concrete beams.

Additionally, the study will exclusively use cement-based concrete mixtures without any added fibre material. This approach isolates the specific challenges related to BFRP shear reinforcement, avoids the complexities of fibre-reinforced concrete mixtures, and benefits from the well-understood behavior of cement-based concrete.

1.4. Research Objectives

The main objective of this research is to evaluate the potential of BFRP stirrups in enhancing the shear capacity of reinforced concrete beams. The specific sub-objectives are:

1. To investigate various forms of BFRP shear reinforcement and their production methods.
2. To determine the contributing mechanisms to the shear capacity of reinforced concrete beams with and without stirrups, and to analyze the relevant shear failure modes.
3. To explore analytical models for designing concrete beams reinforced with BFRP stirrups and predicting their shear capacity.
4. To compare the cross-sectional and mechanical tensile properties of various forms of BFRP reinforcement with pultruded bars and traditional steel reinforcement.
5. To compare the performance of BFRP stirrups as shear reinforcement in reinforced concrete beams to the performance of traditional steel stirrups.
6. To compare the experimental results for BFRP stirrups in reinforced concrete beams with the predictions from analytical models regarding their shear capacity.

1.5. Research Questions

The main research question is formulated to address the research objective:

"To what extent can BFRP stirrups enhance the shear capacity of reinforced concrete beams?"

To help answer this main research question, a series of sub-questions are derived:

1. How are BFRP stirrups produced?
2. What mechanisms contribute to the shear capacity of reinforced concrete beams with and without stirrups, and what are the relevant shear failure modes?
3. Which analytical models can be used to design concrete beams reinforced with BFRP stirrups and predict their shear capacity?
4. What are the cross-sectional and mechanical tensile properties of different forms of BFRP reinforcement, and how do these compare to traditional steel reinforcement?
5. How does the enhancement in shear capacity of reinforced concrete beams with BFRP stirrups compare to the enhancement provided by traditional steel stirrups?
6. How do the experimental results for BFRP stirrups in reinforced concrete beams compare to the predictions from analytical models?

1.6. Methodogy

This study aims to systematically investigate the mechanical and structural performance of basalt fibre-reinforced polymer shear reinforcement in concrete structures. The methodology involves a comprehensive experimental program, analytical modeling, and comparative analysis with traditional steel reinforcement. The following steps outline the methodology adopted for this research:

Literature Review

A thorough literature review is conducted to gather existing knowledge on FRP materials, particularly BFRP, and their applications in concrete structures. The review covers various types of FRP fibres, matrix materials, production methods, and the mechanical properties of FRP composites compared to traditional steel reinforcement.

Finding suppliers for BFRP stirrups or raw materials

Identifying reliable sources for BFRP materials is a critical step in ensuring the success of the research. This process involves locating suppliers of either pre-fabricated BFRP stirrups or raw materials for manual fabrication. In the case of manual fabrication, production methods are evaluated to determine what is feasible within the research timeframe.

Validation of Cross-sectional Properties and Tensile Testing

The cross-sectional properties of the BFRP samples are validated to determine the cross-sectional area, density and the fibre volume fraction. Mechanical testing of the BFRP stirrups is conducted to evaluate their tensile properties, including tensile strength and modulus of elasticity. Additional tests are performed to assess the tensile capacity at the bent regions of the stirrups. These tests help in understanding the impact of kinked fibres and stress concentrations on the structural performance of BFRP stirrups.

Beam design and preparation

Reinforced concrete beams are prepared. Two beams, with and without steel stirrups, will serve as a reference. Subsequently, beams with basalt FRP stirrups as shear reinforcement are prepared. Reinforcement cages are prepared and optical fibres are bonded to each stirrup to continuously measure its strain. The concrete mix is prepared using cement-based materials without additional fibres to maintain consistency in the experimental setup.

Shear Testing of Reinforced Concrete Beams

The reinforced concrete beams with BFRP stirrups undergo shear testing to determine their shear capacity. The tests are conducted using a controlled setup to measure load, displacement, and crack propagation. The performance of BFRP-reinforced beams is compared to that of beams reinforced with traditional steel stirrups.

Data Analysis and validation of Analytical Model

The experimental data is analyzed to identify key performance indicators such as shear capacity, crack patterns, and failure modes. The results are used to validate theoretical models that predict the shear capacity of reinforced concrete beams with BFRP stirrups. Comparative analysis with steel-reinforced beams is performed to highlight the differences and potential advantages of BFRP reinforcement.

Conclusions and Recommendations

Based on the analysis and discussion, conclusions are drawn regarding the feasibility and effectiveness of BFRP shear reinforcement in concrete structures. Recommendations for future research and potential practical applications are provided, aiming to advance the use of FRP materials in the construction industry.

1.7. Thesis Outline

The outline of this thesis report is as follows. Chapter 2 provides a literature review, examining various aspects of FRP materials, forms of FRP shear reinforcement, design methodologies and the influencing factors for the shear capacity of reinforced concrete beams. Chapter 3 presents the design for the BFRP stirrups, the experimental setup and results for the verification of cross-sectional properties, uniaxial tensile testing and corner tensile capacity testing of basalt FRP reinforcement. Subsequently, the results from these experiments are used as input parameters in the final experiment to determine the shear strength of concrete beams reinforced with these alternative types of BFRP shear reinforcement. Chapter 4 presents the procedures and conditions of the experimental setup conducted for the reinforced concrete beams. Chapter 5 provides the results from the beam experiments, while Chapter 6 offers an in-depth analysis, comparison, and discussion of the beam test results. Finally, Chapter 7 presents the conclusions drawn from the study, along with recommendations for future research and practical applications.

2

Literature review

This literature review explores the use of basalt FRP shear reinforcement in concrete structures, focusing on its properties, applications, and design considerations. Basalt FRP, made from natural volcanic rock, offers an interesting alternative to traditional steel and other types of FRP due to its optimum balance in strength and potential environmental benefits. Understanding its performance and behavior in shear reinforcement applications is essential for fully utilizing its potential in modern construction.

2.1. Fibre-Reinforced Polymer Materials

Fibre-reinforced polymers (FRPs) are advanced composite materials consisting of a polymer matrix embedded with high-strength fibres. As depicted in Figure 2.1, it integrates two distinct components, each contributing to the overall performance of the material. The fibres act as the primary reinforcement, offering strength and stiffness in its longitudinal direction, which are essential for the load-bearing capacity of the composite. These fibres, typically made from materials such as carbon, aramid, glass or basalt, are the main contributors to the enhanced mechanical properties of FRPs.

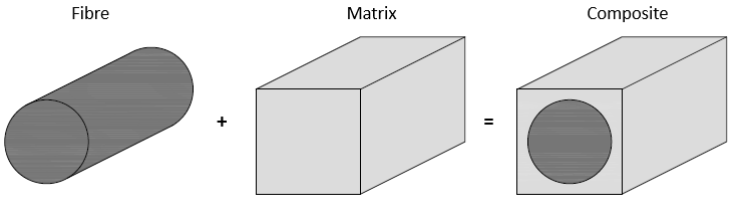

Figure 2.1: Schematic composition of FRP materials

The polymer matrix is essential for binding the fibres together, ensuring proper alignment and orientation to maximize the composite's mechanical performance. This matrix also plays a pivotal role in distributing loads among the fibres, ensuring that stress is evenly spread across the material's entire cross-section. Furthermore, the polymer matrix protects the fibres, shielding them from environmental factors such as moisture, chemicals, and UV radiation, as well as from mechanical damage. The combination of high-strength fibres and a resilient polymer matrix creates a synergistic effect in FRPs, resulting in a material that leverages the best properties of both components.

2.1.1. Fibres

Fibres are essentially thin filaments with diameters ranging from 3 to 20 microns. These tiny fibres are bundled into long or short groups, often comprising around 2,000 filaments. These bundles form reinforcement structures such as rovings, mats, or fabrics with unidirectional or bidirectional orientation.

The production of fibres for FRP composites involves precise processes that ensure consistent quality

and performance. These processes typically include polymerization of raw materials, followed by spinning, drawing, and heat treatment to align the fibre molecules and enhance their mechanical properties.

According to Campbell (2010), fibres generally possess much higher strengths compared to the bulk form of the same material. This is because the likelihood of flaws per unit length decreases with the volume of material. Due to their low volume per unit length, fibres are generally stronger than bulk materials, which have a higher volume per unit length and thus a greater number of flaws. However, bulk materials show more consistent strength due to their uniform distribution of flaws. Consequently, smaller diameter and shorter length fibres exhibit higher average and maximum strengths but also greater variability.

The higher strength of fibres compared to their bulk counterparts comes with increased variability, largely due to the flaws they contain, particularly on their surfaces. To minimize these flaws, careful manufacturing processes and protective coatings are applied, reducing mechanical and environmental damage and improving the overall performance of the fibres in FRP composites (Campbell, 2010).

The most commonly fibres used for FRP reinforcement are carbon, aramid, glass and basalt. Figure 2.2 and Table 2.1 give an overview of the tensile strength characteristics of these fibre types.

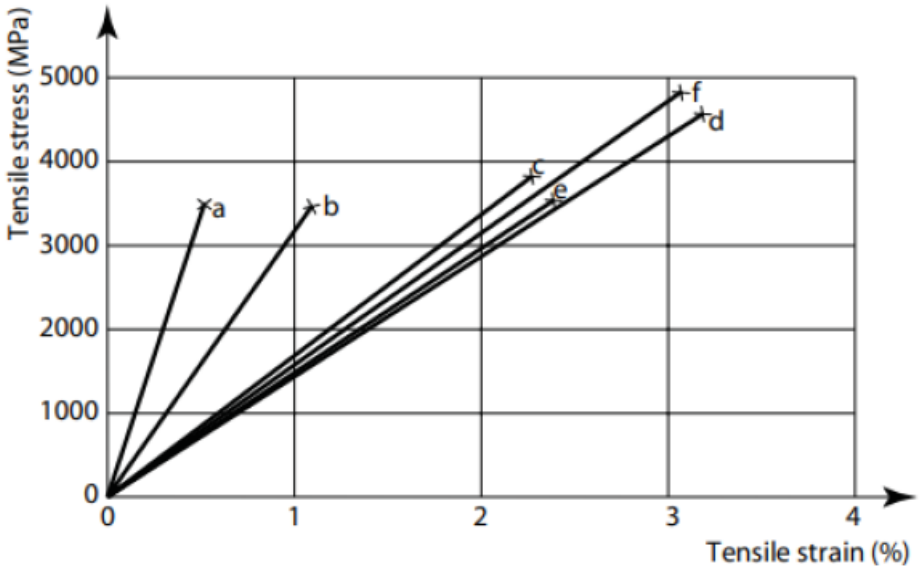

Figure 2.2: Stress-strain diagram of typical reinforcing fibres: a) high modulus carbon; b) high strength carbon; c) aramid; d) S-glass; e) E-glass; f) basalt (fib, 2007)

Table 2.1: Typical mechanical properties for single filament fibres that are commonly used for FRP composites (fib, 2007).

Fibre type	Density ρ [kg/m^3]	Tensile strength f_u [MPa]	Young's modulus E [GPa]	Strain at failure ε_u [%]
Carbon (high modulus)	1950	2500-4000	350-650	0.5
Carbon (high strength)	1750	3500	240	1.1
Aramid (Kevlar49)	1440	3620	124	2.2
S-glass	2500	4580	86	3.3
E-glass	2500	3450	72	2.4
Basalt	2800	4840	89	3.1

From this figure and table, it can be observed that carbon fibres display the highest tensile strength and stiffness. Aramid fibres, such as Kevlar49, are next in line, providing high strength but lower stiffness. Glass fibres, including S-glass and E-glass, offer high tensile strength with moderate stiffness at a

moderate density. Basalt fibres are the densest, with the highest tensile strength, and a comparable (but somewhat higher) stiffness to glass fibres.

Carbon fibres

Carbon fibres are essential in numerous applications due to their exceptional mechanical properties, their lightweight, and high thermal and chemical stability (Peng et al., 2024). Carbon fibres are widely utilized in aerospace, automotive, and sporting goods industries owing to their high strength-to-weight ratio and rigidity. In aerospace, they are used to manufacture aircraft components, contributing to weight reduction and improved fuel efficiency (Koumoulos, 2019). Additionally, carbon fibres are utilized in the production of wind turbine blades, sporting equipment, and as reinforcement for concrete structures, enhancing strength and durability (Ajay Kumar et al., 2020; Daniyan et al., 2020).

The production process involves several stages, including spinning precursor fibres from PAN or pitch and stabilizing them through oxidation at 200-300°C. This is followed by carbonizing at 1000-1500°C in an inert atmosphere and graphitizing at temperatures over 2000°C. This sequence removes non-carbon elements and aligns carbon atoms into tightly bonded, carbon-rich structures. Surface treatments and sizing are then applied to improve fibre-matrix adhesion in composite materials. (Ajay Kumar et al., 2020; Koumoulos, 2019).

Aramid fibres

Aramid fibres, known for their high strength and heat resistance, are synthetic fibres made from aromatic polyamides. Brands like Kevlar (by DuPont) and Twaron (by Teijin) are well-known examples (Campbell, 2010). These fibres exhibit remarkable mechanical properties, including high tensile strength and modulus, making them suitable for demanding applications such as aerospace, military, and automotive industries. They are commonly used in ballistic body armor, aerospace components, and marine cords or ropes (García et al., 2010; F. Wang et al., 2018).

Aramid fibres are produced through the polycondensation reaction of aromatic polyamides, involving the polymerization of monomers like terephthaloyl chloride and p-phenylenediamine. This forms long molecular chains with strong hydrogen bonds, contributing to the fibres' exceptional mechanical properties and thermal stability (García et al., 2010). The fibres are spun into filament yarns or processed into staple fibres for use in fabrics or composite materials.

The production process includes dissolving the polymer in a solvent to create a spinning dope, which is extruded through spinnerets to form fibres. These fibres are drawn to align the molecular chains, enhancing their strength and stiffness. The final product undergoes heat treatment to stabilize its molecular structure, ensuring the fibres retain their properties under high stress (H. Yang, 2000).

Glass fibres

Glass fibres are integral components in composite materials, particularly glass-fibre-reinforced polymers (GFRP). These composites are preferred in the automotive, marine, and construction industries due to their strength-to-weight ratio and their relative low cost. E-glass fibres, noted for their high electrical resistivity, are extensively used in electrical and thermal insulation, as well as in the fabrication of wind turbine blades and sports equipment (Rue et al., 2017; Veit, 2022). S-glass fibres, which possess superior tensile strength and modulus, are employed in aerospace and military applications where advanced mechanical performance is of importance (Veit, 2022).

The manufacturing process of glass fibres involves melting raw materials, predominantly silica, along with other oxides such as alumina (Al□O□) and calcium oxide (CaO). The molten glass is extruded through fine orifices to create thin filaments, which are subsequently cooled and solidified. These filaments can be transformed into continuous strands or chopped into shorter fibres, depending on the intended application. Coating the fibres with sizing agents enhances their adhesion to resin matrices in composite materials (Campbell, 2010; Veit, 2022). Advanced manufacturing techniques, such as high-performance glass (HPG) processes, have improved the efficiency and quality of glass fibre production, making them more cost-effective and environmentally friendly (Veit, 2022).

Basalt fibres

Basalt fibres are increasingly valued in various industrial applications due to their impressive mechanical properties, cost-effectiveness, and environmental benefits. These fibres are derived from basalt rock, a naturally occurring volcanic rock, and are known for their superior thermal stability, high tensile strength, and resistance to chemical and environmental degradation.

According to Nanni et al. (2014) and Veit (2022), the production of basalt fibres begins with the extraction of basalt rock, which is crushed and heated to temperatures between 1400 and 1700°C. This process transforms the solid rock into a molten state, which is subsequently extruded through alloy bushings to form thin filaments. These filaments are rapidly cooled, e.g. by water or air spray, to create continuous fibres (Campbell, 2010). To enhance their bond with the polymer matrix, the fibres are coated with sizing agents before being wound onto spools for further processing. These steps are illustrated in Figure 2.3.

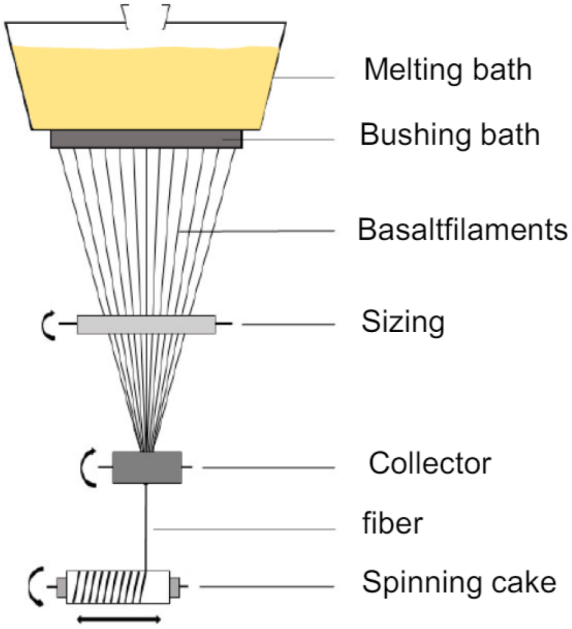

Figure 2.3: Production of basalt fibres (Deutsche Basalt Faser, n.d.)

Basalt fibres find extensive use in a variety of industries, such as construction, automotive, aerospace, and marine sectors. They are highly valued for their high strength-to-weight ratio, fire resistance, acoustic insulation, vibration isolation, and resistance to chemical environments (Indraneel R. Chowdhury, 2022; Mancini, 2023). These properties position basalt fibres as a suitable replacement for glass fibres in many applications and a more cost-effective alternative to carbon fibres.

Figure 2.4 illustrates the energy required to produce 1 kg of basalt, glass, steel, and carbon fibres. Basalt fibres are more environmentally friendly compared to other types of FRP because their production process does not necessitate chemical additives or hazardous substances (Al-Rousan et al., 2023), and they have a significantly lower energy requirement than other fibre materials. The relative energy ratios for these materials are approximately 1:2:3:40, highlighting basalt fibres as a cost-effective and sustainable option.

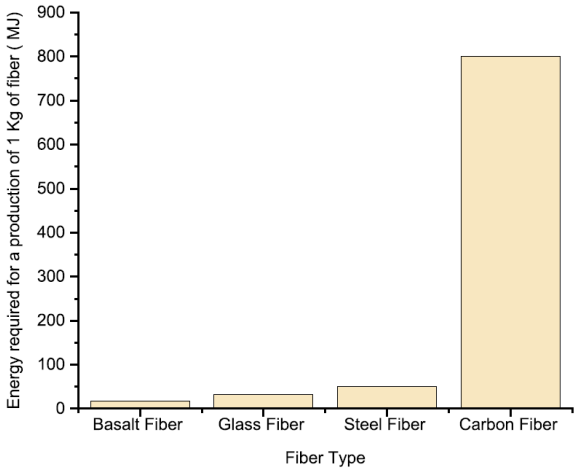

Figure 2.4: Energy required for manufacturing different fibres (Al-Rousan et al., 2023)

Moreover, Nanni et al. (2014) state that basalt fibres can be chemically modified to enhance their bio-solubility, which allows them to gradually dissolve when exposed to biological fluids, meeting international regulatory requirements for bio-solubility in the glass fibre industry.

2.1.2. Matrix material

The matrix structure in FRPs plays a crucial role as the binding agent that secures the fibres in place, ensuring the load is effectively transferred between individual fibres and from the concrete to the fibres. This matrix also provides essential protection to the fibres against environmental factors such as moisture, chemicals, and UV radiation. The selection of the appropriate matrix material is vital as it significantly influences the overall mechanical properties and durability of the composite material.
According to Nanni et al. (2014), fib (2007) and Askar et al. (2022), the matrix materials in FRP can be broadly divided into two most categories: thermoset resins and thermoplastic resins. The most common types of thermoset resins are epoxies, polyesters and vinyl esters. They are preferred for civil engineering purposes for several reasons. Firstly, thermoset resins exhibit superior heat resistance, maintaining their structural integrity at elevated temperatures, unlike thermoplastics that soften when exposed to heat. Secondly, thermoset resins offer better mechanical properties including high strength and stiffness, which makes them suitable for structural applications. Thirdly, thermoplastics offer better chemical resistance, which makes it more suitable for environments with exposure to corrosive environments. Lastly, thermoset resins are compatible with various manufacturing processes used in FRP production, such as resin transfer moulding, pultrusion and filament winding. Thermoplastics are less suited for this purpose due to its high viscosity.

An overview of the most common types of thermoset matrix materials is shown in Table 2.2.

Table 2.2: Typical mechanical properties for common types of thermoset matrix materials used for FRP (fib, 2007).

Material characteristic		Epoxy	Polyester	Vinyl ester
Density	[kg/m^3]	1200 - 1400	1200 - 1400	1150 - 1350
Tensile strength	[MPa]	55 - 130	35 - 104	73 - 81
Elastic modulus	[GPa]	2.8 - 4.1	2.1 - 3.5	3.0 - 3.5

The disadvantage of thermoset resin is that its shape cannot be altered by applying heat, unlike thermoplastic resins. This is due to cross-links that form during curing in thermosets. Figure 2.5 illustrates the structural differences between thermoset and thermoplastic polymers before and after processing. In thermoset polymers, polymer chains undergo a chemical reaction during processing that forms cross-links, creating a rigid and strong three-dimensional network. These cross-links, which are covalent bonds, prevent the material from melting and reshaping upon reheating, thereby giving thermosets their heat-resistant and structurally stable properties (Campbell, 2010). It should be noted, however,

that if the temperature rises beyond a specific point, the mechanical properties of thermosets degrade significantly as the resin transitions from a rigid, glass-like state to a more flexible, rubber-like state (Nijssen, 2015).

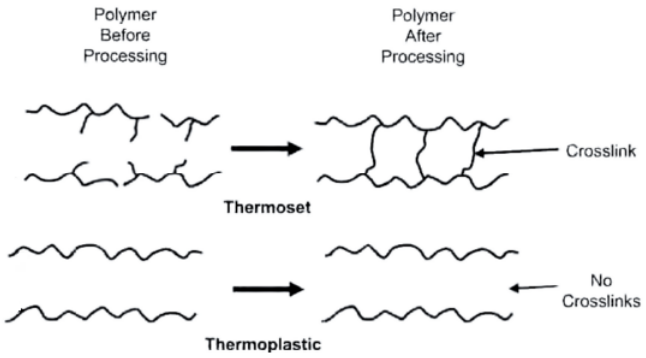

Figure 2.5: Thermoset versus thermoplastic polymers (edited figure from Campbell, 2010).

In contrast, Campbell (2010) explains that thermoplastic polymers do not form cross-links during processing. Instead, the polymer chains remain separate and can slide past one another, allowing thermoplastics to be melted and reshaped multiple times. This means that, if desired, FRP reinforcement can only be bent into the desired stirrup shape before the resin has cured. Consequently, FRP stirrups must be pre-produced according to specific requirements, unlike steel reinforcement stirrups, which can be bent on-site to meet varying specifications.

This necessity for pre-production adds complexity and potential delays to construction projects using FRP reinforcement, thus the highest potential FRP stirrups are in prefabrication, allowing for the production of custom shapes and sizes in a controlled environment.

Durability of matrix materials

The selection of an appropriate matrix material is a critical factor in determining the tensile strength, impact resistance, and overall durability of FRP composites. The matrix serves not only as the binder for the reinforcing fibres but also as a protective barrier against environmental and mechanical stresses. When the matrix material is inadequately chosen, it can lead to premature failure of the composite, especially under conditions of stress or exposure to adverse environmental factors. The long-term performance of FRP composites can be significantly compromised by the degradation of the matrix due to influences such as UV radiation, temperature fluctuations, water ingress, alkalinity, and creep.

For instance, epoxy matrices are commonly used due to their excellent adhesion properties and chemical resistance. However, they can be susceptible to degradation in highly alkaline environments such as those found in concrete. This involves sodium hydroxide (NaOH) and sodium carbonate (Na2CO3) and necessitates further research to ensure long-term stability (Chen et al., 2007; J. Wang et al., 2016).

Polyester matrices, while cost-effective, generally exhibit lower resistance to chemical and moisture ingress, which can compromise the integrity of the FRP over time (Karbhari et al., 2002). On the other hand, vinyl ester matrices offer improved resistance to corrosive environments but may still face challenges in maintaining structural integrity over extended periods, particularly in harsh alkaline conditions (Feng et al., 2022).

In summary, the matrix material in FRP composites is a critical determinant of the composite's mechanical and environmental performance. The ongoing research and development efforts are essential to enhance the resilience and longevity of these materials when applied as shear reinforcement for concrete structures, ensuring their reliability and effectiveness. (Davalos et al., 2012; Chu et al., 2004).

2.1.3. FRP Composites

The tensile properties of traditional steel reinforcement and for the most common types of FRP are summarized in Table 2.3. From this table it can be observed that the tensile strength characteristics of FRP demonstrate a wide range of mechanical properties.

Table 2.3: Typical tensile properties for FRP composites* and steel rebar (ACI 440.3R-15, 2015; fib, 2007).

Material	Nominal yield strength f_y [MPa]	Tensile strength f_u [MPa]	Young's modulus E [GPa]	Yield strain ε_y [%]	Ultimate strain ε_u [%]
Steel	500	540 - 650	200	0.2 - 0.25	5 - 20
CFRP	N.A.	600 - 3500	100 - 580	N.A.	0.5 - 1.7
AFRP	N.A.	1000 - 2500	40 - 125	N.A.	1.9 - 4.4
GFRP	N.A.	450 - 1600	35 - 60	N.A.	1.2 - 3.7
BFRP	N.A.	600 - 1650	40 - 65	N.A.	1.6 - 3.0

* based on a typical fibre volume fraction of 50%-75%

Traditional steel reinforcement, such as FeB 500B, is widely used in construction due to its reliable mechanical properties. This type of steel has a nominal yield stress of 500 MPa, which means it can withstand significant stress before deforming permanently. The ultimate tensile strength of FeB 500B ranges from 540 to 600 MPa, indicating the maximum stress it can endure before breaking. Additionally, it possesses a Young's modulus of 200 GPa, reflecting its stiffness and ability to resist deformation under stress.

After yielding, FeB500B steel reinforcement undergoes strain hardening, a process where the material becomes stronger and more resistant to further deformation. The design does not take this into account, thus it is often stronger than accounted for. Furthermore, B500B has a failure strain greater than 5%, signifying that it can stretch considerably before breaking. This high failure strain ensures the ductility of steel-reinforced structures, meaning they can bend and deform significantly without sudden failure. This combination ensures that steel-reinforced structures exhibit safe failure behavior, since they can absorb and dissipate energy through deformation, providing critical warning signs in the form of substantial cracking or deflection before collapsing.

In contrast, FRP materials generally exhibit a linear elastic stress-strain behaviour upon failure, without an evident yielding phase as seen in steel. Additionally, FRP reinforcements typically exhibit low transverse strength and stiffness because the matrix material primarily influences these properties in the transverse direction, rather than the fibres which dominate in the longitudinal direction. This anisotropic behavior highlights the need for careful consideration of loading directions in design applications to fully utilize the advantages of FRP materials while accounting for their limitations.

From the table it can be observed that carbon FRP (also known as CFRP) shows exceptional tensile strength, ranging from 600 to 3500 MPa, and an elastic modulus between 100 and 580 GPa. However, CFRP has a much lower failure strain, which is in the range of 0.5% to 1.7%. Aramid FRP (or AFRP) also shows high tensile strength (1000 to 2500 MPa) and a moderate Young's modulus (40 to 125 GPa), with a failure strain of 1.9% to 4.4%, offering better ductility than CFRP but still lacking the yielding phase. Glass FRP (or GFRP), with tensile strength between 450 and 1600 MPa and a Young's modulus of 35 to 60 GPa, provides a more balanced profile of strength and stiffness but with lower values compared to CFRP and AFRP. Its failure strain ranges from 1.2% to 3.7%, which is higher than CFRP. Basalt FRP (BFRP) offers tensile strength between 600 and 1650 MPa and a Young's modulus of 40 to 65 GPa, with a failure strain of 1.6% to 3.0%, positioning it between GFRP and AFRP in terms of both strength and ductility.

Durability of FRP in alkaline environments

The long-term durability of FRP reinforcements, particularly under exposure to environmental factors like alkalinity, is crucial for their effective use in civil engineering structures. Concrete environments present a highly alkaline environment, with pH values typically ranging between 12 and 13.5. Unlike traditional steel reinforcements, which generally do not corrode at such high pH levels due to the for-

mation of a passive oxide layer, FRP materials may experience significant durability challenges. This is particularly true for glass FRP, which are prone to degradation in alkaline conditions. The primary mechanism involves the hydrolysis of the silica network within the glass fibres, leading to a reduction in tensile strength and stiffness. Studies have shown that GFRP can suffer from a reduction in tensile strength by as much as 50% after prolonged exposure to alkaline conditions (Bank, 2006).

Carbon fibre-reinforced polymers (CFRP) and aramid fibre-reinforced polymers (AFRP) offer superior resistance to alkaline environments compared to GFRP. The carbon fibres in CFRP, characterized by their graphite-like structure, are chemically inert and therefore resistant to hydrolytic degradation. Aramid fibres, although not as chemically inert as carbon fibres, exhibit better performance than glass fibres due to their aromatic polyamide structure, which is less prone to hydrolysis. However, both CFRP and AFRP are still subject to potential degradation of the polymer matrix, which can occur through hydrolytic processes, especially if the matrix material itself is susceptible to breakdown by water in alkaline environments (Benmokrane et al., 2002).

Basalt FRP, or BFRP, has emerged as a promising alternative to GFRP due to their natural resistance to alkalis and other corrosive agents. Basalt fibres are derived from volcanic rock and possess a structure that is less prone to hydrolytic degradation compared to glass fibres. This makes BFRP more durable in alkaline environments, where the mechanical properties of basalt fibres are better maintained over time (Singh et al., 2015). However, as with other FRP systems, the durability of BFRP is also influenced by the matrix material and the fibre-matrix interface, which can be affected by prolonged exposure to moisture and alkaline conditions.

2.1.4. Corner tensile strength

The determination of corner tensile capacity for FRP reinforcement is a critical aspect of evaluating the performance of FRP in structural applications. According to the guidelines provided by the American Concrete Institute (ACI 440.3R-12, 2012), two distinct testing methods are recommended for assessing the tensile strength of FRP reinforcements at corner locations:

1. **Test Method B.5 - Strength of FRP Bent Bbars and Stirrups in Bend Locations:** This method is designed to evaluate the tensile strength of FRP bent bars and stirrups specifically at the locations of bends. The procedure involves embedding the bent portion of the FRP stirrups within concrete blocks, simulating real-world conditions encountered in structural elements. Tensile forces are then applied to the anchored stirrups until failure occurs, providing a direct measure of the tensile strength at the bend location. The setup for this method is depicted in Figure 2.6 (a).
2. **Test Method B.12 - Effect of Corner Radius on Tensile Strength of FRP Bars:** This method focuses on isolating and understanding the influence of the corner radius on the tensile strength of FRP bars. The FRP specimen is pulled over steel corner inserts with a defined radius until failure, allowing for an assessment of how the corner geometry affects tensile capacity. This method does not simulate the embedding of the FRP in concrete but rather isolates the geometric factor of the corner radius. The setup for this method is illustrated in Figure 2.6 (b).

The primary distinction between these two methods lies in their approach to simulating the conditions under which FRP reinforcement operates in structural elements. Test Method B.5 offers a more comprehensive simulation by embedding the FRP corners within concrete blocks, thereby mimicking the actual stress conditions that occur in concrete structures. On the other hand, Test Method B.12 provides a more controlled analysis of the effect of corner radius by utilizing steel inserts, thus isolating this variable from other potential influences.

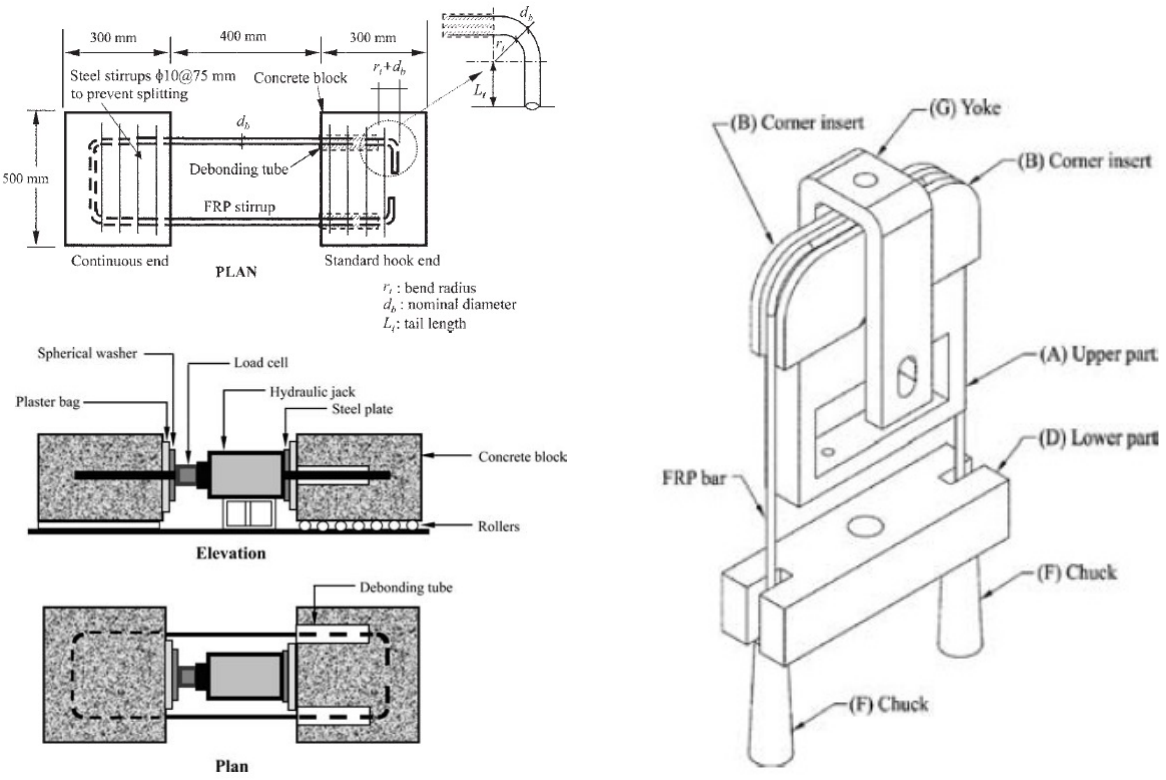

(a) B.5 test method **(b)** B.12 test method

Figure 2.6: Corner tensile test methods (ACI 440.3R-12, 2012)

In a comparative analysis conducted by Ahmed et al. (2010), these two methods were evaluated to determine their effectiveness in predicting the tensile strength of FRP reinforcement at corners based on experimental data. The study revealed that the B.12 test method, which isolates the corner radius effect, tends to underestimate the tensile strength of FRP stirrups. This underestimation is likely due to the method's inability to replicate the complex stress conditions present in real structural applications where the FRP is embedded in concrete. Conversely, the B.5 test method demonstrated greater reliability, as its testing conditions more accurately reflect the stress states experienced by FRP reinforcement in actual concrete structures. This suggests that B.5 is a more suitable approach for assessing the tensile strength of FRP in practical scenarios where the reinforcement is integrated into structural elements.

For practical considerations, a revised design of this test is proposed in Appendix A, adapted for use with a Universal Testing Machine (UTM).

2.2. Shear capacity of reinforced concrete beams

Shear failure in reinforced concrete beams is a critical aspect of structural engineering, often dictating the design and reinforcement strategies to ensure the safety and durability of structures. Shear failure occurs when a beam cannot withstand the internal shear forces induced by the applied loads, leading to a sudden and brittle fracture. Unlike flexural failure, which is often ductile and provides warning through significant deflections and cracking, shear failure can occur with little to no warning, making it particularly dangerous.

Under loading, shear forces cause diagonal tensile stresses in the beam. When these stresses exceed the tensile strength of the concrete, diagonal cracks form, typically originating near the supports and propagating towards the load application points. These cracks can intersect the compression zone and, if left unchecked, can lead to the beam's failure.

Shear reinforcement, such as stirrups, is designed to intercept and bridge these diagonal cracks, pro-

viding additional tensile capacity and preventing the cracks from widening. The stirrups work by taking over the tensile forces that the concrete can no longer resist due to cracking. Without adequate shear reinforcement, the beam relies solely on the concrete's tensile strength and aggregate interlock, both of which can be insufficient under high shear stresses.

2.2.1. Mechanisms contributing to shear capacity

According to fib (2007), the shear response of reinforced concrete elements is an intricate phenomenon that relies on internal load-bearing mechanisms of which the extend and combination still remains a topic of discussion. Nonetheless, it is acknowledged that the shear strength of RC components is mainly influenced by the contribution from the uncracked compression zone, aggregate interlock at the interface of shear-induced cracks, reinforcement's dowel action, and the presence of shear reinforcement (when provided). These mechanisms do not only depend on the mechanical properties of the concrete and the reinforcing material itself, but also on the interaction between the two.

An overview of these shear transfer mechanisms and their respective locations are illustrated in Figure 2.7.

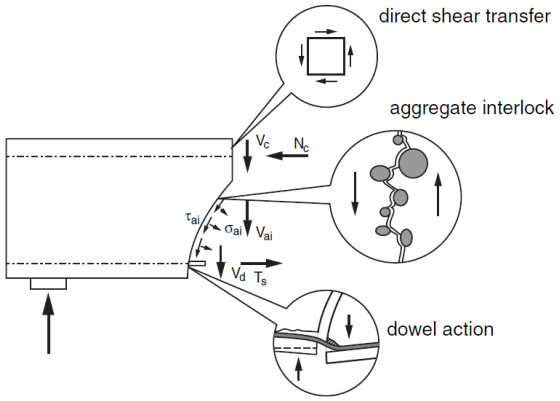

Figure 2.7: Shear transfer mechanisms in a reinforced concrete beam (Y. Yang et al., 2017)

Contribution of (uncracked) compression zone

In an uncracked concrete beam, shear forces are parabolically distributed across its height, with the maximum shear stress at the neutral axis. Initially, the concrete resists these forces effectively due to its intact structure. However, when tensile stresses exceed the concrete's tensile strength, cracks form, altering the internal force distribution as the lower-stiffness reinforcement becomes active.

After cracking, the uncracked compression zone above the shear crack becomes of importance for transferring shear forces. This zone, with its higher stiffness and intact structure, effectively carries shear forces, maintaining the beam's structural integrity by bridging the cracked tension zone. This is shown in 2.8.

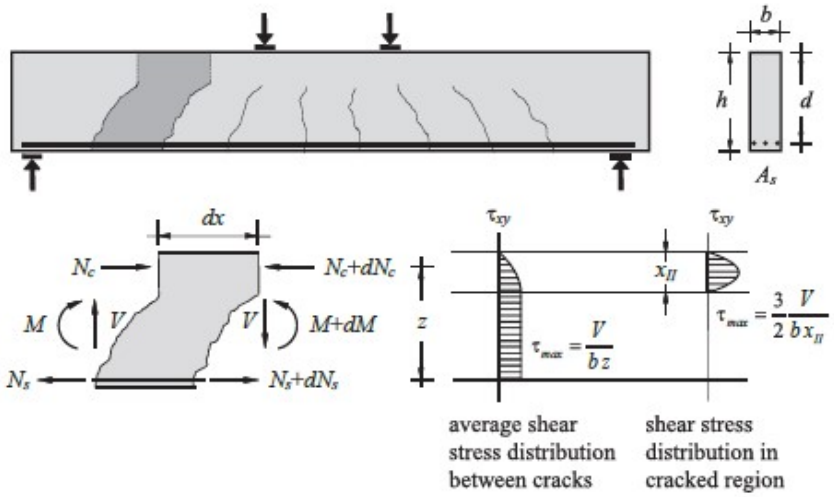

Figure 2.8: Shear transfer through the compression zone (Bogdándy, 2021)

Aggregate interlock

In the tensile zone, mechanical interlock facilitates shear transfer across a crack when there is a shear displacement parallel to the crack. This phenomenon is illustrated in Figure 2.9. Numerous experiments have been conducted over the years to explore this phenomenon and quantify its contribution to the overall shear capacity of a concrete structure. Findings by Taylor (1970) indicate that, for beams without shear reinforcement, aggregate interlock can account for approximately 33 to 50% of the shear capacity of uncracked concrete. However, this percentage decreases as the crack width increases (Walraven, 1981).

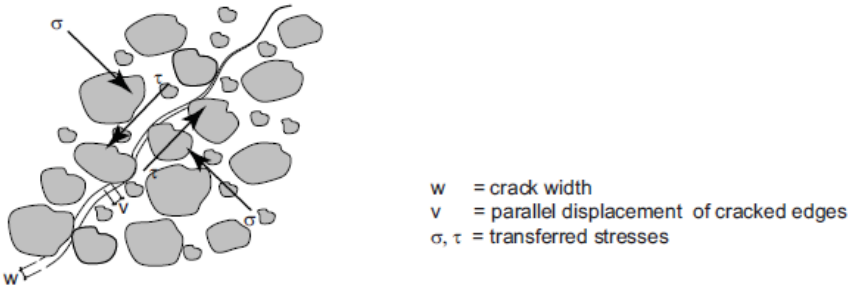

Figure 2.9: The principle of aggregate interlock through an inclined shear crack surface (fib, 2007)

The maximum aggregate size influences shear resistance because larger aggregates increase the roughness of crack surfaces. This increased roughness allows higher shear stresses to be transferred across cracks, enhancing shear resistance through aggregate interlock. However, in high-strength concrete beams, the tensile strength of the concrete surpasses that of the aggregates, causing cracks to pass through the aggregates rather than around them. As a result, the crack surfaces become smoother, leading to a reduction in shear transfer via aggregate interlock.

Dowel action of flexural reinforcement

When a shear crack forms in a concrete beam, it can cause the beam to slip and open. Dowel action refers to the mechanism where the longitudinal reinforcement in concrete beams acts like dowels, bridging the crack and resisting this slipping and opening. This resistance is achieved through a combination of bending and shear forces in the longitudinal rebar, as illustrated in Figures 2.10 (a) and (b), respectively.

(a) Flexural resistance for increased crack widths

(b) Shear resistance for limited crack widths

Figure 2.10: Dowel action mechanisms for longitudinal reinforcement (fib, 2007)

Tests conducted by Baumann and Rüsch (1970) indicate, however, that the maximum shear force that dowel action can support is quite limited. Regan (1993) found that dowel action typically contributes only 15–25% of the total shear resistance. Moreover, once the maximum dowel force is reached, the behavior observed is nearly plastic. Additionally, the maximum resistance provided by dowel action is influenced by the tensile strength of the concrete cover, which can fail through splitting if the dowel action force becomes too high. Consequently, dowel action is often disregarded in literature based on these force criteria.

Parameters that affect the shear strength of reinforced concrete beams without stirrups

From experiments, it was empirically found that the following factors influence the shear capacity of beams without shear reinforcement:

- **Concrete strength class:** All the mentioned contributions increase with the strength of the concrete, as long as the cracks form around the aggregates. This typically holds true up to a concrete compressive strength of approximately 60 MPa. For higher concrete strengths, cracks tend to propagate through the aggregates, which reduces crack surface roughness and subsequently diminishes the shear capacity contribution from aggregate interlock.
- **Longitudinal reinforcement ratio:** With a higher longitudinal reinforcement ratio, the crack width is smaller, resulting in higher tensile stresses σ_{ct} and increased crack friction τ_a. In case when the longitudinal reinforcement ratio is low, flexural cracks open wider. This increase in crack width causes a decrease in the values of the components of shear resistance, which are transferred across the inclined cracks.
- **Beam dimensions:** The cross-sectional dimensions, including the width and height of the beam, affect its shear strength. Taller beams generally have higher shear capacities, although this relationship is not directly proportional.
- **Position of the load:** The position of the load in relation to the support is characterized by the ratio of shear span a over effective height d. There are two primary ranges for the a/d ratio that influence shear failure mechanisms:
  - **Small a/d ratio (a/d < 2.5):** When the a/d ratio is small, the beam tends to exhibit what is known as ”arch action”. The applied load is transferred directly to the support through a compressive strut in the concrete, forming an arch shape. In this scenario, the shear cracks that form are often restrained within the load introduction zone, and the beam can sustain higher loads without immediate failure. Failure is likely to occur due to crushing of the concrete in the arch or by splitting along the compression struts.
  - **Large a/d ratio (a/d > 2.5):** When the a/d ratio is large, the behavior of the beam is governed more by flexural action rather than arch action. In this scenario, shear forces are resisted by the shear capacity of the concrete (through previously described mechanisms) and by the shear reinforcement if present. Diagonal tension cracks typically form and propagate towards the compression zone, causing the beam to fail in shear. The shear cracks can develop rapidly and lead to a more brittle failure. The failure mechanism is often due to diagonal tension failure where the concrete cracks and the beam fails suddenly without significant prior warning.

Shear reinforcement (if provided)

When the load-bearing capacity of an element without shear reinforcement cannot support the design load, it is necessary to increase the shear capacity by adding shear reinforcement. Typically provided as vertical links, this transverse reinforcement transfers tensile forces across inclined shear cracks, enhancing the concrete element's overall shear capacity. By compensating for the force lost due to cracking, shear reinforcement allows for a further increase in load capacity. This is illustrated in Figure 2.11.

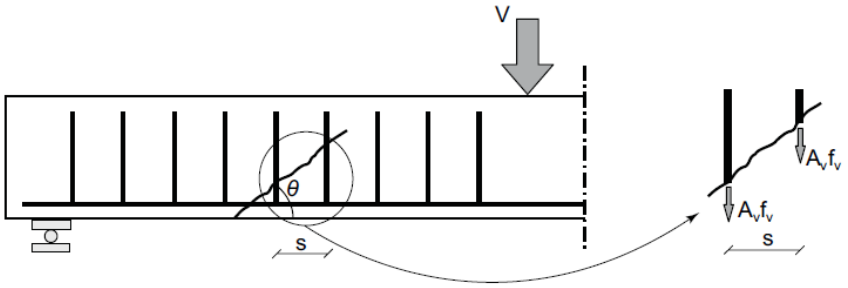

Figure 2.11: Tensile force transfer across inclined shear cracks through vertical stirrups (fib, 2007)

Beams with shear reinforcement exhibit a significantly different cracking pattern than those without it. In shear-loaded zones, cracks tend to deflect above the longitudinal reinforcement and run almost parallel to each other. This behavior was described by Mörsch (1908) using the "truss analogy". According to this analogy, the beam's compression zone and longitudinal reinforcement are modeled as the upper and lower chords of a truss, separated vertically by the internal lever arm z. The truss includes compression diagonals at an angle θ and vertical tension members spaced at $z \cdot \cot\theta$. This is illustrated in Figure 2.12.

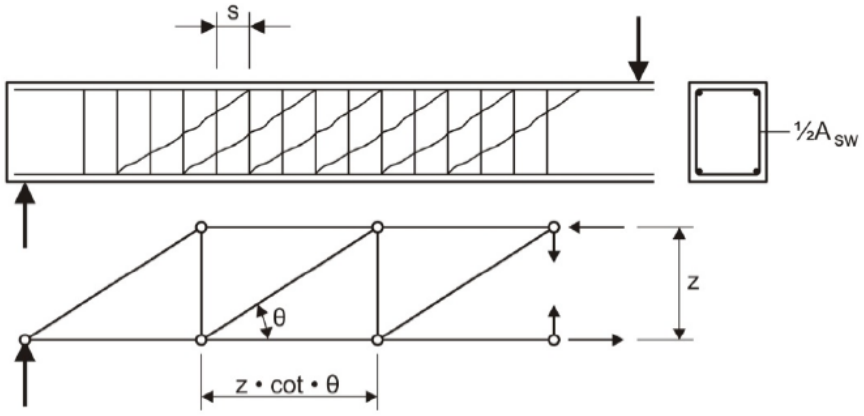

Figure 2.12: Truss analogy: vertical tension links and diagonal compression struts (Figure by Fennis, 2013)

The cross-sectional area of a vertical tension member in the truss is given by:

$$A_s = \frac{A_{sw}}{s} \cdot z \cdot \cot\theta \tag{2.1}$$

Here, A_{sw} is the cross-sectional area of a stirrup, and s is the spacing between stirrups. If a shear force V is applied to the element, the force in the vertical tension member is also V. The tensile stress in the shear reinforcement is denoted as:

$$\sigma_{ct} = \frac{V}{A_s} = \frac{V}{A_{sw}} \frac{s}{z \cdot \cot\theta} \tag{2.2}$$

Since the stress-strain behaviour of reinforcement steel is generally assumed to be bi-linear for design purposes, it is assumed that the stress in the steel cannot exceed its yield stress f_y. According to the truss analogy, the maximum shear force then becomes:

$$V = \frac{A_{sw}}{s} \cdot z \cdot \cot\theta \cdot f_y \tag{2.3}$$

The only unknown factor remaining is the angle θ of the compression diagonals. Research by Reinhardt and Walraven (1982) shows that the angle θ decreases under load, meaning the compression diagonals rotate during loading. Moreover, the study finds that θ goes through several phases, as illustrated in Figure 2.13.

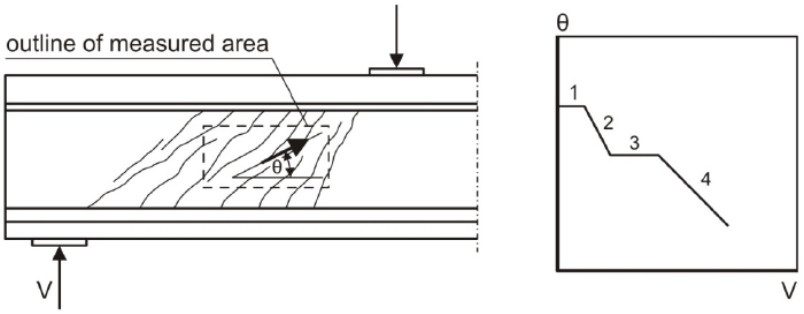

Figure 2.13: Angle of inclination of the concrete compression struts θ in a concrete beam (Reinhardt & Walraven, 1982).

The study finds that the concrete compressive strut angle θ goes through 4 distinct phases that schematized in the right diagram in Figure 2.13:

- **Phase 1**: The web is uncracked: the compressive stresses follow the compression trajectories, approximately θ = 45°.
- **Phase 2**: Diagonal cracks form in the web, altering the stress state. The angle θ decreases.
- **Phase 3**: A (temporary) stable state is reached: no new diagonal cracks form, and both concrete and steel behave elastically. The slope of the compression diagonals remains constant.
- **Phase 4**: The shear reinforcement yields, causing further rotation of the diagonals. As they rotate, the stress in the compression diagonals increases until the concrete reaches its crushing stress, leading to shear failure of the beam.

The test results show that a compressive strut angle θ = 21.8° is typically achieved, provided the beam geometry and reinforcement configurations permit it. This limit is considered normative and therefore it is used in the shear design of concrete structures.

2.2.2. Concrete beams reinforced with FRP shear reinforcement

Unlike Eurocode 2 (NEN-EN 1992-1-1, 2011), which only considers the contribution of stirrups, most existing national and international design codes, such as ACI 318-14 (2014), NEN 6720 (2005) and NEN 8702 (2017) adopt a semi-empirical approach that is based on the assumption that various mechanisms develop plastically and that internal stress redistribution occurs after the reinforcement yields. According to this methodology, the shear capacity is composed of a contribution from the concrete and an additional contribution from the shear reinforcement when present, of which both components can be added together.

However, the redistribution of stresses becomes more complex when using elastic-brittle reinforcement materials like FRP. According to fib (2007), researchers have argued that the design methods used for steel-reinforced concrete, which rely on significant stress redistribution and plasticity theory principles, may not be directly applicable to FRP-reinforced concrete. Despite this, evidence indicates that if shear cracks are effectively controlled and the shear resistances of both the concrete and the shear reinforcement are fully mobilized, combining the contributions of these two mechanisms can produce analytical predictions that closely match experimental results (fib, 2007; Guadagnini et al., 2003;

Guadagnini et al., 2006).

Furthermore, fib (2007) emphasizes that the primary principle behind current recommendations for designing FRP RC structures is that, assuming an adequate bond between concrete and reinforcement, the concrete section will undergo forces and strains regardless of the type of reinforcement used. Therefore, if an FRP design maintains the same strain in the reinforcement and develops the same design forces, it will produce similar results to a design using steel reinforcement. This methodology is commonly known as the ”strain approach” (e.g. Guadagnini et al., 2003).

FRP typically has a lower modulus of elasticity (E-modulus) than traditional steel reinforcement, causing it to elongate more under the same applied force. For shear reinforcement, this results in wider shear cracks, which can diminish one of the shear capacity contributions from the concrete (e.g. aggregate interlock). To mitigate this, early calculations set the strain limit for FRP stirrups to the yielding strain of steel, approximately 0.25%, to maintain section integrity and ensure the additive nature of the resisting mechanisms. However, experimental research by Guadagnini et al. (2003) and Guadagnini et al. (2006) found this limit overly conservative. It was shown that the strain limit could be safely increased to 0.45% to better reflect the true behavior of concrete elements reinforced with FRP and to enhance structural performance and economic viability. At this higher strain level, cracking remains effectively controlled and the shear resisting mechanisms from both concrete and shear reinforcement are fully mobilized, thus allowing their contributions to be summed.

The maximum stress in the shear links can be calculated using the following equation:

$$f_{fw} = \varepsilon_{fw} \cdot E_{fw} \tag{2.4}$$

where ε_{fw} corresponds to this imposed stirrup strain limit and E_{fw} corresponds to the elastic modulus of the FRP reinforcement material considered. Thus, by increasing the strain limit for FRP shear links from 0.2% to 0.45%, higher stresses can be developed. Yet, due to the relatively low elastic modulus of most FRP types, the generated stresses in the FRP stirrups are still relatively low compared to the yield stress of steel or the ultimate tensile strength at this increased limit. This principle is illustrated in Figure 2.14.

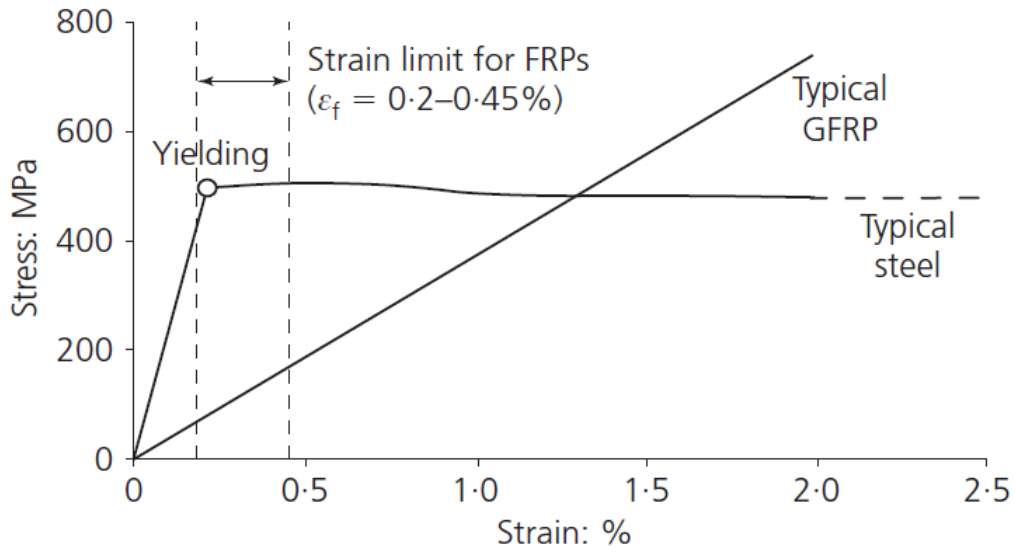

Figure 2.14: Limiting strain for FRP shear reinforcement in concrete structures (fib, 2007)

Additionally, fib (2007) reports that in FRP-reinforced concrete elements, common shear failure modes such as diagonal tension failure and shear compression failure occur similarly to those in traditional reinforced concrete members. Consequently, the shear problem in FRP-reinforced concrete is often addressed using methods similar to those used for steel-reinforced concrete elements. This means

that the stirrup shear capacity contribution can be calculated by using the same equation as for steel stirrups (as previously displayed in Equation (2.3)), but replacing the yield strength of steel f_y with the stress level developed under the limited strain level f_{fw}, as described in Equation (2.4). The formula for predicting the FRP stirrup shear capacity then becomes:

$$V_s = \frac{A_{sw}}{s} \cdot z \cdot \cot\theta \cdot [f_{fw}] = \frac{A_{sw}}{s} \cdot z \cdot \cot\theta \cdot [\varepsilon_{fw} \cdot E_{fw}] \tag{2.5}$$

This equation suggests the use of a variable concrete strut angle θ. However, Guadagnini et al. (2006) recommends a simpler, though potentially more conservative, approach with a fixed concrete strut angle θ = 45° for calculating the shear resistance of concrete beams reinforced with FRP stirrups.

2.2.3. Shear failure modes

Shear failure in reinforced concrete elements is consistently preceded by the formation of cracks inclined to the main axis of the element. These shear cracks modify the internal behavior of the element, leading to failure either concurrently with the formation of new or existing shear cracks or following an increase in the applied load.

According to Ferguson et al. (1988), shear failure can be categorized into three types: diagonal tension failure, diagonal compression failure, and splitting or true shear failure. These modes are illustrated in Figure 2.15. Shear compression and shear tension failure mode typically occur when the shear span over effective depth ratio, a_v/d, lies between 1 and 2.5. On the other hand, diagonal shear failure typically occurs when this ratio is in the range of 2.5 to 6.

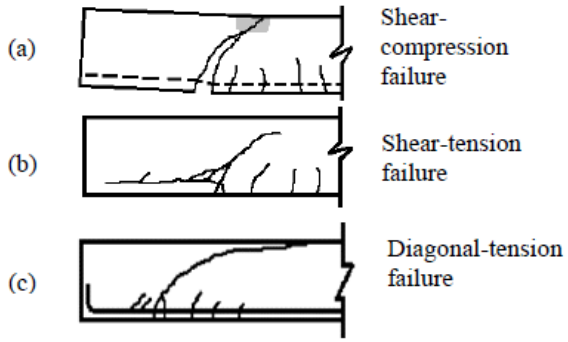

Figure 2.15: Shear failure modes for reinforced concrete beams (Abdul Samad et al., 2016)

Shear compression failure

After the formation and growth of cracks in the beam's cross-section, shear compression failure occurs when these cracks extend into the compression zone and the concrete's compressive strength is exceeded. Consequently, the concrete crushes at the tip of the diagonal crack near the load application area. This is illustrated in Figure 2.15 (a).

Shear compression failure is commonly associated with high levels of shear reinforcement. This type of failure typically occurs in beams with a span-to-depth ratio of less than 4, although it is most frequently observed in the range of 1.0 to 2.5(Abdul Samad et al., 2016). The failure mechanism is governed by the concrete's properties, making existing steel-reinforced concrete design codes applicable to FRP-reinforced elements (fib, 2007).

Shear tension failure

Shear tension failure results from inadequate anchorage of the longitudinal reinforcement bars. Diagonal cracks propagate horizontally along these bars as the concrete cover splits from below the bars, leading to the ultimate failure of the beam. This is illustrated in Figure 2.15 (b).

Diagonal tension failure

Diagonal tension failure occurs when flexural cracks form at the bottom of the beam due to tensile stress. As the load increases, these cracks grow and propagate diagonally towards the load point, leading

to a sudden shear failure of the concrete. This type of failure is common in beams with insufficient shear reinforcement and typically occurs in beams with a shear span-to-depth ratio greater than 2.5 (Karunanidhis, 2019). This is illustrated in Figure 2.15 (c).

FRP stirrup rupture
In addition to the failure mechanisms observed for steel reinforced concrete elements, FRP reinforced concrete elements with FRP stirrups can fail due to the rupture of the shear reinforcement stirrup. Implementing a strain limit, along with an imposed limit for the maximum tensile strength in corner sections (e.g. Equation (2.6)), should help prevent this failure mode.

2.3. Forms of FRP shear reinforcement

This section explores the diverse forms of fibre-Reinforced Polymer (FRP) shear reinforcement used in concrete structures, each with its unique properties and applications. While pultruded bars are the most commonly recognized form of FRP reinforcement, there are several other innovative options available, including braided bars, laminated strips, and T-headed bars.

2.3.1. Pultruded FRP rebar

FRP reinforcement bars are commonly produced through a process called pultrusion. This is a continuous manufacturing process used to create FRP material with a constant cross-section. The term combines ”pull” and ”extrusion,” highlighting its key characteristic: unlike extrusion, which pushes the material through a die, pultrusion involves pulling the material.

In this process, multiple parallel bundles of continuous fibres, called rovings, are guided through a bath containing a matrix material to impregnate and saturate the fibres, ensuring complete coverage and bonding. Subsequently, the saturated rovings are drawn though a (pre-)forming and curing die that is set to the desired final diameter. The material is then cured to allow the resin to harden, which bonds the basalt fibres together in the polymer matrix. In the last step, the bars are cut to length (Qureshi, 2022). This pultrusion process is schematized in Figure 2.16.

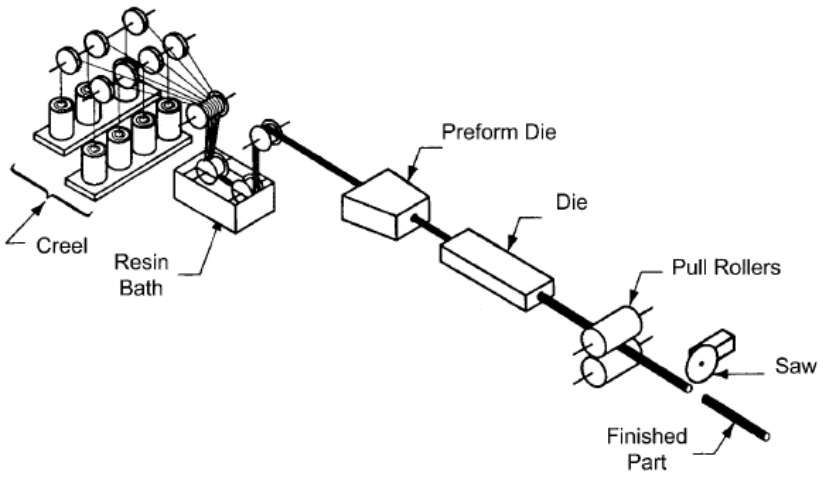

Figure 2.16: Pultrusion production process (Grover & Anderson, 1996)

According to Bank (2006) and fib (2007), the common fibre volume fraction of pultruded FRP rebar is in the range of 50% to 75%. Through this production process, the fibres are aligned to optimize strength and stiffness along the longitudinal direction of the rebar. At corners, this alignment is disrupted due to kinking of fibres at the inside of the bend, and the material cannot effectively carry tensile loads as it does along the straight sections because only the unkinked part of the fibres is activated upon applying a tensile force (Ahmed et al., 2010). Furthermore, stress concentrations in corner sections, which are induced by the confinement of concrete, further reduce the tensile strength of the FRP rebar (fib, 2007).

On the basis of experimental research, ACI 440.3R-15 (2015) has adopted a formula that expresses the strength of FRP reinforcement in corner sections f_{jb} in terms of the uni-axial tensile strength of the composite f_{fu}, the inner corner radius r_b and diameter of the bar d_b:

$$f_{ub} = (0.05 \cdot \frac{r_b}{d_b} + 0.3)\ f_{fu} \leq f_{fu} \tag{2.6}$$

For traditional steel reinforcement, NEN-EN 1992-1-1 (2011) requires that the minimum corner radius is 2 (for rebar diameter $\leq$ 16 mm) to 2.5 (for rebar diameters $\geq$ 16 mm) times the diameter of the bar. If the same minimal ratio of rebar diameter and corner radius for pultruded FRP rebar is used as input for Equation (2.6), the tensile strength at bent locations is only 40-42.5% of the uniaxial (longitudinal) tensile strength of pultruded FRP rods. For FRP reinforcement, however, larger corner radii of 3-5 times the bar diameter are commonly used. Using Equation (2.6) this leads to a corner tensile capacity that is 45-55% of the uniaxial tensile strength.

Mechanical characteristics

The fibres within pultrusion bars have relatively good parallel alignment and high fibre volume fraction due to efficient packing of fibres in production. They are considered Very efficient in the form of straight rebars with strength and stiffness values near the upper limit of the displayed BFRP characteristics in Table 2.3. However, pultrusion bars are considered unfit for shear reinforcement due to the relatively low corner tensile strength.

2.3.2. Braided FRP rebar

Braided bars are created by interweaving strands of fibres into a flexible, braided configuration, which is then impregnated with a polymer resin to create a high-strength composite. This flexibility allows the bars to conform to the required shape for stirrups, increasing the strength in corner sections by reducing the kinking action of fibres.

A study of Nanni et al. (1993) focuses on the tensile properties of braided FRP reinforcement rods made from three different types of fibres: glass, aramid, and polyvinyl alcohol (PVA). The research aims to evaluate the static tensile properties, including stress-strain behavior, elastic modulus, Poisson's ratio, ultimate strength, and ultimate elongation of these rods. The rods in this study were manufactured using a braiding method, which results in a deformed surface to the rods that can improve the bond with the surrounding concrete. This method of braiding also provides flexibility in producing rods of various diameters (ranging from 1 mm to 20 mm) and can result in rods that are easier to handle and install. The distinct production techniques for pultruded rods and braided rods are illustrated in Figure 2.17.

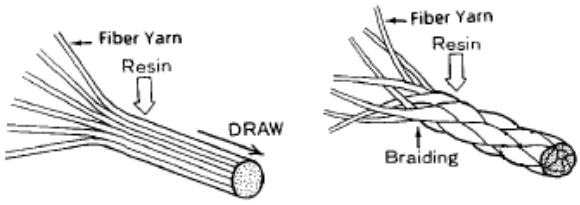

Figure 2.17: Production principle of FRP rebar. Left: pultrusion; right: braiding. (Nanni et al., 1993)

The study finds that braided FRP rods behave almost linearly in terms of their stress-strain relationship.If the epoxy exhibits an ultimate elongation greater than that of the fibres, the rod's stiffness and ultimate strength are likely to be around 80% of the values predicted by the rule of mixture based on the constituent materials. This rule of mixtures states that the overall stiffness of an unidirectional FRP composite in the direction parallel to the fibres may be as high as:

$$E_c = V_f \cdot E_f + (1 - V_f) \cdot E_m \tag{2.7}$$

where V_f is the volume fraction of the fibres and E_f and E_m are the stiffness of the fibres and matrix, respectively.

The 20% reduction in stiffness and strength is attributed to the braiding process. In this process, fibres are oriented at an angle to the rod axis, resulting in them not being fully aligned with the direction of the applied tensile load. This recution was consistently observed across all fibre types tested.

The tests also revealed that the ultimate strength of the FRP rods decreases with increasing rod diameter. This can be explained by the increased deviation of individual fibres from the rod axis as the diameter grows, which intensifies the stress on fibres further from the center. For aramid fibres, the braided rods showed a better performance compared to glass and PVA fibres, mainly because the epoxy resin used was more compatible with aramid fibres, although it lacked sufficient elongation when used with glass and PVA.

In conclusion, the study highlights that while braided FRP rods can be manufactured using various fibre types, the compatibility of the epoxy resin and the braiding process plays a crucial role in their performance. The findings support the potential use of FRP rods as a viable alternative to steel reinforcements in concrete structures, although further research is needed to explore the effects of environmental factors such as temperature, time, and loading conditions on the long-term performance of these materials.

Lindner et al. (2018, 2019) explore the potential of innovative FRP stirrups as reinforcement in concrete structures. The research spans multiple papers and provides a comprehensive analysis of the mechanical properties, durability, and practical applications of FRP stirrups, particularly those made from braided basalt fibre-reinforced polymer (BFRP).

One of the notable developments in their research is the creation of FRP stirrups with reduced radii of curvature, which are designed to improve load-carrying capacity and resource efficiency. The innovative fibre architecture and manufacturing processes employed in these stirrups allow for smaller bending radii while maintaining high tensile strength, which is a significant advancement over conventional FRP stirrups. The key findings from their extensive tests indicate that BFRP stirrups exhibited higher tensile strength and modulus of elasticity compared to glass fibre-reinforced polymer (GFRP) stirrups. Specifically, the BFRP stirrups showed tensile strengths of up to 725 MPa with significantly reduced bending radii (down to four times the bar diameter). This performance marks a substantial improvement over traditional FRP stirrups.

Enhanced durability in alkaline environments was another critical finding. Both GFRP and BFRP stirrups demonstrated excellent durability when exposed to alkaline environments that simulate the conditions within concrete. The results showed minimal mass loss and no significant degradation, indicating that these stirrups can maintain their structural integrity over time. Improved bond strength was also a significant result. Pull-out tests to assess the bonding behavior between FRP reinforcements and the concrete matrix revealed that BFRP stirrups had a higher bond strength compared to GFRP stirrups. This finding further validates the suitability of BFRP stirrups for concrete reinforcement, as strong bonding is crucial for the overall performance and safety of reinforced concrete structures.

2.3.3. Fibre sheet strips (FSS) reinforcement

Fibre sheet strip (FSS) stirrups represent another form of FRP shear reinforcement. These stirrups are constructed from a laminate, typically using unidirectional (UD) fibre cloth that aligns the fibres in a single direction to maximize strength along that axis. This configuration provides several benefits in reinforcing concrete structures.

One significant advantage of FSS stirrups is their ability to improve the relative strength of corner sections. In traditional FRP reinforcement methods, the difference in radius between the innermost and outermost fibres can lead to kinking of fibres, especially in areas with sharp bends or corners. However, because FSS stirrups are relatively thin and wide, this radius difference is minimized. The uniform distribution of fibres within the laminate ensures more consistent strength across the section, reducing the likelihood of failure at these critical points.

Furthermore, FSS stirrups can be manufactured as completely closed loops, unlike traditional open or partially closed stirrups. This closed-loop design enhances the anchorage of the stirrups within the concrete, reducing the risk of slip or anchorage failure. The closed design ensures that the entire perimeter of the stirrup contributes to resisting shear forces, leading to more efficient load distribution and improved overall performance of the reinforced section.

Mechanical characteristics

To produce fibre sheet strip stirrups, multiple layers of UD fabric are stacked and infused with epoxy resin and cured under vacuum. These strips are characterized by longitudinal, parallel fibres, which are intended to be strong and stiff. However, since the laminate is made using woven unidirectional basalt fibre fabric (with cross-threads to maintain fabric integrity and fibre alignment), the fibres are not perfectly aligned and parallel to one another. Instead, they often exhibit a degree of waviness or undulation, known as marcelling (Chung, 2017). This principe is illustrated by a longitudinal section of a composite manufactured from UD-fabric, shown in Figure 2.18.

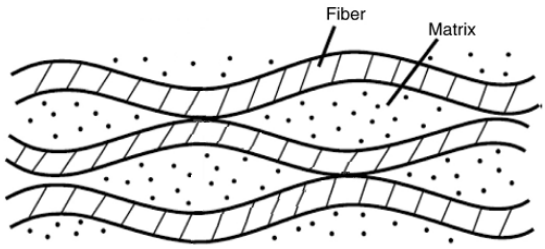

Figure 2.18: Fibre waviness in a UD-laminate (edit from Chung, 2017)

This waviness can adversely affect the mechanical properties of the composite, as the misalignment of fibres reduces their load-carrying efficiency, leading to decreased strength and stiffness compared to pultruded bars.

Lee et al. (2010) examines the use of FSS stirrups in comparison with traditional steel and carbon FRP rod stirrups. The study involved testing ten concrete beams with various shear reinforcement configurations under three-point loading. These beams were assessed based on shear strength, load-deflection behavior, and crack patterns. The findings revealed that FSS stirrup-reinforced beams exhibited enhanced shear strength compared to beams without shear reinforcements. The performance of these beams was comparable to that of beams reinforced with steel stirrups, particularly in terms of overall load-deflection relationships and shear strengths.

Notably, the study addressed several limitations of conventional pultruded FRP rod stirrups, such as their rigidity and susceptibility to premature failure at bent portions. FSS stirrups, fabricated from commercially available carbon fibre sheets, demonstrated improved flexibility and ease of installation. The impregnation of FSS stirrups with epoxy resin further enhanced their shear resistance by enabling them to act more effectively as a composite material, thus improving their overall performance. Strengthening the bent portions of FSS stirrups was found to prevent premature failure and increase strain capacity, further contributing to the structural integrity of the reinforced beams.

In another paper by Lee et al. (2014), the authors explore the bend strength of closed-type carbon FRP stirrups. This research aimed to mitigate issues related to the bending and transverse strength of traditional FRP stirrups. Various configurations of FRP stirrups, including steel, carbon FRP rod, and FSS stirrups, were tested. The results indicated that beams with FSS stirrups could maintain comparable shear behavior to those with steel stirrups, demonstrating similar crack patterns and widths at maximum load. The innovative use of FSS stirrups, particularly in closed configurations with additional overlaps, was found to significantly reduce the likelihood of premature failure and improve shear strength.

Both studies underscore the potential of FSS stirrups as an effective alternative to traditional steel and FRP rod stirrups for concrete reinforcement. The ease of fabrication and installation, combined with enhanced shear strength and crack control, make FSS stirrups a promising solution for structural applications.

Closed-type winding GFRP strip stirrups

A paper by Yuan et al. (2022) investigates the performance of closed-type winding glass fibre-reinforced polymer (CW-GFRP) strip stirrups. According to the authors, these stirrups are designed to address the common issues associated with conventional pultruded FRP stirrups, such as premature bent corner rupture and bond slip failure at the overlapping legs. The CW-GFRP stirrups feature a fully closed rectangular cross-section, which enhances their performance by eliminating slip and significantly improving the strength of the bent portion. The production process of these stirrups is illustrated in Figure 2.19.

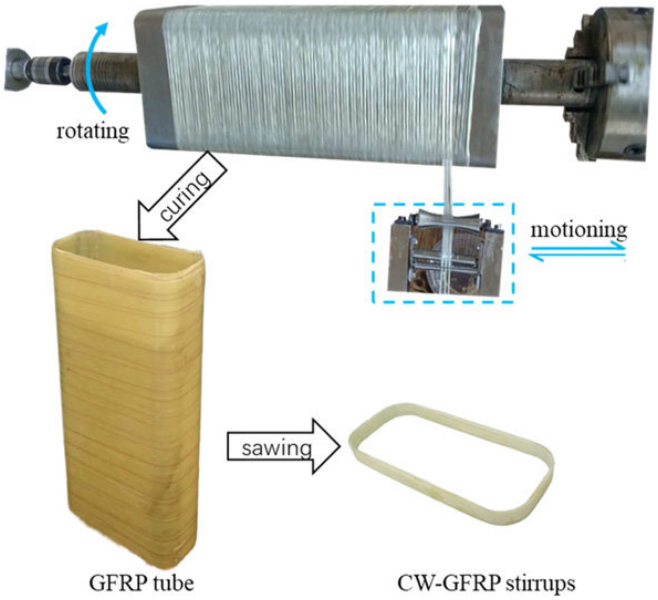

Figure 2.19: Production of closed-winding GFRP stirrups (Yuan et al., 2022)

The experimental program involved shear tests on eight concrete beams reinforced with various configurations of either conventional pultruded GFRP rod-type stirrups or CW-GFRP strip stirrups. The beams, each measuring 300 mm in depth and 150 mm in width, were tested under three-point loading conditions to evaluate the effects of stirrup material, stirrup spacing, and the width of CW-GFRP strip stirrups on shear performance.

The results showed that beams reinforced with CW-GFRP stirrups exhibited significantly improved shear capacity, enhanced stiffness, and narrower shear crack widths compared to those with conventional pultruded stirrups. Specifically, the CW-GFRP stirrups prevented bond slip failures and improved the strength of the bent portions, resulting in a 1.09 to 1.12 times higher shear capacity. In contrast, beams with pultruded stirrups demonstrated bond slip failures, particularly at greater stirrup spacings.

The study also highlighted two distinct failure modes for CW-GFRP stirrups: bent corner rupture for narrower stirrups and splitting failure at the straight legs for wider stirrups. The splitting failure was attributed to the combined tension and shear stresses acting on the stirrups at the intersection with diagonal shear cracks. The findings suggested that reducing the width of CW-GFRP stirrups could prevent splitting failures and achieve higher stirrup strains at ultimate loads.

To predict the shear strength of the beams, the researchers utilized strut-and-tie models based on ACI 318-14 (2014) and S806-02 (2002) standards. Both models provided conservative and relatively

accurate predictions of shear strength, demonstrating their applicability for designing beams reinforced with CW-GFRP stirrups.

Overall, the study demonstrates that CW-GFRP stirrups significantly improve the shear performance of concrete beams, making them a promising alternative to conventional pultruded FRP stirrups. The findings highlight the potential of CW-GFRP stirrups to enhance the durability and structural integrity of reinforced concrete beams.

2.3.4. T-headed rebar

T-headed rebar is a specialized type of reinforcement engineered to enhance anchorage and optimize load transfer in concrete structures. Unlike traditional ribbed steel rebar, T-headed bars feature a cone- or T-shaped head at one or both ends, acting as a mechanical anchor. The mechanical anchorage provided by the cone-shaped head makes T-headed bars particularly effective in applications where traditional reinforcement may be prone to slippage or inadequate anchorage, reducing the risk of pullout failure (Chiu et al., 2013). Furthermore, T-headed bars also exist in FRP and they can be employed as shear reinforcement, offering additional versatility in structural applications. An example of this type of reinforcement is the ComBAR® T-headed bar, produced by Schöck Bauteile GmbH (2022), which is fabricated from pultruded glass fibre reinforced polymer rebar. This product, featuring a cone-headed end, is depicted in Figure 2.20.

Figure 2.20: ComBAR® T-headed bar by Schöck Bauteile GmbH (2022)

Coenen (2007) has performed experiments to determine the shear capacity of concrete beams reinforced with these ComBAR® T-headed GFRP pultrusion rebars as longitudinal and shear reinforcement compared to beams with traditional . The key findings from this research are as follows:

The glass fibre reinforcement used, specifically the ComBAR T-headed bar, exhibits a strength exceeding 1000 N/mm^2, with a stiffness of 60 GPa. Compared to FeB500 reinforcement, the strength of ComBAR bars is up to twice as high, but their stiffness is more than three times lower. The lower elastic modulus of GFRP compared to steel results in a reduced shear capacity in concrete structures reinforced with GFRP. This is because when a concrete beam reinforced with ComBAR is subjected to loading, the lower stiffness of the glass fibre reinforcement causes the stirrups to elongate more than the steel stirrups at the same load. This increased elongation of the stirrups results in wider and deeper cracks. Wider cracks diminish the effectiveness of mechanisms that contribute to shear capacity, such as aggregate interlock and dowel action. Aggregate interlock relies on the roughness of crack surfaces to transfer shear forces, which becomes less effective as cracks widen. Similarly, dowel action, which is the ability of reinforcement bars to transfer shear across cracks, is compromised because the larger deformations reduce the contact area and the effectiveness of the dowel action.

Despite this, the reinforcement's strength does not impact the shear capacity. GFRP-reinforced concrete structures exhibit similar shear failure patterns to those reinforced with FeB500 steel bars, indicating comparable performance under shear stress. The proposed model for predicting the shear capacity of GFRP-reinforced concrete structures aligns well with experimental data, particularly for specimens without shear reinforcement. An increase in the amount of GFRP reinforcement leads to higher shear capacity, as observed in the experimental results and reflected in the model predictions.

Three series of experiments were conducted: Series 1 included beams reinforced with FeB500 steel and GFRP bars (ComBAR), while Series 2 and 3 involved the use of T-headed bars as shear reinforcement. Differences in the placement and interaction between longitudinal reinforcement and T-headed bars significantly influenced the results. Configurations where longitudinal reinforcement was placed against the T-headed bars showed improved shear capacity. The experimental results were compared with various design standards, including NEN 6720, EC 2, ACI 318 for steel reinforcement, and ACI 440, CSA S806 for GFRP reinforcement. Adjustments to the NEN 6720 formula provided a good indication of shear capacity for GFRP-reinforced beams, while ACI 440 tended to underestimate the shear strength.

The angle between the compression diagonal and the beam axis is generally larger for GFRP reinforcement than for traditional steel. This affects the truss action within the beam, suggesting the need for further research to optimize the node design between longitudinal reinforcement and T-headed bars. These findings support the feasibility of using GFRP T-headed bars as shear reinforcement in concrete structures, while highlighting the need for adjustments in existing design models to accurately predict their performance.

2.4. Knowledge gaps

The literature review reveals that basalt fibres present an advantageous balance between material properties and the energy required for their production, making them a promising option for various reinforcement applications. However, when it comes to shear reinforcement, pultruded basalt FRP rebar faces significant limitations due to the prevalence of kinked fibres in the corner sections, a result of the production process. This limitation opens the door for further exploration into alternative forms of basalt FRP shear reinforcement that are less susceptible to this issue.

To the best of the author's knowledge, no existing research has explored the use of strip stirrups made from basalt fibres as internal shear reinforcement in concrete beams. The majority of previous studies have focused predominantly on carbon FRP, leaving a substantial gap in the investigation of basalt FRP for similar structural applications.

A comparison between BFRP and CFRP reveals notable differences in mechanical properties, particularly in strength and stiffness, with basalt FRP generally exhibiting lower values. This disparity suggests that under identical loading conditions, basalt FRP may result in wider cracks, thereby diminishing the effectiveness of aggregate interlock within the concrete matrix. Consequently, BFRP stirrups are likely to experience not only tensile forces but also transversal shear forces at the locations where shear cracks intersect. Given that the shear strength of FRP reinforcement bars is primarily determined by the properties of the matrix material rather than the fibres themselves, there is a concern that basalt FRP stirrups could fail at the intersection of shear cracks before reaching the uniaxial tensile strength of the fibres. This observation implies that the tensile corner strength, which is a critical consideration in the design of CFRP stirrups, may not hold the same level of importance for basalt FRP stirrups.

Moreover, while uniaxial tensile and corner tensile tests have been conducted on braided basalt FRP rods, their effectiveness as shear reinforcement in concrete beams has not yet been validated. This lack of empirical validation highlights the pressing need for further investigation. Understanding the performance of braided BFRP stirrups in shear reinforcement applications is crucial, as it has significant implications for structural design and construction practices. Comprehensive testing and analysis are essential to determine both the capabilities and limitations of BFRP stirrups in concrete structures, ensuring that they meet the necessary performance standards and safety regulations.

In conclusion, BFRP presents potential advantages, including cost-effectiveness and a lower environmental impact compared to carbon FRP and steel. However, these benefits can only be fully realized through rigorous research and thorough validation to address the existing knowledge gaps. Establishing reliable design guidelines for the use of BFRP in concrete structures is critical to unlocking its full potential as a viable alternative in structural reinforcement.

3

Design of alternative BFRP stirrups

Basalt Fibre-Reinforced Polymer (BFRP) has emerged as a promising material for reinforcing concrete structures, mainly due to their high strength-to-weight ratio and the potential sustainability and durability compared to traditional steel reinforcement bars. Furthermore, basalt fibres exhibit a superior balance of material properties and energy efficiency in production compared to other types of fibres commonly used in FRPs. This advantage is due to basalt being a naturally occurring material that requires fewer energy-intensive processes during production compared to carbon fibres, and unlike glass fibres, basalt fibres do not require additional additives (Fiore et al., 2015).

Straight, pultruded BFRP reinforcement rods are commonly used due to their high tensile strength and stiffness, which are derived from the continuous alignment of parallel fibres in the direction of loading, bonded together with a matrix material, commonly epoxy resin. However, pultruded BFRP rods are deemed unsuitable for shear reinforcement applications, because a relatively high amount of fibres tend to kink in corner sections. As a result, the relative tensile strength in corners is about half of the tensile strength in straight sections. To address this issue, alternative forms of BFRP reinforcements are being explored with a higher expected relative tensile strength in corner sections.

The experimental research aims to comprehensively investigate and evaluate the applicability and performance of alternative BFRP shear reinforcement in reinforced concrete beams through the following steps:

- **Exploration of production and design of alternative FRP shear reinforcement types**: This step serves as the foundation for identifying potential candidates for improved shear reinforcement.
- **Verification of cross-sectional properties**: This involves determining the cross-sectional area, density and fibre volume fraction for the materials selected in the previous step. This analysis will form the basis for comparing the efficiency and effectiveness of different reinforcement types.
- **Uniaxial tensile strength tests**: These tests aim to determine key mechanical properties, including tensile strength, modulus of elasticity, and strain capacity. The results will provide a fundamental understanding of the material's behaviour under tensile loading.

3.1. Alternative forms of BFRP shear reinforcement

In this research, two alternative forms of basalt FRP reinforcement to pultruded bars are examined: braided bars and laminated strip stirrups. The following subsections will elaborate on these materials. These two alternatives are chosen for practical reasons: a manufacturer was found for the braided bars, and the strip stirrups could be produced in-house using woven basalt fabric supplied by a supplier.

Unfortunately, no manufacturer was found to supply pultruded BFRP shear reinforcement stirrups for direct comparison with the braided bars and laminated strips. Additionally, FRP T-headed bars are currently available only in glass fibre variants. As this research focuses on basalt FRP, direct comparisons with T-headed bars are not possible.

3.1.1. Braided basalt FRP bars

The braided BFRP reinforcement used in this study was produced through a collaboration of two German companies: Deutsche Basalt Faser GmbH, which produces basalt fibres and BFRP products, supplied the fibres to Thoenes Solutions®, a company with expertise in braiding techniques, which then produced the braided bars. Due to its unique braiding geometry, fibre kinking is expected to be minimized. The braided structure includes a braided chord around straight fibres in the core to provide additional longitudinal strength and stiffness. This braided configuration is anticipated to improve corner strength, as the individual fibre bundles conform better around corners, thus enhancing overall performance. However, the expected higher tensile strength in corner sections may come at the cost of reduced strength and stiffness in the straight portions due to the multi-directional forces induced by the braid structure.

Production

According to the manufacturers, 4500 tex basalt fibre roving was used for the braided BFRP rebar. The braiding was done in a 2-diagonal pattern around a core of longitudinal fibres situated in the center. During this process, the fibres were impregnated with epoxy resin. This is shown in Figure 3.1 (a). After braiding, the product is tightened up in a rack in the desired stirrup shape for the resin to cure. This is shown in Figure 3.1 (b). According to the producer, an additional layer of epoxy is brushed on the outside surface of the stirrups for extra alkali protection. The straight braided BFRP rod samples for uniaxial tensile tests are also derived from these stirrups.

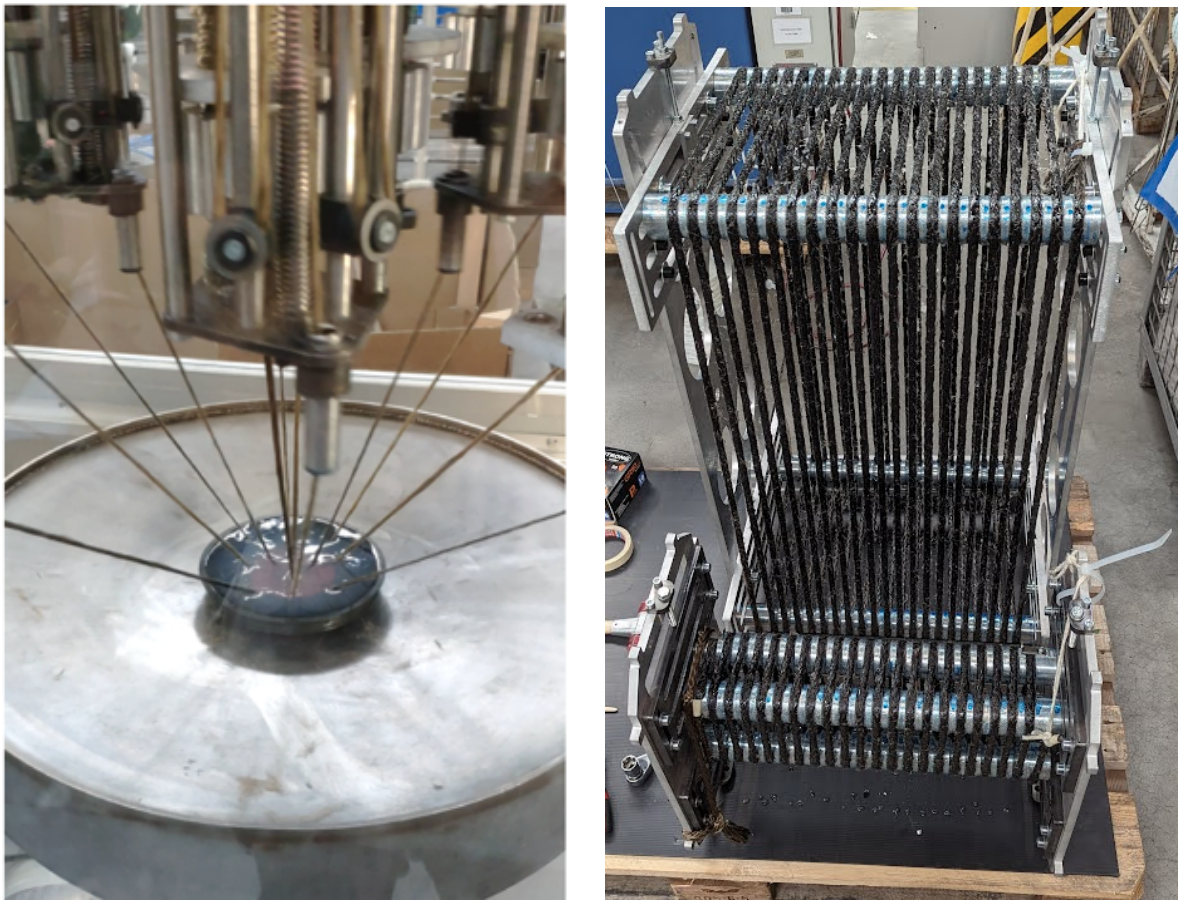

(a) Braiding and impregnation process

(b) Secured in rack for stirrup shaping during resin curing

Figure 3.1: Production of braided BFRP reinforcement (Thoenes Solutions®, 2024)

3.1.2. Laminated BFRP strips

Laminated BFRP strips are expected to exhibit mechanical properties similar to pultruded rods under uniaxial loading but with higher relative corner strength. This advantage is due to the nearly equal inner

and outer radii of the thin, tightly wound strips, which prevent fibre kinking and ensure uniform stress distribution. However, the strength and stiffness might be slightly lower than pultruded bars because the fibres in the unidirectional fabric can be wavy and not packed as densely.

Experimenting with strip production

The basalt FRP strip stirrups will be manufactured by hand. Initially, the production these stirrups is explored by using bi-directional woven basalt fabric and epoxy resin. Rectangular strips were cut from bi-axial woven basalt fabric. These strips were impregnated with epoxy resin using a brush and then wrapped around a custom-built frame to cure into single-layer rectangular stirrups with overlapping at the top, as shown in Figure 3.2 (a).

(a) First batch with frayed edges **(b)** Second batch

Figure 3.2: Experimenting with the production of basalt FRP strip stirrups

This first batch had frayed edges due to the fabric unraveling during cutting and brushing with epoxy. To prevent this in the second batch, a thin layer of epoxy was applied to the dry fabric before cutting, which reduced fraying but made the fabric too stiff to accurately follow the corners, as shown in Figure 3.2 (b).

Production of UD actual strip samples

A single layer of basalt fabric was insufficient to match the cross-sectional area of Ø8 mm steel stirrups without becoming excessively wide. To resolve this, multiple layers of basalt fibre fabric were combined through lamination. The university's composites manufacturing lab in the Dream Hall provided essential facilities and support for this process.

For these laminate strips, unidirectional (also known as "UD") woven basalt fibre fabric was selected over bidirectional woven basalt fabric due to its superior longitudinal strength and stiffness. This basalt UD-fibre cloth ("BAS UD 400") used for all the BFRP strip samples in this research was provided by a Belgian company called Basaltex®. According to the manufacturer, the fabric weighs 430 grams per square meter and is made using 600 tex basalt fibre yarns. It was delivered in roll form, as depicted in Figure 3.3 (a). Upon unrolling, a detailed image of the fabric is presented in Figure 3.3 (b). In this figure, the continuous basalt fibres are oriented horizontally, while white cross-threads run vertically to keep the fibres in place.
The production of the laminate begins by cutting the basalt fabric to a length of 750 mm while retaining its full width of 1270 mm. To ensure full saturation of the fibres, a 50-50 mass ratio of fibres to epoxy is used to impregnate the fabric with epoxy resin. This is shown in Figure 3.4 (a). After evenly spreading the epoxy, the fabric is cut in half along the fibre direction. One half is stacked upon the other, forming a layered structure with careful alignment of the fibres. This process is repeated twice more to create an eight-layer wet layup, measuring 750 mm in length and approximately 158 mm in width.

To facilitate easy removal after curing, the layup is covered with peel-ply and release film on both sides. Peel-ply ensures that the surface remains textured for subsequent bonding, while the release film prevents the laminate from sticking to the vacuum bag or other surfaces. The entire assembly is then placed on a glass plate to maintain a flat and smooth surface during curing. Breather material is added to the exposed surface of the layup to assist with resin flow and ensure uniform pressure

(a) Fabric rolled up

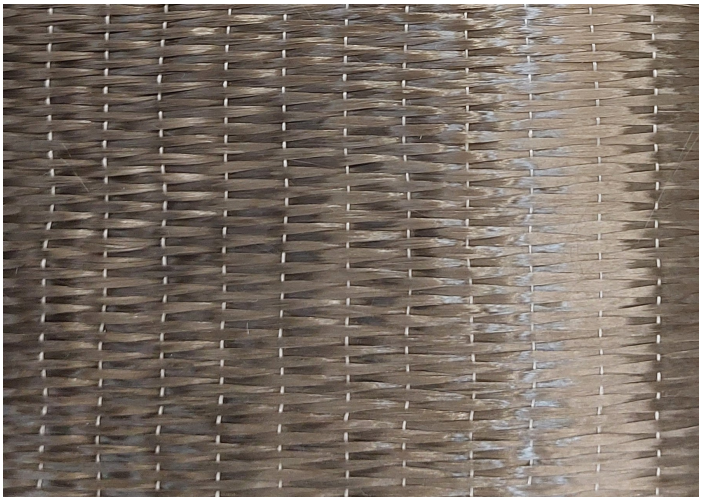

(b) Close-up horizontally orientated basalt fibres

Figure 3.3: Unidirectional woven basalt fibre fabric used for the production of laminate strips

distribution.

The assembly is then enclosed within a plastic vacuum bag. The vacuum bagging process involves sealing the edges of the bag and connecting it to a vacuum pump. When the vacuum is applied, it compresses the fibres and expels excess resin into the breather material. The breather material, typically a porous fabric, absorbs the excess resin and allows air to escape, ensuring even resin distribution and maintaining consistent pressure throughout the laminate. This compaction is crucial for achieving a uniform fibre-resin distribution across the entire laminate, enhancing the mechanical properties of the final product. Figure 3.4 (b) illustrates the wet layup after the vacuum is applied, showing this compacting process.

(a) Production of wet layup

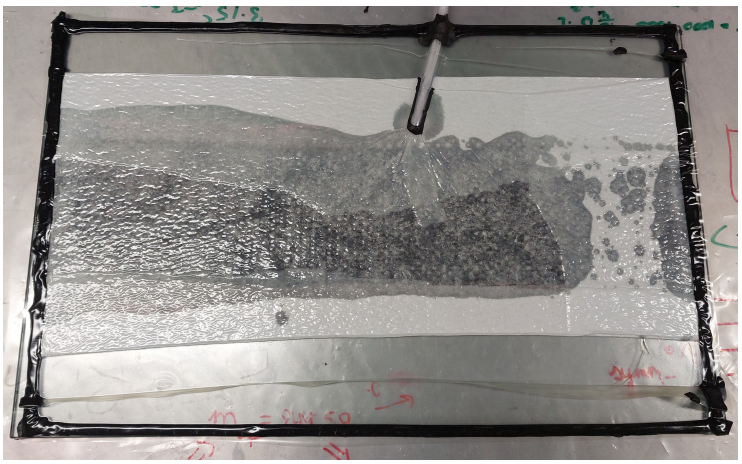

(b) Vacuum curing of the wet layup

Figure 3.4: Production of BFRP UD laminate strips

After a curing period of 24 hours, the epoxy resin within the basalt FRP laminate reaches full polymerization, signifying that the laminate is fully cured. At this stage, the laminate is carefully removed from the vacuum bag, and the supplementary layers, including the peel-ply and release film, are peeled away to expose the cured material. Given that the cured laminate may exhibit protruding fibres and sharp edges, protective measures are taken by applying blue tape along the edges, as illustrated in Figure 3.4 (a), to prevent damage and ensure safe handling.

Subsequently, the laminate is sectioned into longitudinal strips, each approximately 25 mm in width, using a diamond-bladed saw. This width is chosen to match the cross-sectional area of the braided bars, ensuring comparability during testing. A precise cutting process is essential to maintain uniformity across all samples, as inconsistencies can affect the reliability of the results. The strips are then prepared for the cross-sectional validation and uniaxial tensile tests. The cross-sectional validation confirms that the dimensions and structural integrity are as intended and the uniaxial tensile tests assess the tensile strength and stiffness, providing important information on the material's mechanical performance. The prepared strip samples are shown in Figure 3.5 (b).

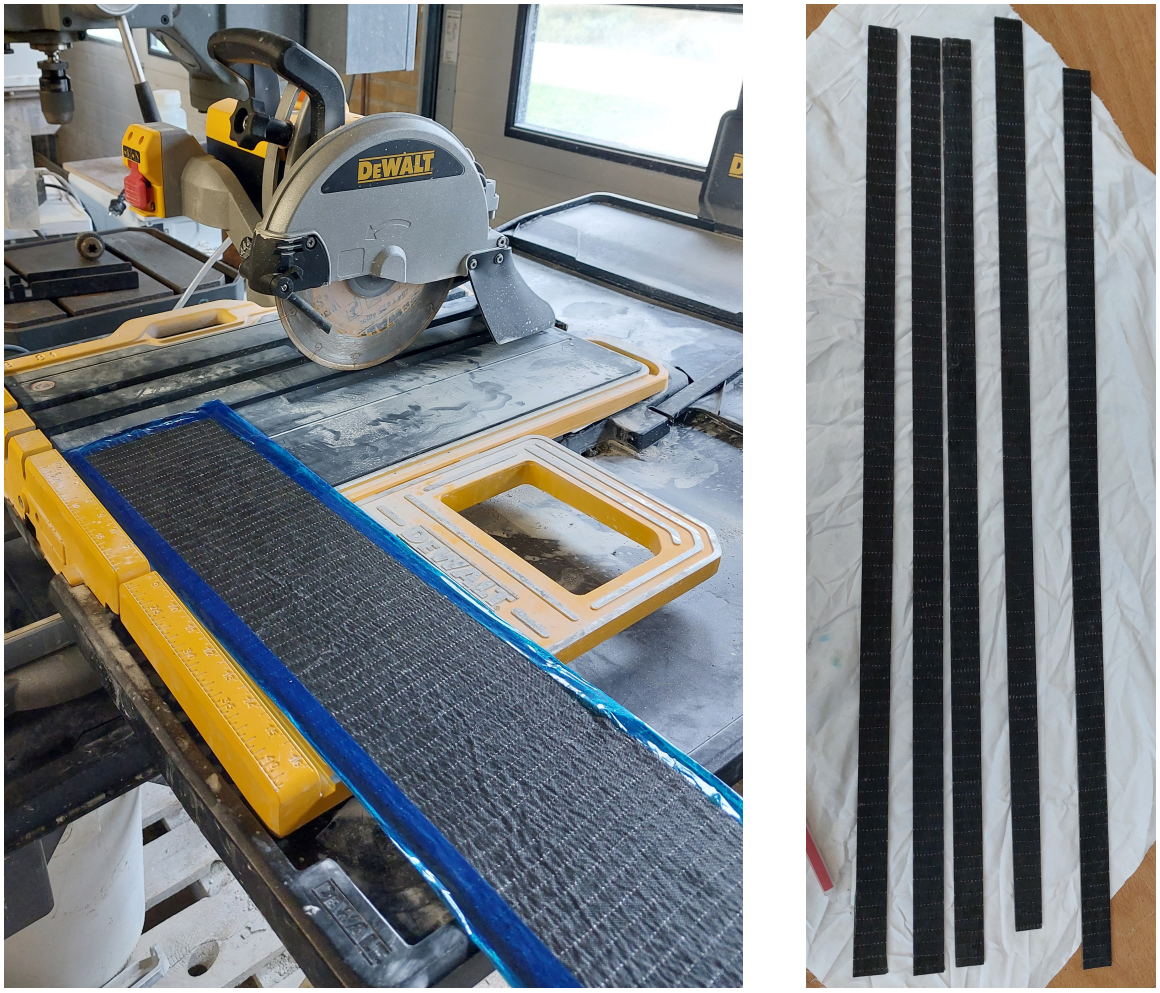

(a) Prior to cutting **(b)** Resulting samples

Figure 3.5: Preparation of basalt FRP UD-laminate samples

3.2. Verifying cross-sectional properties

This section aims to verify the cross-sectional properties of various BFRP reinforcement types, including pultruded bars, braided bars, and laminated strips. The primary objective is to determine and compare the cross-sectional area and fibre volume fraction of these reinforcement forms. Fibre volume fraction, defined as the ratio of fibre volume to the total composite volume, is an important parameter because fibres mainly contribute to the tensile strength and stiffness in the longitudinal direction of FRP rebar. Consequently, the verification of the fibre volume fraction is vital for meaningful comparisons among the reinforcement types.

3.2.1. Procedure

To determine the cross-sectional properties of the basalt FRP samples, the following steps were performed:

1. **Sample preparation:** Representative samples of each BFRP type (pultruded bars, braided bars, and laminated strips) were cut to a length of approximately 150 mm. Care was taken to ensure the cutting face was perpendicular to the longitudinal direction, and any burrs were removed.
2. **Initial length measurement:** Each specimen was measured three times using a caliper, rotating the specimen by 120 degrees for each measurement. The average value was recorded as the length L of the specimen.
3. **Initial weight measurement:** The samples are dried in an oven at 100 °C for 30 minutes to remove surface moisture and then weighed on a calibrated scale.
4. **Sample volume measurement:** The cross-sectional area A was determined by measuring the volume displacement. A graduated cylinder was filled with water to an appropriate height, and the specimen was immersed, ensuring no air was trapped. The volume displacement (ΔV) was calculated as the difference between the final volume (V_1) and the initial volume (V_0): $\Delta V = V_1 - V_0$.
5. **Calculating cross-sectional area**: The cross-sectional area A was calculated by dividing the volume displacement (ΔV by the specimen's length L:

$$A = \frac{\Delta V}{L} = \frac{V_1 - V_0}{L} \tag{3.1}$$

6. **Resin burn-off process**: The samples were placed in a furnace, with the temperature gradually increased to 550 °C and maintained for 30 minutes to ensure complete combustion of the resin. Any residual ash or burnt resin was gently brushed off, leaving only the fibres (and for pultruded bars, also the sand-coating).
7. **Final weight measurement:** The remaining fibres and, if applicable, the sand-coating were weighed using a calibrated scale to obtain the fibre weight (m_f). For the pultruded bar, the fibres and sand (m_s) are weighed separately.
8. **Calculation of Fibre Volume Content:** The fibre weight (m_f) was divided by the density of basalt fibres (ρ_f) to calculate the fibre volume fraction (V_f):

$$V_f = \frac{m_f}{\rho_f} \tag{3.2}$$

   The difference between the initial weight and the post-burn-off weight was assumed to be the matrix material weight (m_m). The specified density of basalt fibres (ρ = 2650 kg/m^3) from the technical data sheet was used for all samples, including pultruded and braided BFRP samples, due to the lack of specific density information from other suppliers.

Some of the samples used in this experiment are displayed in Figure 3.6, while the samples after the incineration of the matrix material are shown in Figure 3.7.

(a) Pultrusion rebar sample **(b)** Laminated UD-strip sample

Figure 3.6: Samples before incineration of matrix material

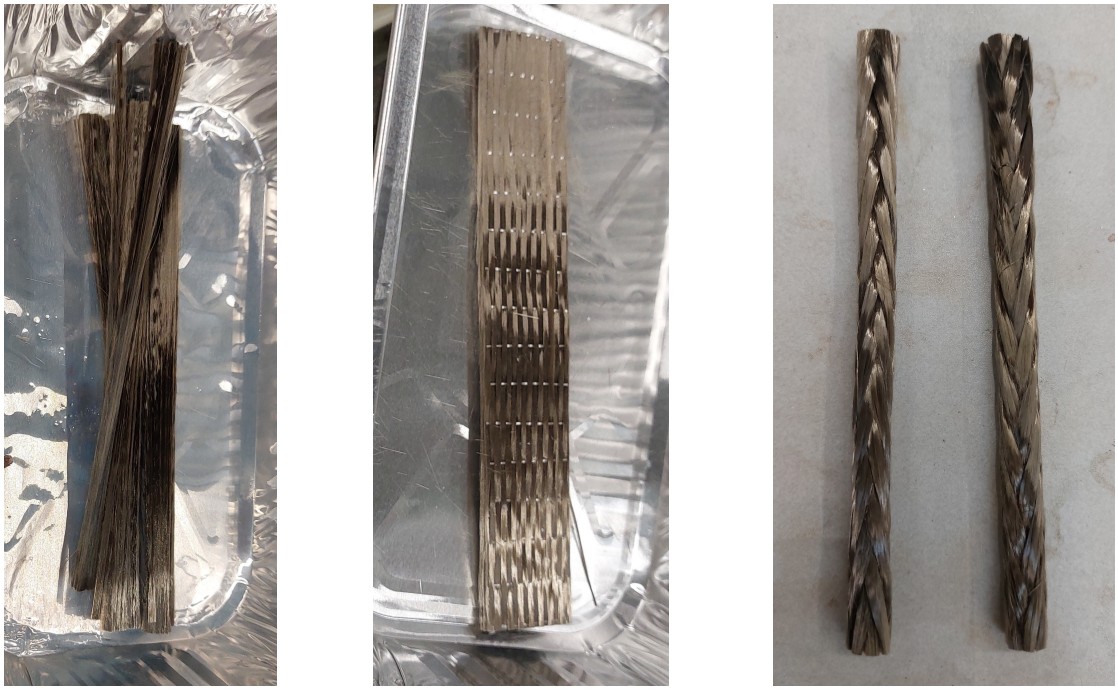

(a) Pultrusion rod sample **(b)** Laminate strip sample **(c)** Braided rod samples

Figure 3.7: BFRP samples after incineration of matrix material

3.2.2. Results

The samples included one sand-coated Ø10 mm pultruded BFRP bar, two Ø8 mm braided BFRP bars and two unidirectional (UD) laminated strips with an average width of 23.4 mm. The primary parameters determined are the cross-sectional area, density, and fibre volume fraction, as summarized in Table 3.1.

Table 3.1: Determining sample fibre volume fractions. Subscripts c, f, m and s correspond to the total composite (fibres+matrix+sand), fibre, matrix and sand, respectively.

BFRP sample	Length L [mm]	Volume v_c [ml]	Area A [mm^2]	Mass m_c [gr]	Density [kg/m^3]	Fibre mass m_f [gr]	Matrix mass m_m [gr]	Sand mass m_s [gr]	Fibre volume fraction V_f [%]
Pultruded rod	150.0	11.9	79.3	25.2	2118	19.5	3.3	2.4	61
Braided rod	148.5	8.8	59.1	15.9	1809	12.6	3.3	-	54
	149.7	8.5	56.8	15.4	1814	12.5	2.9	-	55
average			**58.0**		**1812**				**54**
UD-strip	149.7	8.1	53.8	14.6	1817	11.4	3.2	-	53
	150.4	8.0	53.2	15.0	1879	11.1	4.0	-	52
average			**53.5**		**1848**				**53**

3.2.3. Conclusions

The width of the strips was selected to be comparable to that of the braided rods. Among the reinforcement options, the pultruded bar demonstrates a higher fibre volume fraction (V_f = 61%) compared to both the braided rods and laminated strips, which have fibre volume fractions of V_f = 54% and V_f = 53%, respectively. This difference in fibre volume fraction is expected due to the production process of pultruded bars, which more effectively aligns and compacts the longitudinal fibres. This alignment maximizes fibre density and minimizes voids within the material. Given that the mechanical properties and overall performance of FRP reinforcement are predominantly determined by the fibre content, pultruded bars are anticipated to offer superior strength and durability compared to their braided and laminated counterparts.

It was hypothesized that the fibre volume fraction of the laminated strips would fall between that of the pultruded bars and the braided rods. This expectation arises from the observation that, while the fibres in the laminated strips are not as densely packed as in the pultruded bars, they are still more

efficiently arranged than in the braided rods, which may contain voids due to their production method. However, the actual difference in fibre volume fraction between the braided rods and the UD-strip samples proved to be minimal, indicating that the packing efficiency of the fibres in the strips is closer to that of the braided rods than initially anticipated.

This minimal difference in fibre volume fraction suggests that the anticipated performance advantages of the laminated strips over the braided rods may be less pronounced than expected. Nonetheless, the slight variation in fibre content should still be considered when evaluating the mechanical properties and suitability of each reinforcement type for specific structural applications. Further analysis and testing are necessary to fully understand the implications of these differences on the performance of FRP reinforcement in concrete structures.

3.3. Uniaxial tensile capacity test

The purpose of the uniaxial tensile test on various BFRP reinforcement forms is to evaluate and characterize the material's mechanical properties when subjected to tensile loads. Through these tests, the ultimate tensile strength and strain of the BFRP can be determined. Additionally, the modulus of elasticity is evaluated to determine the stiffness or rigidity of BFRP by calculating the slope of the stress-strain curve. This property is essential for predicting how the material deforms under applied loads. Subsequently, the results allow for a comparative analysis of the tensile properties of BFRP against traditional steel reinforcement, highlighting the advantages and limitations of using BFRP in structural applications.

3.3.1. Setup

The procedure used for the uniaxial tensile testing of the braided basalt FRP rods and the unidirectional (UD) strips was based on a combination of ACI 440.3R-4 (2004), ASTM D7205M (2016), and CSA S806-02 (2002). These standards provide comprehensive guidelines to ensure accurate and reliable testing of FRP materials.

To ensure uniform stress conditions in the middle of the sample, ACI 440.3R-12 (2012) suggests that the free length between the anchors should be at least 40 times the sample's diameter (d) in millimeters. Given the nominal diameter of 8 mm specified by the manufacturer, a minimal free length of 320 mm is set for both the braided bars and the laminated strips.

Since the fibre volume fraction of the braided rods and the UD-laminate strips is approximately the same (as determined in Section 3.2), the width of the strips was selected to ensure that their cross-sectional area approximately matches that of the braided basalt FRP rods. This approach guarantees that the comparison between the two types of reinforcement is based on equivalent cross-sectional fibre areas, which is essential for a fair evaluation of their mechanical properties. By aligning the cross-sectional areas, any differences observed in the tensile behavior can be attributed to the inherent characteristics of the reinforcement types rather than discrepancies in fibre content.

The uniaxial tensile tests utilized a Zwick testing machine with an ultimate capacity of 250 kN. Although specific testing speeds are not prescribed by the consulted standards, it is recommended that the strain rate should induce failure within 1 to 10 minutes from the start of force application. To adhere to this guideline, a constant top cross-head displacement rate of 1 mm/min (0.0167 mm/s) was selected, effectively causing all samples to fail near the upper range of this interval, around 10 minutes.

Accurate deformation readings under load were obtained using an extensometer. According to the recommendations of CSA S806-02 (2002), the extensometer was removed once the load reached 75% of the estimated failure load to prevent potential damage. After detachment, strain measurements relied on the cross-head displacement, adjusted by the last ratio of extensometer to cross-head displacement, ensuring continuity and accuracy throughout the testing process.

All experiments were recorded using a video camera. This footage allowed for post-test analysis, ensuring that any unexpected behaviors or anomalies could be investigated and corrected in the results.

To enhance visibility and ensure proper lighting conditions, a bright lamp was employed throughout the testing process. The tensile testing machine used for this experiment, holding a laminated strip sample, is shown in Figure 3.8.

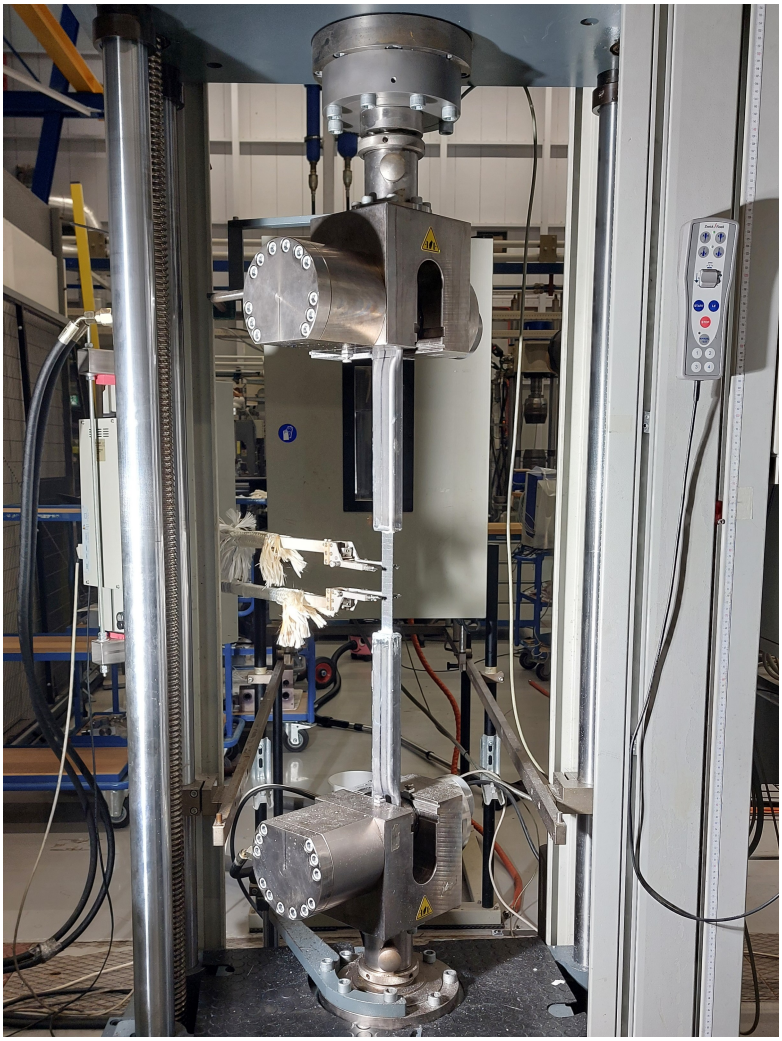

Figure 3.8: Set-up for uniaxial tensile testing

3.3.2. Sample preparation

For uniaxial tensile testing of composite samples, it is crucial to prevent lateral crushing from the cross-head clamps, as this can compromise the accuracy and reliability of the test results by introducing additional stress and deformation to the specimen, leading to premature failure. To mitigate this issue, the experimental setup incorporates a method to protect the composite specimens. Specifically, the samples are bonded into steel hollow sections using an epoxy adhesive (Henkel Loctite EA 9492). These steel hollow sections function as tensile anchors, ensuring that the composite specimens are securely held while distributing bond stresses more evenly.

This approach effectively prevents localized crushing and maintains the specimen's integrity during testing. The method, recommended in the reviewed standards, has proven effective in uniaxial tensile testing of pultruded BFRP rods, as demonstrated in the research by Lingen (2024). By employing this technique, the experimental setup achieves a more accurate representation of the material's mechanical properties under tensile loads, ensuring reliable and reproducible test results.

Braided BFRP rods

Given the circular cross-sectional shape of the braided BFRP samples, a steel circular hollow section (CHS) is utilized to ensure the tensile force is evenly applied from the anchor to the sample through bonding stresses. The steel anchors are flattened at one end using a hydraulic press to facilitate clamping within the testing device. To properly center the BFRP sample within the anchor, a steel washer with an inner opening slightly larger than the sample's diameter is spot-welded onto the remaining open end of the anchor. Before inserting the sample, the anchor is vertically leveled and filled with epoxy adhesive through this top steel washer. As the samples are inserted vertically through the washer plate, vertical alignment is checked and any excess adhesive that emerges from the top of the anchor is immediately removed. Once the epoxy adhesive has cured, this process is repeated for the steel anchor on the other end of the sample.

The hot rolled S355 steel circular hollow sections (CHS), used as anchors for the BFRP braided rods, have an outer diameter of 26.9 mm and a wall thickness of 2.6 mm. The cross-sectional area A is 198 mm^2 and the yield strength f_y is 355 MPa. Consequently, the tensile yield strength F_y is determined by multiplication of the cross-sectional area A and the yield stress f_y:

$$F_y = A \cdot f_y = 198 \cdot 355 = 70.3 \text{ kN}. \tag{3.3}$$

For braided BFRP rods produced by the same manufacturer, experimental research by Lindner et al. (2018, 2019) reports that the average ultimate tensile stress of this material is f_{FRP} 634 MPa. However, because some more margin is preferred, an ultimate stress of 900 MPa is taken as normative. The cross-sectional area of the braided BFRP bars was determined to be 58.0 mm^2, thus the ultimate tensile force required to break the samples then becomes:

$$F = A \cdot f_{FRP} = 58.0 \cdot 900 = 52.2 \text{ kN}. \tag{3.4}$$

Since the tensile force required to break the sample is lower than the yield strength of the tensile anchors, it is expected that the braided basalt FRP samples will fail before the tensile anchor yields.

Subsequently, a high-strength epoxy adhesive was used to securely bond the specimens within the anchors. To ensure the samples would not be pulled out of the anchors during tensile testing, the required anchorage lengths were determined. Based on the bond strength (τ_{bond} of 30 MPa for braided BFRP bars reported by Lindner et al. (2018), the minimum required bond length ($L_{bond,min}$) is calculated as follows:

$$L_{bond,min} = \frac{\text{FRP sample strength}}{\text{FRP sample perimeter} \times \text{bond strength}} = \frac{52.2 \cdot 10^3}{(8 \cdot \pi)\ 30} \approx\ 70 \text{ mm}. \tag{3.5}$$

Please note that, for simplicity, this calculation assumes a circular cross-section with a diameter of 8 mm. However, in this study, the braided bars actually have an oval cross-section and received an additional epoxy surface coating during production to improve their resistance to alkali. This extra coating eliminated the typical surface roughness associated with braided bars, potentially reducing this maximum achievable bond stress. Furthermore, the process of filling the steel anchor with epoxy adhesive is challenging to control precisely, potentially leading to air pockets that could reduce the bonded area between the sample and the anchor. Additionally, the smooth interface between the steel anchor and the epoxy adhesive could be normative for failure. The epoxy glue may also exhibit shrinkage behavior during curing, potentially resulting in it peeling off the steel anchor surface and thus limiting the bond capacity.

To mitigate these risks, a bond length of 300 mm was used, significantly longer than the minimum required bond length calculated above. This increased bond length ensures a more secure anchorage and compensates for any potential deficiencies in bonding quality.

The braided bars have longitudinal fibres primarily in the core, with the surrounding braided fibre structure angled relative to the rod direction. It is expected that this angled fibre structure will affect the strength and stiffness, which means they might and might not perform as well as the laminated strips or pultruded bars in terms of mechanical properties.

Laminated BFRP strips

A similar procedure is employed for laminated BFRP strips as for braided BFRP rods, with modifications to accommodate the rectangular cross-section of the strips. The steel circular hollow section (CHS) anchors are replaced by rectangular hollow sections (RHS). Additionally, a steel plate with a wide, narrow slot milled in its center replaces the steel washer, aiding in the precise alignment of the sample within the anchor. An oversized round hole is drilled in the center of this steel plate to facilitate the application of epoxy adhesive inside the anchor. This adapted method ensures that the laminated strips are securely held and the bond stresses are evenly distributed across the sample.

For the first two UD-laminate samples, this slotted plate was given a a thickness of 1 mm and it was only spot-welded to the RHS-section. For the third and fourth sample, the thickness was increased to 3 mm and it was structurally welded all around to the RHS-section. The design of this slotted top plate and its dimensions are illustrated in Figure 3.9.

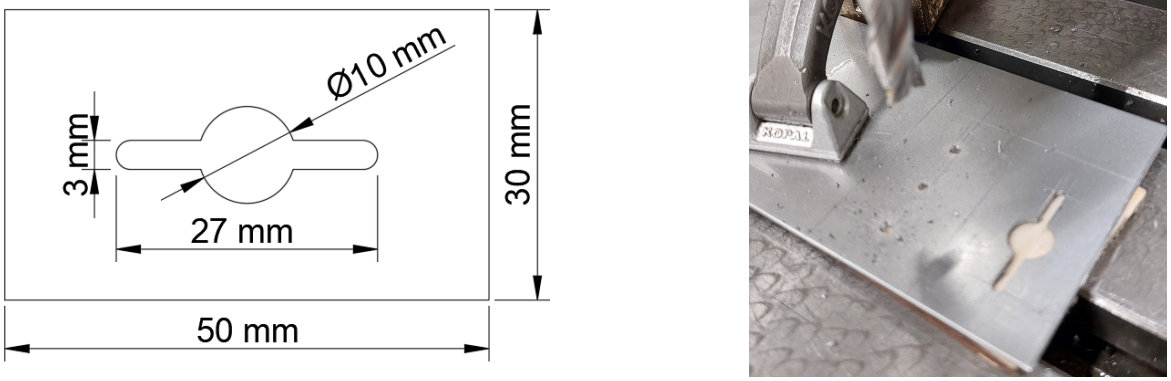

(a) Design and dimensions **(b)** Production

Figure 3.9: Steel slotted top plate for uniaxial tensile testing of laminated strip samples

Since the ratio of perimeter/cross-sectional area is more favourable for the laminated strips than for the braided bars, the anchorage length is reduced to 200 mm for the first test and increased in the case of sample pull-out from the anchors.

The laminated strips, composed of longitudinal fibres, are expected to exhibit strength and stiffness comparable to pultruded bars. However, their performance may be slightly lower due to the waviness of the fibres in the strips, which results from their woven texture.

3.3.3. Test results

The stresses and E-modulus are determined based on the full composite cross-sectional area, which includes both fibres and matrix. The tensile strength (f_u) is determined using the following formula:

$$f_u = F_u / A \tag{3.6}$$

where F_u is the tensile capacity, and A is the full cross-sectional area of the composite specimen as previously determined in Section 3.2.

The axial modulus of elasticity E_L of the BFRP samples is determined using the formula:

$$E_L = \frac{F_1 - F_2}{(\varepsilon_1 - \varepsilon_2)A} \tag{3.7}$$

Where:
E_L = axial (longitudinal) modulus of elasticity, [MPa];
A = cross-sectional area of the FRP reinforcement sample, [mm^2];
F_1 and ε_1 are the load and corresponding strain at the upper end of the interval;
F_2 and ε_2 are the load and corresponding strain at the lower end of the interval.

According to ACI 440.3R-4 (2004) B.2, the test method for longitudinal tensile properties of FRP bars specifies using the interval of 20% to 50% of ultimate force and the corresponding strain values. This standard has been replaced by ASTM D7205M (2016), which specifies that the strain range should be within the lower half of the stress-strain curve, starting at a strain of 0.001 and ending at a strain of 0.003. Additionally, NEN ISO 527-5 (2009) recommends using a strain interval of 0.005 to 0.0025 and the corresponding forces for these limits to determine the elastic modulus.

The stress-strain diagrams of all samples are shown in Figure 3.10. In this figure, the black lines correspond to the braided BFRP rod samples, whereas the red lines are the BFRP strip samples. During analysis, discrepancies were observed at the lower end of the stress-strain curve, affecting the E-modulus in the intervals recommended by ASTM and ISO standards. These discrepancies were attributed to factors such as eccentric loading, misalignment-induced bending of samples, slipping within the anchors, and misalignment of the anchor rods in the testing device.

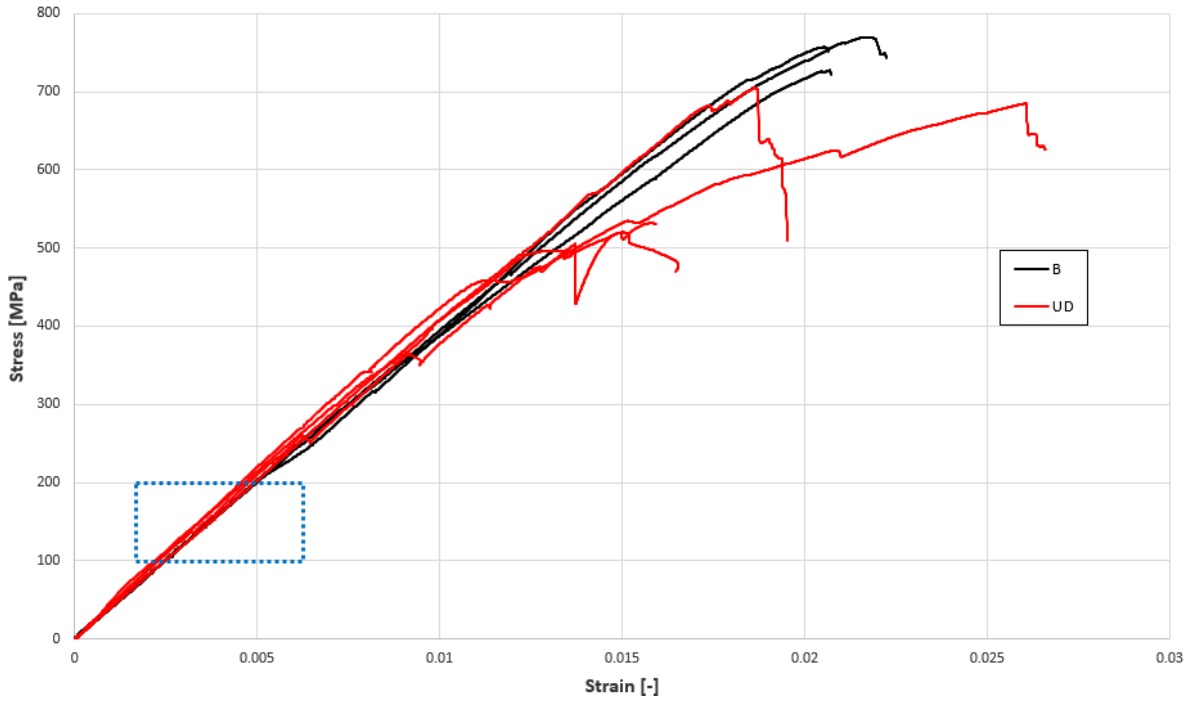

Figure 3.10: Stress-strain diagrams for braided BFRP bars (B) and laminated BFRP UD-strips (UD). The blue dotted box represents the interval used to determine the elastic modulus of the samples.

To address these issues, the decision was made to use a stress range of 100 to 200 MPa and the corresponding strain values for each sample to determine the elastic modulus, rather than the intervals described in the standards. This interval is illustrated with a blue dotted box in Figure 3.10. This approach avoids the initial discrepancy zone, ensuring more accurate and consistent results. Using these constraints, the length of the strain interval is approximately the same as specified in ASTM or ISO standards.

The next subsections will describe the results for the braided BFRP rods and laminated BFRP UD-strips separately, providing detailed insights into their tensile properties and mechanical behavior.

Braided BFRP rods

A total of three Ø8 mm braided basalt FRP samples were tested, each with a total length of 840 mm. The bond length was 300 mm within the steel anchors on either side. During testing, all samples experienced slipping within the tensile anchors, which resulted in small horizontal steps in the elongation measurements. This slipping was confirmed by analyzing the video footage from the experiments and was subsequently corrected in the results.

The stress-strain diagrams are shown in Figure 3.11, illustrating the mechanical behavior of the braided BFRP rods under tensile loading. The results for the uniaxial tensile test of the braided BFRP rods are shown in Table 3.2. For all samples, it is assumed that the cross-sectional area is the same as the average cross-sectional area determined previously in Section 3.2: A = 58.0 mm^2.

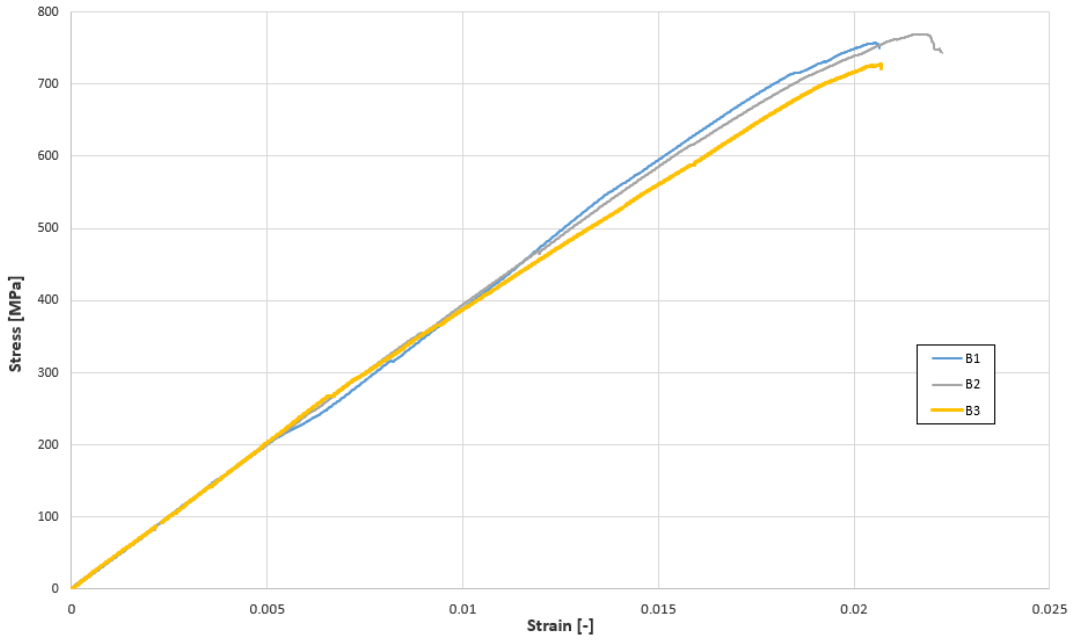

Figure 3.11: Stress-strain diagrams for the braided BFRP rod samples (B)

From this figure it can be observed that the braided BFRP specimen do indeed show linear-elastic behaviour until failure. The first and last sample failed in the middle between the tensile anchors and the second sample failed close to the bottom tensile anchor. The failed specimen after testing are shown in Figure 3.12.

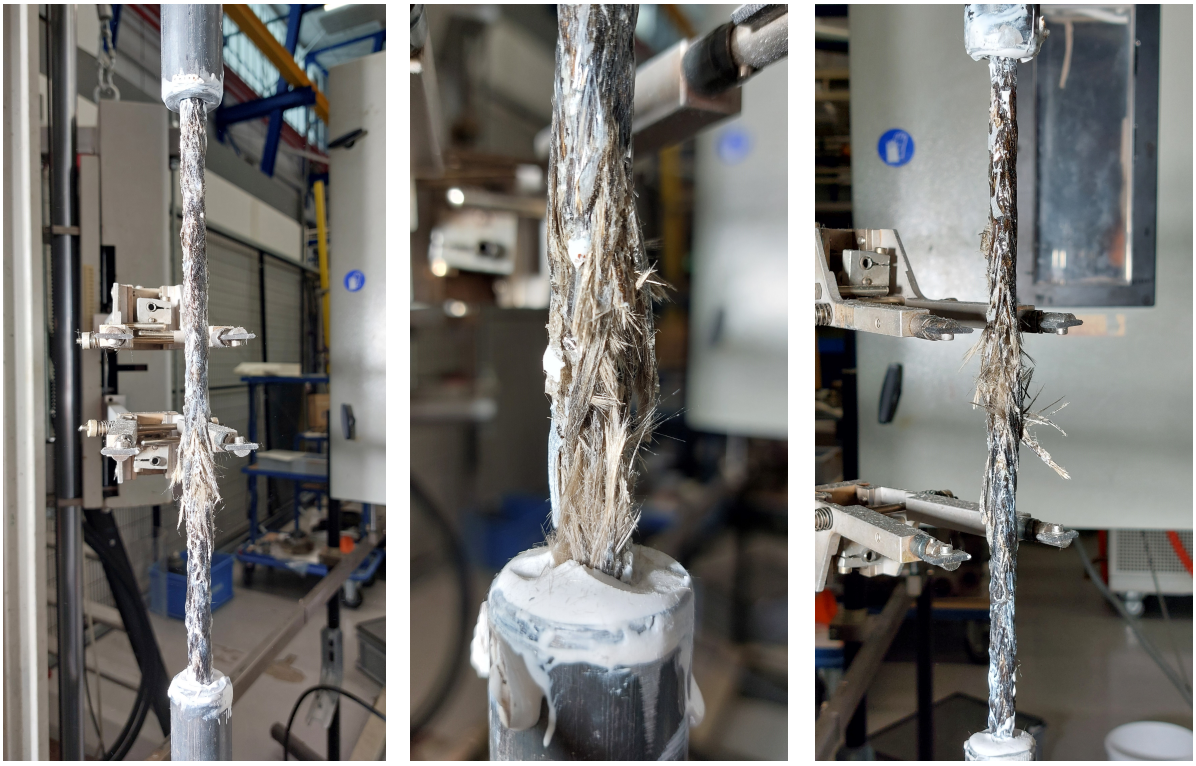

(a) Sample B1 **(b)** Sample B2 **(c)** Sample B3

Figure 3.12: Braided BFRP samples after uniaxial tensile testing

From observing Figure 3.12, it is evident that sample B2 failed near the bottom tensile anchor rather than at the midpoint of the specimen as samples B1 and B3 did. This deviation indicates the presence of localized stress concentrations near the anchorage point. Such stress concentrations are likely a result of imperfections or irregularities within the material's microstructure at that specific location. These flaws could have intensified the stress at the anchor, leading to premature failure at that point.

Table 3.2: Uniaxial tensile results for braided BFRP rods

Braided BFRP sample	Ultimate force F_u [kN]	Cross-sectional area A [mm^2]	Ultimate stress f_u [MPa]	Rupture strain ε_u [%]	Elastic modulus E [GPa]
B1	43.9	58.0	757	2.05	39.6
B2	44.6	58.0	769	2.19	40.5
B3	42.2	58.0	727	2.07	41.0
		avg	751	2.10	40.4
		sd	18.5	0.062	0.71
		cv	2.9%	2.94%	1.8%

From this table it can be observed that uniaxial tensile test results for the braided BFRP rods demonstrate consistent mechanical properties across all samples tested. With the assumption that all samples shared the same average cross-sectional area determined previously, and a bonded length of 300 mm within the steel tensile anchors, the results show minimal variation. The average ultimate stress was found to be 751 MPa, with a rupture strain of 2.3% and an elastic modulus of 40.4 GPa.

The standard deviation (SD) values — 18.5 MPa for ultimate stress, 0.105 % for rupture strain, and 0.709 GPa for elastic modulus — indicate a high degree of uniformity and repeatability in the tensile properties of the braided BFRP rods. This consistency suggests that the manufacturing process and material quality are well-controlled, leading to reliable and uniform mechanical properties across different samples.

Additionally, the coefficients of variation (cov) further emphasize the consistency of the results. The covariance for ultimate stress is 2.88%, for rupture strain is 5.08%, and for elastic modulus is 1.76%. These low covariance percentages indicate that the data points are tightly clustered around the mean, highlighting the precision and reliability of the measurements.

Laminated BFRP strips

The widths of the tested strips vary because they were not cut with high precision. To address this, the cross-sectional area of each specimen has been scaled according to the actual width of the strip, using the cross-sectional area that was determined in Section 3.2. This adjustment ensures that the measured properties accurately reflect the true cross-sectional area of each strip, allowing for a more precise comparison between the different samples. By scaling the cross-sectional area, the data account for any discrepancies in the cutting process, ensuring that the evaluation of mechanical properties is based on the corrected and true dimensions of the strips.

The stress-strain diagrams for the laminated BFRP strips are presented in Figure 3.13.

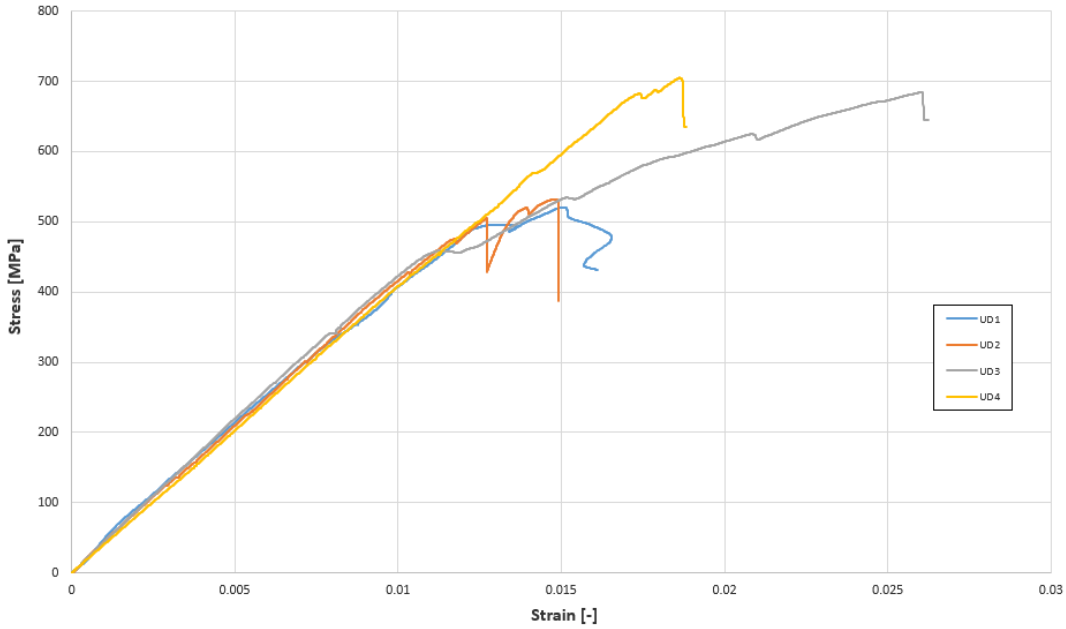

Figure 3.13: Stress-strain diagrams for the uniaxial tensile testing of the laminated unidirectional BFRP strip samples

For each subsequent strip sample, the failure mode observed led to adjustments in the preparation of the next sample, eventually achieving the desired fibre failure in the middle of the test section between the tensile anchors on the fourth attempt. The failure modes and corresponding adjustments are described below, and the samples after testing are shown in Figure 3.14.

The first sample, UD1, had a bonded length of 250 mm. During testing, it experienced delamination characterized by vertical and slightly inclined cracks. Some parts of the sample were insufficiently anchored within the anchors, resulting in fibre pull-out. This caused the entire force to be supported by the remaining anchored part, leading to brittle, premature failure of a limited part of the cross-sectional fibres. The full sample is shown in Figure 3.14 (a) and a close-up image is shown in Figure 3.15 (a).

The second sample, UD2, had an increased anchorage length of 300 mm. During this test, at a tensile force approximately equal to the failure force of sample UD1, the shear interface between the anchor and the glue plug became normative. It sheared out of the top steel anchor along with the sample and top slotted plate. The full sample is shown in Figure 3.14 (b) and a close-up image is shown in Figure 3.15 (b).

For the third sample, UD3, the inner surface area of the anchors was more thoroughly degreased

using isopropyl alcohol (IPA) instead of acetone, because IPA leaves no residue. This is done to enhance bond strength of the steel surface with the epoxy adhesive. Additionally, the thickness of the slotted plate was increased from 1 mm to 3 mm, and instead of spot-welding at each corner, it was structurally welded all around the rectangular hollow section. During testing, the shear interface between the glue plug and anchor did not fail. However, the sample suffered from vertical and slightly inclined delamination cracks and subsequent pullout as described for sample UD1. This is shown in Figure 3.14 (c).

For the fourth and final sample, UD4, a new batch of BFRP UD-laminate was produced to be able to increase the bonded length within the anchors, while complying with the prescribed free length between the anchors at the same time. The same preparations as used for UD3 were followed. Additionally, since the epoxy adhesive experienced some settling and shrinkage upon curing, the tensile anchors were topped up with epoxy adhesive for a second time. Upon clamping the sample and its tensile anchors in the testing device, it was observed that the flattened ends of the anchors were slightly skewed relative to the longitudinal direction of the anchor. Despite this misalignment, the test proceeded as planned. The stress-strain graph for sample UD4 showed that the initial stiffness was significantly lower than that of the other samples. This was attributed to the bending of the flattened ends of the tensile anchors, rather than uniaxial loading until they straightened between the cross-heads. After this initial phase, the sample exhibited linear elastic behaviour again, upon failure in the middle of the test section right between the anchors. This is depicted in Figure 3.14 (d).

All four strip samples developed vertical and slightly inclined cracks during the experiments. These inclined cracks, best shown in Figure 3.14 (b), are likely due to slight misalignment in the cutting of the strips relative to the fibre direction, causing parts of the cross-section to have insufficient anchorage length or no anchorage in the steel tensile anchors. Since the strips are composed solely of unidirectional fibres, the matrix material primarily governs the transfer of shear forces, and it was evident that its shear strength was insufficient to prevent delamination. Additionally, the inter-layer alignment of fibres within the strips depended on the stacking process during production, which is likely to be imperfect.

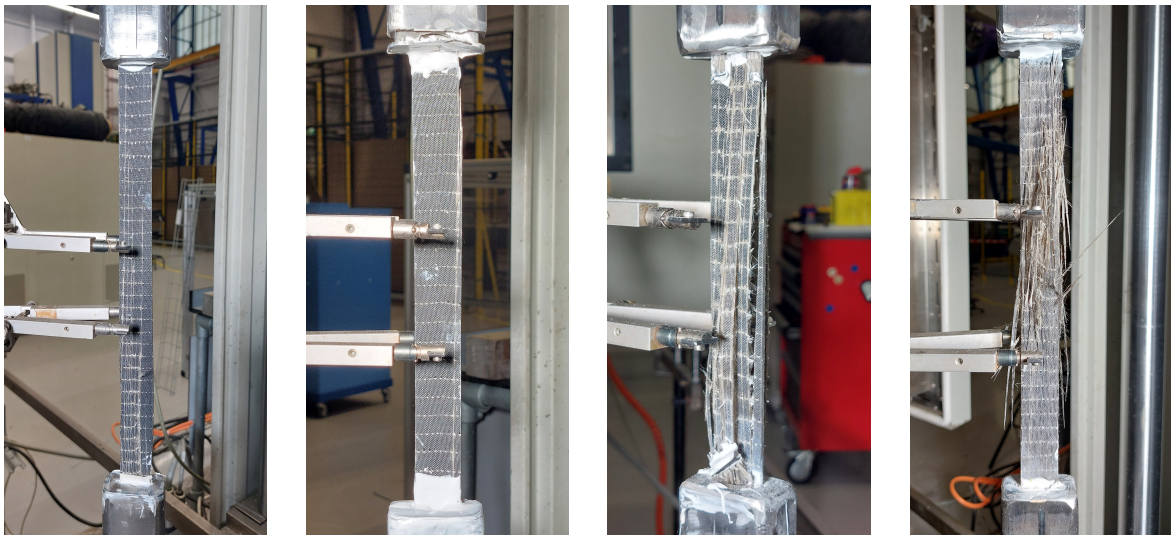

(a) Sample UD1: fibre pull-out **(b)** Sample UD2: anchor plug fail **(c)** Sample UD3: fibre pull-out **(d)** Sample UD4: fibre rupture

Figure 3.14: Uniaxial tensile testing of laminated UD-strip samples

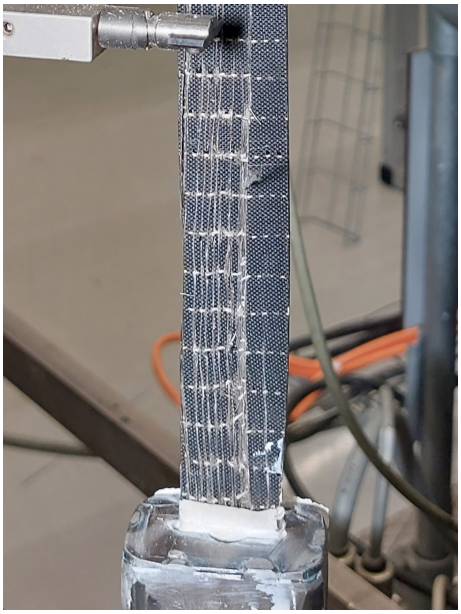

(a) UD1: longitudinal cracks and fibre pullout failure

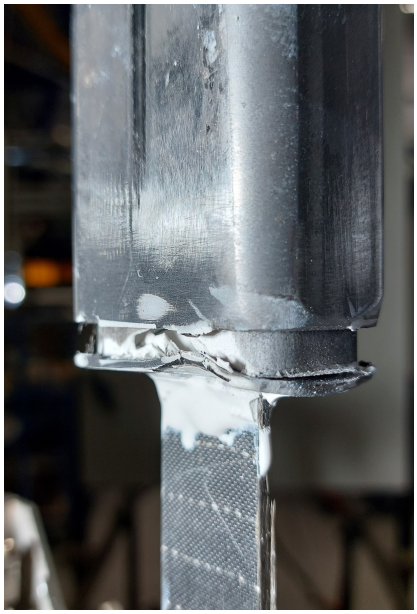

(b) UD2: glue plug pull-out from the top anchor

Figure 3.15: Close-up of samples after testing

Table 3.3 presents an overview of the results. The cross-sectional area of these samples are scaled by their actual width compared to the samples used for verification in Section 3.2. The ultimate force and strain values from the final sample ("UD4") are considered normative due to its successful failure in the center of the testing region between the steel tensile anchors, while the other samples failed prematurely due to pull-out. This central failure indicates a uniform stress distribution and a representative measure of the material's tensile strength, with an ultimate stress of 706 MPa and a rupture strain of 1.9%.

Table 3.3: Uniaxial tensile testing results for laminated basalt FRP UD-strips

Laminated strip sample	Ultimate force F_u [kN]	Cross-sectional area A [mm^2]	Ultimate stress f_u [MPa]	Rupture strain ε_u [%]	Elastic modulus E [GPa]
UD1	29.7	57.2	520	1.50	40.6
UD2	30.1	56.6	532	1.58	40.6
UD3	38.2	55.8	685	2.60	43.8
UD4	**39.0**	**55.2**	**706**	**1.86**	40.5
				avg	**41.4**
				std	0.85
				cov	1.99%

Note: The ultimate force, stress, and rupture strain for sample UD4 are considered normative because this sample was successfully loaded to the point of failure of the fibres in the middle of the test region. The elastic modulus, however, is based on all samples, as they did not exhibit any signs of premature failure at the load levels used for this calculation.

The elastic modulus, calculated using data from all samples, averaged 41.4 GPa. This modulus was determined over an interval with relatively low stresses, ensuring that no signs of fibre pull-out or other premature failures had initiated. The low standard deviation of 3.36% for the elastic modulus further supports the consistency of the material's mechanical properties across different samples.

3.3.4. Comparison with pultruded BFRP and steel reinforcement

Table 3.4 presents an overview of the ultimate stress, rupture strain, and elastic modulus of three different BFRP materials: pultruded BFRP rods (derived by Lingen, 2024), braided BFRP rods and BFRP UD-laminate strips (derived in this study). Additionally, the table provides relative strength and

stiffness values with respect to the pultruded BFRP rods, which serve as the baseline material in this comparison.

Table 3.4: Overview of average uniaxial tensile test results

Basalt FRP sample material	Ultimate stress f_u [MPa]	Rupture strain ε_u [%]	Elastic modulus E [GPa]	Relative strength f_u / 1141	Relative stiffness E / 53.5
Pultruded rods*	1141	2.12	53.5	(1.0)	(1.0)
Braided rods	751	2.10	40.4	0.66	0.76
UD-laminate strips	706	1.86	41.4	0.62	0.77

* Derived in a study by Lingen (2024) using Ø8 mm pultruded BFRP rods with sand-coating from Orlitech®

This table shows that pultruded BFRP rods outperform both braided BFRP rods and BFRP UD-laminate strips in terms of ultimate stress and stiffness. This is due to the parallel orientation and high fibre volume fraction, resulting from efficient fibre packing.

The relative uniaxial strength and stiffness of the braided BFRP rods are 0.66 and 0.76, respectively, when compared to the pultruded rods. This indicates that the braided structure and lower fibre volume fraction have a greater impact on strength than on stiffness. The reduction in strength is primarily due to the angled orientation of the strands within the braided structure, which introduces stresses perpendicular to the fibre direction. Because the fibres are not perfectly aligned with the load direction, the load is distributed among fibres oriented in various directions rather than being carried directly along the fibre length. As these misaligned fibres reorient under load, shear stresses arise, increasing the likelihood of micro-buckling or kinking within the braid. These effects diminish the overall load-bearing capacity, resulting in reduced ultimate strength.
In contrast, the stiffness of the braided rods is less adversely affected by the angled fibre orientation. Even when fibres are not perfectly aligned, they still contribute to the overall stiffness of the material due to the combined elastic response of both the fibres and the matrix. The contributions to stiffness from fibres in different directions tend to average out, making stiffness less sensitive to fibre orientation compared to strength. While stress concentrations in braided structures are critical for strength, as they can act as initiation points for failure, stiffness is less impacted under moderate loads. This distinction underscores the relative resilience of stiffness in braided structures, despite the presence of misaligned fibres.
For UD laminate strips, the relative uniaxial strength and stiffness are respectively 0.62 and 0.77 compared to the pultruded bars. Again, this is due to the lower fibre volume fraction, but fibre misalignment or waviness also reduces the effective load-bearing cross-section. This misalignment causes local buckling or kinking under load, significantly impacting tensile strength more than stiffness. Wavy fibres create points of weakness where failure can initiate under tensile stress. Perfectly aligned fibres would distribute the tensile load evenly, maximizing strength. However, deviations from perfect alignment reduce this efficiency, leading to lower strength. Stiffness is less affected by these imperfections because it relies on the cumulative elastic response of the fibres and matrix. fibre waviness and misalignment create stress concentrations, critical for tensile strength as they can lead to crack initiation and propagation. These concentrations have a less pronounced effect on stiffness because the material's response to elastic deformation is more distributed. Manufacturing imperfections, such as resin-rich areas, voids, or incomplete fibre impregnation, also contribute to reduced strength by creating weak points, further compromising the material's ultimate tensile strength.

3.3.5. Discussion

Influence of strain rate variations on tensile test results

The cross-head separation speed was consistently maintained at 1 mm/min (0.0167 mm/s) for all samples. However, the grip-to-grip separation distances differed between the braided BFRP rod samples and the laminated strip samples within the testing device. Consequently, these samples were subjected to different strain rates.

The grip-to-grip separation distance was approximately 920 mm for the braided samples, whereas for the laminated strip sample UD4 it was 1043 mm. The strain rate ($\dot{\varepsilon}$) is calculated using the formula:

$$\dot{\varepsilon} = \frac{\text{crosshead separation speed}}{\text{crosshead grip to grip distance}} \tag{3.8}$$

Applying this equation, the strain rate for the braided samples ($\dot{\varepsilon}_{\text{braid}}$) is:

$$\dot{\varepsilon}_{\text{braid}} = \frac{0.0167 \text{ mm/s}}{920 \text{ mm}} \approx 1.82 \cdot 10^{-5} \text{ s}^{-1} \tag{3.9}$$

For the laminated strip sample UD4 ($\dot{\varepsilon}_{strip}$), the strain rate is:

$$\dot{\varepsilon}_{\text{strip}} = \frac{0.0167 \text{ mm/s}}{1043 \text{ mm}} \approx 1.60 \cdot 10^{-5} \text{ s}^{-1} \tag{3.10}$$

The strain rate for the braided BFRP samples is approximately 12.5% higher than for the laminated strip samples. In general, materials often exhibit increased apparent strength and stiffness at higher strain rates due to reduced time for stress relaxation and damage progression. Such differences complicate the accurate comparison of the mechanical properties of the two reinforcement types.

For more reliable comparisons, it would have been preferable to maintain a constant strain rate across all samples rather than a constant cross-head displacement speed. Consistent strain rates ensure that observed variations in tensile strength, stiffness, and failure modes are attributable to the inherent material properties rather than differences in testing conditions. Standardizing the strain rate would thus yield more reliable and comparable data, facilitating better assessment of BFRP reinforcement performance.

However, studies such as those by Protchenko et al. (2020) and Elmahdy et al. (2024) indicate that while strain rate variations can impact the magnitude of measured properties, significant effects typically require much larger variations in strain rates. Consequently, the relatively small difference in strain rate observed in this study is unlikely to have significantly affected the results. Therefore, the overall trends observed in the data are assumed to remain consistent.

Slipping of samples within anchors

For the braided rods, it was necessary to correct the recorded strain values due to the observed slipping of the sample within the tensile rods. This slippage can lead to an overestimation of the actual strain experienced by the sample, thus skewing the results. To address this issue, corrections were applied to ensure that the strain measurements accurately reflect the material's true response under load.

Failure modes of strip samples

The laminated strips exhibited a different set of challenges. The imperfect alignment of fibres from the individual layers of UD-fabric within the sample and the non-perfect alignment of the cutting angle to the fibre direction during the cutting process resulted in the formation of vertical shear cracks and delamination during testing. This misalignment induces stress concentrations and weak points that propagate cracks more readily than in perfectly aligned fibres, compromising the integrity of the material. Consequently, these imperfections can significantly affect the tensile properties measured, because the samples will suffer from premature failure. Furthermore, it was anticipated that the more favourable ratio between cross-sectional perimeter and area would result in a smaller required bond length, but this was not the case: a bond length of 350 mm (50 mm longer than for the braided samples) was required to prevent fibre pull-out from the anchors.

Among the laminated strip samples tested, only one sample successfully failed in the middle of the free length between the anchors. This successful failure is indicative of a more uniform stress distribution and a representative tensile strength of the material. The failure in the middle of the testing region suggests that this sample had better anchorage, fibre alignment and/or fewer initial defects compared to the others. This could be explained by the fact that this sample is derived from another batch of UD-laminate. This sample's results are therefore taken as normative for assessing the ultimate force and strain characteristics of the laminated strips.

Strain measurements after removal of extensometer

For all uniaxial tensile test samples, the extensometer was removed at approximately 75% of the ultimate load to prevent damage to the equipment during the brittle failure. After removal of the extensometer, the strain of the samples was based on the cross-head displacement that accounted for the last recorded ratio between the elongation displacement in the extensometer and the cross-head displacement. This is a potential source of error, because extensometers provide highly accurate and localized strain measurements directly on the specimen, whereas cross-head displacement measurements can include additional deformations from the sample within the anchors and the testing machine setup, such as fibre pull-out and compliance in the grips and machine frame. As a consequence, relying on cross-head displacement may lead to overestimating of the actual strain experienced by the specimen as slip increases. Furthermore, the ratio of elongation displacement measured by the extensometer to cross-head displacement may change as the load increases. This holds especially near the point of failure, because the samples exhibited plastic deformation, e.g. in the form of delamination in the strips. This could result in inaccuracies if the last recorded ratio is applied uniformly for the remaining part of the test.

4

Method of beam shear capacity test

Three-point bending tests of reinforced concrete beams are performed to assess the shear capacity of the composite structures. By subjecting the beams to controlled loading conditions, this experiment will offer a comprehensive understanding of the effectiveness of BFRP as shear reinforcement when compared to steel reinforcement, and of its influence on the overall structural integrity and load-carrying capacity of reinforced concrete beams.

4.1. Beam design

The primary goal of the beam test is to quantify the enhancement in shear capacity by introducing BFRP stirrups in concrete beams that initially have no stirrups. To quantify the maximum increase in shear capacity using this specific type and configuration, the beams are designed to fail in shear tension mode. Shear tension failure occurs when the diagonal tensile stresses in a beam exceed the tensile strength of the concrete, leading to the formation and propagation of diagonal cracks. By designing the beams to fail in this mode, the test directly assesses the effectiveness of the shear reinforcement in resisting these stresses and controlling crack development. To achieve a valid comparison, the increase in shear capacity in beams with BFRP stirrups will be measured against the increase provided by traditional steel stirrups.

4.1.1. Beam specimen

A total of six distinct reinforced concrete beam samples with dimensions 1650 x 200 x 150 mm (length x height x width) are tested. The span between the supports is kept constant at a distance of 1000 mm for all samples. The main difference between these samples is the type and the number of stirrups used. The control beams include one with no stirrups (”NS”) and another with a total of four steel Ø8 stirrups (”S4”). The remaining beams are reinforced with either braided (”B”) basalt fibre reinforced polymer (BFRP) stirrups or laminated unidirectional (”UD”) strip stirrups. These BFRP-reinforced beams are further differentiated by having either a total of four or eight stirrups, which again corresponds to the number in the sample name. This variation allows for a comprehensive analysis of the performance and shear capacity of different types and quantities of BFRP stirrups compared to beams without stirrups and beams reinforced with traditional steel stirrups.

To rule out any influence by a varying corner radius, all stirrups were supposed to have the same corner radius. A corner radius of 32 mm was selected, since this is standard practice for the producer of the braided BFRP stirrups. The beam samples and their distinct stirrup configuration is listed in Table 4.1.

Table 4.1: Beam specimen and stirrup details

Beam ID	Stirrup Material	Spacing s [mm]	Diameter D [mm]	Width w [mm]	Thickness t [mm]	Shear reinf. area A_v [mm^2]	Shear reinf. ratio [%]
NS	None	-	-	-	-	-	-
S4	Steel	250	8	-	-	100	0.27
B4	BFRP braided rod	250	8	-	-	116	0.31
B8	BFRP braided rod	125	8	-	-	116	0.62
UD4	BFRP UD-strip	250	-	19	2.3	86	0.23
UD8	BFRP UD-strip	125	-	19	2.3	86	0.46

In this testing configuration, a concentrated load is applied at the midpoint of the beam via a hydraulic jack securely mounted on a robust, modular bolted portal frame. This frame is designed to provide the necessary support and stability throughout the testing process, ensuring that the applied forces are accurately transmitted to the beam without causing unintended deformations or displacements in the testing setup.

The resulting moment and shear force distributions along the length of the beam, generated by the centrally applied load, are illustrated in Figure 4.1. For the purposes of this analysis, the self-weight of the beams is disregarded. The moment distribution reaches its peak at the midpoint of the beam, directly beneath the applied load, while the shear force remains constant along the entire span of the beam.

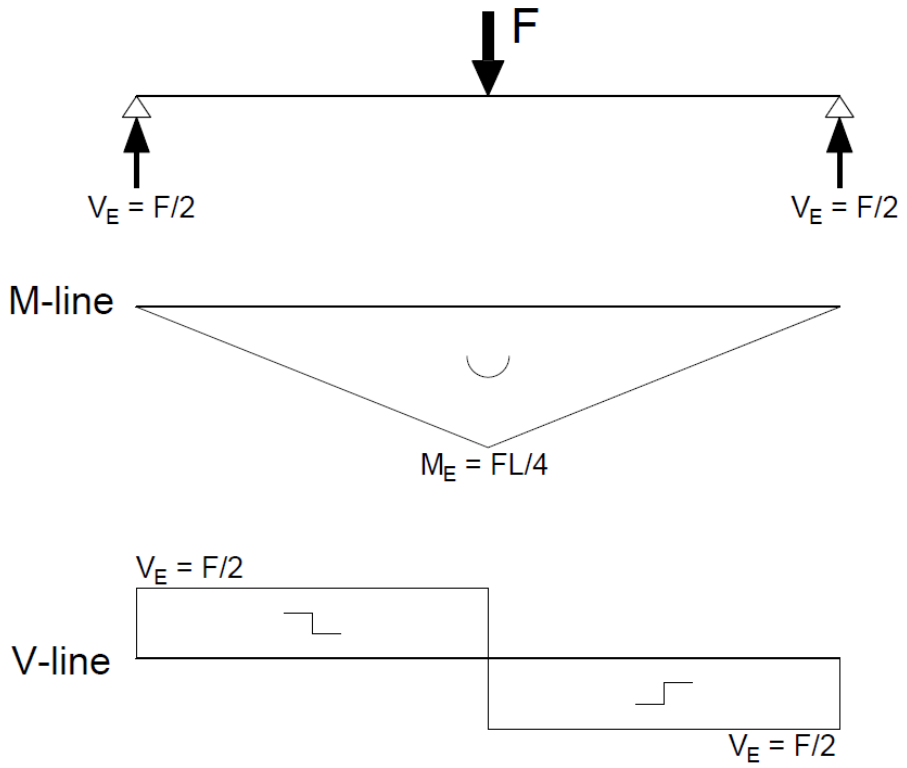

Figure 4.1: Three-point bending test configuration: moment and shear force distribution along the length of the beam

To ensure the beam specimen do not fail prematurely in bending before achieving the desired shear tension failure mode, an adequate amount of flexural capacity is required. This is achieved by incorporating two Ø20 mm and two Ø25 traditional ribbed steel reinforcement bars in longitudinal direction, with its centers at a height of 36 mm and 157.5 mm below the beam's top surface, respectively. To prevent direct force transfer from loading point to the supports through compression arches, the shear span-to-effective depth ratio a/d is maintained at 500 / 157.5 = 3.2. Table 4.2 gives an overview of the

general beam dimensions and design parameters. The longitudinal sections for all the different beam samples are shown in Figure 4.2.

Table 4.2: General beam details

Beam geometry		**Steel reinforcement B500B**	f_{ym} = 560 MPa
Height h	200 mm	**Long. tensile steel reinf.**	2x Ø25 mm
Width b	150 mm	Cross-sectional area A_{st}	928 mm^2
Length L	1650 mm	Concrete cover c	30 mm
Span L_0	1000 mm	Effective height d	200-30-(25/2) = 157.5 mm
Shear span a	500 mm	a/d [-]	500/157.5 = 3.17
Concrete strength class		**Long. compr. steel reinf.**	2x Ø20 mm
C30/37	f_{ck} = 30 MPa	Cross-sectional area A_{sc}	628 mm^2
f_{cm} = f_{ck} + 8	f_{cm} = 38 MPa	Concrete cover c_2	26 mm
E-modulus	32837 MPa*	Effective height d_2	26+(20/2) = 36 mm

* From NEN-EN 1992-1-1 (2011), corresponding to C30/37

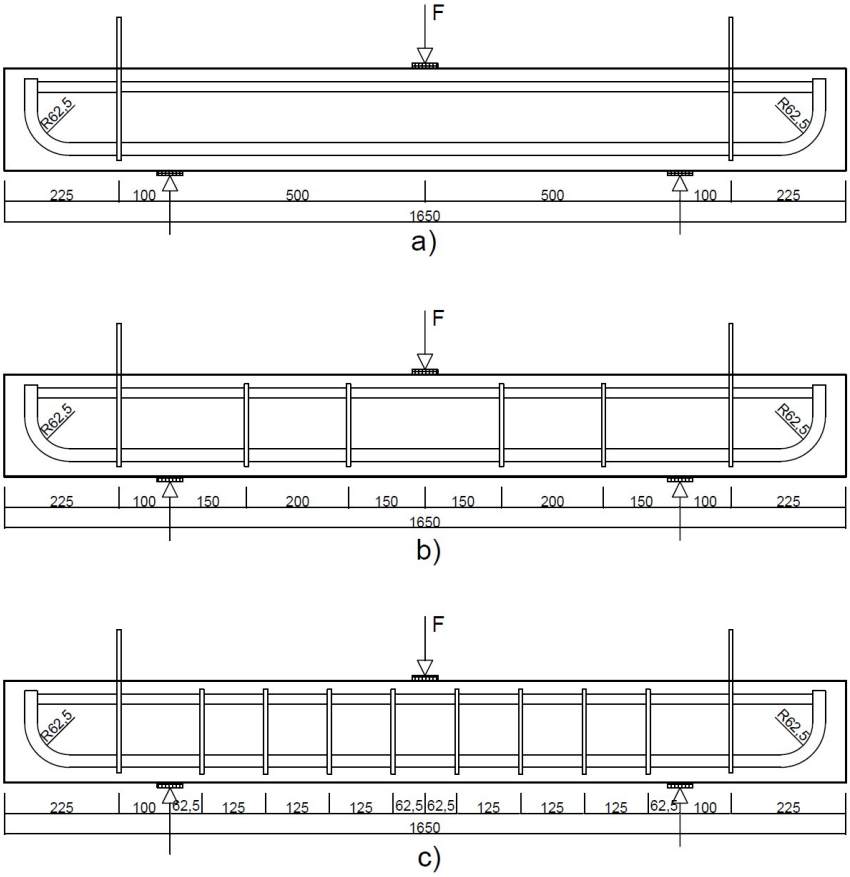

Figure 4.2: Longitudinal cross-section of beam specimen: a) Beam without stirrups (NS); b) Beams with 4 stirrups (S4, B4 and UD4); c) Beams with 8 stirrups (B8 and UD8)

The original cross-sections of the beams, as defined during the design phase, are depicted in Figure 4.3. It is important to note that these cross-sections were subsequently modified to accommodate adjustments in the stirrup geometry, specifically related to the inner corner radius. These adjustments were necessary to ensure that the longitudinal reinforcement was properly enclosed by the stirrups, in compliance with the requirements set forth by Eurocode 2 design regulations.

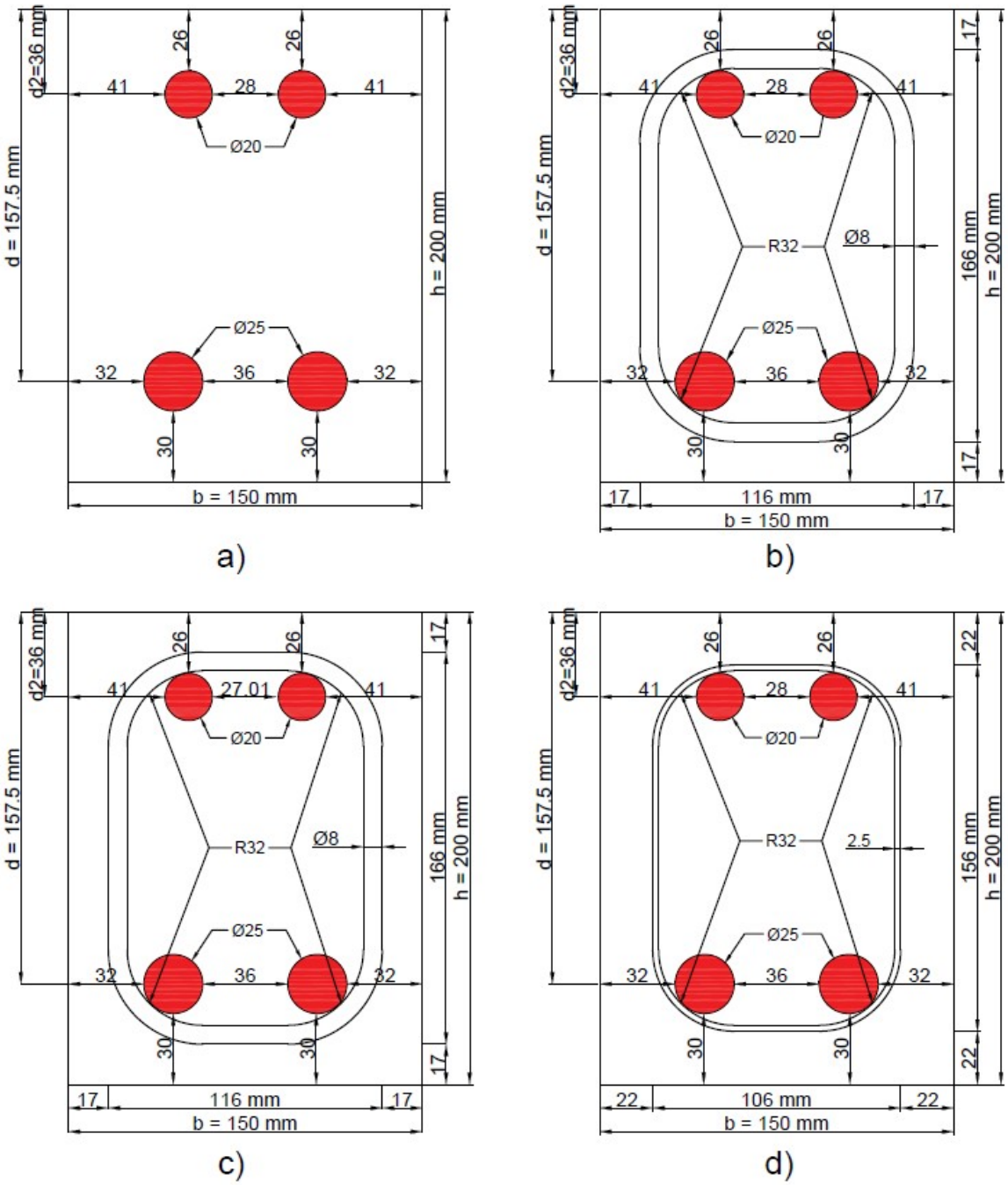

Figure 4.3: Beam cross-sections: a) No Stirrups in sample NS; b) Steel stirrups in sample S4; c) Braided BFRP stirrups in samples B4 and B8; d) Laminated BFRP UD strip stirrups in samples UD4 and UD8.

4.1.2. Flexural capacity

The flexural capacity should be sufficient in order for the beams to fail in shear. In this section, the flexural capacity is calculated. The strain in concrete (ε_c) at the top surface of the beam is set as unknown, while assuming that the tensional steel is yielding. Internal horizontal equilibrium is then found by setting the normal force in the tensional steel (subscript ”st”) equal to the compressive forces in the compressive reinforcement steel plus the compressive force in the concrete compression zone (subscripts ”sc” and ”c”, respectively):

$$N_{st} = N_{sc}(\varepsilon_c) + N_c(\varepsilon_c) \tag{4.1}$$

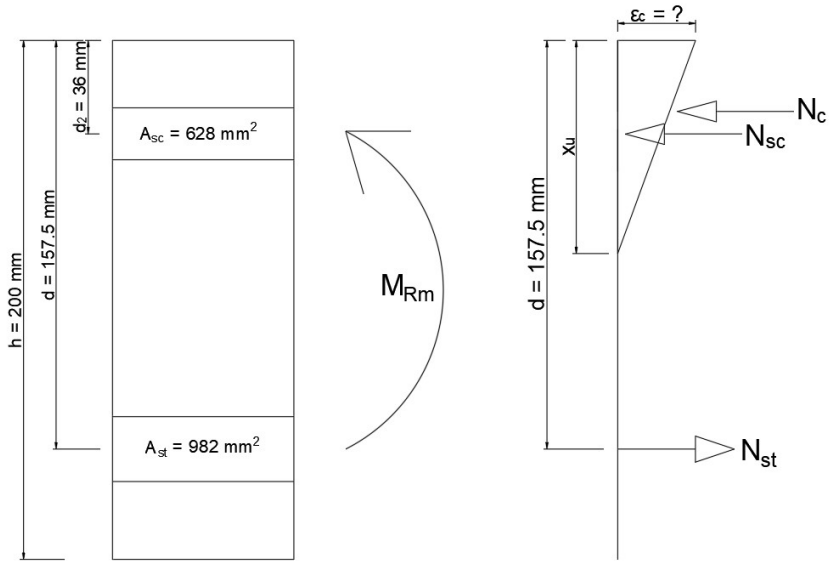

Figure 4.4: Longitudinal beam section and horizontal equilibrium through internal normal forces in the concrete and steel reinforcement bars.

Since it is assumed that the flexural steel at the bottom of the beam is yielding (ε_{st} = 0.0028 [-]), N_{st} is calculated:

$$N_{st} = A_{st} \cdot f_y = 982 \cdot 560 = 549.8 \text{ kN} \tag{4.2}$$

From geometry it can be derived that;

$$\varepsilon_{sc} = \frac{x_u - d_2}{x_u} \cdot \varepsilon_c \longrightarrow \varepsilon_c = \frac{x_u}{d - x_u} \tag{4.3}$$

and;

$$\frac{\varepsilon_c}{x_u} = \frac{\varepsilon_{st}}{d - x_u} \longrightarrow x_u = \frac{\varepsilon_c \cdot d}{\varepsilon_{st} + \varepsilon_c} \tag{4.4}$$

The formula for the compressive force in the longitudinal steel top bars is formulated as:

$$N_{sc}(\varepsilon_c) = A_{sc} \cdot \varepsilon_{sc} \cdot E_s = A_{sc} \cdot (\frac{x_u - d_2}{x_u} \varepsilon_c) \cdot E_s \tag{4.5}$$

The compressive force in the concrete is assumed to be bi-linear. Since it is yet unknown whether crushing of the concrete (ε_{cu3} = 0.0035) is reached, the two contributions in the concrete are split up into a rectangular and a square part:

$$N_c = N_{c1} + N_{c2} \tag{4.6}$$

$$N_{c1} = 0.5 \cdot b \cdot \frac{1.75‰}{\varepsilon_c} \cdot x_u \cdot f_{cm} \tag{4.7}$$

$$N_{c2} = b \cdot \frac{\varepsilon_c - 1.75‰}{\varepsilon_c} \cdot x_u \cdot f_{cm} \tag{4.8}$$

$$e_1 = (\frac{\varepsilon_c - 1.75‰}{\varepsilon_c} + \frac{1.75‰}{3 \cdot \varepsilon_c}) \cdot x_u = (\frac{\varepsilon_c - 1.75‰}{\varepsilon_c} + \frac{1.75‰}{3 \cdot \varepsilon_c}) \cdot \frac{\varepsilon_c \cdot d}{\varepsilon_{st} + \varepsilon_c} \tag{4.9}$$

$$e_2 = 0.5 \cdot \frac{\varepsilon_c - 1.75‰}{\varepsilon_c} \cdot x_u = 0.5 \cdot \frac{\varepsilon_c - 1.75‰}{\varepsilon_c} \cdot \frac{\varepsilon_c \cdot d}{\varepsilon_{st} + \varepsilon_c} \tag{4.10}$$

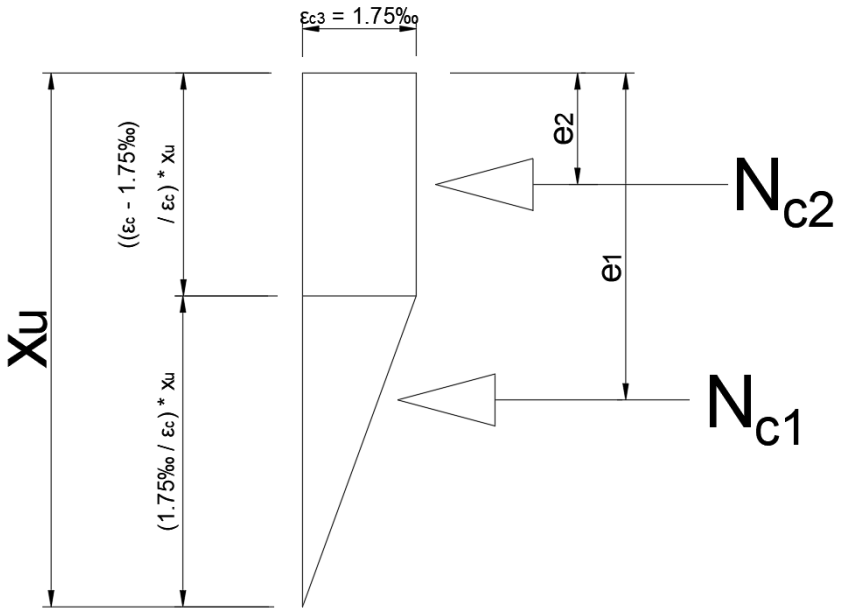

Figure 4.5: Normal force in concrete compression zone

$$
\begin{aligned}
N_{st} &= N_{c1}(\varepsilon_c) + N_{c2}(\varepsilon_c) + N_{sc}(\varepsilon_c) \\
A_{st} \cdot f_y &= [0.5 \cdot b \cdot \frac{1.75‰}{\varepsilon_c} \cdot x_u \cdot f_{cm}] + [b \cdot \frac{\varepsilon_c - 1.75‰}{\varepsilon_c} \cdot x_u \cdot f_{cm}] + \\
&\quad [A_{sc} \cdot \varepsilon_{sc} \cdot E_s = A_{sc} \cdot (\frac{x_u - d_2}{x_u}\varepsilon_c) \cdot E_s] \\
981.7 \cdot 560 &= (0.5 \cdot 150 \cdot \frac{1.75‰}{\varepsilon_c} \cdot \frac{\varepsilon_c \cdot 157.5}{0.0028 + \varepsilon_c} \cdot 38) \ + (150 \cdot \frac{\varepsilon_c - 0.00175}{\varepsilon_c} \cdot \frac{\varepsilon_c \cdot 157.5}{0.0028 + \varepsilon_c} \cdot 38) + \\
&\quad (628.3 \cdot \frac{\frac{\varepsilon_c \cdot 157.5}{0.0028 + \varepsilon_c} - 36}{\frac{\varepsilon_c \cdot 157.5}{0.0028 + \varepsilon_c}} \cdot \varepsilon_c \cdot 200000)
\end{aligned}
\tag{4.11}
$$

Solving the equation with the strain of the concrete at the top surface of the beam ε_c as the only unknown results an approximate value of 0.305%. This strain value is below the crushing strain of concrete, ε_{cu3} = 0.35%, indicating that the steel flexural tensile reinforcement near the bottom of the cross-section will yield prior to the concrete at the top surface reaching its crushing limit. This condition ensures that the failure behavior of the beam is ductile and controlled in case the beam does not experience a premature failure in shear tension mode.

Subsequently, the height of the concrete compression zone x_u can be determined through the following equation:

$$x_u = \frac{\varepsilon_c \cdot d}{\varepsilon_{st} + \varepsilon_c} = \frac{0.305\% \cdot 157.5}{0.28\% + 0.305\%} = 82.2 \text{ mm} \tag{4.12}$$

From this value, the compressive steel strain is calculated:

$$\varepsilon_{sc} = (\frac{x_u - d_2}{x_u}) \cdot \varepsilon_c = \frac{82.2 - 36}{82.2} \cdot 0.305\% = 0.00172 \ [-] \tag{4.13}$$

The bending capacity can then be calculated by taking moment equilibrium from the height of the

tensional steel reinforcement using the formula:

$$M_{Rm} = N_{c1} \cdot (d - e1) + N_{c2} \cdot (d - e2) + N_{sc} \cdot (d - d_2) = 68.5 \text{ kNm} \tag{4.14}$$

When the self-weight of the beam is neglected, and given that three-point bending tests are conducted (as illustrated in Figure 4.1), the required force at midpoint of the beam to induce bending failure can be determined using the following equation:

$$M = \frac{F \cdot L}{4} \longrightarrow F_M = \frac{4M_{Rm}}{L} = 274 \text{ kN} \tag{4.15}$$

This indicates that the beam will not fail in bending until a force of F = 274 kN is applied at its mid-span. Consequently, this results in a shear force of $V = \frac{F}{2} = \frac{274}{2} = 137$ kN within the beam.

The distance from the top surface of the cross-section to the resultant from the concrete compression zone and compressive reinforcement is equal to

$$d_3 = \frac{N_{c1} \cdot e_1 + N_{c2} \cdot e_2 + N_{sc} \cdot d_2}{N_{c1} + N_{c2} + N_{sc}} = 32.9 \text{ mm} \tag{4.16}$$

and the internal lever arm z then becomes

$$z = d - d_3 = 157.5 - 32.9 = 124.6 \text{ mm} \tag{4.17}$$

4.1.3. Prediction of beam "NS": shear capacity without stirrups

The shear capacity of a reinforced concrete beam without shear reinforcement is calculated according to the design formulas from the Dutch annex for Eurocode 2 (NEN-EN 1992-1-1, 2011). First, the shear capacity of the concrete only $V_{Rm,c}$ is calculated for the beam without stirrups:

$$\rho_l = min[\frac{A_{slt}}{b_w d} \ ; \ 0.02] = min[\frac{982}{150 \cdot 157.5} \ ; \ 0.02] = min[0.0416 \ ; \ 0.02] = 0.02 \ [-] \tag{4.18}$$

$$k = min[1 + \sqrt{\frac{200}{d}} \ ; \ 2.0] = min[1 + \sqrt{\frac{200}{157.5}} \ ; \ 2.0] = min[2.13 \ ; \ 2.0] = 2.0 \tag{4.19}$$

$$v_{Rm,min} = 0.035 \cdot k^{3/2} \cdot f_{cm}^{1/2} = 0.035 \cdot 2^{3/2} \cdot 38^{1/2} = 0.61 \text{ MPa} \tag{4.20}$$

$$v_{Rm,c} = C_{Rd,c} \cdot k \cdot (100 \cdot \rho_l \cdot f_{cm})^{1/3} = 0.18 \cdot 2.0 \cdot (100 \cdot 0.02 \cdot 38)^{1/3} = 1.525 \text{ MPa} \tag{4.21}$$

$$V_{Rm,c} = v_{Rm,c} \cdot b \cdot d = 1.525 \cdot 150 \cdot 157.5 = 36.03 \text{ kN} \tag{4.22}$$

4.1.4. Prediction of shear capacity with steel stirrups

For the prediction of shear capacity in beams reinforced with steel stirrups, it is essential to consider the contribution of each stirrup leg. Given that each steel stirrup consists of two legs with a diameter of Ø8 mm, both legs contribute to the overall shear capacity. The total cross-sectional area of the stirrup legs can be calculated as follows:

$$A_{sv,\varnothing 8} = 2 \cdot 0.25 \cdot \pi \cdot 8^2 = 100 \text{ mm}^2 \tag{4.23}$$

The normative stirrups for the beams with 4 stirrups are defined as the two stirrups closest to the mid-span on either side of the beam. The spacing for these stirrups is calculated as:

$$s = 150 + \frac{200}{2} = 250 \text{ mm} \tag{4.24}$$

For the purpose of shear design, a shear crack angle θ = 21.8° is employed, as this angle proves to be normative in Eurocode 2. The shear capacity of the beam is then determined using equation 6.8 from (NEN-EN 1992-1-1, 2011):

$$V_{Rm,s} = \frac{A_{sw}}{s} \cdot z \cdot f_{ym} \cdot \cot(\theta) = \frac{100}{250} \cdot 124.6 \cdot 560 \cdot \cot(21.8°) = 70.15 \text{ kN} \tag{4.25}$$

The failure of the concrete compression struts will occur when the shear force reaches the following value:

$$V_{Rm,max} = \frac{\alpha_{cw} \cdot b \cdot z \cdot \nu_1 \cdot f_{cm}}{\cot(\theta) + \tan(\theta)} = \frac{1 \cdot 150 \cdot 124.6 \cdot 0.6 \cdot 38}{\cot(21.8°) + \tan(21.8°)} = 146.93 \text{ kN} \tag{4.26}$$

Since $V_{Rm,s}$ is smaller than $V_{Rm,max}$, it is expected that the stirrup yield strength will be the limiting factor, leading to a shear tension failure mode for the beam.

4.1.5. Prediction of shear capacity of concrete beams reinforced with basalt FRP shear reinforcement stirrups

In predicting the shear capacity of concrete beams reinforced with FRP stirrups, the approach adheres to established principles in the design of FRP-reinforced concrete structures, as detailed by fib (2007). These principles assert that, if the FRP longitudinal reinforcement strain and design forces are maintained equivalent to those in steel reinforcement designs, the outcomes should be comparable. This philosophy, often referred to as the ”strain approach” Guadagnini et al., 2003, ensures that the concrete section behaves independently of the reinforcement type, provided that adequate bond conditions are achieved at the stirrup and concrete interface.

The design of shear reinforcement using FRP focuses on controlling the maximum allowable strain in the stirrups. Initially, strain limits were set conservatively to reflect the yielding strain of steel (0.2% - 0.25%) to maintain section integrity and ensure the additive nature of structural resistance. However, recent research supports a higher allowable strain value of 0.45%, which more accurately reflects the actual behavior of FRP-reinforced concrete elements and results in more optimized and efficient structural designs.

The stress in FRP shear links (f_{fw}) is computed as follows:

$$f_{fw} = \varepsilon_{fw} \cdot E_{fw} \tag{4.27}$$

where ε_{fw} is the allowable strain (set at ε_{fw} = 0.0045) in the shear links, as advised in literature by Guadagnini et al. (2006), and E_{fw} is the modulus of elasticity of the FRP material. This approach follows the well-known truss analogy theory, similar to steel RC, with the stress level adjusted to accommodate this maximum allowable strain for FRP. For design purposes, this method is used as a lower limit prediction for the shear capacity of the beams reinforced with BFRP stirrups ($V_{Rm,FRP,low}$). The equation is derived by modifying equation (6.8) from NEN-EN 1992-1-1 (2011): in this formula, the the yield strength of steel (f_{ym}) is replaced by the FRP stirrup stress determined by Equation (4.27):

$$V_{Rm,FRP,low} = \frac{A_{FRP,w}}{s} \cdot z \cdot [\varepsilon_{fw} \cdot E_{fw}] \cdot \cot(\theta) \tag{4.28}$$

where $V_{Rm,FRP,low}$ represents the predicted shear strength, $A_{FRP,w}$ is the area of the FRP stirrups, s is the spacing of stirrups, z is the internal lever arm, ε_{fw} is the strain limit (0.45%) set for FRP stirrups, E_{fw} is the modulus of elasticity of the FRP stirrup, and θ is the shear crack angle.

Subsequently, the upper limit for the shear strength of the concrete beams reinforced with BFRP stirrups is set by the uniaxial tensile strength that was previously determined in Section 3.3. In this case, the mean yield stress of steel (f_{ym}) is replaced by the mean failure stress of the braided BFRP rod-type or laminated BFRP strip stirrup ($f_{\text{FRP},u}$), which was previously derived from the uniaxial tensile testing in Section 3.3, in Equation (4.25). This equation then becomes:

$$V_{Rm,FRP,up} = \frac{A_{FRP,w}}{s} \cdot z \cdot f_{\text{FRP},w,u} \cdot \cot(\theta) \tag{4.29}$$

In the Eurocode 2 approach, the concrete contribution is disregarded for members with shear reinforcement. The calculated values for the estimation of the shear capacity for the BFRP stirrup is listed for

each beam sample with BFRP stirrups in Table 4.3.

Table 4.3: Shear strength predictions for beams reinforced with FRP stirrups

Beam sample	Cross-sectional area A_v [mm^2]	Span s [mm]	Strain criterion ε_{FRP} [-]	E-modulus [GPa]	Ultimate stress f_{FPR} [MPa]	Shear capacity $V_{Rm,s,low}$ [kN]	Shear capacity $V_{Rm,s,up}$ [kN]
B4	116	250	0.0045	40.4	750	26.28	108.41
B8	116	125	0.0045	40.4	750	52.56	216.82
UD4	86	250	0.0045	41.4	700	20.20	75.89
UD8	86	125	0.0045	41.4	700	40.39	151.77

The maximum compressive capacity in the concrete struts, denoted as $V_{Rm,max}$, is determined solely by the beam's geometry and the properties of the concrete. Consequently, for the reference beams, this capacity remains constant at 146.93 kN, as calculated in Equation (4.26). This capacity is anticipated to be sufficient, as the lower bound of the stirrups' shear capacity is expected to govern the design.

4.1.6. Discussion

this uniformity was not possible due to the differing geometries of the stirrups: the circular cross-section of ribbed steel and braided basalt FRP stirrups contrasts with the rectangular cross-section of the UD-laminate strip stirrups. Given that the stirrups are required to enclose the longitudinal reinforcement, a decision was necessary between two alternatives. The first option was to maintain a consistent concrete cover for the stirrups, which would necessitate positioning the longitudinal reinforcement closer to the concrete surface. The second option was to keep the longitudinal reinforcement in its original position, which would require moving the stirrups inward to ensure they continued to enclose the longitudinal reinforcement.

The decision was made to maintain the longitudinal reinforcement at a consistent horizontal and vertical distance from the concrete surface across all beams. This choice was guided by several key considerations:

- **Splitting forces and minimum cover:** Reducing the concrete cover on the longitudinal bars would increase the demand on the shear reinforcement stirrups to absorb splitting forces. This situation is particularly critical for FRP strip stirrups, as it would result in a concrete cover for the longitudinal that is less than the minimum required by Eurocode 2 (c$_m in$ is equal to the diameter of the longitudinal reinforcement) for adequate bonding. Insufficient cover could compromise the structural integrity by diminishing the bond strength between the concrete and the reinforcement.
- **Distribution of splitting stresses:** The distribution of splitting stresses varies between circular reinforcement bars and rectangular strip stirrups. For circular stirrups, when placed at the same distance from the concrete surface, the center of the stirrup is located approximately 21 mm from the surface. As illustrated in Figure 4.6, the splitting stresses are evenly distributed around the circumference and penetrate deeply into the concrete. In contrast, for strip stirrups, the center is located about 19 mm from the surface, leading to highly concentrated splitting stresses both inward and outward. This concentration, combined with reduced effective concrete cover, could create a potential splitting plane parallel to the concrete surface, increasing the risk of concrete spalling and subsequent loss of bond.
- **Consistency in effective height:** To facilitate proper force transfer into the stirrups, the longitudinal reinforcement bars need to be positioned at the bottom corners of the stirrups to achieve this. If the strip stirrups were placed with equal concrete cover at the bottom, the longitudinal bars would sit lower in the cross-section, altering the effective height (d) and leading to inconsistencies in the structural response among the test specimens. This would make the comparison of results unreliable.

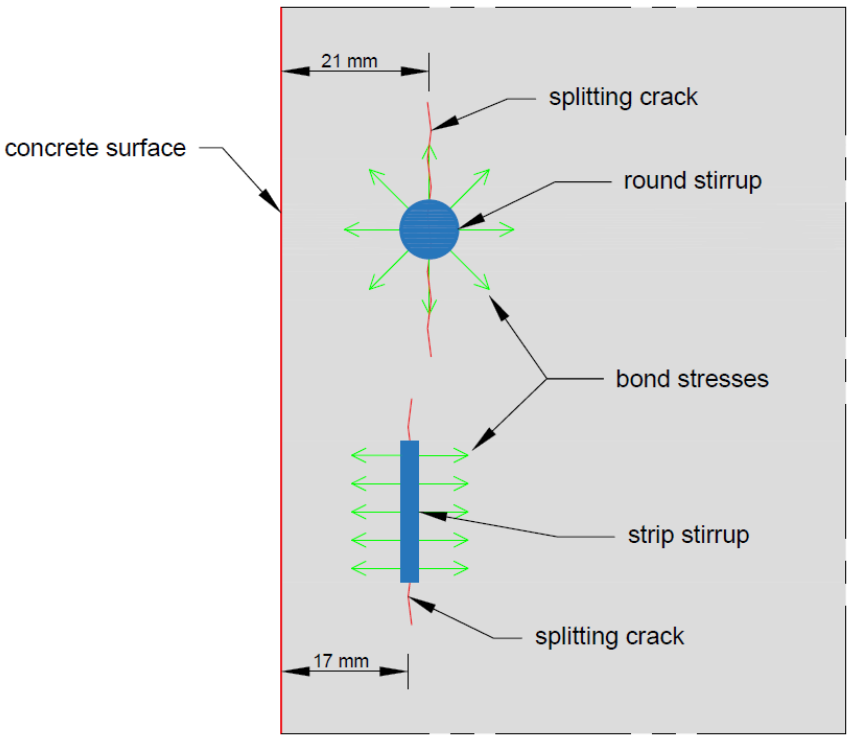

Figure 4.6: Top view of longitudinal section: direction of bond stresses

To prevent any disadvantage for the BFRP strips, it was decided to maintain the longitudinal reinforcement at a consistent horizontal distance across all beams. Consequently, the strip stirrups were given a slightly increased concrete cover (22 mm instead of 17 mm), as shown in Figure 4.3 d).

4.2. Materials

In the original design, as outlined in Section 4.1, the stirrups were intended to have a uniform corner radius R of 32 mm, which was standardized for the production of the braided basalt FRP stirrups. However, production constraints for the steel stirrups, combined with an error by the supplier of the braided BFRP bars, resulted in variations from this specification. By the time the discrepancy was identified, the beams with steel stirrups had already been cast, and the BFRP UD-laminate strip stirrups had been produced and cut to match the cross-sectional area of the braided BFRP bars. Given the time constraints, it was decided to proceed with the three different corner radii for the various types of stirrups.

4.2.1. Steel stirrups

The steel stirrups are fabricated from standard Fe B500B ribbed steel reinforcement. Due to production constraints, the steel stirrups have an inside corner radius of R = 25 mm, which is the closest achievable approximation to the originally specified R = 32 mm in the beam design. To ensure adequate anchorage length, as required by paragraph 8.5(2) of NEN-EN 1992-1-1 (2011), the legs of the stirrups overlap at the top horizontal section and along one of the vertical sides. The final dimensions of the steel stirrups, including the hatched section indicating the overlapping length, are shown in Figure 4.7.

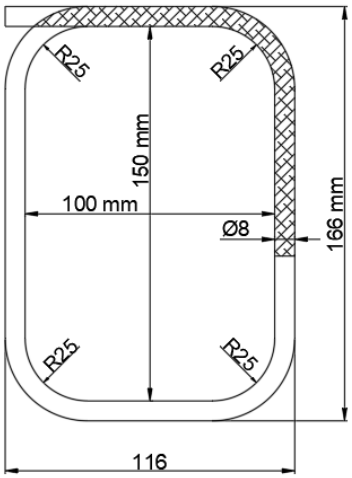

Figure 4.7: Dimensions and overlapping for the steel stirrups

4.2.2. Braided BFRP stirrups

Similar to the braided BFRP rods, the braided stirrups were manufactured by Thoenes Solutions. To ensure proper anchorage, the stirrups overlap at the top until the mid-height of the stirrup. However, due to a production error, the stirrups were made with a corner radius of 16 mm instead of the specified 32 mm. This discrepancy is illustrated in Figures 4.8 (a) and (b). A picture of the actual braided BFRP stirrup is shown in Figure 4.9.

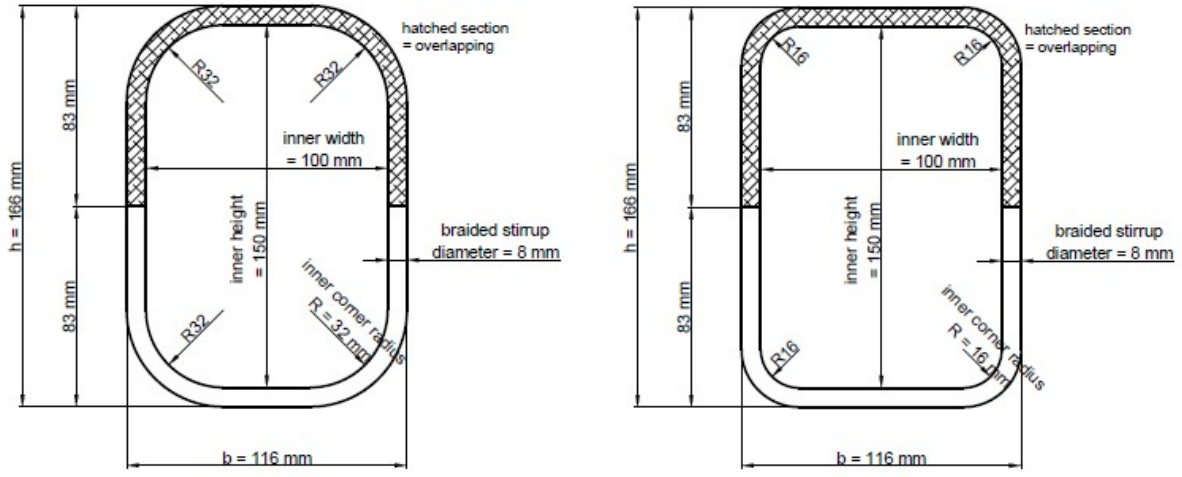

(a) Specified dimensions

(b) Actual dimensions

Figure 4.8: Dimensions and overlapping for braided BFRP stirrups

Figure 4.9: Picture of the actual braided BFRP stirrups

4.2.3. BFRP laminate strip stirrups

The basalt FRP UD laminate strip stirrups are fabricated in a similar way to straight strip specimens used in uniaxial tensile testing, but using a four-layer wet lay-up instead of eight, doubling the strip width to approximately 320 mm. This approach ensures sufficient stirrups for both UD4 and UD8 beam specimens from a single batch. The production of the wet layup is shown in Figure 4.10 (a).

The fabrication process of the stirrups involves wrapping the wet lay-up around a CNC-milled Styrofoam mold, starting from a corner section. The lay-up is wrapped twice around the mold, with additional length at the top for proper anchoring. The mold is precisely milled to ensure accurate dimensions and corner radii, and the anchorage length is carefully selected to prevent overlap in the vertical legs of the stirrups, thereby avoiding potential wrinkles or kinks in the straight sections of the final product.

(a) Production of the wet layup

(b) Wet layup wrapped around the mold and left to cure in vacuum bag

Figure 4.10: Production of the BFRP UD-laminate strip stirrups

After the lay-up process and wrapping is complete, the composite is enclosed within a vacuum bag to facilitate curing over a period of 24 hours. This is shown in Figure 4.10 (b). The cured composite results in a wide strip stirrup with a width of approximately 320 mm. The edge sections of the stirrup are cut off, and the remaining wide strip is further divided into 14 smaller strips using a diamond-bladed saw, each approximately 19 ± 0.5 mm in width. Figure 4.11 (a) provides a cross-sectional view of the stirrup lay-up, while Figure 4.11 (b) presents the final stirrups after they have been cut to the specified width.

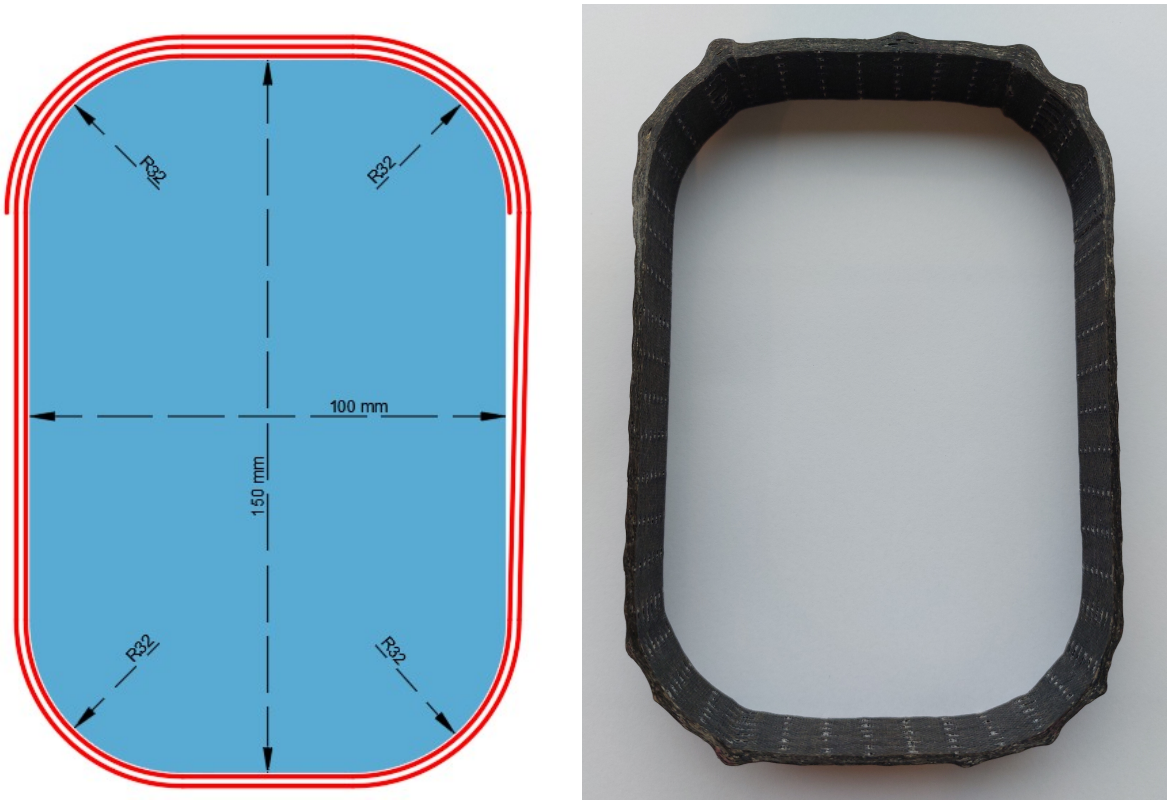

(a) Concept: red line corresponds to 4 layers of basalt UD fabric, blue represents the CNC-milled Styrofoam mold

(b) Resulting stirrup after vacuum curing and cutting the individual stirrups

Figure 4.11: Cross-section of a basalt FRP UD-laminate stirrup

In Figure 4.11 (b), the stirrup displays out-of-plane wrinkles, particularly in the corner sections, which are a notable imperfection in the final product. These wrinkles occur due to the specific conditions of the vacuum bagging process used during fabrication. As the vacuum bag is applied, it exerts pressure on the wet lay-up, pressing it tightly against the Styrofoam mold to conform to its shape while simultaneously extracting any excess resin. This pressure, while essential for achieving proper compaction and resin distribution, leads to localized distortions in the fabric, especially in areas with complex geometry such as corners. These distortions manifest as wrinkles, which are out-of-plane deformations of the laminate layers.

The presence of these wrinkles is significant because they represent areas where the fibre alignment is disrupted, potentially compromising the mechanical integrity of the stirrup in those regions. The full cross-section at the wrinkled areas, being localized to the corners, might not fully engage under tensile stress, thus limiting the ultimate tensile capacity and overall stirrup performance.

Despite the presence of these defects, it is recognized that such wrinkles are an inherent and unavoidable consequence of the vacuum bagging process, particularly when dealing with corner sections. As a result, the decision has been made to accept these imperfections as a trade-off for the benefits offered by the current production method. These advantages include efficient resin compaction, which ensures that the laminate is adequately saturated and free of voids. The continued use of these stirrups reflects a pragmatic approach, acknowledging that while the wrinkles are not ideal, they are within acceptable limits for the intended application in static testing.

However, when considering applications beyond static testing, such as fatigue testing, these imperfections may pose a greater concern. In fatigue testing, where the material is subjected to repeated cyclic loading, the presence of wrinkles could potentially lead to stress concentrations and premature failure. The localized distortions caused by the wrinkles might act as initiation points for cracks or delamination under cyclic stress, thereby compromising the long-term durability and performance of the

stirrup. Therefore, for fatigue testing, the presence of these wrinkles could necessitate a reassessment of the production method to ensure the durability and reliability of the stirrups under cyclic loading. One potential alternative to mitigate these imperfections is the adoption of filament winding as a production method. Filament winding allows for more precise control over fibre placement and tension, significantly reducing the likelihood of wrinkles and other defects associated with the vacuum bagging process.

By winding continuous basalt fibres directly onto a mandrel or mold, filament winding ensures that the fibres remain uniformly aligned and tightly compacted, even in areas with complex geometries such as corners. This method also allows for more consistent resin distribution, enhancing the overall structural integrity of the laminate. As a result, the stirrups produced through filament winding would likely exhibit improved performance under fatigue loading, with reduced risk of stress concentrations or premature failure due to manufacturing defects.

4.2.4. Final beam cross-sections

The final cross-sections for the beams are shown in Figure 4.12 on the next page. In this figure, the position of the longitudinal bars was adjusted so that they are directly enclosed by the stirrups. For control beams NS and S4, the horizontal concrete cover on the longitudinal tensile reinforcement was reduced from 32 mm to 28 mm. Due to the smaller corner radii of the braided BFRP bars, the horizontal concrete cover for the Ø25 longitudinal reinforcement bars decreased from 32 mm to 25 mm. The cross-section for the BFRP UD-laminate strip stirrups remained unchanged, as these strip stirrups were produced according to the design described in Section 4.1.

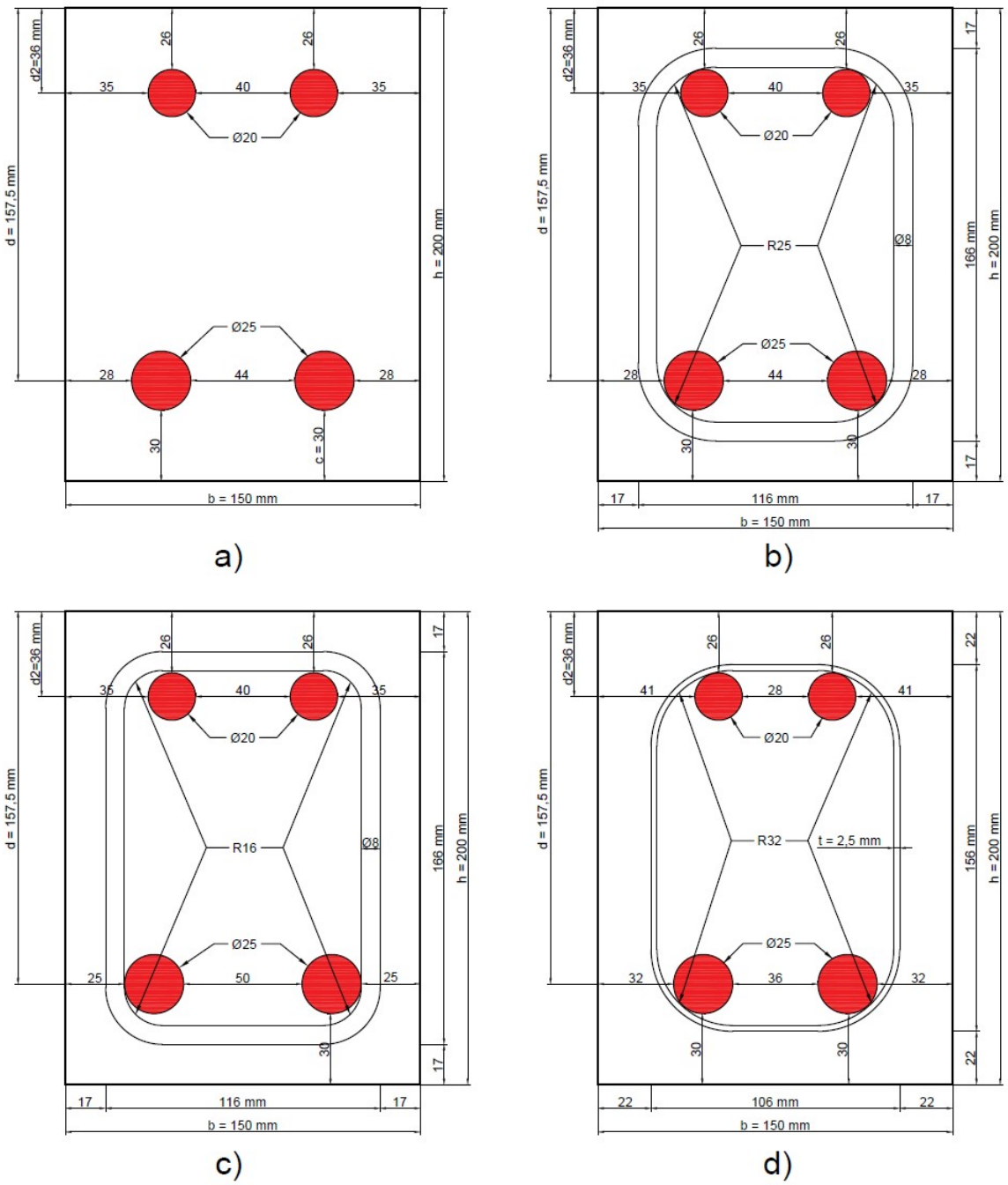

Figure 4.12: Beam cross-sections: a) Control beam without stirrups; b) Control beam with Ø8 mm steel stirrups; c) Beam with Ø8 mm braided BFRP stirrups; d) Beam with laminated BFRP UD-fibre strip stirrups.

Implication of varying horizontal concrete cover

Varying the horizontal concrete cover for the longitudinal reinforcement in this series of reinforced concrete beam tests could have implications for the structural behavior of the beams. The concrete cover serves as a protective layer, distributing stresses around the reinforcement bars. When this cover is reduced, the stress distribution becomes less uniform, leading to localized high-stress areas around the reinforcement. These high-stress concentrations can exceed the tensile strength of the concrete, initiating splitting cracks. These cracks generally align with the longitudinal reinforcement, starting from areas of high stress and moving outward toward the concrete surface.

When splitting cracks intersect with stirrups, the stirrups must absorb additional tensile forces intro-

duced by the cracks. This interaction places extra demand on the stirrups, requiring them to not only perform their primary function of shear reinforcement but also to help arrest and control the splitting cracks. This dual role can stress the stirrups beyond their intended capacity if the crack load is significant.

4.2.5. Concrete mixture

Table 4.4 presents the concrete mixture used for the beam specimen, which is designed with a concrete strength class of C30/37.

Table 4.4: Concrete mixture for the beam samples

Component	Weight [kg/m^3]
CEM III/B 42.5 N	381.2
Water	183.0
Sand 0.125 – 0.25 mm	130.3
Sand 0.25 – 0.5 mm	346.2
Sand 0.5 – 1 mm	102.3
Sand 1 – 2 mm	70.8
Sand 2 – 4 mm	62.9
Gravel 4 – 8 mm	74.7
Gravel 4 – 16 mm	946.9
Absorbed water	10.4
Total	**2308.9**

4.3. Instrumentation

4.3.1. Measuring techniques

In this study, the combination of LVDTs, DIC and DFOS provides a comprehensive approach to monitoring concrete beams under load. Together, they deliver a detailed understanding of the beam's structural response, capturing both localized and global deformation patterns, thereby enabling accurate assessment of the beam's performance and early detection of cracks and potential failures.

The following subsections provide a more detailed description of these individual techniques and how they are used in the experiments.

Linear Variable Differential Transformers (LVDTs)

Linear Variable Differential Transformers (LVDTs) are displacement sensors that operate by detecting linear displacement. It consist of a core that moves within a coil assembly, producing an electrical output proportional to the position of the core. Their high sensitivity and robustness make them suitable for capturing the subtle deformations in a material that occur under loading, providing critical data on the structural performance and behavior under stress.

In each of these experiments, a total of seven LVDTs are positioned at mid-span. LVDTs 1, 2 and 3 are placed side-by-side in the longitudinal direction at vertical distances of 7.5 mm, 22.5 mm, and 37.5 mm from the top surface to measure the horizontal displacement in the concrete compression zone over a span of 200 mm. LVDTs 4 and 5 are positioned longitudinally at distances of 7.5 mm and 35 mm from the bottom surface, also measuring displacement over 200 mm. LVDT 6 is positioned horizontally underneath the beam to measure horizontal displacements over a span of 500 mm. Finally, LVDT 7 is positioned vertically at mid-span. It is attached to a wooden beam that spans from support to support at mid-height of the beam, allowing it to freely rotate and move horizontally. This LVDT measures the beam's mid-span deflection against a steel plate fixed to the bottom of the beam. This layout is shown in Figures 4.13 (a) and (b).

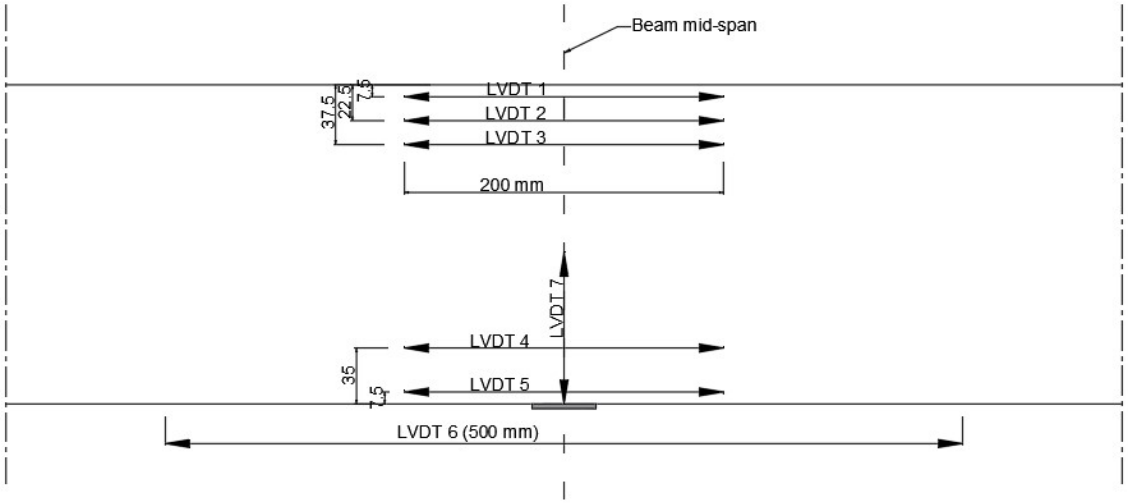

(a) Schematized LVDT layout

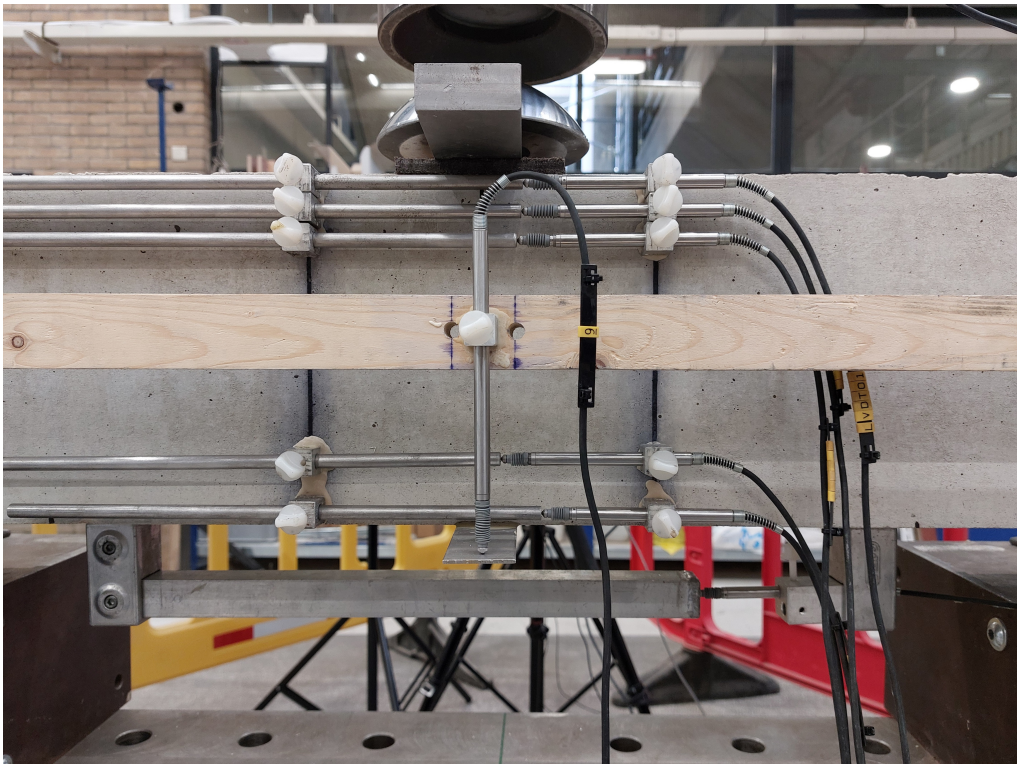

(b) Actual LVDT layout

Figure 4.13: Side view of beam samples: LVDT layout at beam mid-span

Digital Image Correlation (DIC)

Digital Image Correlation (DIC) is a sophisticated optical technique employed for the precise measurement of surface deformations, displacements, and strains. This method involves capturing a sequence of high-resolution digital images of a speckle pattern applied to the surface of an object, such as a reinforced concrete beam, both before and during the application of loads. By analyzing the variations in the speckle pattern across these images, DIC algorithms enable the calculation of full-field displacement and strain distributions. When applied to reinforced concrete beams undergoing loading, DIC provides detailed monitoring of the beam's deformation and cracking behavior over time.

Given the nature of the three-point bending tests conducted in this study, the area of interest for DIC

involves the entire region between the supports on either side of the beam. To prepare for these measurements, the beams are first coated with a thin layer of white paint, which enhances the contrast needed for accurate image capture. Following this, a speckle pattern is applied using a paint sprayer filled with black paint, which is connected to a pneumatic system. Achieving the optimal size and distribution of speckles on the beam's surface requires meticulous calibration of the paint and air throughput settings prior to the application. This careful preparation ensures that the speckle pattern is suitable for high-precision DIC analysis.

Before each experimental test begins, a sequence of 10 reference photographs is captured to establish a baseline for subsequent analysis. These initial images undergo a processing technique where they are averaged to produce a single, static reference image. This reference image serves as a benchmark against which all subsequent deformed images are compared. This approach significantly enhances the accuracy and reliability of the results by minimizing the influence of random noise arising from environmental variations and camera inconsistencies.

During the testing process, additional photographs are taken at 10-second intervals to continuously monitor the specimen's behavior. Consistent and optimal lighting conditions are maintained throughout the experiment using a bright flashlight. This ensures uniform illumination across all captured images, further reducing the risk of lighting-related variability that could otherwise compromise the integrity of the correlation process. The setup for the DIC system is shown in Figure 4.14.

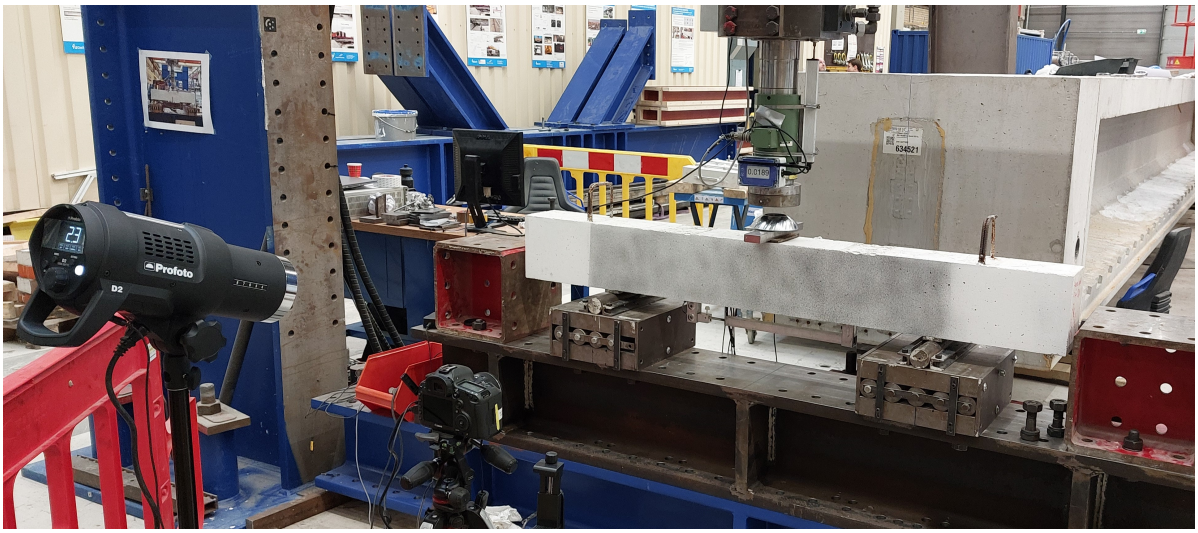

Figure 4.14: Test set-up with camera perpendicular to the beam for DIC

An example from the resulting analysis, displaying the major strain and highlighting the flexural and shear cracks in the beam, is shown in Figure 4.15. In this figure, strain levels are color-coded, with deep blue representing 0% strain and gradually transitioning to red at a maximum strain level of 7%. This interval is specifically chosen to providing a clear visualization of the cracks in the beam.

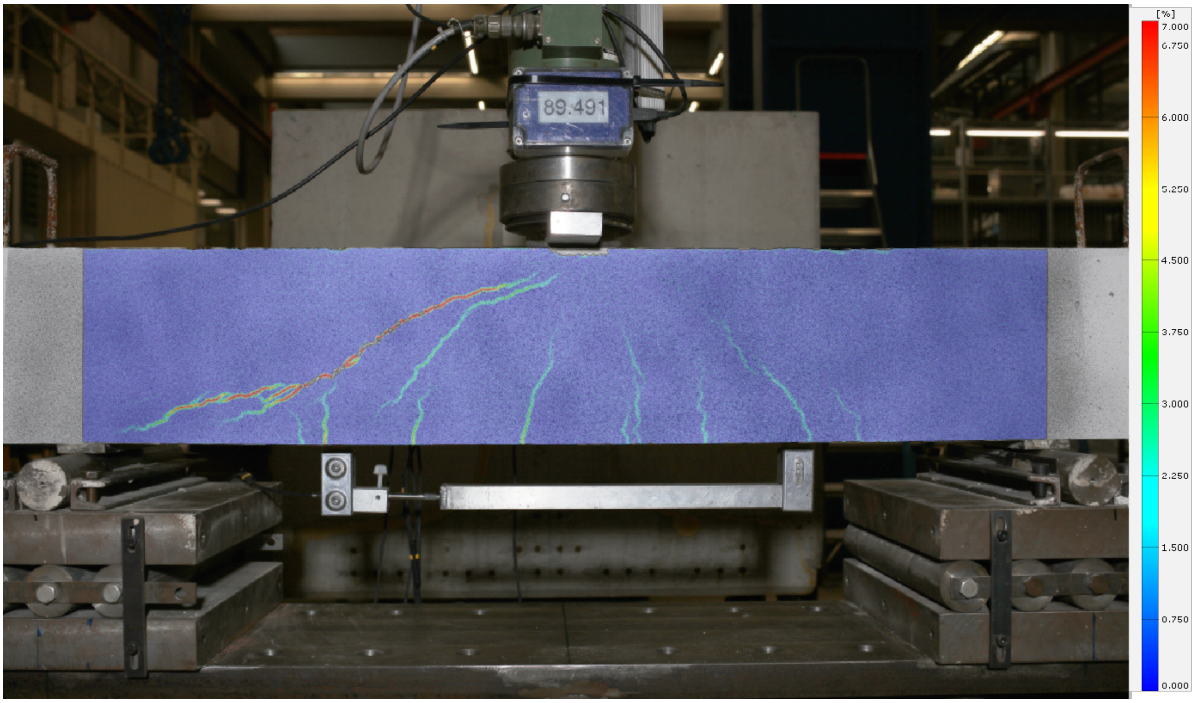

Figure 4.15: DIC analysis example: major strain map, highlighting flexural and shear cracks

Optical fibres (DFOS)

Distributed fibre Optic Sensing is a cutting-edge technology used for continuous, real-time monitoring of various parameters along extensive lengths of fibre optic cables. This innovative approach leverages the principles of light scattering within the fibre. By analyzing the variations in the light signal as it travels through the fibre, DFOS systems can provide precise and continuous measurements of strain.

In this study, optical fibres are attached to the stirrups to measure their strain. They are placed at the outside of the stirrups, so they are less likely to be damaged during the casting of concrete. The optical fibres are bonded along the vertical sides, bottom corners, and the horizontal bottom section of all stirrups. This configuration is schematized in Figure 4.16 (a). The red lines represent plastic tubes that protect the fibre in the debonded regions, allowing it to enter and exit the top surface of the concrete beam for connection to the hardware.

In the experimental setup, the system allowed for the simultaneous connection of up to four optical fibres. For beams reinforced with four stirrups, each stirrup was individually equipped with its own optical fibre sensor. In the case of beams containing eight stirrups, each optical fibre was affixed to two stirrups, with a section of the fibre left unbonded as in between.
Prior to conducting the experiment, the optical fibre sensors undergo a calibration process known as fingerprinting. This process involves creating a unique identification profile for each fibre by recording its inherent imperfections. These imperfections, which are unique to each fibre, shift in location and shape when the fibre experiences strain, thereby altering the refraction of the light signal transmitted through the fibre. The DFOS system detects these shifts in the light signal, allowing the software to calculate the strain.

In this study, a virtual strain gauge length of 0.65 mm is utilized, with measurements captured at a frequency of 3.33 Hz. During each trigger event, occurring every 10 seconds, between 2 to 5 measurements are recorded, synchronized with a photograph for DIC analysis. This synchronization ensures that the strain data corresponds precisely with the visual data captured by the DIC system. To enhance the accuracy and reliability of the data, further processing steps are employed. The measurements are averaged to reduce noise, and the virtual strain gauge length is adjusted to 4 mm to account for any inconsistencies. Additionally, any uncorrelated data points or outliers are systematically filtered out to ensure that the final strain data reflects only the relevant and accurate information.

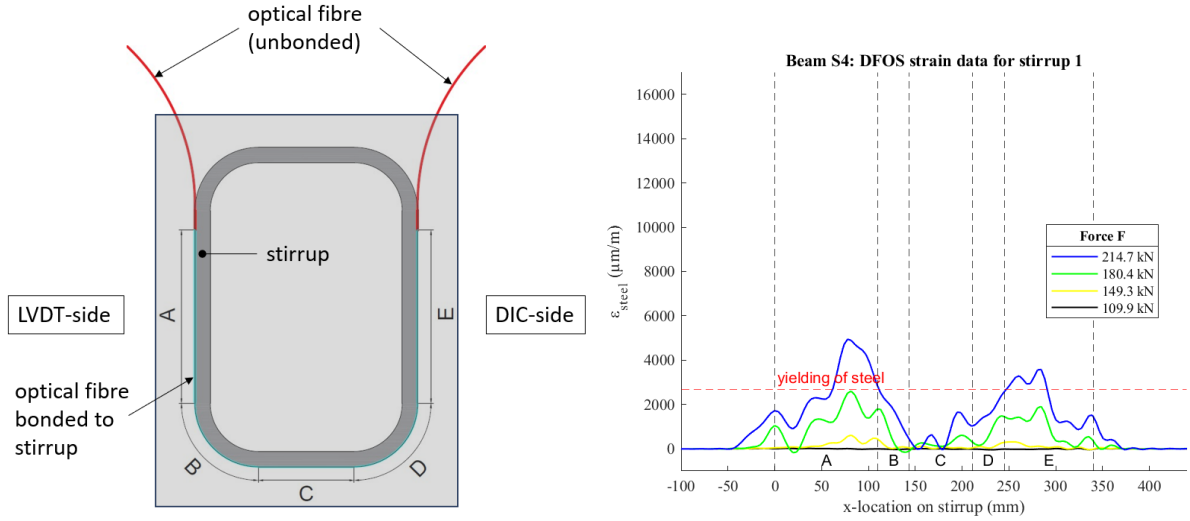

(a) Beam cross-section at location of stirrup

(b) Example of DFOS strain data at certain loads

Figure 4.16: Optical fibres bonded to stirrups. A = vertical section LVDT-side; B = corner section LVDT-side; C = bottom section; D = corner section at DIC-side; E = vertical section at DIC-side.

4.3.2. Loading conditions

In the three-point bending test of the reinforced concrete beam samples, the loading conditions are controlled to ensure accurate and reliable results. This test is displacement controlled, with a hydraulic jack applying a constant speed of 0.01 mm/s. This method is chosen because it allows for better observation of post-peak behavior, especially as the beams are designed to fail in a brittle shear mode. By maintaining a constant displacement rate, the test can capture the entire load-displacement curve, including the descending branch after peak load, which is critical for understanding fracture properties and ductility. The beam is supported by rollers on both sides to allow rotation and horizontal movement, minimizing restraint forces.

The load from the hydraulic jack is distributed evenly across the full width of the beam using a spherical hinge and a steel bar, ensuring uniform application. Between the spherical hinge and the steel spreader bar, a soft pad is placed to even out the uneven top surface of the beam, which results from the concrete casting process. Steel plates measuring 150x50x10 mm are placed underneath the beam at the supports to distribute the reaction forces and prevent local crushing of the concrete due to stress concentrations.

4.4. Beam sample preparation

The beam samples will be cast in series, with two beams per batch. The first batch will consist of control beams (NS and S4), the second batch will include beams reinforced with braided BFRP stirrups (B4 and B8), and the third batch will contain beams with BFRP unidirectional laminate strip stirrups (UD4 and UD8). For each batch, three concrete cubes, each with dimensions of 150 x 150 x 150 mm, will also be cast. After 28 days of curing, these cubes will undergo uniaxial compression testing at a loading rate of 13.5 kN/s (0.65 MPa/s) in accordance with NEN-EN 12390-3 (2009), to determine the compressive strength of the concrete used in the beam samples.

The preparation of the beam specimens begins with the assembly of the reinforcement cages. To ensure the correct positioning of the compression reinforcement, a vertical leg is added to the hoisting stirrups. The hoisting stirrups, along with the longitudinal tensile and compressive reinforcement bars, are tack welded together to create a rigid reinforcement cage. For beam sample S4, the steel stirrups within the shear span are also tack welded to the longitudinal reinforcement to keep it in place. Figure This is shown in Figure 4.17.

Figure 4.17: Tag welding of the reinforcement cage

For the steel stirrups in beam S4, the optical fibres were aligned along the continuous spine of the ribs closest to the outer edge. This positioning, as depicted in Figure 4.18 (a), was specifically chosen to mitigate the risk of damage during the concrete pouring process and the subsequent use of a vibrating needle to densify the concrete mixture in the formwork. In the case of the braided BFRP stirrups, the bonding process required additional preparation. The outermost surface of these stirrups, which was initially covered by excess epoxy, was carefully smoothed using a metal file. This step was essential to create an even surface on which the DFOS sensor could be securely attached to the stirrup without gaps or misalignment, which could otherwise compromise the accuracy of the strain measurements.

For the BFRP strip stirrups, however, the approach differed due to the nature of their surface. The outer surface of these strips was found to be too wavy and uneven for effective bonding of the optical fibres. This issue is shown in Figure 4.18 (b). To address this the optical fibre sensors were instead bonded to the thin sides of the strips, where the surface was sufficiently smooth. This allowed for a continuous and secure attachment. During the application of the optical fibres, the reinforcement cages were inverted to facilitate easier access and more precise bonding. This inversion of the cages was a practical step to ensure that the fibres were applied correctly and to avoid any potential misalignment or damage during the bonding process.

After the casting of the beam samples, the formworks are immediately covered with plastic sheets, as illustrated in Figure 4.19. This measure is essential to prevent the evaporation of water from the concrete mix, a critical step in ensuring adequate moisture retention for the curing process. Proper curing is vital for the development of the concrete's strength and durability.

A minimum compressive strength of 10 MPa is commonly used as threshold for formwork removal. Compressive strength tests conducted on concrete cubes from the same batch at 1 and 7 days post-casting it indicated that this strength level is typically achieved within 48 to 72 hours. Once the concrete has sufficiently cured and attained the requisite strength, the beams are demolded and transferred to a controlled curing environment, commonly known as the fog room. In this fog room, the humidity level is kept above 95% at a temperature of 20 °C to ensure the concrete can absorb sufficient moisture. This facilitates the complete hydration of cement particles, which is essential for achieving the desired mechanical properties of the concrete. The beams remain in this high-humidity environment until the day before the scheduled experiments.

Prior to the experiments, the DIC speckle pattern is applied. The result for one of the beam samples is shown in Figure 4.20. Subsequently, holders are attached to the beams to ensure that the LVDTs are securely positioned to capture the displacement data during the experiments.

Before the beam experiments are performed, further preparation steps include the calibration of cameras and the taring of the optical fibres used to measure the strain in the stirrups. Camera calibration is vital for DIC as it ensures that the captured images are accurately aligned and scaled, which is

(a) Application of DFOS on steel stirrups

(b) Wavy, irregular surface on BFRP strip stirrups

Figure 4.18: Bonding the optical fibres to the stirrups

necessary for precise deformation measurements. Taring the DFOS involves setting a baseline measurement to account for any pre-existing strain or deformation in the fibre optic sensors that may have occurred during the casting and curing of the concrete. This ensures that subsequent measurements reflect only the changes occurring during the experiment.

Figure 4.19: Formwork

Figure 4.20: Applied speckle pattern for DIC after demoulding the beams

5

Results of beam shear capacity test

5.1. Beam test results

This section presents the experimental results from the three-point bending tests of the beam samples that are described in Chapter 4. The section begins with a summary of all beam test results, followed by detailed descriptions of individual beam performances.

The failure mode observed for all beams was shear tension mode. Specifically, beams with basalt FRP stirrups failed due to the rupture of one of the stirrups at a corner section. The load-deflection graphs for all beam samples are shown in Figure 5.1. Table 5.1 summarizes the forces, mid-span deflections, and total beam shear capacities at peak load capacity. For beams with basalt FRP stirrups, these values are also provided prior to stirrup rupture.

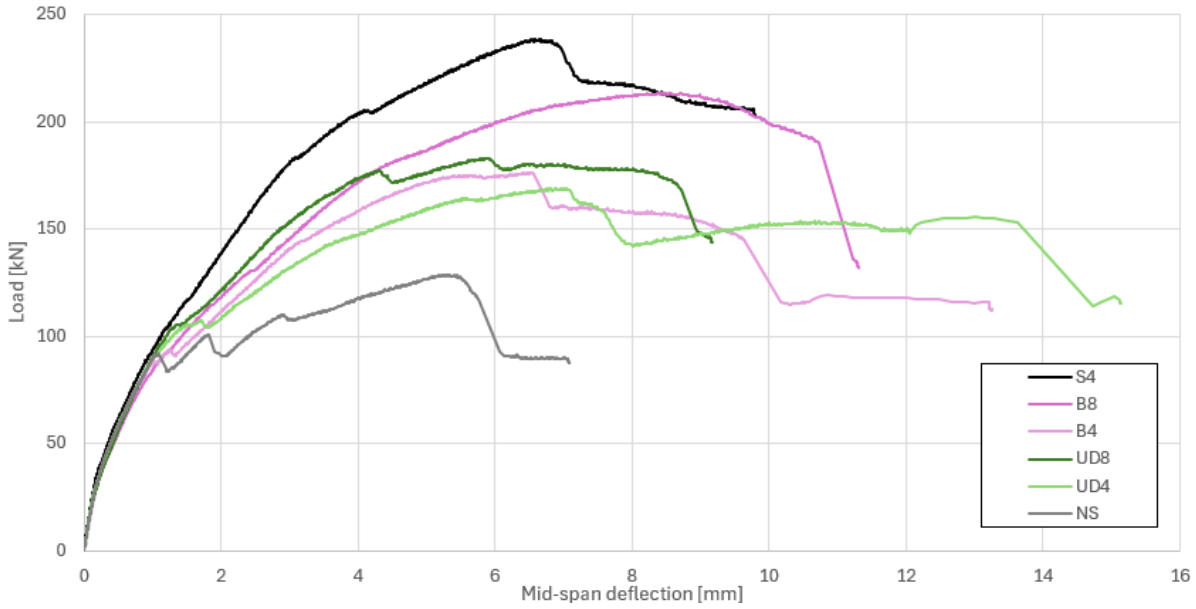

Figure 5.1: Load-displacement diagrams for all beam samples

In this figure, it is evident that all beams exhibit the same initial stiffness up to a force of approximately 90 kN. This consistency is expected, as all beams contain the same size and amount of longitudinal rebars positioned at the same depth within the cross-section. Around this load, the first shear cracks begin to form. From this point onward, the load-deflection response varies for each beam depending

on the individual shear reinforcement configuration and how this is able to control the propagation of these shear cracks.

Table 5.1: Overview of beam shear capacity test results

	Maximum capacity			**Stirrup rupture**		
Beam	Force F_{max} [kN]	Mid-span defl. δ_u [mm]	Shear capacity V [kN]	Force $F_{rupture}$ [kN]	Mid-span defl. δ_s [mm]	Shear capacity V [kN]
NS	128.5	5.24	64.3	-	-	-
S4	238.5	6.66	119.3	-	-	-
B4	175.5	6.48	87.8	144.7	9.55	72.35
B8	213.2	8.49	106.6	190.4	10.63	95.2
UD4	168.0	7.02	84.0	153.3	13.27	76.65
UD8	183.0	5.85	91.5	168.3	8.58	84.15

From these results it can be observed that an increase of BFRP stirrups results in an increase of shear capacity. Moreover, it can be observed that control beam NS, which lacks stirrups, demonstrates the lowest shear capacity of 64.3 kN at a mid-span deflection of 5.24 mm. In contrast, the other control beam S4, which includes steel stirrups, exhibits the highest shear capacity of 119.3 kN with a mid-span deflection of 6.66 mm, indicating the significant contribution of steel stirrups to the shear capacity.

Beams B4 and B8, which include braided BFRP stirrups, show notable improvements in shear capacity over the control beam. B4 achieves a shear capacity of 87.8 kN with a mid-span deflection of 6.48 mm, and B8 reaches 106.6 kN with a mid-span deflection of 8.49 mm. Before stirrup rupture, B4 and B8 exhibit shear capacities of 72.35 kN and 95.2 kN, with corresponding mid-span deflections of 9.55 mm and 10.63 mm, respectively.

Beams UD4 and UD8, which include BFRP UD-laminate strip stirrups, also outperform the control beam without stirrups. UD4 has a shear capacity of 84.0 kN, and UD8 achieves 91.5 kN, with mid-span deflections of 7.02 mm and 5.85 mm, respectively. Prior to stirrup rupture, UD4 and UD8 display shear capacities of 76.65 kN and 84.15 kN, with mid-span deflections of 6.80 mm and 4.36 mm, respectively.

5.1.1. Beam sample "NS"

The load-displacement diagram of the beam sample without stirrups (NS) is shown in Figure 5.2. Specific points in this graph are highlighted with a red dot. The corresponding major strain diagrams and descriptions of the events happening at these specific points are shown in 5.3. Since this beam does not contain stirrups, there is no available strain data from the optical fibres.

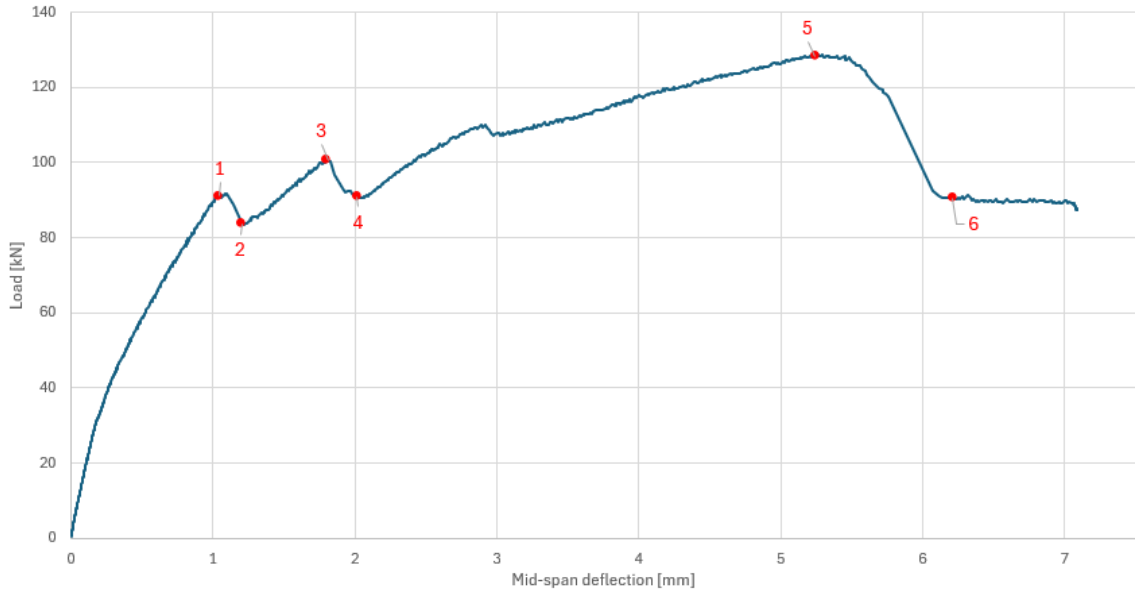

Figure 5.2: Load-deflection diagram for beam sample NS

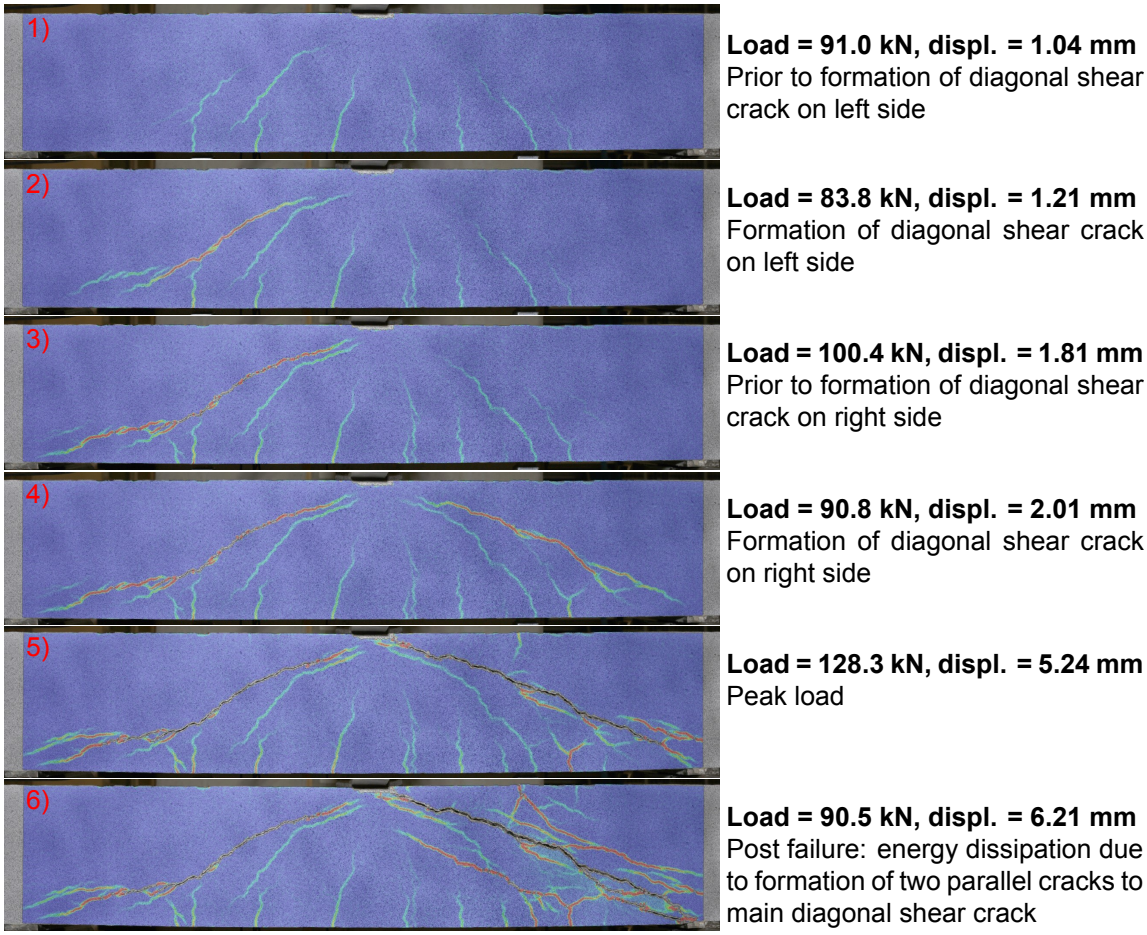

Figure 5.3: NS beam sample: shear crack formation images from DIC-data. The event numbers correspond to the numbers at specific points shown in the graph in Figure 5.2.

Figure 5.4 displays failed beam sample NS after execution of the three-point bending test test.

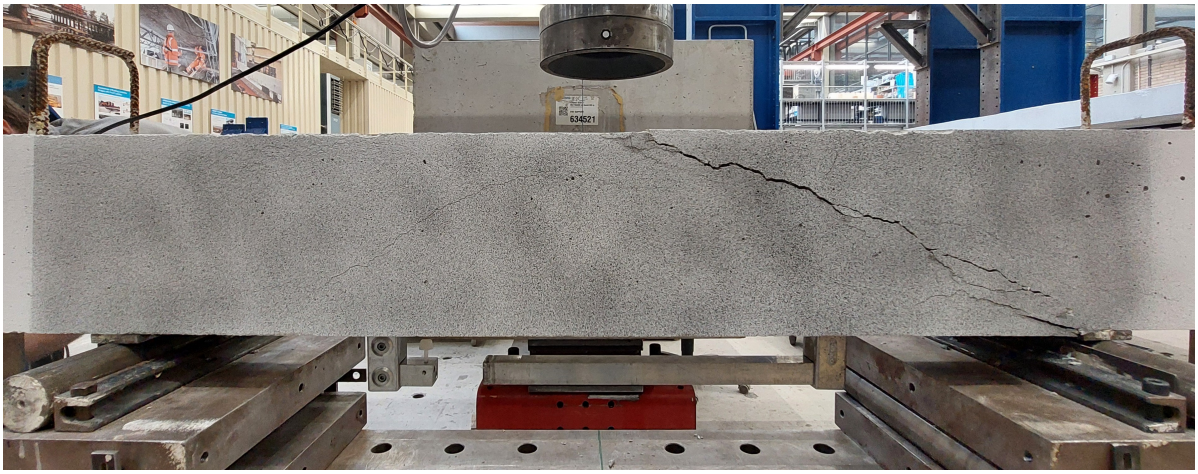

Figure 5.4: Beam sample NS after the test

From these figures, it can be observed that the dips in the load-displacement graph are caused by the formation of diagonal shear cracks. The normative shear crack on the right side of the beam extends directly from the loading point to the supports in between the steel support plates.

5.1.2. Beam sample "S4"

This subsection presents the experimental results for beam sample S4. This beam has four traditional Ø8 mm ribbed steel shear reinforcement stirrups with a governing spacing of 250 mm for the stirrups closest to mid-span. The load-displacement diagram for this beam is illustrated in Figure 5.5, with specific points marked by red dots. The corresponding major strain diagrams and descriptions of the events occurring at these specific points are presented in Figure 5.6. The measured strain data from the distributed fibre optic sensors (DFOS) attached to the stirrups is shown in Figure 5.7. There is no data available for stirrup number 4, likely because it was compromised during the casting or preparation phase of the beam. Furthermore, the optical fibre that was bonded to stirrup 1 was compromised before the maximum load on the beam was reached.

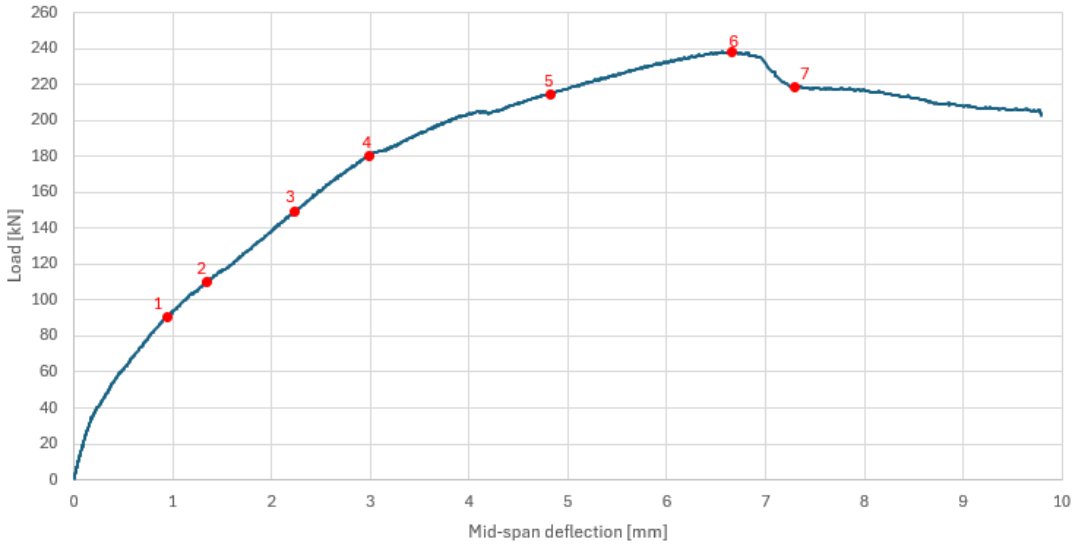

Figure 5.5: Load-deflection diagram for beam sample S4

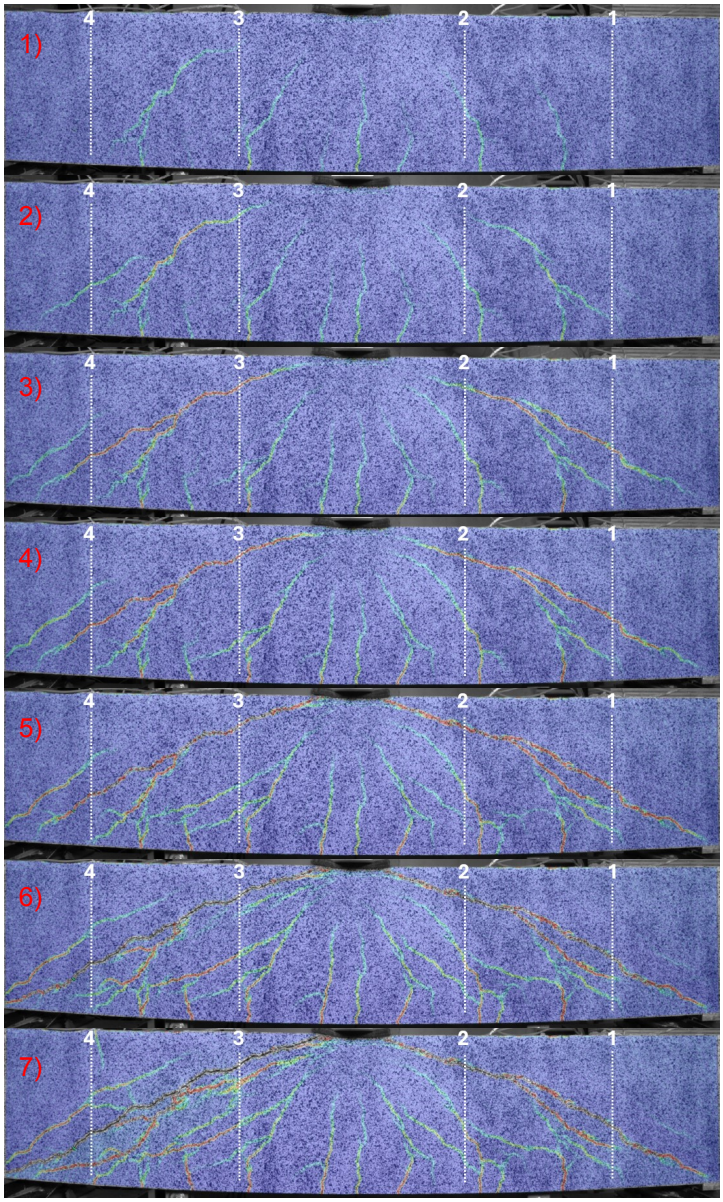

Load = 90.9 kN, displ. = 0.95 mm
Bending crack starting to grow diagonally into shear crack on the left side

Load = 109.9 kN, displ. = 1.34 mm
Formation of diagonal shears crack on both side

Load = 149.3 kN, displ. = 2.24 mm
Shear cracks present on both sides

Load = 180.4 kN, displ. = 2.99 mm
Prior to yielding of stirrups.

Load = 214.7 kN, displ. = 4.82 mm
Last strain data recording for DFOS on stirrup no. 1

Load = 238.2 kN, displ. = 6.66 mm
Peak load

Load = 218.8 kN, displ. = 7.29 mm
Post peak: energy dissipation due to formation of parallel cracks to main diagonal shear crack on the left side of the beam

Figure 5.6: Beam sample S4: shear crack formation images from DIC-data. The numbers correspond to the numbers at specific points shown in the graph in Figure 5.5.

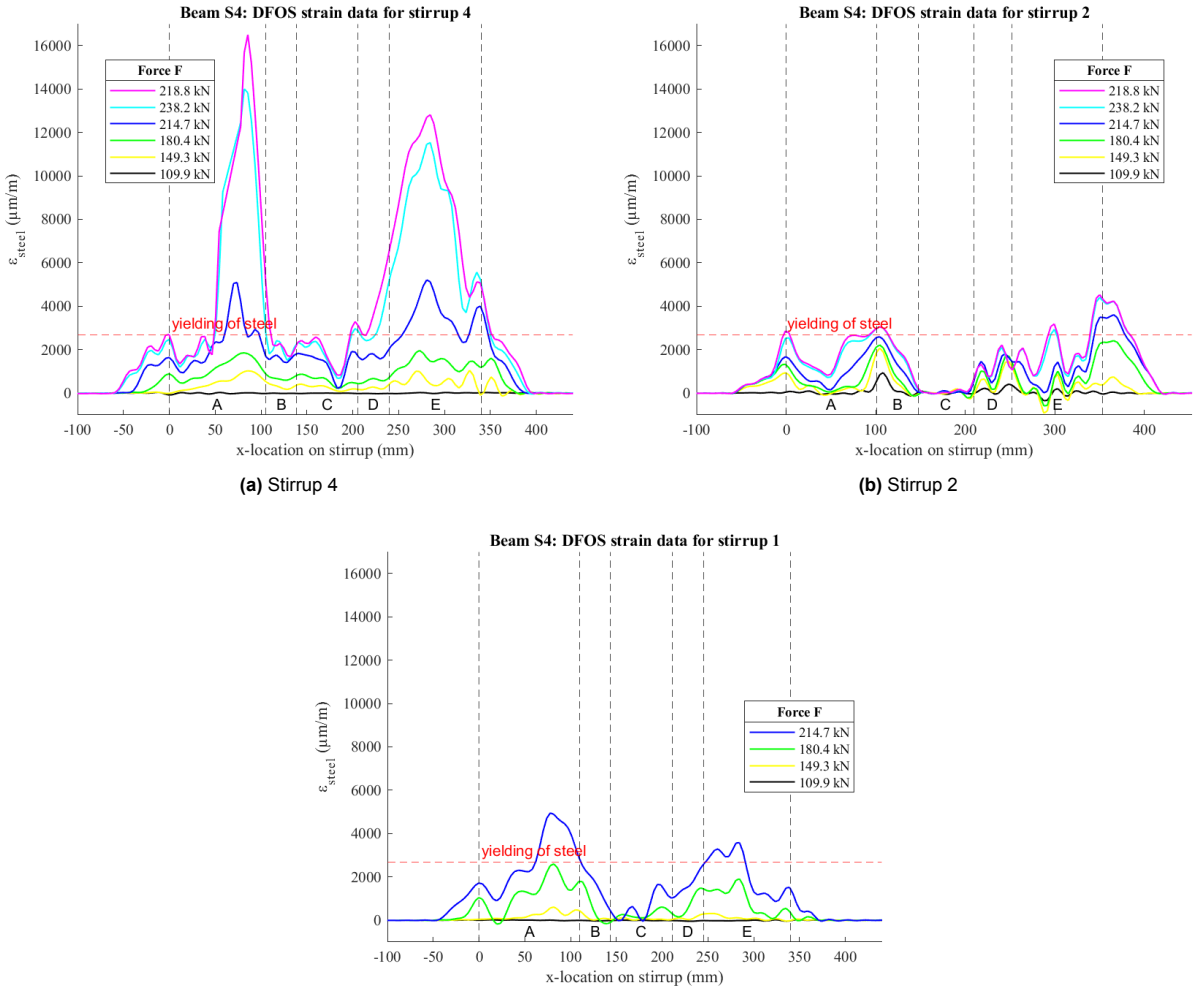

(a) Stirrup 4

(b) Stirrup 2

(c) Stirrup 1

Figure 5.7: DFOS strain data for stirrups in beam sample S4. A = vertical section (LVDT-side), B = corner section (LVDT-side), C = bottom section, D = corner section (DIC-side), E = vertical section (DIC-side), see Figure 4.16 (a).

Figure 5.8 displays failed beam sample NS after execution of the shear test.

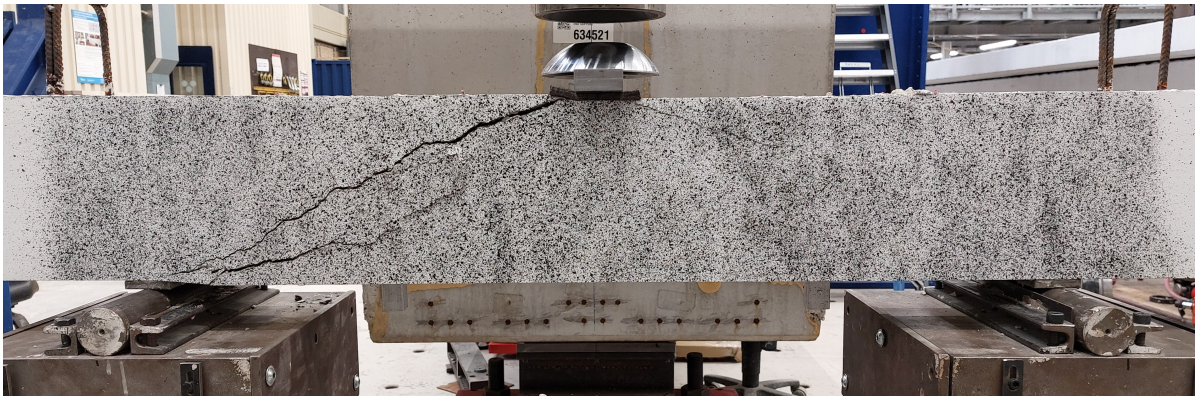

Figure 5.8: Beam sample S4 after performing the experiment

From the strain data in Figure 5.7, it can be observed that stirrups 2 and 3 begin to yield at some places when the beam is subjected to a load of approximately F = 180 kN. This is evident as most stirrups reach a strain value near the yielding strain of steel, estimated to be ε = 2700 µm/m, or 0.0027 [-]. Additionally, the load-displacement graph in Figure 5.5 shows a decrease in stiffness from this point onward.

After the peak load (F = 238 kN) is reached, it can be observed that stirrups 1, 2 and 4 are yielding at certain locations. There is no strain data for stirrup 3, but it can be assumed that it is also yielding at this point. When yielding, the stirrups cannot take any more tensile forces and start to elongate. The main diagonal shear crack on the right side of the beam opens up and parallel diagonal cracks form on either side of it. Additionally, it can be observed that the main diagonal shear crack on the left side of the beam opens up. During this process, the strain in stirrup number 4 increases to approximately 16000 µm/m, or 0.016 [-], particularly near the bottom half where the shear crack intersects the stirrup. After the peak load is reached, all stirrups have locations that are yielding and the shear capacity decreases, because the shear crack widths increase.

5.1.3. Beam sample "B4"

This subsection presents the experimental results for beam sample B4. This beam contains a total of four Ø8 mm braided BFRP shear reinforcement stirrups with a governing spacing of 250 mm for the stirrups closest to mid-span. The load-displacement diagram for this beam is illustrated in Figure 5.9, with specific points marked by red dots. The corresponding major strain diagrams and descriptions of the events occurring at these specific points are presented in Figure 5.10. The measured strain data from the distributed fibre optic sensors (DFOS) attached to the stirrups is shown in Figure 5.11. The strain data for stirrup 3 is incomplete due to damage sustained by the optical fibre during the testing process.

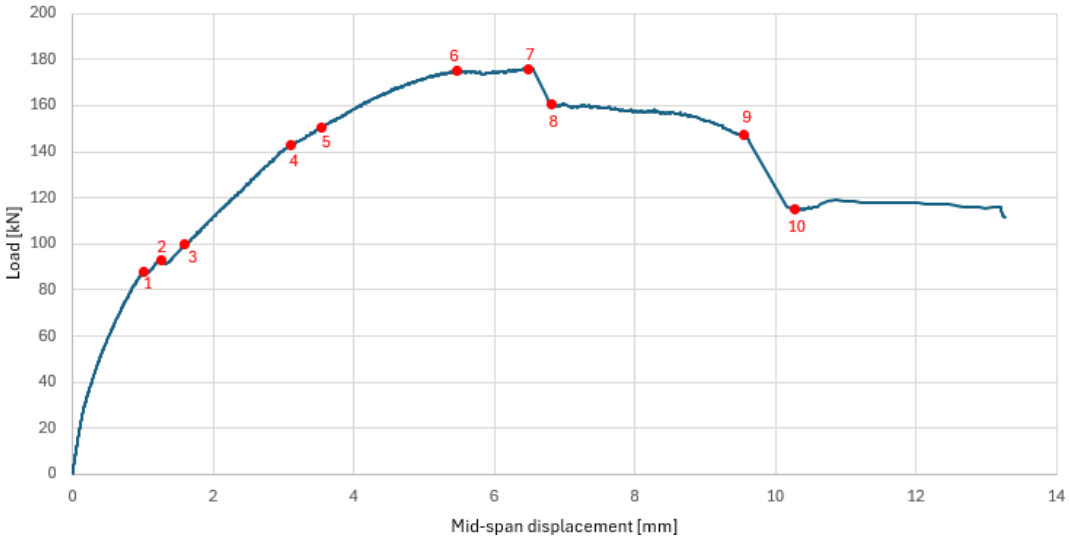

Figure 5.9: Load-deflection diagram for beam sample B4

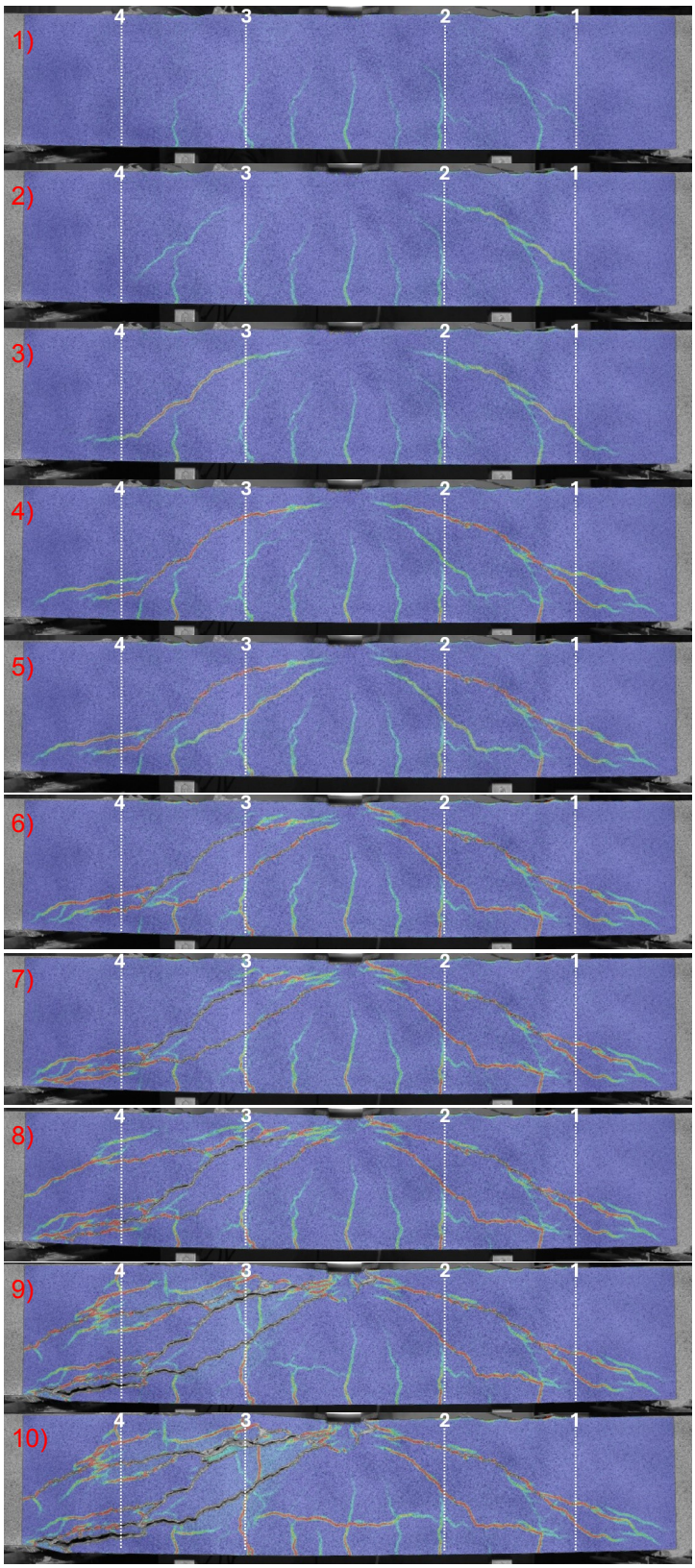

Load = 88.0 kN, displ. = 1.02 mm
Bending crack diagonally expanding into a shear crack on the right side of the beam

Load = 93.1 kN, displ. = 1.27 mm
Formation of diagonal shear crack on right side of the beam

Load = 99.6 kN, displ. = 1.60 mm
Formation of diagonal shear crack on the left side of the beam

Load = 143.0 kN, displ. = 3.10 mm
Formation of sharp secondary shear cracks on the right side of the beam

Load = 150.2 kN, displ. = 3.53 mm
Secondary steep shear crack forming on the left side

Load = 175.0 kN, displ. = 5.46 mm
Load plateau reached, secondary cracks increase in length/width

Load = 218.8 kN, displ. = 6.48 mm
Peak load. Secondary shear cracks have grown in length and width

Load = 160.5 kN, displ. = 6.82 mm
Post peak load: formation of shallow diagonal crack on the left side of the beam

Load = 147.1 kN, displ. = 9.55 mm
Prior to rupture of stirrup no. 3.

Load = 115.2 kN, displ. = 10.27 mm
Post rupture of stirrup no. 3

Figure 5.10: Beam sample B4: shear crack formation images from DIC-data. The event numbers correspond to the numbers at specific points shown in the graph in Figure 5.9.

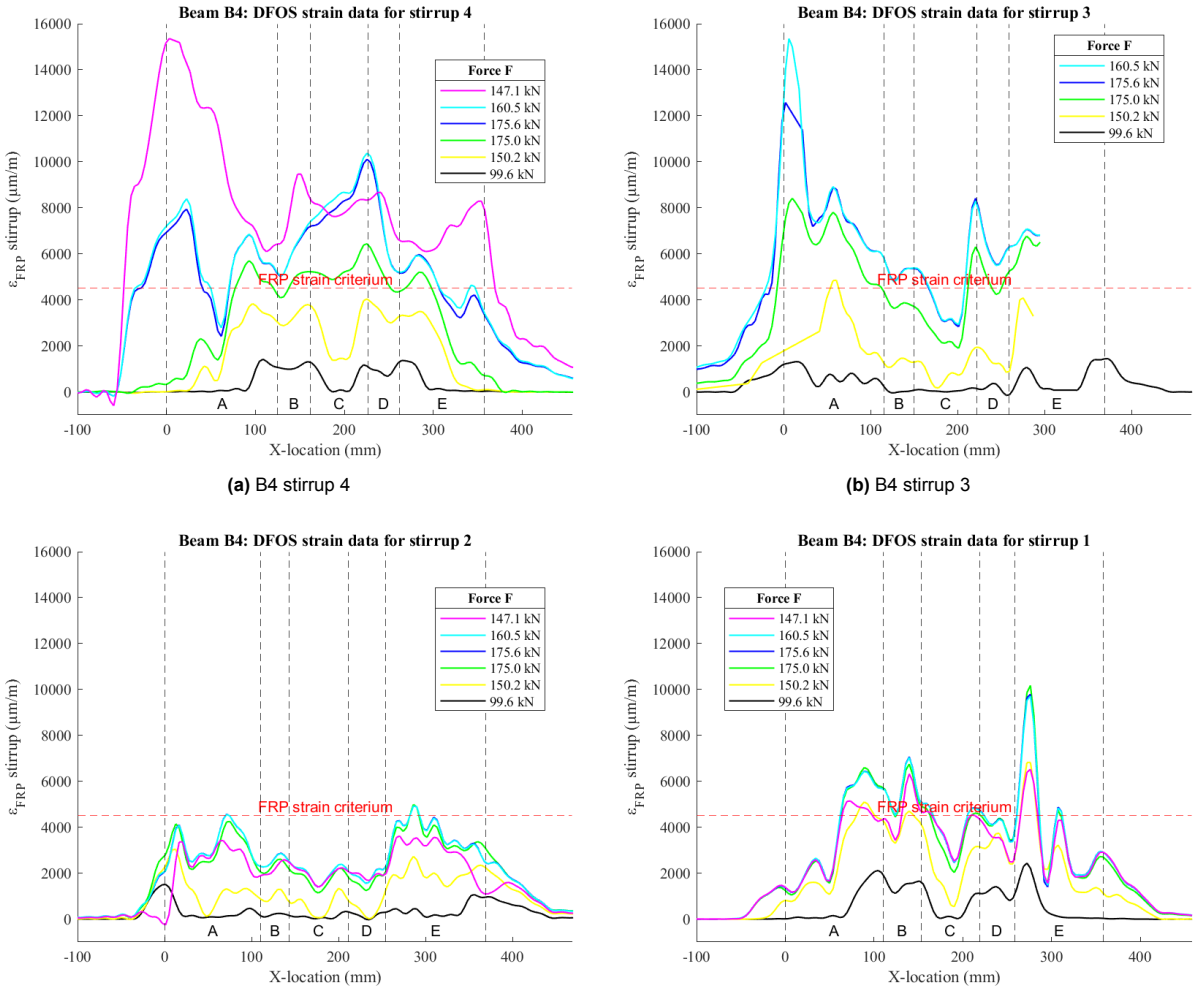

(a) B4 stirrup 4

(b) B4 stirrup 3

(c) B4 stirrup 2

(d) B4 stirrup 1

Figure 5.11: DFOS strain data for stirrups in beam sample B4. A = vertical section (LVDT-side), B = corner section (LVDT-side), C = bottom section, D = corner section (DIC-side), E = vertical section (DIC-side), see Figure 4.16.

The general behavior of beam sample B4 under the test conditions showed a progressive development of cracks and structural damage. Initially, bending cracks emerged, which then expanded into diagonal shear cracks. As the load increased, these cracks propagated and secondary shear cracks began to form on both sides of the beam, resulting in a drop after the peak load was reached. The beam's structural integrity continued to degrade as the cracks grew in length and width, eventually leading to the rupture of stirrup 3. After the test, the surrounding concrete was removed to expose this stirrup. The result is shown in Figure 5.12.

Figure 5.12: Rupture of stirrup 3 in the top corner (LVDT-side of the beam)

During the experiment, it was observed that the beam was not loaded centrally across its width; the hydraulic jack was positioned closer to the side with the LVDTs. This eccentricity is estimated to be approximately 20 mm.

Additionally, the graph shows that the strain near the top corner (LVDT-side, zone ”A”) of stirrup 3 significantly increases just before, during, and after the peak load is reached ($\varepsilon \approx 8200$, 12500, and 15200 µm/m, respectively). After the peak load, the strain in the stirrups continues to rise, suggesting that while the stresses in the stirrups increase, the shear capacity decreases.

5.1.4. Beam sample "B8"

This subsection contains the experimental results for beam sample B8. It starts with a load-deflection graph in Figure 5.13, in which specific points are marked. These points are further analysed using the footage from the DIC in Figure 5.14.

Strain data from the optical fibres that are bonded to the stirrups is shown in Figure 5.15. There is no data available for stirrups 5 and 6, because the optical fibre was compromised during the casting or preparation phase of the beam.

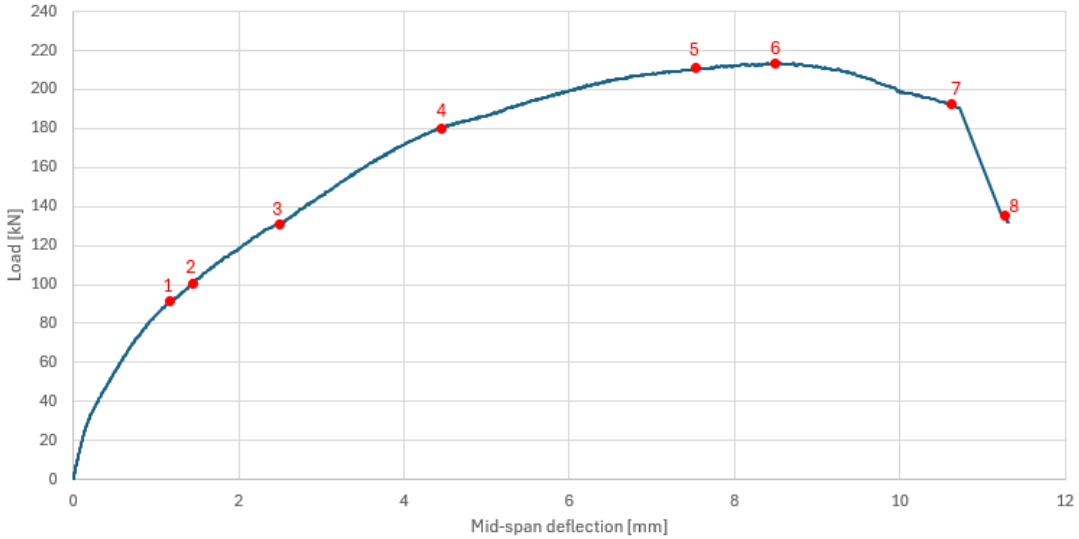

Figure 5.13: Load-deflection diagram for beam sample B8

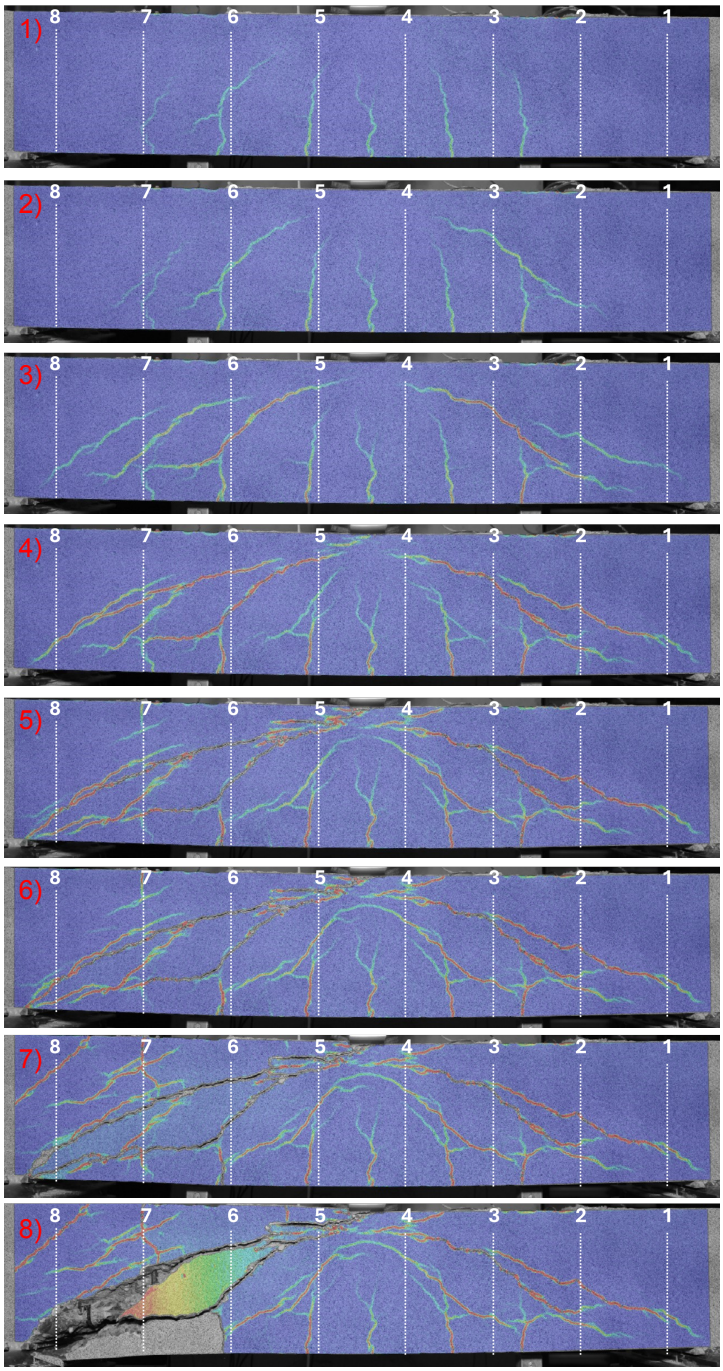

Load = 91.2 kN, displ. = 1.17 mm
Bending cracks starting to grow into shear cracks

Load = 100.5 kN, displ. = 1.44 mm
Formation of diagonal shear cracks on both side

Load = 130.6 kN, displ. = 2.49 mm
New shear crack appears on the left side.

Load = 180.2 kN, displ. = 4.45 mm
Change in stiffness due to length-/width increase of shear cracks

Load = 210.9 kN, displ. = 7.53 mm
Secondary shear cracks have increased in length and width

Load = 213.0 kN, displ. = 8.49 mm
Peak load. Main diagonal shear cracks have reached all the way down to the supports

Load = 192.4 kN, displ. = 10.63 mm
Prior to rupture of stirrup 7: shear cracks opening up on the left side of the beam

Load = 135.2 kN, displ. = 11.26 mm
Post rupture of stirrup 7

Figure 5.14: Beam sample B8: shear crack formation images from DIC-data. The event numbers correspond to the numbers at specific points shown in the load-displacement graph in Figure 5.13.

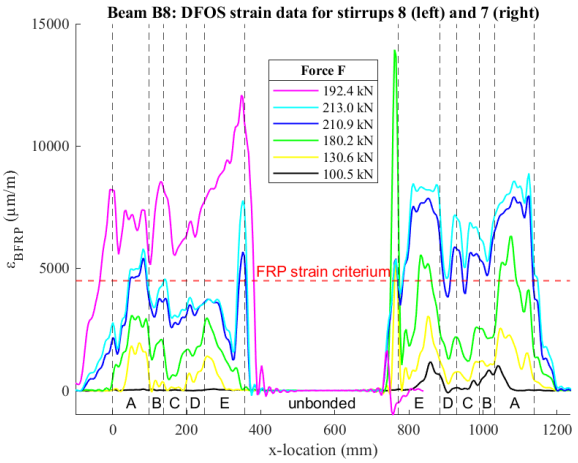

(a) Stirrups 8 (left) and 7 (right)

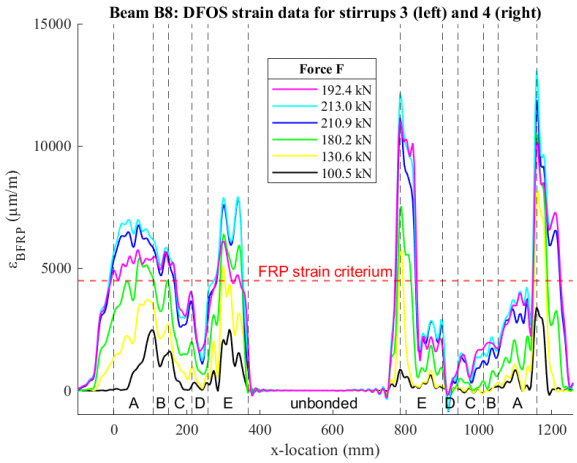

(b) Stirrups 3 (left) and 4 (right)

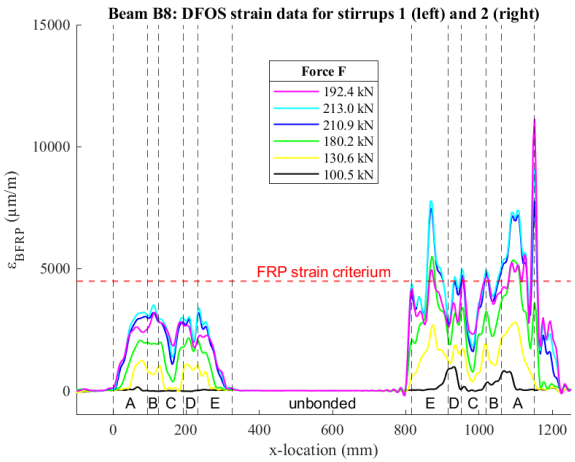

(c) Stirrups 1 (left) and 2 (right)

Figure 5.15: DFOS strain data for stirrups in beam sample B8. A = vertical section (LVDT-side), B = corner section (LVDT-side), C = bottom section, D = corner section (DIC-side), E = vertical section (DIC-side), see Figure 4.16.

The load-displacement graph shows a continuous increase in load without any noticeable drops due to crack formation until the peak load is reached. This behavior suggests that the beam maintained its structural integrity and did not experience significant cracking or damage up to the peak load. The absence of load drops indicates that the material remained intact and effectively distributed the applied force at mid-span.

However, just before reaching the peak load, a new inclined crack began to form and propagate, crossing stirrup 7 at the top. Additionally, the main diagonal shear cracks on the left side started to open up, leading to increased stresses in stirrup 7. These additional stresses exceeded the strength of stirrup 7, causing it to fail at the bottom corner located at the side of the beam with the LVDTs. This failure is illustrated in Figure 5.16.

Figure 5.16: Rupture of stirrup 7 in the bottom corner of the beam (LVDT-side of the beam)

From the strain data, it can be observed that the optical fibre bonded to stirrup 7 reached a strain value of approximately 7000 µm/m at peak load in the corresponding corner. Unfortunately, the optical fibre was compromised after the peak load, so no data is available beyond this point. On the other hand, stirrups 8, 4 and 2 reached strain values up to $\varepsilon \approx 12000$ µm/m before rupture of stirrup 7 and ultimate failure of the beam. This suggests that the tensional force in the stirrups continued to increase, even as the shear capacity began to decrease and drop upon rupture of stirrup 7.

5.1.5. Beam sample "UD4"

This subsection contains the experimental results for beam sample UD4. It starts with analyzing the load-displacement graph shown in Figure 5.17, in which specific points are marked with a red dot. These points are further analysed using the DIC-footage in Figure 5.18. The strain data from the optical fibres that are bonded to the stirrups is presented in Figure 5.19. However, for the optical fibres bonded to stirrups 1, 2 and 4, the strain data is incomplete because the optical fibres were compromised in the preparation phase or during the test. In this case, the unfiltered, raw data is plotted in the graphs.

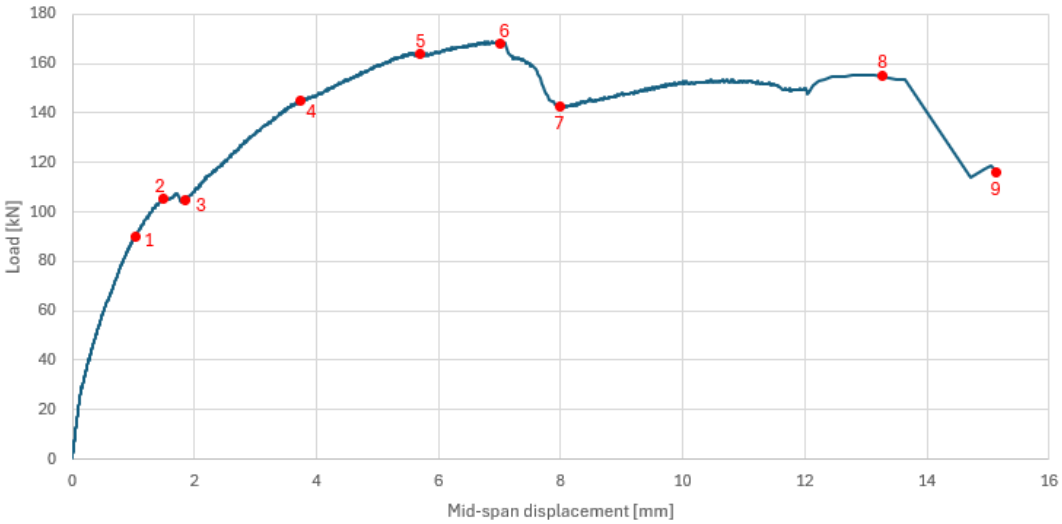

Figure 5.17: Load-deflection diagram for beam sample UD4

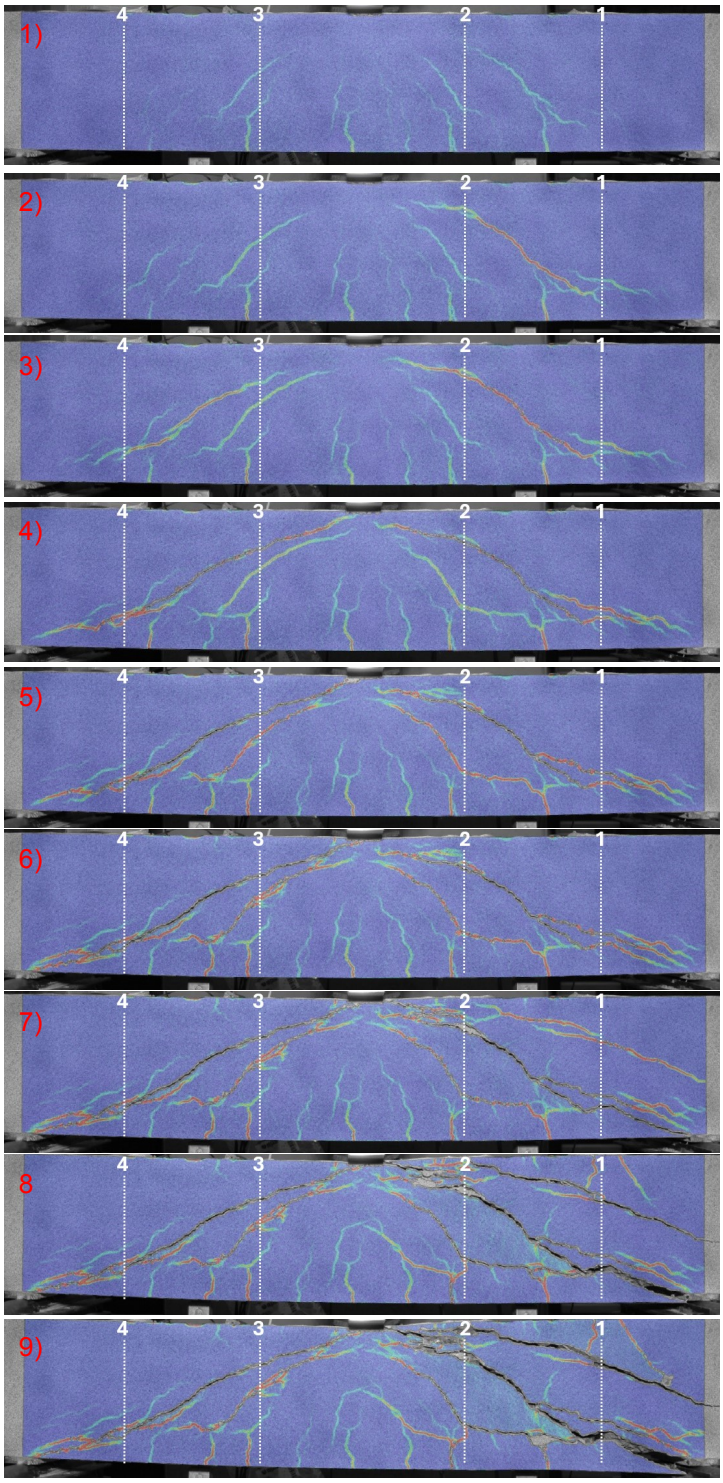

Load = 90.2 kN, displ. = 1.03 mm
Bending cracks are present and shear cracks are starting to form

Load = 105.2 kN, displ. = 1.49 mm
Formation of diagonal shear cracks on both sides of the beam

Load = 104.7 kN, displ. = 1.85 mm
New shear crack appears on the left side.

Load = 144.7 kN, displ. = 3.74 mm
Change in stiffness due to increase of shear cracks length and width

Load = 163.7 kN, displ. = 5.70 mm
Secondary steep shear cracks have increased in length and width

Load = 168.2 kN, displ. = 7.02 mm
Peak load. Main diagonal shear cracks have reached all the way down to the supports

Load = 142.5 kN, displ. = 8.00 mm
New shallow crack forms in top right of the beam

Load = 154.8 kN, displ.= 13.27 mm
Prior to rupture of stirrup 1: cracks on the right side of the beam have opened up

Load = 116.2 kN, displ. = 15.12 mm
Post rupture of stirrup 1

Figure 5.18: Beam sample UD4: shear crack formation images from DIC-data. The event numbers correspond to the numbers at specific points shown in the graph in Figure 5.17.

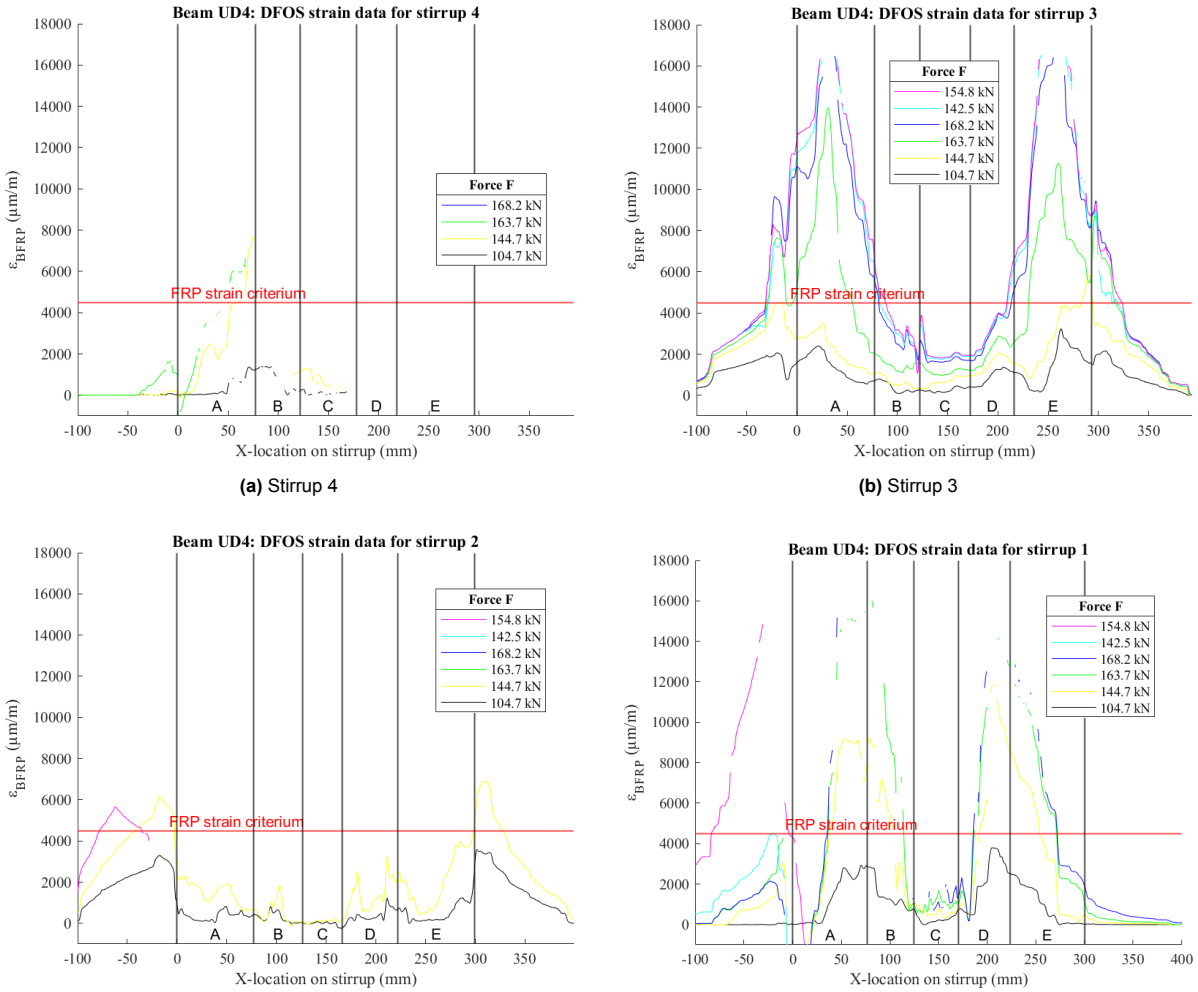

(a) Stirrup 4

(b) Stirrup 3

(c) Stirrup 2

(d) Stirrup 1

Figure 5.19: DFOS strain data for stirrups in beam sample UD4. A = vertical section (LVDT-side), B = corner section (LVDT-side), C = bottom section, D = corner section (DIC-side), E = vertical section (DIC-side), see Figure 4.16.

Stirrup 1 failed in the top corner on the LVDT-side of the beam. This is shown in Figure 5.20. Unfortunately, only part of the strain data is available for this stirrup, because the optical fibre was compromised during the experiment. From the raw data in 5.19d, however, it can be observed that the optical fibre bonded to stirrup 1 reached a strain of $\varepsilon \approx 15000$ µm/m near the point of rupture. Furthermore, the figure suggests that there were strain peaks near the bottom corners (sections B and D) of the stirrup as well.

Figure 5.20: Rupture of stirrup 1 in the top corner (LVDT-side) of beam sample UD4

5.1.6. Beam sample "UD8"

This subsection presents the experimental results for beam sample UD8. It begins with an analysis of the load-displacement graph shown in Figure 5.21, where specific points are marked with a red dot. These points are further examined using the DIC-footage in Figure 5.22.

The strain data from the optical fibres bonded to the stirrups is displayed in Figure 5.23. There is no data available for stirrups 7 and 8 because the optical fibre bonded to these stirrups was compromised during the casting or preparation phase of the beam. Additionally, the optical fibre bonded to stirrups 1 and 2 was compromised during the experiment, resulting in no data being available after a load of F = 162.0 kN was applied at mid-span.

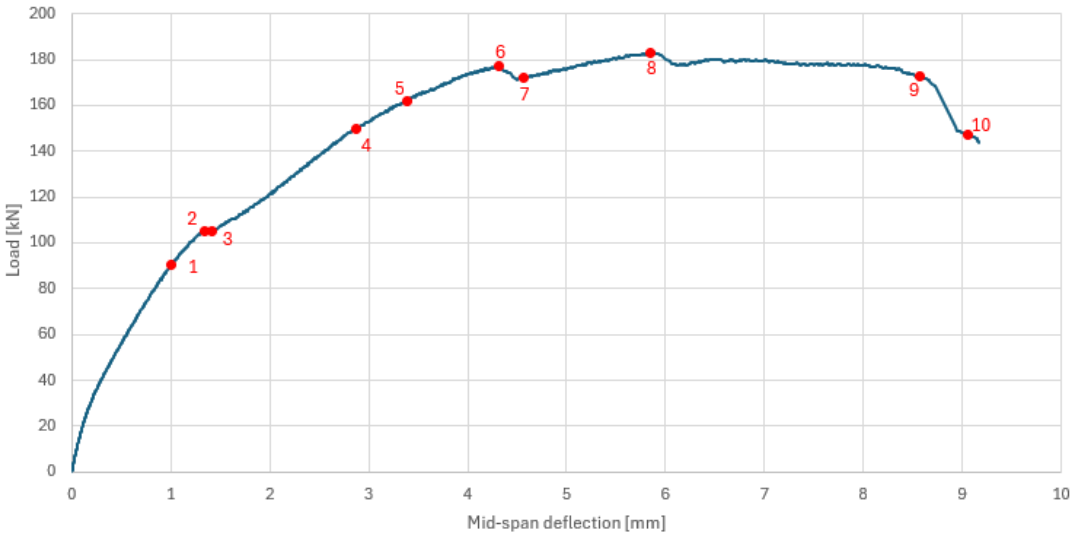

Figure 5.21: Load-deflection diagram for beam sample UD8

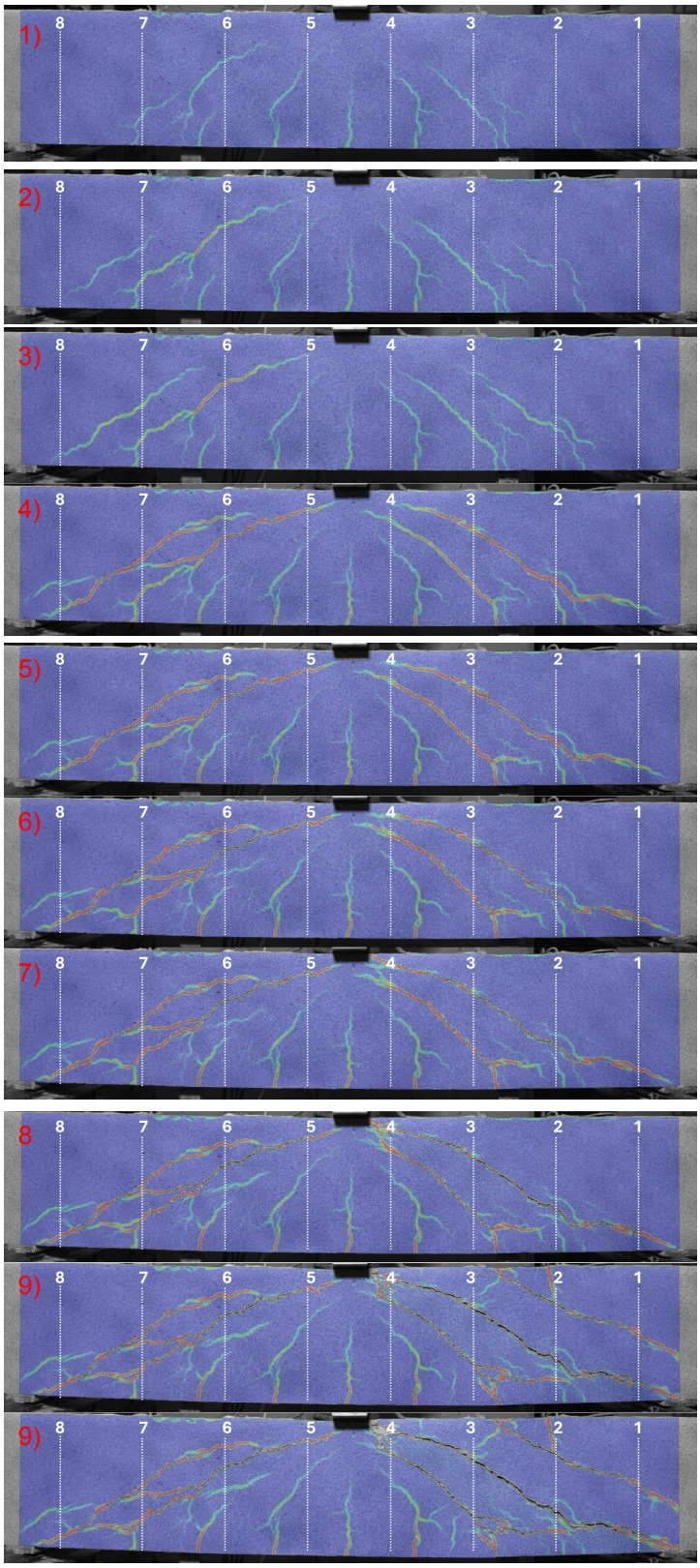

Load = 90.3 kN, displ. = 1.01 mm
Bending cracks starting to grow into shear cracks

Load = 105.1 kN, displ. = 1.34 mm
Diagonal shear cracks appearing on the left side of the beam

Load = 104.9 kN, displ. = 1.41 mm
New shear cracks appearing on both the far left and far right side sides of the beam

Load = 150.0 kN, displ. = 2.87 mm
Change in stiffness of the beam: existing shear cracks have increased in length and width

Load = 162.0 kN, displ. = 3.39 mm
Shear cracks on the right side have increased in length and width. Last record of DFOS strain data for stirrups 1 and 2

Load = 176.9 kN, displ. = 4.32 mm
Existing shear cracks increase in length and width

Load = 172.2 kN, displ. = 4.56 mm
Small dip in load due to the shear crack on the right reaching the top surface of the concrete beam at the loading point

Load = 182.9 kN, displ. = 5.85 mm
Peak load: diagonal shear cracks on the right side have started to opening up

Load = 172.8 kN, displ. = 8.58 mm
Prior to rupture of stirrup 3. New diagonal crack has formed in the top right, parallel to the existing cracks.

Load = 146.9 kN, displ. = 9.06 mm
After rupture of stirrup 3 on an out-of-plane wrinkle at the top corner on the DIC-side

Figure 5.22: Beam sample UD8: shear crack formation images from DIC-data. The event numbers correspond to the numbers at specific points shown in the graph in Figure 5.21.

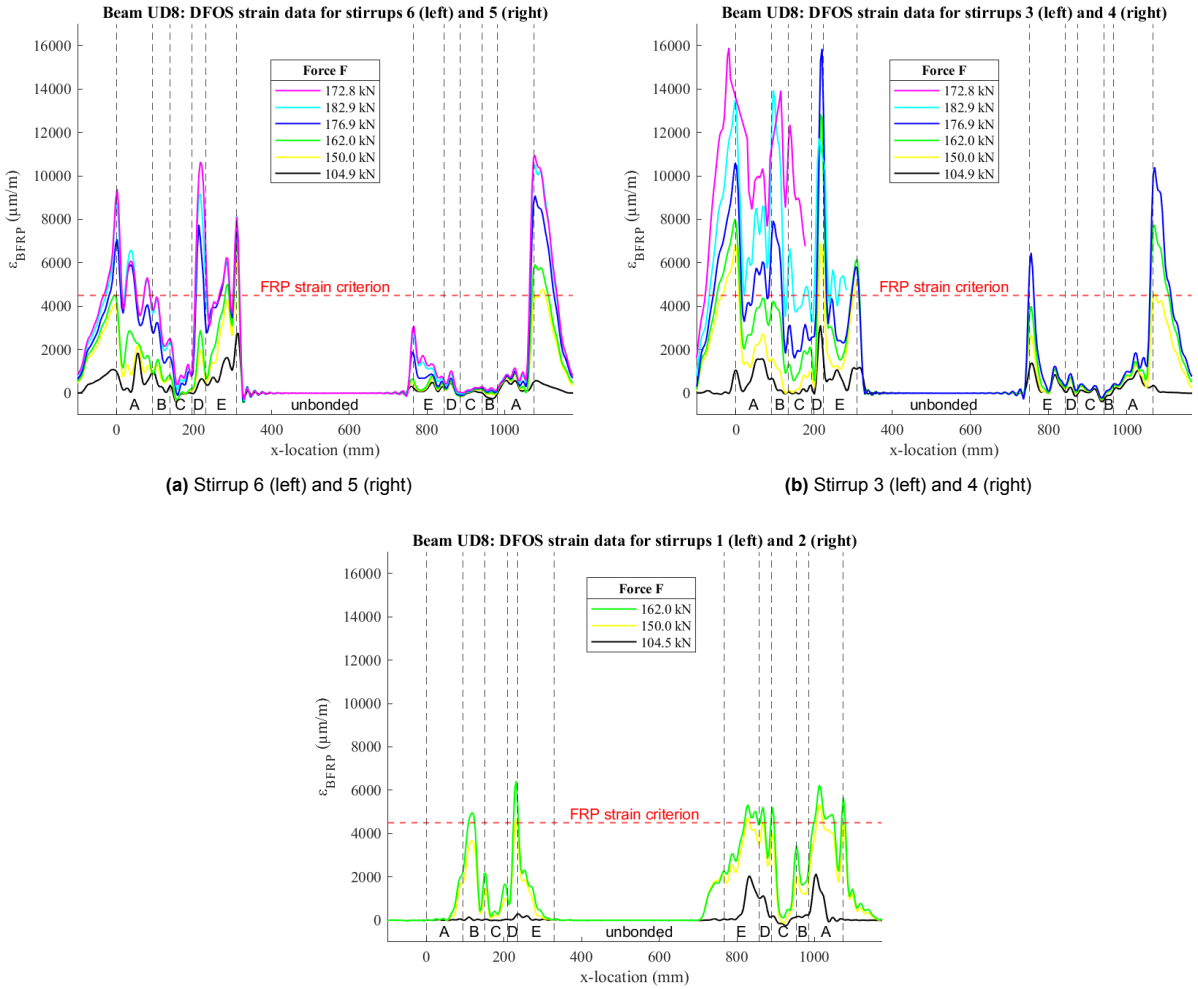

(a) Stirrup 6 (left) and 5 (right)

(b) Stirrup 3 (left) and 4 (right)

(c) Stirrup 1 (left) and 2 (right)

Figure 5.23: DFOS strain data for stirrups in beam sample UD8. See Figure 4.16 for explanation on ”A”, ”B”, ”C”, ”D” and ”E”.

After the peak load was reached, a new inclined shear crack formed, crossing stirrup 1 at mid-height and stirrup 2 at the top. Unfortunately, the optical fibres bonded to these stirrups were compromised during the test, as were parts of stirrups 3 and 4. However, Figure 5.23 shows that the strain in stirrups 6, 5, and the remaining part of stirrup 4 continued to increase after the peak shear capacity was reached. This suggests that the tensional force in the stirrups continued to rise, even as the beams peak shear load was surpassed and began to decrease.

After the experiment, the ruptured stirrup was exposed, as shown in Figure 5.24. It appears that stirrup 3 broke in the top corner section on the LVDT side of the beam. In Figure 5.23b, this corresponds to section ”E” on the left half of the graph. The maximum strain in the stirrup close to this point was approximately 6000 µm/m at the moment of the beam its peak load capacity. The strain data of the stirrup prior to failure is unknown because the sensor was compromised during the test.

Figure 5.24: Rupture of stirrup 3 at the top corner (LVDT-side) of beam sample UD8

5.2. Concrete compressive strength

The concrete compressive mean strength $f_{cm,cube}$ for the 150x150x150 mm concrete cube specimen is calculated using the formula:

$$f_{cm,cube} = F_u / A_c \tag{5.1}$$

where F_u is the maximum load at failure in N, and A_c is the cross-sectional area of the specimen on which the compressive force acts in mm^2. The results of the concrete cube compressive tests are shown in Table 5.2.

Table 5.2: Experimental results for the concrete compressive strength of cube samples

Corresponding beam batch	Sample no.	Sample age	Force [kN]	Stress [MPa]	AVG [MPa]	STD [MPa]	COV [%]
NS, S4	1	28 days	1101.2	48.94	49.53	0.482	0.97
	2		1127.8	50.12			
	3		1114.1	49.52			
B4, B8	1	28 days	1090.4	48.46	47.23	0.868	1.84
	2		1049.4	46.64			
	3		1048.5	46.60			
UD4, UD8	1	28 days	1021.0	45.38	46.05	0.713	1.55
	2		1029.1	45.74			
	3		1058.4	47.04			

From this table, it can be observed that the mean uniaxial concrete compressive strength ($f_{cm,cube}$) of the 150x150x150 mm concrete cubes after 28 days was 49.53 MPa for the batch with the reference beam samples (NS+S4), 47.23 MPa for the batch with sampels B4 and B8 beams, and 46.05 MPa for beam samples UD4 and UD8. The compressive strength values show good consistency across different batches, with standard deviations of 0.482 MPa, 0.868 MPa, and 0.713 MPa respectively. This low variability suggests a uniform quality of concrete production and curing processes.

Typically, the relationship between the compressive strength of 150 mm cubic samples and cylindrical samples with dimensions 150 mm in diameter by 300 mm in height exhibits a ratio of approximately 0.8. This ratio allows for the determination of the mean compressive strength of cylindrical samples, which can be expressed by the equation:

$$f_{cm} = f_{cm,\text{cylinder}} = 0.8 \cdot f_{cm,\text{cube}} \tag{5.2}$$

The mean compressive strengths obtained for the different concrete beam batches—NS+S4, B4+B8, and UD4+UD8—were 39.6 MPa, 37.8 MPa, and 36.8 MPa, respectively. These values align closely with the compressive strength class C30/37, which was utilized in the design calculations for the beams. The C30/37 classification corresponds to a mean compressive cylinder strength f_{cm} calculated as f_{ck} + 8, where f_{ck} = 30 MPa, yielding a mean compressive strength f_{cm} of 38 MPa. This correlation confirms that the concrete mix used in the beam fabrication was consistent with the design assumptions.

6

Analysis, comparison and discussion of beam shear capacity test results

6.1. Analysis of experimental results

Table 6.1 provides a detailed comparison of the maximum load, relative strength, shear capacity, and stirrup efficiency across various beam samples. The relative strength is calculated as the ratio of the maximum load capacity of each beam to that of either the beam without stirrups (sample NS) or the beam with 4 steel stirrups (sample S4).

The analysis of the beam test results considers both the intrinsic shear strength of the concrete (V_c) and the additional shear strength contributed by the stirrups (V_s) to determine the total shear capacity (V). This methodology enables a thorough evaluation of how different types of shear reinforcement affect the overall shear capacity of the beams. In this analysis, it is assumed that the concrete contribution to shear capacity remains constant and is equivalent to the capacity observed in the beam without stirrups (sample NS). The contribution of the stirrups is then calculated as the difference between the shear capacity of the respective beam sample and that of the beam without stirrups. This additional shear capacity provided by the stirrups is further normalized against the contribution of the steel stirrups in sample S4.

The efficiency of the stirrups, based on their cross-sectional area, is quantified using the following equation:

$$\left(\frac{V_s}{\text{shear reinf. ratio}}\right) \Big/ \left(\frac{(V_s)_{\text{S4}}}{(\text{shear reinf. ratio})_{\text{S4}}}\right) \tag{6.1}$$

where V_s denotes the contribution of the stirrups to the shear capacity for any beam, whether reinforced with steel or FRP stirrups, relative to the concrete-only shear capacity (as observed in beam sample NS). The term $(V_s)_{\text{S4}}$ represents the enhancement of shear capacity provided by the steel stirrups in beam sample S4 compared to the beam without stirrups (sample NS). The shear reinforcement ratio is taken from the values provided in Table 4.1.

In Section 3.2 the densities of the BFRP samples are specified as 1812 kg/m^3 for braided BFRP rods and 1848 kg/m^3 for laminated UD-strips. For steel stirrups, a density of ρ = 7850 kg/m^3 is used. To account for differences in material weight, the stirrup efficiency calculated from Equation (6.1) is adjusted by multiplying it by the ratio of the BFRP stirrup density (either braided rod-type or UD-laminate strip) to the steel stirrup density. The resulting values are presented in the last column of Table 6.1, offering a normalized comparison of stirrup efficiency by weight.

6.1.1. Relative strength and shear capacity

The NS beam, which does not include any shear reinforcement, serves as the baseline with a maximum load of 128.5 kN and a mid-span deflection of 5.24 mm. This beam has a shear capacity of 64.3 kN.

Table 6.1: Analysis of experimental beam test results

	Maximum load		Relative strength		Shear capacity			Relative stirrup efficiency	
Beam sample	Force F_u [kN]	Mid-span defl. [mm]	Max. load /128.5	Max. load /238.5	Total V [kN]	Added by stirrups V_s [kN]	Relative to steel stirrups V_s / 55.0	Normalized by stirrup area [-]	Normalized by stirrup weight [-]
NS	128.5	5.24	1.00	0.54	64.3	-	-	-	-
S4	238.5	6.66	1.86	1.00	119.3	55.0	1.00	1.00	1.00
B4	175.5	6.48	1.37	0.74	87.8	23.5	0.43	0.37	1.61
B8	213.2	8.49	1.66	0.89	106.6	42.4	0.77	0.34	1.45
UD4	168.0	7.02	1.31	0.70	84.0	19.8	0.36	0.42	1.79
UD8	183.0	8.85	1.42	0.77	91.5	27.3	0.50	0.29	1.24

In comparison, the S4 beam, which uses steel stirrups, demonstrates a significant improvement with a maximum load of 238.5 kN and a deflection of 6.66 mm. The relative strength of this beam is 1.86 times that of the NS beam, indicating the high effectiveness of steel stirrups. The total shear capacity for the S4 beam is 119.3 kN, with the stirrups contributing an additional 55.0 kN. This beam sets the reference for stirrup efficiency, with normalized values of 1.00 for both area and weight.

The beams with BFRP stirrups show varied performance. The B4 beam, which uses braided BFRP stirrups, has a maximum load of 175.5 kN and a deflection of 6.48 mm. Its relative strength is 1.37, and the total shear capacity is 87.8 kN, with 23.5 kN contributed by the stirrups. The B8 beam, with a higher quantity of braided BFRP stirrups, shows a maximum load of 213.2 kN and a deflection of 8.49 mm. This beam's relative strength is 1.66, and its total shear capacity is 106.6 kN, with 42.4 kN added by the stirrups.

The UD4 and UD8 beams, which utilize unidirectional laminated BFRP strip stirrups, show lower performance compared to the steel stirrup beam but still notable improvements over sample NS, which is the beam sample without stirrups. The UD4 beam has a maximum load of 168.0 kN and a deflection of 7.02 mm. Its relative strength is 1.31, and the total shear capacity is 84.0 kN, with 19.8 kN from the stirrups. The UD8 beam, with a maximum load of 183.0 kN and the highest deflection at 8.85 mm, has a relative strength of 1.42. Its total shear capacity is 91.5 kN, with the stirrups contributing 27.3 kN.

6.1.2. Stirrup efficiency

When examining stirrup efficiency normalized by stirrup area, the steel stirrups in the S4 beam outperform the basalt FRP stirrups in each beam. Beam UD4 ranks second, with a relative stirrup efficiency by area of 0.42 compared to the steel stirrups. Beams B4 and B8 follow, with similar relative stirrup efficiency by area values of 0.37 and 0.34, respectively. For beams UD4 and UD8, the relative efficiency for the laminated UD-stirrups shows significantly different values of 0.42 and 0.29, respectively.

When normalizing stirrup efficiency by weight, Table 6.1 shows that all beams with BFRP stirrups exhibit higher efficiency compared to steel stirrups. For instance, the B4 beam, despite its lower efficiency by area, demonstrates a high weight efficiency of 1.61. Similarly, the B8 beam shows a weight efficiency of 1.45. The UD4 and UD8 beams also exhibit significant weight efficiencies of 1.79 and 1.24, respectively. This higher efficiency by weight highlights the potential of BFRP stirrups in applications where weight reduction is critical.

6.1.3. Stirrup strain distribution and failure modes

General stirrup behaviour

For the beam with steel stirrups, S4, strain graphs for stirrups 1, 2, and 4 show that these stirrups were yielding when the peak load was reached. Unfortunately, there was no data for stirrup 3. However, DIC data indicates that the main diagonal crack crossing stirrup 3 significantly widens from the peak load onward. This suggests that stirrup 3 was also yielding. Once the stirrups yield, the beam cannot sustain additional loads because the stirrups have reached their load-bearing capacity. As the strain in the stirrups increases, shear cracks widen, and the concrete's internal mechanisms contributing to the total shear capacity begin to diminish.

In contrast, the behavior of basalt FRP stirrups differs significantly. The strain graphs indicate that the BFRP stirrups continue to elongate even after the peak load capacity of the beam is reached. Be-

cause the load behaviour of BFRP can be described as linear elastic, these stirrups continue to carry additional load as strain increases beyond the beam's peak shear capacity. However, despite this increased load-bearing by the BFRP stirrups, the overall shear capacity of the beam begins to decline after the peak load is reached. This decline can be attributed to the reduction in the effectiveness of the concrete's internal shear-resisting mechanisms, as described below:

- **Transfer of shear forces through the uncracked compression zone:** As the diagonal shear cracks extend to the top of the beam, the contribution from the uncracked compression zone is effectively eliminated.
- **Aggregate interlock:** The relatively low E-modulus of basalt FRP stirrups results in wider shear cracks, which reduces the aggregate interlock as the crack faces move further apart.
- **Dowel action:** The longitudinal reinforcement does not yield at the failure loads of the beams, suggesting it still contributes to the beam's capacity. However, horizontal cracks observed along the flexural reinforcement indicate that vertical cover may be insufficient, thereby reducing the dowel action contribution.

Relating Stirrup Strain to Uniaxial Tensile Strain

Subsequently, the strain at the location of rupture in the normative stirrups of the beam samples is related to the uniaxial tensile strength determined in Section 3.3. The braided stirrups had a failure strength f_u of 751 MPa and a rupture strain ε_u of 2.10%.

- **B4, Stirrup 3:** The recorded strain at the peak load capacity of the beam was approximately 12,500 µm/m, corresponding to 1.25% strain. Just before rupture, the strain was about 15,300 µm/m, or 1.53%. This translates to stresses of 447 MPa and 547 MPa, respectively, which are 60% and 73% of the uniaxial tensile strength.
- **B8, Stirrup 7:** At peak load, the strain in section B of stirrup 7 was approximately 6,500 µm/m. This correspond to a stress of 232 MPa, or 31% of the uniaxial tensile strength. Unfortunately, the strain data just before rupture is unavailable due to a sensor failure during the test, preventing a complete analysis of the stirrup's performance at the critical moment of failure.

For laminated strip stirrups, an ultimate stress f_u of 706 MPa and rupture strain ε_u = 1.86% is found in section 3.3. The following observations were made:

- **UD4, Stirrup 1:** The highest recorded strain at the beam's peak load was approximately 13,300 µm/m, corresponding to a strain of 1.33% or a stress level of 505 MPa, which corresponds to 72% of the uniaxial tensile strength. Although data immediately prior to rupture is missing, another stirrup in the same beam (Stirrup 3) exhibited a strain of approximately 16,000 µm/m at peak load, corresponding to 1.6% strain and a stress level of 607 MPa, which is 86% of the stirrup's uniaxial tensile capacity
- **UD8, Stirrup 3:** The strain recorded at the peak load capacity of the beam was approximately 6,500 µm/m, corresponding to a strain of 0.65% or a stress level of 247 MPa. Similar to the B8 stirrup, the strain data immediately before the stirrup's rupture is missing due to a compromised DFOS sensor, limiting the ability to fully assess the stirrup's performance under peak loading conditions.

Stirrup bond capacity

Further analysis and comparison of DFOS data with DIC data indicates that the peak strains are predominantly concentrated in the vertical legs of the stirrups, particularly where diagonal shear cracks intersect these sections. As illustrated in Figures 6.1a and 6.1b for the steel and BFRP strip stirrups, respectively, the relatively narrow distribution of these peak strains, combined with the comparatively low strain levels observed in the bottom sections of the stirrups, suggests effective bonding between the concrete and the stirrups. This strong bond facilitates efficient force transfer from the concrete to the stirrups, facilitating efficient interaction and force transfer between these components.

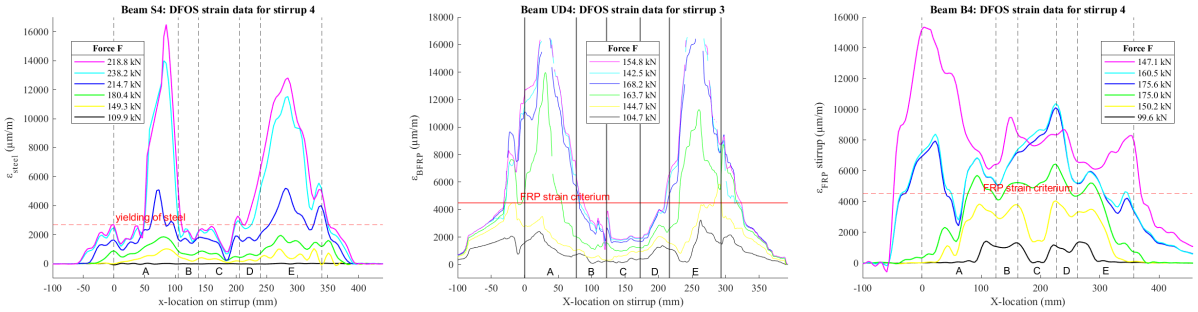

(a) S4 steel stirrup 4 **(b)** UD laminated BFRP stirrup 3 **(c)** B4 braided BFRP stirrup 4

Figure 6.1: Strain distribution for different stirrup materials

In contrast, the braided basalt FRP stirrups exhibit higher overall strain levels, particularly in the bottom vertical sections, indicating a lower bond strength between the BFRP and the concrete. An example for this is the strain data for beam sample B4, stirrup 4, which is shown in Figure 6.1c. Although literature suggests that braided FRP reinforcement bars typically offer enhanced bonding due to its enhanced surface roughness compared to other types of FRP reinforcement, the braided BFRP rebar in this study was coated with an additional layer of epoxy resin, resulting in a smoother surface finish. While reduced bond strength might initially appear to be a disadvantage, it can, in this context, be beneficial as it enables peak loads to be distributed across a larger area of the stirrup. This distribution reduces local peak stresses that might otherwise exceed the stirrup's maximum stress capacity, potentially leading to failure. Provided the BFRP stirrups are adequately anchored, this characteristic could improve their overall performance by mitigating the risk of premature failure.

To validate these observations and gain a deeper understanding of the bond behavior of BFRP stirrups, it is essential to conduct experimental testing, such as pull-out tests, to precisely assess their bond capacity. Such testing could confirm the observed lower bond strength and explore whether this characteristic can indeed be leveraged to enhance the structural performance of BFRP-reinforced concrete beams.

6.1.4. Conclusions

The experimental results highlight the superior performance of traditional steel stirrups in enhancing shear capacity and controlling crack widths. This effectiveness is crucial in preserving the concrete's internal shear transfer mechanisms and allowing for the full development of both the concrete and stirrups' contributions to overall shear capacity. Steel's higher modulus of elasticity (E-modulus), isotropic material properties, and yielding behavior are key factors in this advantage. The higher E-modulus enables better restraint of shear crack propagation, while the isotropic nature of steel ensures uniform stress distribution. Additionally, steel's ability to yield allows it to absorb and redistribute local peak stresses, preventing stress concentrations and enhancing the beam's structural integrity.

In contrast, BFRP stirrups, despite their lower efficiency properties compared to steel, offer a favorable performance-to-weight ratio that could result in greater efficiency when evaluated from an environmental cost perspective. BFRP's ability to achieve comparable structural performance at a reduced weight has the potential to lower overall material usage, thereby decreasing the environmental impact associated with the extraction, production, and transportation of raw materials. As a result, BFRP stirrups may represent a more sustainable alternative, aligning well with principles of environmentally conscious design. However, further analysis, specifically focusing on the Environmental Cost Indicator (ECI), is necessary to fully quantify and validate these potential environmental benefits.
Strain measurements during testing provided important insights into the behavior of steel and BFRP stirrups under load. In the S4 beam, steel stirrups reached their yield point at peak load, limiting the beam's ability to take on additional loads and leading to wider shear cracks, which in turn reduce the concrete's internal shear-resisting mechanisms. Conversely, BFRP stirrups, due to their approximate linear elastic behavior, continued to bear loads beyond the peak capacity, even as the concrete's shear resistance diminished. The strain distribution in the stirrups suggests efficient force transfer between steel stirrups and concrete, attributed to better bonding. Meanwhile, the potentially lower bond strength

of BFRP stirrups may help distribute peak stresses and prevent failure, provided they are adequately anchored.

6.2. Comparison of Analytical and Experimental Results

6.2.1. Control beams

For the evaluation of the shear capacity of control beams NS and S4, the design methodology prescribed by Eurocode 2 (NEN-EN 1992-1-1, 2011) was employed. The shear strength prediction for the beams without shear reinforcement, denoted as $V_{Rm,c}$, was adjusted based on the experimentally derived mean compressive cylinder strength f_{cm} for each respective batch. These updated shear capacity predictions are presented in the second column of Table 6.3.

Upon incorporating the true mean compressive strength of the concrete into the predictive model, the shear capacity for the control beam batch was recalculated as $V_{Rm,c}$ = 36.52 kN. Despite this adjustment, the predicted shear capacity remains significantly lower than the experimentally observed shear capacity for the NS beam sample, which was determined to be V_{exp} = 64.3 kN, as detailed in Chapter 5. This substantial discrepancy underscores the conservative nature of the Eurocode 2 approach, which, while ensuring structural safety, can lead to significant underestimations of actual shear capacity.

The shear capacity predictions for the beam with steel stirrups, sample S4, were similarly revisited in light of the experimental results. The S4 sample exhibited failure due to a normative shear crack extending directly from the loading point to the supports, excluding the steel support plates. This observed crack pattern necessitated an adjustment in the shear crack angle θ, changing it from the normative value of 21.8° used during the design phase to a more realistic value of 24°, which better reflects the actual behavior observed during testing.

With this revised shear crack angle, the shear capacity for the S4 beam was recalculated using the following equation:

$$V_{Rm,s} = \frac{A_{sw}}{s} \cdot z \cdot f_{ym} \cdot \cot(\theta) = \frac{100}{250} \cdot 124.6 \cdot 560 \cdot \cot(24^\circ) = 62.7\ kN \tag{6.2}$$

Despite this adjustment, the computed shear capacity of 62.7 kN remains significantly lower than the experimentally determined shear capacity of 119.3 kN. Interestingly, this recalculated capacity aligns closely with the contribution attributed to the steel stirrups in beam sample S4 when compared to the shear capacity of the concrete alone in beam sample NS (V_s = 55.0 kN for beam sample S4, as shown in Table 6.1). This suggests that the formula primarily captures the capacity provided by the stirrups. The significant discrepancy, with the predicted capacity being roughly half of the observed value, further underscores the inherent conservatism embedded in the Eurocode 2 design methodology. This conservative approach is particularly evident in its tendency to overlook the concrete's contribution to the overall shear capacity of a reinforced concrete beam, thereby potentially underestimating the beam's actual performance. The Eurocode 2 method, while prioritizing safety, may thus not fully account for the interactive role between concrete and reinforcement in resisting shear forces.

One of the critical conservative assumptions within Eurocode 2 relates to the contribution of concrete to the overall shear capacity of the beam. The code employs a simplified, empirical methodology that does not fully capture the complex shear behavior of concrete beams. A key aspect of this simplification is the limitation imposed on the longitudinal reinforcement ratio, which is capped at a maximum of 2%. This restriction, while intended to ensure conservative design, can lead to an underestimation of the actual shear capacity, especially in cases where the longitudinal tensile reinforcement ratio exceeds this prescribed limit. Other design approaches that allow for higher permissible reinforcement ratios may provide predictions that more accurately reflect the true shear capacity of the beam.

To further illustrate this effect, the shear capacity of the beam was recalculated using the actual longitudinal tensile reinforcement ratio, as follows:

$$\rho_l = \frac{A_l}{b_w d} = \frac{982}{150 \cdot 157.5} = 0.0416\ \text{[-]} \tag{6.3}$$

$$k = \min\left[1 + \sqrt{\frac{200}{d}}\ ;\ 2.0\right] = \min\left[1 + \sqrt{\frac{200}{157.5}}\ ;\ 2.0\right] = \min\left[2.13\ ;\ 2.0\right] = 2.0 \tag{6.4}$$

$$\begin{aligned} V_{Rm,c} &= \left[C_{Rd,c} \cdot k \cdot (100 \cdot \rho_l \cdot f_{cm})^{1/3}\right] b_w d \\ &= \left[0.18 \cdot 2.0 \cdot (100 \cdot 0.0416 \cdot 39.6)^{1/3}\right] 150 \cdot 157.5 = 46.6 \text{ kN} \end{aligned} \tag{6.5}$$

This recalculation, which accounts for the actual reinforcement ratio, yields a higher shear capacity than initially predicted. However, even this adjusted prediction may still fall short of the actual performance observed in the experimental tests due to the conservative assumptions of the Eurocode 2.

Another significant limitation within the Eurocode 2 framework is its approach to the contribution of stirrups in the shear design. When stirrups are present, the code primarily considers their contribution to shear strength, effectively neglecting the potential contribution of the concrete itself. This assumption, while conservative and aimed at ensuring safety, may lead to further underestimation of the beam's shear capacity. By overlooking the synergistic effects of concrete and shear reinforcement working together, the code potentially misrepresents the actual behavior of the structure under load. The combined effect of these conservative assumptions is a design methodology that prioritizes safety but may result in significant discrepancies between predicted and observed structural performance.

6.2.2. Other methods to predict the shear capacity of the control beams

Given the conservative estimates provided by the Eurocode 2 formulas, alternative methods were employed to obtain a more accurate prediction of the shear capacity of the control beams. These methods are discussed in the following subsections.

Fixed strut approach

Unlike the Eurocode 2 approach, the method proposed by fib Model Code 2010 (2013) permits the additive contribution of both concrete and stirrups to shear capacity. Similarly, standards such as ACI 318-14 (2014), NEN 6720 (2005), and NEN 8702 (2017) also allow for this additive effect but only when employing a fixed strut approach that restricts the stirrups' contribution to a shear crack angle of $\theta = 45°$.

When applying this approach to calculate the shear strength of the control beams, the shear capacity of the beam without stirrups remains unchanged, as it is independent of the concrete strut angle θ. However, for the concrete beam with steel stirrups, the shear capacity is determined by summing the contributions from both the concrete and the stirrups, as expressed in the following equation:

$$V = V_{Rm,c} + V_{Rm,s} \tag{6.6}$$

where $V_{Rm,c}$ is determined using the average concrete compressive stress for beam batch NS+S4 (f_{cm} = 39.6 MPa) using EC2 formula's, and $V_{Rm,s}$ is determined in the same way as in EC2. The stirrups contribution is also calculated in the same way as described in EC2, but now with concrete strut angle θ = 45°:

$$V_{Rm,s} = \frac{A_{sw}}{s} \cdot z \cdot f_{ym} \cdot \cot(\theta) = \frac{100}{250} \cdot 124.6 \cdot 560 \cdot \cot(45°) = 27.91 \text{ kN} \tag{6.7}$$

Combining these equations gives

$$V_{Rm,tot} = V_{Rm,c} + V_{Rm,s} = 36.52 + 27.91 = 64.44 \text{ kN} \tag{6.8}$$

General Shear Design Method

The General Shear Design Method (GSDM), proposed by Cladera and Mari (2004a), offers several unique features that distinguish it from the design equations provided in Eurocode 2 (EC2) (NEN-EN 1992-1-1, 2011) and demonstrate its superior predictive capability for the shear strength of concrete beams with and without shear reinforcement.

One of the key aspects that sets this method apart is its foundation in extensive empirical research and the application of artificial neural networks (ANNs) to model and predict the shear strength of reinforced concrete beams. This method allows for a more accurate representation of the complex interactions between various parameters affecting shear strength, such as the amount and arrangement of shear reinforcement, the concrete compressive strength, the beam's size, and the longitudinal reinforcement. By utilizing ANNs, it can capture non-linear relationships and interactions between these parameters, which traditional methods like those in EC2 might oversimplify or overlook.

This method provides a holistic approach by integrating different shear transfer mechanisms within a single cohesive framework. It considers the contributions of both concrete and steel to the shear capacity, with explicit consideration of factors like aggregate interlock, dowel action, and the truss model for shear transfer. This comprehensive approach enables the GSDM to more accurately reflect the physical behavior of concrete beams under shear forces, particularly when compared to EC2, which might not fully account for all these mechanisms simultaneously.

Another notable advantage of the GSDM is its adaptability to different types of beams, including those made of high-strength concrete and beams with varying amounts of shear reinforcement. The method's ability to adjust for size effects and non-linear responses in highly reinforced beams ensures that it remains reliable across a broad range of conditions. This versatility contrasts with the more rigid and sometimes unconservative predictions provided by EC2, especially in cases involving high-strength concrete or beams with significant shear reinforcement.

The validation of the GSDM through comparisons with a large database of experimental results further underscores its reliability. The method has been shown to predict shear strength with better accuracy and lower coefficients of variation compared to EC2. According to the authors, this method achieved a coefficient of variation (CoV) of 18.77 % for the V_{fail}/V_{pred} ratio, which is significantly lower than the 40.29% observed for EC2, which indicates more consistent and dependable predictions.

In the following part of this subsection, the General Shear Design Method is used to predict the shear strength of reinforced concrete beam samples with(out) shear reinforcement (NS and S4). The shear strength of reinforced concrete beams without web reinforcement is given by the following equation:

$$V_c = \left[0.13 \cdot \xi (100 \cdot \rho_l)^{1/2} \cdot f_c^{1/3}\right] b_w \cdot d \tag{6.9}$$

where size effect ξ is determined as follows:

$$\begin{aligned} \xi &= \min\left[\left(\frac{135000 \cdot f_{cm}^{-1.1}}{s_x}\right)^{0.25\left(1+\frac{f_{cm}-25}{75}\right)} ;\ 2.75\right] \\ &= \min\left[\left(\frac{135000 \cdot 39.6^{-1.1}}{142}\right)^{0.25\left(1+\frac{39.6-25}{75}\right)} ;\ 2.75\right] \\ &= \min\left[2.54 ;\ 2.75\right] = 2.54 \end{aligned} \tag{6.10}$$

and s_x is the minimum of the internal lever arm (estimated to be 0.9·d) or the vertical distance between longitudinal distributed reinforcement. In this case, the effective height is estimated by d_v = 0.9·157.5 = 142 mm and the vertical center-to-center distance between the steel tensile and compressive longitudinal rebar is $d - d_2$ = 157.5 - 36 = 121.5 mm, thus this last factor is governing: s_x = 121.5 mm. For the concrete compressive strength the result from the uniaxial compressive cube test is taken for the control beam batch (NS+S4): f_{cm} = 39.6 MPa.

$$\begin{aligned} \rho_l &= \min\left[\frac{A_l}{b_w d} ;\ 0.02\left(1+\frac{f_c}{100}\right)\right] = \min\left[\frac{982}{150 \cdot 157.5} ;\ 0.02\left(1+\frac{39.6}{100}\right)\right] \\ &= \min[0.0416 ;\ 0.0299] = 0.0299\ [-] \end{aligned} \tag{6.11}$$

Substituting Equations (6.10) and (6.11) into Equation (6.9) gives:

$$V_c = \left[0.13 \cdot 2.54(100 \cdot 0.0299)^{1/2} \cdot 39.6^{1/3}\right] 150 \cdot 157.5 = 56.9 \text{ kN} \tag{6.12}$$

For predicting the shear capacity of the reinforced concrete steel stirrups in the beam with steel reinforcement, Cladera and Mari (2004b) adds an extra term that takes into account the stirrups' influence on the shear friction. This General Shear Design Method for beams with stirrups adds up the concrete and stirrups' contribution to the total shear capacity of the beams:

$$V = V_c + V_s \tag{6.13}$$

The concrete's contribution for a beam with shear reinforcement stirrups is determined as follows

$$V_c = \left[0.17 \cdot \xi(100 \cdot \rho_l)^{1/2} f_c^{0.2} \cdot \tau^{1/3}\right] b_w d \tag{6.14}$$

where s_x is, again, the minimum of the internal lever arm z or the vertical distance between longitudinal distributed reinforcement. Also here, s_x = d - d2 = 121.5 mm. This was previously determined in Equation (4.17). Furthermore, f_c is the concrete compressive strength. In section 5.2 it was found that the average concrete compressive strength (f_{cm}) for the control beam batch was equal to 49.5 MPa.

$$\xi = \min\left[1 + \sqrt{\frac{200}{s_x}}\ ;\ 2.75\right] = \min\left[1 + \sqrt{\frac{200}{121.6}}\ ;\ 2.75\right] = \min\left[2.28\ ;\ 2.75\right] = 2.27 \tag{6.15}$$

The longitudinal reinforcement ratio and used in this method is determined through the following equations:

$$\rho_l = \min\left[\frac{A_l}{b_w d}\ ;\ 0.04\right] = \min\left[\frac{982}{150 \cdot 157.5}\ ;\ 0.04\right] = \min\left[0.0416\ ;\ 0.04\right] = 0.04\ [-] \tag{6.16}$$

$$\tau = \min\left[\frac{V_d}{b_w z}\ ;\ 3\right] = \min\left[\frac{119.3 \cdot 10^3}{150 \cdot 124.6}\ ;\ 3\right] = \min\left[6.38\ ;\ 3\right] = 3 \text{ MPa} \tag{6.17}$$

where V is the designing (factored) shear strength, which is set equal to the experimentally found shear capacity for the beam with steel stirrups ($V_{exp,S4}$ = 119.3 kN).

Substituting Equations (6.15), (6.16) and 6.17 into Equation (6.14) results in the following value for the concrete contribution to the total shear capacity:

$$V_c = \left[0.17 \cdot 2.28(100 \cdot 0.04)^{1/2}\ 39.6^{0.2}\ 3^{1/3}\right] 150 \cdot 157.5 = 62.5 \text{ kN} \tag{6.18}$$

Next, the stirrups' contribution to the total shear capacity of the beam is determined. ε_x is the longitudinal strain in the web. In this method, the longitudinal strain in the web is a conservative estimate of the actual strain: it assumes that the strain in the web is half that of the tension reinforcement, with a maximum longitudinal strain of 0.002 [-] in the reinforcement. It is illustrated in Figure 6.2, considered in 1/1000 and determined through the following equation:

$$\begin{aligned} \varepsilon_x \ &\approx\ \min\left[0.5\frac{\frac{M}{z} + V}{E_s A_l} \cdot 1000\ ;\ 1\right] = \min\left[\frac{\frac{41.7 \cdot 10^6}{124.6} + 119.3 \cdot 10^3}{200000 \cdot 982} \cdot 1000\ ;\ 1\right] \\ &= \min\left[1.16\ ;\ 1\right] = 1 \end{aligned} \tag{6.19}$$

in which M and V are the (factored) moment and shear strength. This value is determined on the basis of the maximum load at mid-span that the beam with steel stirrups (sample S4) could withstand: V = $F_u/2$ = $238.5/2$ = 119.3 kN and M = $\frac{FL}{4}$ = $\frac{238.5 \cdot 1}{4}$ = 59.6 kNm in the middle of the beam. At the position of the normative stirrups that are closest to either side of the middle of the beam, the bending moment M is $\frac{350}{500} \cdot 59.6$ = 41.7 kNm.

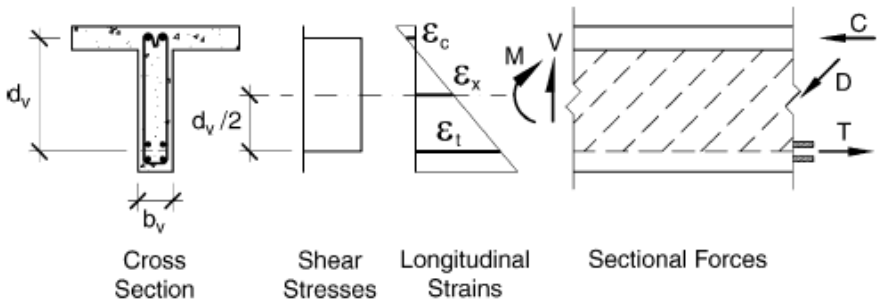

Figure 6.2: Longitudinal strain in the web (Collins, 2001)

The ratio between the concrete compressive strength and the mean shear stress is calculated as follows:

$$\frac{\tau}{f_{cm}} = \frac{3}{49.5} = 0.061 \geq 0.05 \tag{6.20}$$

Next, the angle of the compression struts θ is determined:

$$\begin{aligned} \theta &= \min\left[20 + 15\varepsilon_x + 45\frac{\tau}{f_c}\ ;\ 45^\circ\right] = \min\left[20 + 15 \cdot 1 + 45 \cdot 0.061\ ;\ 45^\circ\right] \\ &= \min\left[37.7^\circ\ ;\ 45^\circ\right] = 37.7^\circ \end{aligned} \tag{6.21}$$

Subsequently, the stirrups' contribution to the total shear capacity is determined through:

$$V_s = \frac{A_w}{s} \cdot z \cdot f_{ym} \cdot \cot(\theta) = \frac{100}{250} \cdot 124.6 \cdot 560 \cdot \cot(37.7^\circ) = 36.1 \text{ kN} \tag{6.22}$$

Substituting Equations (6.18) and (6.22) into Equation (6.13) results in a predicted total shear force for the beam sample "S4":

$$V = V_c + V_s = 57.4 + 36.1 = 93.2 \text{ kN} \tag{6.23}$$

Critical Shear Displacement Method

This paragraph presents the Critical Shear Displacement Method, as described by Y. Yang et al. (2016) and Y. Yang et al. (2017). The core concept is the critical shear displacement (Δ_{cr}), defined as the shear displacement in a flexural crack that triggers the opening of a critical inclined crack, leading to shear failure. This method, based on experimental observations, considers the contributions of aggregate interlock and dowel action in shear transfer mechanisms across the cracked section. Using a shear stress-displacement relationship, it quantifies these mechanisms and incorporates them into the overall shear capacity evaluation, using a simplified crack profile for practical calculation.

In this method, the total shear force (V) is the sum of the shear force in the compression zone (V_c), dowel action (V_d), and aggregate interlock (V_{ai}). Since direct measurement of Δ_{cr} is challenging, back-analysis is used from experimental results to derive generalized values for different beam configurations.

Unlike traditional stress or strain-based criteria, this method uses a displacement-based criterion (Δ_{cr}), offering a new perspective on shear failure mechanisms. It provides a realistic physical background by linking shear failure to critical shear displacement, reflecting the actual behavior of cracked concrete beams more accurately. By integrating multiple shear transfer mechanisms into a single framework, the method offers a holistic approach to shear capacity assessment. Back-analysis ensures practical applicability and reliability across different beam configurations, making it suitable for design practice. This method shows better accuracy in predicting shear capacity compared to existing empirical models, as demonstrated through experimental results.

The flowchart for using this method is shown in Figure 6.3.

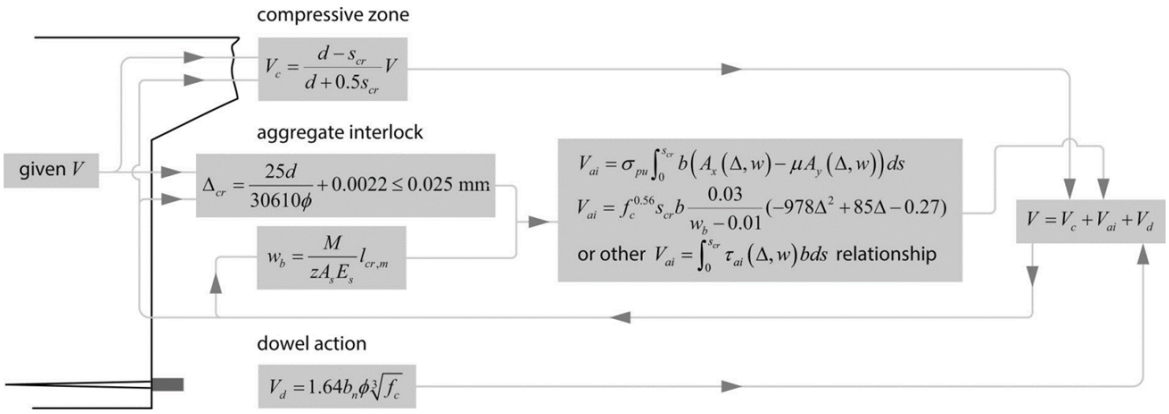

Figure 6.3: Flowchart for CSDM (Y. Yang et al., 2016)

The authors of this method note that a rough estimate of the concrete elastic modulus is adequate, as it only impacts the crack height calculation. According to Table 3.1 in EC2, the mean elastic modulus (E_{cm}) for concrete class C30/37 is 33 GPa, which is the value used here.

A MATLAB-script, which can be found in Appenix D, is used to evaluate this method. The outcome is a shear capacity of 53.9 kN for the control beam without shear reinforcement.

Conclusions

Table 6.2 provides an overview of the shear capacity predictions for the control beams NS (without stirrups) and S4 (with steel stirrups) using various analytical methods. It also presents the corresponding experimental shear capacities, along with the relative ratios of predicted to experimental values. This comparative analysis highlights the accuracy and conservatism of different predictive approaches.

Table 6.2: Overview of shear capacity predictions and their relative capacity compared to the experimental value

	Experimental results	**EC2 approach** θ = 24°		**Fixed strut approach** θ = 45°		**General Shear Design Method**		**Critical Shear Displacement Method**	
Beam	V_{exp} [kN]	V [kN]	Relative	V [kN]	Relative	V [kN]	Relative	V [kN]	Relative
NS	64.3	36.5	0.57	36.5	0.57	56.9	0.88	53.9	0.84
S4	119.3	62.7	0.53*	64.4	0.54**	93.2	0.78	-	-

This table offers a detailed comparison of the predicted shear capacities using various approaches and their alignment with the experimentally observed capacities. The following key observations and conclusions can be drawn from this analysis:

- **Conservatism of Eurocode 2:** The shear capacity predictions derived from NEN-EN 1992-1-1, 2011 are notably conservative. For the NS beam, the predicted capacity of 36.5 kN corresponds to only 57% of the experimental value, while for the S4 beam, the predicted shear capacity of 62.7 kN represents just 53% of the experimental result. This conservatism is inherent to the EC2 design philosophy, which emphasizes safety by accounting for various uncertainties. While this approach reduces the risk of structural failure, it may lead to overdesign, potentially resulting in the inefficient use of materials and increased construction costs.
- **Fixed Strut Angle Approach:** For the S4 beam, the fixed strut angle approach, which considers the combined contributions of concrete and steel with an assumed concrete compressive strut angle of 45°, results in a predicted shear capacity of 64.4 kN. This value corresponds to 54% of the experimental capacity, which, while slightly better than the variable strut angle approach of EC2 that neglects the concrete contribution, still indicates a conservative prediction. This suggests that the variable strut method, although marginally less conservative, may not fully capture the complex interactions between concrete and shear reinforcement in real-world conditions.
- **General Shear Design Method:** The General Shear Design Method proves to be more effective in predicting shear capacities that closely match the experimental values. For the NS beam, this

method predicts a shear capacity of 56.9 kN, achieving a relative ratio of 0.88 compared to the experimental result. For the S4 beam, the predicted capacity is 93.2 kN, corresponding to 78% of the experimental value. These results indicate that the General Shear Design Method offers a more accurate reflection of the actual behavior of concrete structures under shear loads, making it a preferable alternative to the more conservative approaches.

- **Critical Shear Displacement Method:** The Critical Shear Displacement Method also demonstrates a relatively close alignment with experimental data, particularly for the NS beam. It predicts a shear capacity of 53.9 kN, resulting in a relative ratio of 0.84. This method, which considers the displacement behavior of the structure, provides a reasonable estimate of the shear capacity, though it still falls slightly short of the experimental value.

6.2.3. Beams with BFRP stirrups

This subsection evaluates how well the total shear capacity of the beams with BFRP stirrups can be predicted using experimental results. During the design phase of the beams, upper and lower bounds for shear capacity were established to ensure adequate longitudinal reinforcement for sufficient flexural resistance. This flexural resistance was necessary to ensure that the beams would fail in shear rather than bending. The lower bound predicted value for shear capacity $V_{Rm,s,low}$ is determined using the increased strain limit ε = 0.45% from literature (Guadagnini et al., 2003), while the upper bound limit $V_{Rm,s,up}$ assumes that the stirrups can be loaded up to the uniaxial tensile stress of the corresponding BFRP material that was determined in Section 3.3.

The shear capacity of beams with basalt FRP shear reinforcement is predicted using a strain criterion of 0.45%, as proposed by Guadagnini et al. (2003). The authors recommend a more conservative, but simplified, fixed strut angle approach with θ = 45° when calculating the shear resistance of RC beams with FRP shear reinforcement. The additive nature of the shear resistance offered by concrete and shear reinforcement is maintained.

The design equations assume that shear force is evenly distributed across all stirrups, but in practice, this is not the case. Differences between DFOS strain graphs for the same beam, as observed in Section 5.1, show that stirrups in the middle of the beam are generally more heavily loaded, often at the top where the decisive shear crack crosses the bracket.

Table 6.3 presents the predicted shear capacities for a concrete beam without shear reinforcement $(V_{Rm,c})$, as well as for stirrups $(V_{Rm,s})$ with compression strut angles of θ of 24° and θ = 45°. Additionally, the table provides the summation of predicted concrete and stirrup contributions for these two strut angles. These values are compared to the experimentally derived shear capacity of the beams, and to the stirrup contribution to shear capacity compared to a beam without stirrups.

Table 6.3: Overview of predicted and experimental shear capacity

	Predicted shear capacity							**Experimental shear capacity**	
		Shear crack angle θ = 24°			Shear crack angle θ = 45°			Total shear capacity	Added stirrup shear capacity
	EC2	Strain	Strength	Strain	Strain	Strength	Strain		
	$V_{Rm,c}$	$V_{Rm,s,low}$	$V_{Rm,s,up}$	$V_{Rm,c}$ +	$V_{Rm,s,low}$	$V_{Rm,s,up}$	$V_{Rm,c}$ +	V_{exp}	$V_{exp,s}$
Beam	[kN]	[kN]	[kN]	$V_{Rm,s,low}$ [kN]	[kN]	[kN]	$V_{Rm,s,low}$ [kN]	[kN]	[kN]
NS	36.5	-	-	36.5	-	-	36.5	64.3	-
S4	36.5	-	62.7	62.7*	-	28.1	64.6**	119.3	55.0
B4	36.0	23.6	97.4	59.6	10.5	43.4	46.5	87.8	23.5
B8	36.0	47.2	194.8	83.2	21.0	86.7	57.0	106.6	42.3
UD4	35.6	18.1	68.2	53.8	8.1	30.4	43.7	84.0	19.7
UD8	35.6	36.3	136.4	71.9	16.2	60.7	51.8	91.5	27.2

*) Based on 2(NEN-EN 1992-1-1, 2011) variable strut angle approach, neglecting concrete contributing: V_{total} = $V_{stirrups}(\theta = 24°)$
**) Based on ACI 318-14 (2014), NEN 8702 (2017) and NEN 6720 (2005) fixed strut angle approach: V_{total} = $V_{concrete}$ + $V_{stirrups}(\theta = 45°)$

Table 6.4 presents the relative predicted results from Table 6.3. These results are shown as ratios of the predicted shear capacity to the total experimental shear capacity and the shear capacity added by the stirrups. Additionally, a new column includes the actual shear capacity of the beam without stirrups $(V_{exp,c})$ summed with the predicted added shear capacity of the stirrups $(V_{Rm,s,low})$.

For beam S4, the concrete contribution is neglected for $\theta = 24°$ to align with the EC2 design approach. For $\theta = 45°$, however, the concrete and stirrup contributions are summed to represent the fixed strut approach from fib Model Code 2010 (2013), NEN 8702 (2017) and NEN 6720 (2005).

Table 6.4: Relative predicted and experimental shear capacity values

	Relative predicted to experimental shear capacity					
	Shear crack angle θ = 24°			Shear crack angle θ = 45°		
Beam	($V_{Rm,c}$ + $V_{Rm,s,low}$) / V_{exp} [-]	$V_{Rm,s,low}$ / $V_{exp,s}$ [-]	($V_{exp,NS}$ + $V_{Rm,s,low}$) / V_{exp} [-]	($V_{Rm,c}$ + $V_{Rm,s,low}$) / V_{exp} [-]	$V_{Rm,s,low}$ / $V_{exp,s}$ [-]	($V_{exp,NS}$ + $V_{Rm,s,low}$) / V_{exp} [-]
B4	0.68	1.00	1.00	0.53	0.45	0.85
B8	0.78	1.12	1.05	0.53	0.50	0.80
UD4	0.64	0.92	0.98	0.52	0.41	0.86
UD8	0.79	1.33	1.10	0.57	0.59	0.88

Evaluation for θ = 24°

Table 6.4 shows that for θ = 24°, the summation of the predicted contributions from concrete and stirrups for the beams with BFRP stirrups results in a relative shear capacity between 0.64 and 0.79 of the experimental shear capacity. These relatively low values result from the conservative estimation of concrete shear capacity from EC2, which significantly underestimates the shear capacity of the concrete in the beam without stirrups.

For the added shear capacity by the basalt FRP stirrups, the relative predictions range from 0.92 to 1.33 of the experimental values. For beam B4, this value is 1.00, indicating that the predicted added shear capacity for the braided basalt stirrups is equal to the experimental value. Beam B8's predicted added shear capacity by the stirrups overestimates the actual capacity by 12%, while beam UD4's prediction underestimates it by 8%. For beam UD8, the predictions overestimated the actual stirrups' contribution by 33%.

Summing the experimental shear capacity of the beam without stirrups ($V_{exp,NS}$ = 64.3 kN for beam sample NS) with the predicted stirrup contribution results in relative shear capacity predictions between 0.98 to 1.10 compared to the experimental shear capacity. This method is somewhat accurate but requires prior knowledge of the actual shear capacity of the beam without stirrups, which is impractical for design purposes.

In the third column for θ = 24°, the experimental shear capacity of the beam without stirrups, NS, is summed with the predicted stirrup contribution. This results in relative shear capacity predictions between 0.98 to 1.10 compared to the shear capacity observed in the experiments. This suggests that this method is somewhat accurate in predicting the shear capacity of a beam with basalt stirrups. However, the actual shear capacity of the beam without stirrups is not known beforehand, which makes this difficult to apply in practice.

An alternative approach uses the General Shear Design Method (GSDM) for predicting the concrete contribution and the strain criterion of ε = 0.45 % and the respective modulus of elasticity for the stirrups' contribution with strut angle θ = 24°. This equation then becomes:

$$\begin{aligned} V_{Total} = V_{Rm,c} + V_{Rm,s,low} &= V_{Rm,c,\text{GSDM}} + \frac{A_{\text{FRP},w}}{s} \cdot z \cdot \varepsilon_{\text{FRP}} \cdot E_{\text{FRP}} \cdot \cot(\theta) \\ &= 56.9\ [\text{kN}] + \frac{A_{\text{FRP},w}}{s} \cdot z \cdot 0.0045 \cdot E_{\text{FRP}} \cdot \cot(24°) \end{aligned} \tag{6.24}$$

For the E-modulus, the respective average result from the uniaxial tensile testing is used. The results for this approach for all beam samples are displayed in Table 6.5. This approach is fairly accurate for predicting the shear capacity of concrete beams reinforced with basalt stirrups, because it results in relative values of 0.89 to 1.02 compared with the experimental outcomes for the shear capacity.

Table 6.5: Results for shear capacity: GSDM + strain approach

Relative pred. vs exp. shear capacity		
Beam sample	θ = 24°	θ = 45°
B4	0.92	0.77
B8	0.98	0.73
UD4	0.89	0.77
UD8	1.02	0.88

Evaluation for θ = 45°
The right columns of Table 6.4 present the relative predicted to experimental shear capacities for θ = 45°. The summation of the predicted concrete and stirrup contributions with this crack angle range from 0.52 to 0.57 for the beams with basalt FRP stirrups, indicating that the predicted values underestimate the experimental values by approximately half. The predicted stirrups' contribution to the shear capacity ranges from 0.41 to 0.59, demonstrating similar behavior. However, summing the experimental shear capacity of the beam without stirrups, $V_{exp,NS}$ = 64.3 kN, with the predicted stirrups' contribution results in relative predicted to experimental values ranging from 0.80 to 0.88. This approach is more accurate but still somewhat conservative.

This method is, again, difficult for practical application because the shear strength of the beam without stirrups is only known after experimental testing. Using GSDM for predicting the concrete contribution and θ = 45° for the stirrups' contribution will yield more conservative, yet safe values for predicting the total shear capacity for the beams with basalt FRP stirrups in this research: 0.77, 0.73, 0.77 and 0.80 compared to the experiments for respective beams B4, B8, UD4 and UD8, as can be seen in the third column of Table 6.5.

6.2.4. Conclusions

The experimental results for the control beams (NS and S4) underscore substantial discrepancies between the predicted shear capacities based on Eurocode 2 (EC2) and the empirically determined values. The predicted shear strength for the beam devoid of shear reinforcement (NS) was markedly lower than the experimental value, signifying the conservative nature of EC2's assumptions. Likewise, the predicted shear capacity for the beam with steel stirrups (S4) was approximately half of the experimentally observed value, further highlighting the conservative approach inherent in EC2's methodology.

Alternative methods for predicting shear capacity, including the variable strut approach and the General Shear Design Method (GSDM), yielded predictions that more closely approximated the experimental results. The fixed strut approach, which accounts for the additive contributions of concrete and stirrups, demonstrated improved, albeit still conservative, predictions. The GSDM, which integrates empirical research and artificial neural networks, generates predictions that were more aligned with the experimental data.

For beams reinforced with basalt FRP stirrups, the study revealed that utilizing uniaxial tensile strength to ascertain the shear contribution of the stirrups is not valid. The shear capacity of the beam reached its peak load before the stirrups attained their uniaxial tensile stresses. This phenomenon is attributed to the degradation of other shear mechanisms within the concrete, worsened by the wide shear cracks induced by the low stiffness of the BFRP material. Conversely, the combined shear resistance approach, which incorporates the concrete contribution using GSDM and the stirrup contributions with a strain criterion of ε = 0.0045 and a strut angle of θ = 24°, provided a more accurate prediction of the shear capacity, achieving 89-102% of the experimental values. A more conservative approach would be to use θ = 45° instead of 24°, as this method results in 73-80% of the actual shear capacity derived from the experiments.

6.3. Discussion

Assumption of a constant concrete contribution to the total shear capacity

In the final analysis of the shear capacity of the beam samples, assuming a constant contribution from the concrete's internal mechanisms poses a significant risk, as it neglects its variability due to changes in crack width. The interaction between concrete and stirrups is complex, and this simplification can result in inaccurate predictions of the actual shear performance of reinforced concrete beams.

The concrete's contribution to shear resistance is strongly influenced by the width of shear cracks, which is, in turn, affected by the presence and configuration of stirrups. The inclusion of stirrups can lead to wider cracks because they control crack propagation; however, this increased crack width can reduce the effectiveness of the concrete's shear-resisting mechanisms, such as aggregate interlock and dowel action. Consequently, the concrete's shear resistance is not constant but varies with crack width, which can differ significantly between beams with varying numbers and arrangements of stirrups. This variability is further amplified when additional stirrups are introduced, as the resulting wider cracks may further diminish the concrete's contribution to shear resistance. Thus, assuming a constant concrete contribution across beams with different stirrup configurations oversimplifies the situation, potentially leading to an inaccurate understanding of the structure's behavior under shear loads.

A more thorough analysis of shear cracks is necessary to accurately assess the shear capacity and the interaction between concrete and stirrups. This analysis should consider the dynamic relationship between crack width, concrete degradation, and the load-carrying capacity of stirrups. Such an approach would enhance the understanding of how varying crack widths affect the overall shear capacity, enabling more precise predictions.

Variation in stirrup corner radii

The discrepancies observed in the test results can be attributed to several factors, underscoring the inherent complexity and variability of experimental setups. A significant factor contributing to these discrepancies is the variation in corner radii of the stirrups used in the experiments. Specifically, the steel stirrups featured a corner radius of R25, the braided BFRP stirrups had a radius of R16, and the laminated BFRP strips were designed with a radius of R32. These differences in corner radii likely influenced the degree of fibre kinking, which in turn affected the relative corner strengths of the stirrups compared to their uniaxial strength. The variation in corner radii also had implications for the positioning of the longitudinal reinforcement. Theoretical considerations suggest that the closer the reinforcement is positioned to the surface, the higher the risk of concrete splitting, thereby increasing the stress imposed on the stirrups. Further analysis is necessary to determine whether this phenomenon occurred in the tests and to quantify its impact on the results.

Eccentric loading of beam sample B4

Furthermore, it is possible that beam B4 was subjected to torsional forces, likely resulting from observed eccentric loading, which could have caused an uneven distribution of stress across the stirrups. As depicted in Figure 6.4, the interaction of shear and torsional forces may have led to increased stresses on one side of the stirrups, potentially contributing to the failure observed on the side where these forces were combined. Although the stirrups in beam B4 generally demonstrated satisfactory performance and a preliminary analysis of the DIC and DFOS data indicates that significant torsional action may not have occurred, this observation highlights the critical importance of ensuring symmetrical loading conditions during testing to avoid unintended stress concentrations.

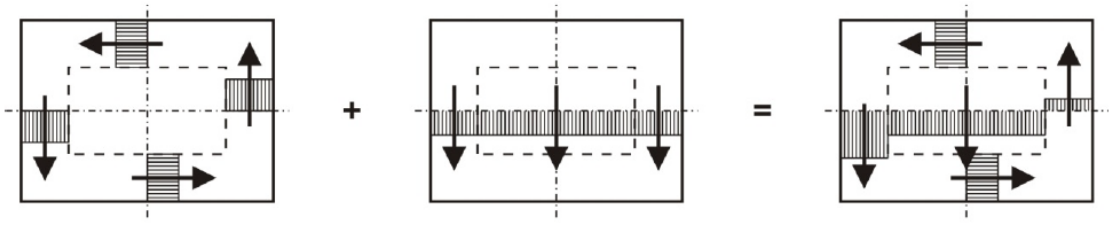

Figure 6.4: Combination of shear and torsion for beam sample B4, stirrup no. 3.

Out-of-plane wrinkles in strip stirrups

The efficiency of the braided BFRP stirrups demonstrates good consistency across both beams, with values of 0.37 and 0.34. However, there is noticeable variability in the efficiency of the laminated BFRP UD-strips, which recorded values of 0.42 and 0.29, respectively. This variation may be influenced by the presence of out-of-plane wrinkles in the strips, particularly in the corner sections. These wrinkles, which are introduced during the production process, are known to potentially affect the structural integrity and tensile capacity of composite materials. Examination of the fracture locations in both beams reinforced with BFRP strip stirrups indicates that strip stirrup ruptures occured at these defects. This suggests that these production-related imperfections could have played a role in the observed differences in performance.

Mitigating these production errors is essential to ensure the consistent quality and performance of BFRP stirrups. One promising approach to address these issues is the adoption of filament winding, a manufacturing process that allows for the precise and controlled winding of resin-impregnated fibres around a rotating mandrel. This production process is illustrated in Figure 6.5. This method is particularly effective in producing stirrups with uniform, defect-free surfaces. Achieving such surface uniformity is critical, as it directly influences the reliability and load-bearing capacity of the stirrups, significantly enhancing their structural integrity and durability.

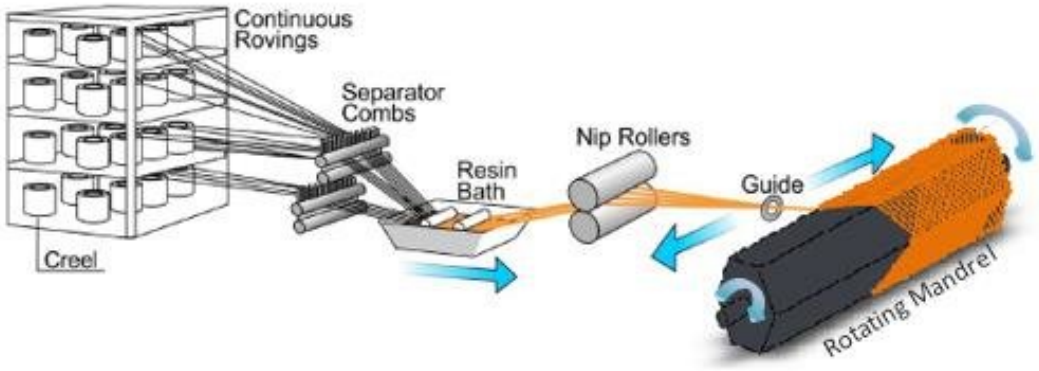

Figure 6.5: Filament winding (Jamaluddin et al., 2018)

In addition to addressing production defects, filament winding also offers the potential benefit of increasing the fibre volume fraction, typically achieving levels between 50% and 70% (Marsh, 2000), which could exceed the 53% fibre volume fraction observed in the strip stirrups used in this study. While the primary focus is on eliminating manufacturing imperfections, an increased fibre content would further contribute to the overall strength and performance of the stirrups. By refining production techniques in this way, both the immediate and long-term performance of BFRP-reinforced structures can be substantially improved, providing more consistent performance and fatigue resistance.

6.4. Implications for shear reinforcement design

The conservative nature of the Eurocode 2 (EC2) design method leads to an underestimation of the shear capacity of beams both with and without steel stirrups. This conservatism stems from EC2's simplified, empirical approach, which fails to fully account for the complex interactions between concrete and shear reinforcement.

For beams reinforced with BFRP stirrups, relying solely on uniaxial tensile capacity to estimate shear contribution is insufficient. This insufficiency arises because the beam's shear capacity peaks well before the BFRP stirrups reach their full tensile strength. The early peak in shear capacity is primarily due to the degradation of shear transfer mechanisms within the concrete, such as aggregate interlock, which is compromised by the formation of wider shear cracks. These wider cracks are a consequence of the lower stiffness of BFRP material compared to steel.

Nevertheless, the residual tensile capacity of the BFRP stirrups, available after the beam has reached its peak load, contributes to a degree of ductility. This residual capacity plays a crucial role in partially compensating for the diminished shear transfer mechanisms within the concrete, thereby preventing the beam from failing immediately after the peak load is surpassed. This form of ductility enhances the overall performance of the beam by providing a measure of post-peak load-bearing capacity.

Using a combined shear resistance approach, incorporating both concrete contribution using the General Shear Design Method by Cladera and Mari (2004a), and stirrup contributions with the strain approach, limiting the strain in the stirrups to ε = 0.45%, a strut angle of θ = 24° and the corresponding E-modulus of the stirrup material, leads to predicted capacities that are 89-102% of the experimental values. This finding justifies enlarging the strain limit from the typical yield strength of steel, typically 0.25%, to 0.45% for BFRP stirrups.

Guadagnini et al. (2003), however, recommend to use a fixed concrete strut angle θ = 45° for the stirrups contribution for simplicity. Combining the results with the concrete's contribution prediction according to the method in GSDM, this results in a more conservative but safe approach with predictions in the range of 80% to 88% compared to the experimental values for the shear capacity in this research. Since only a limited amount of samples is tested in this research, this approach is still recommended for design for safety reasons.

6.5. Limitations of the study

This study presents several limitations that should be acknowledged to fully understand its scope and identify areas for potential improvement. One significant limitation is the variation in corner radii of the stirrups, which complicates direct comparisons between different samples. The corner radius is a critical factor as it influences the stirrups' corner strength capacity and dictates the positioning of the longitudinal reinforcement, both of which affect the stirrups' performance under load. This variability introduces complexities in assessing the true impact of the stirrups on the beam samples shear behavior.

Another limitation is the lack of data on the bond capacity of BFRP reinforcement stirrups to concrete, as pull-out tests were not conducted. The adhesion factor is a crucial determinant of the bond strength between the reinforcement and concrete, which directly influences crack width and the overall structural performance of the beam. Without this information, the study's findings may not fully capture the true behavior of the BFRP stirrups in practical applications. Future research should include pull-out tests to accurately determine the adhesion factor, enabling more precise predictions and validations.
The study also utilized beam samples with large diameter longitudinal reinforcement, resulting in a relatively high longitudinal reinforcement ratio. This configuration influences the contribution of dowel action to the beam's shear capacity and limits the propagation of flexural cracks. Consequently, the results may not be fully representative of reinforced concrete beams with lower reinforcement ratios, potentially skewing the results for reinforced concrete beams with lower reinforcement ratios.

Additionally, the placement of Distributed Fibre Optical Sensors (DFOS) was limited to the vertical sections and bottom horizontal section of the beams, excluding critical areas such as the top corners and top horizontal section. This selective placement may have led to the exclusion of important strain data, thereby providing an incomplete understanding of the stirrups' behavior under load. A more comprehensive sensor placement strategy could yield a fuller picture of the structural performance and the distribution of stresses within the stirrups.

For the broader application of BFRP stirrups in reinforced concrete structures, several key uncertainties should be addressed that currently limit their widespread use. Among the most critical concerns are the long-term tensile strength of BFRP stirrups the matrix durability, both of which are essential for ensuring the structural integrity of BFRP-reinforced elements. Furthermore, the fatigue resistance of BFRP stirrups under cyclic loading conditions requires thorough investigation to ensure their reliability in structures subjected to fatigue.

7

Conclusions and recommendations

7.1. Conclusions

The research presented in this report investigates the extent to which Basalt Fibre-Reinforced Polymer (BFRP) stirrups can enhance the shear capacity of reinforced concrete beams. The evaluation focused on beams reinforced with braided BFRP stirrups and laminated BFRP strip stirrups, using beams with and without steel stirrups as reference points. BFRP was selected for this study because basalt fibres are considered to provide the optimal balance between mechanical strength and the energy efficiency of its production process. The study employs both analytical and experimental approaches to offer valuable insights into the performance of BFRP in structural applications. The primary conclusions are as follows:

1. **Mechanical properties of braided BFRP rods and laminated BFRP strips:**
    - The braided BFRP rebar and laminated BFRP strips used in this study possess similar fibre volume fractions (54% and 53%, respectively), which are lower than those found in pultruded BFRP rebar (61%) due to differences in production methods. This lower fibre volume fraction affects mechanical properties such as tensile strength, ultimate strain, and elastic modulus. The BFRP materials exhibit approximately linear elastic behavior up to the point of failure, which occurs through fibre rupture..
    - The uniaxial tensile strength of the braided BFRP stirrups (751 MPa) and laminated BFRP strips (706 MPa) is lower than that of pultruded BFRP rebar (1141 MPa), but higher than the yield strength of traditional steel reinforcement (typically around 500 MPa). The stiffness of the BFRP reinforcement is significantly lower, with an elastic modulus of approximately 41 GPa, compared to 53.5 GPa for pultruded BFRP rebar and 200 GPa for steel.
2. **Stirrup strain distribution and beam failure modes:**
    - The strain data from the BFRP stirrups, obtained through Distributed Fibre Optic Sensing (DFOS), revealed a progressive increase in strain leading up to the failure of the stirrups, with peak strains observed at the points where shear cracks intersected the stirrups and in corners. All beams with BFRP stirrups failed due to rupture of one of the stirrups in their respective corner section.
    - Design methodologies generally assume that the shear contribution of stirrups is evenly distributed across all stirrups, with stress redistribution occurring as the beam reaches its maximum load capacity. In steel-reinforced beams, this redistribution is facilitated by the yielding of the stirrups, ensuring a uniform contribution to resisting shear forces. However, in beams reinforced with BFRP stirrups, strain data reveals a different behavior. The lower stiffness of BFRP compared to steel leads to increased shear crack widths, which in turn reduces the effectiveness of internal shear transfer mechanisms within the concrete, such as aggregate interlock. Consequently, these beams reach their peak shear capacity before fully utilizing the uniaxial tensile strength of the BFRP stirrups.

- In BFRP-reinforced beams, redistribution still occurs, but rather than being evenly spread among the stirrups, it shifts from the concrete's contribution to the residual tensile capacity of the BFRP stirrups after the peak load is reached. This redistribution imparts a degree of ductility, providing additional post-peak load-bearing capacity. The strain data further indicated that stirrups near the mid-span were more heavily engaged, an uneven distribution of shear load across the stirrups.
- The strain data indicate that the braided BFRP stirrups might have a lower bond capacity with the surrounding concrete compared to steel or laminated BFRP UD-strip stirrups. Although this might seem disadvantageous, it can be beneficial by enabling the distribution of peak loads over a larger stirrup length, thereby reducing local peak stresses. With proper anchorage, this characteristic could enhance the overall performance of the BFRP stirrups and decrease the risk of premature failure.

3. **Analytical Methods for Prediction of Shear Capacity of Beams with BFRP Stirrups:**

   - Experimental results for the reference beams with and without steel stirrups revealed discrepancies with Eurocode 2 predictions, which were conservative and underestimated the shear capacity. Alternative models, such as the General Shear Design Method (GSDM), offered more accurate, though still conservative, estimates.
   - To predict the total shear capacity of reinforced concrete beams with BFRP stirrups, the concrete and stirrups contribution is summed. The concrete contribution is determined through the GSDM-method, and for the stirrup contribution the strain approach is used, limiting the strain of the FRP stirrups to 0.45% to preserve the additive nature of both mechanisms. The variable strut approach, with a concrete strut angle $\theta = 24^{\circ}$, provides predictions within 89% to 102% of experimental results.
   - Combining the GSDM method and a fixed strut approach with a concrete strut angle of $\theta = 45^{\circ}$ as recommended in literature for its straightforwardness, yields a conservative estimation of shear capacity, predicting 80% to 88% of the values observed in experimental tests. Considering the limited sample size in this study and the necessity of prioritizing structural reliability, this approach continues to be recommended as design method.

4. **Shear Capacity Enhancement:**

   - The experimental results and analytical model predictions show that increasing the amount of BFRP shear reinforcement leads to higher shear capacity in concrete beams. While BFRP stirrups effectively enhance shear capacity, their performance did not match that of steel stirrups. This difference is primarily due to the lower elastic modulus of basalt FRP, which leads to wider cracks and consequently reduces the concrete's shear resistance contributions, e.g. aggregate interlock, before the tensile capacity of the stirrups is reached.
   - The efficiency of basalt FRP stirrups, quantified as the additional shear capacity per unit of shear reinforcement ratio and normalized against the performance of steel stirrups, was determined to be 0.37 and 0.34 for beams reinforced with 4 and 8 braided stirrups, respectively. For beams with 4 and 8 laminated strip stirrups, the relative efficiency values were 0.42 and 0.29, respectively. While these results for the beams with braided BFRP stirrups show consistency, the greater variability in efficiency observed for the beams with laminated strip stirrups can be attributed to the presence of out-of-plane wrinkles, a defect originating from the production process. This finding underscores the importance of refining manufacturing techniques, such as adopting filament winding, to eliminate such imperfections and achieve more consistent quality and performance in BFRP stirrups.
   - When the relative efficiency is further normalized by the density of the stirrup material, with steel as the reference, the basalt FRP stirrups exhibit relative efficiency by weight values ranging from 1.24 to 1.79. These findings indicate that basalt FRP stirrups could offer potential advantages in environmental costs compared to steel, although this finding requires further investigation to be validated.

7.2. Contribution to the field

This research contributes to the field of structural engineering and materials science by providing empirical data on the performance of BFRP stirrups in reinforced concrete beams. Key contributions include:

- **Validation of BFRP as Shear Reinforcement:** Demonstrating the viability of BFRP stirrups as an alternative to steel in reinforced concrete beams, as a potential alternative to traditional steel stirrups in reinforced concrete beams, particularly in contexts where enhanced corrosion resistance and environmental sustainability are critical considerations.
- **Refinement of Predictive Models:** Offering insights that can refine existing analytical models, making them more accurate for predicting the behavior of BFRP-reinforced beams.
- **Improvement of Manufacturing Processes:** Highlighting the need for improved manufacturing techniques, such as filament winding, to eliminate defects like out-of-plane wrinkles in BFRP strip stirrups, thereby enhancing their structural integrity and load-bearing capacity.

7.3. Recommendations for future research

To further advance the application of BFRP stirrups in structural engineering, the following areas are recommended for future research:

1. **Comparative analysis with pultruded BFRP stirrups:** This would provide a direct comparisons between braided BFRP stirrups, laminated BFRP UD-strip stirrups and pultruded BFRP stirrups as shear reinforcement in reinforced concrete beams to evaluate differences in performance.
2. **Evaluate the impact of longitudinal reinforcement:** The beam samples in this study possess a high longitudinal reinforcement ratio, which affects dowel action and restricts the propagation of flexural cracks. Consequently, the results found in this study may be skewed for beams with lower reinforcement ratios.
3. **Enhanced strain measurement:** Position and bond Distributed Fibre Optical Sensors (DFOS) around the entire stirrup, including the top corners and top horizontal section. This will provide a more detailed strain profile, enabling a deeper understanding of the strain behavior and the associated failure modes within the stirrup.
4. **Comprehensive testing of bond capacities:** Experimental research on the bond capacity of BFRP braided rods and laminated UD-fibre strips to better understand the adhesion characteristics and their impact on structural performance.
5. **Corner Tensile Capacity Tests:** It is recommended to conduct dedicated tensile corner strength tests to accurately quantify the impact of corner radii on the performance of BFRP braided and laminated strip stirrups. While the current beam tests indirectly assess corner tensile strength, targeted corner tensile capacity testing could provide deeper insights, further refining the design and enhancing the effectiveness of these stirrups in structural applications. Additionally, Appendix A proposes a detailed design for such a test, which could serve as a valuable guideline for conducting these assessments.
6. **Manufacturing process improvements:** Better production techniques, such as filament winding, would enhance the alignment of continuous fibres and reduce imperfections in BFRP strip stirrups. This improvement is crucial for achieving consistent quality and performance, which are essential to derive better conclusions on the performance of the strips.
7. **Evaluate environmental footprint:** Perform a comprehensive analysis of the Environmental Cost Indicator (ECI) for BFRP stirrups to evaluate their sustainability and environmental impact. By comparing this with traditional steel stirrups, the overall environmental benefits and trade-offs can be better understood, supporting the case for using BFRP stirrups in sustainable construction practices.
8. **Comprehensive testing**: Conduct extensive testing across a broader spectrum of beam sizes and loading conditions to gain a thorough understanding of the behavior and limitations of BFRP stirrups in varied scenarios. Focus areas should include the long-term performance, durability under different environmental conditions, and fatigue resistance of BFRP stirrups. Additionally, this extended testing can validate the use of a variable strut approach for predicting the contribution of BFRP stirrups to the overall shear capacity of concrete beams.

These recommendations aim to address the identified knowledge gaps and technical challenges, thereby promoting the broader adoption of BFRP stirrups in reinforced concrete structures. By enhancing the understanding and application of BFRP materials, this research supports the development of more sustainable and resilient construction practices.

References

Abdul Samad, A. A., Mohamad, N., Ali, N., Jayaprakash, J., & Mendis, P. (2016). Rehabilitation of continuous reinforced concrete beams in shear by external bonding of carbon fiber reinforced polymer strips for sustainable construction.

ACI 318-14. (2014). *Building Code Requirements for Structural Concrete* (14th, tech. rep.) [ACI 318-14]. American Concrete Institute. Farmington Hills, MI.

ACI 440.3R-12. (2012). *440.3r-12: Guide test methods for fiber-reinforced polymer (frp) composites for reinforcing or strengthening concrete and masonry structures* (tech. rep. ACI 440.3R-12). American Concrete Institute.

ACI 440.3R-15. (2015). *Guide for the design and construction of structural concrete reinforced with fiber-reinforced polymer (frp) bars* (tech. rep.). American Concrete Institute.

ACI 440.3R-4. (2004). *Guide test methods for fiber-reinforced polymer (frp) composites for reinforcing or strengthening concrete and masonry structures* (tech. rep.). American Concrete Institute.

Ahmed, E. A., El-Sayed, A. K., El-Salakawy, E., & Benmokrane, B. (2010). Bend strength of frp stirrups: Comparison and evaluation of testing methods. *Journal of Composites for Construction*, *14*(1), 3–10. https://doi.org/10.1061/(ASCE)CC.1943-5614.0000050

Ajay Kumar, M., Khan, M., & Mishra, S. (2020). Effect of machine parameters on strength and hardness of fdm printed carbon fiber reinforced petg thermoplastics. *Materials Today: Proceedings*, *27*(2), 975–983.

Al-Rousan, E. T., Khalid, H. R., & Rahman, M. K. (2023). Fresh, mechanical, and durability properties of basalt fiber-reinforced concrete (bfrc): A review. *Developments in the Built Environment*, *14*, 100155. https://doi.org/https://doi.org/10.1016/j.dibe.2023.100155

Askar, M. K., Hassan, A. F., & Al-Kamaki, Y. S. (2022). Flexural and shear strengthening of reinforced concrete beams using frp composites: A state of the art. *Case Studies in Construction Materials*, *17*. https://doi.org/10.1016/j.cscm.2022.e01189

Bank, L. C. (2006). *Composites for construction—structural design with frp materials*. John Wiley & Sons.

Baumann, T., & Rüsch, H. (1970). *Versuche zum studien der verdübelungswirkung der biegezugbewehrung eines stahlbetonbalkens [experimental study on dowel action in reinforced concrete beam]* [in German]. Deutscher Ausschuss für Stahlbeton (DAfStb), Ernst.

Benmokrane, B., Wang, P., Ton-That, T., Rahman, H., & Robert, J.-F. (2002). Durability of glass fiber-reinforced polymer reinforcing bars in concrete environments. *Journal of Composites for Construction*, *6*(3), 143–153.

Bogdándy, B. (2021). The shear resistance of a member without shear reinforcement according to eurocode 2; the error of the calculated value and the mechanical explanation of the problem. *International Review of Applied Sciences and Engineering*, *12*(3), 222–229. https://doi.org/10.1556/1848.2021.00236

Campbell, F. (2010). *Structural composite materials*. ASM International.

Chen, Y., Davalos, J. F., Ray, I., & Kim, H. Y. (2007). Accelerated aging tests for evaluation of durability performance of frp reinforcing bars. *Composite Structures*, *78*(1), 101–111. https://doi.org/10.1016/j.compstruct.2005.08.015

Chiu, C. K., Chi, K. N., & Lin, K. C. (2013). Strength performance of t-headed rebar in concrete. *Applied Mechanics and Materials*, *284-287*, 1401–1408. https://doi.org/10.4028/www.scientific.net/AMM.284-287.1401

Chu, W., Wu, L., & Karbhari, V. (2004). Durability evaluation of moderate temperature cured e-glass/vinylester systems. *Composite Structures*, *66*, 367–376. https://doi.org/10.1016/j.compstruct.2004.04.058

Chung, D. D. (2017). *Carbon composites (second edition)*. Elsevier. https://doi.org/https://doi.org/10.1016/B978-0-12-804459-9.00003-8

Cladera, A., & Mari, A. (2004a). Shear design procedure for reinforced normal and high-strength concrete beams using artificial neural networks. part i: Beams without stirrups. *Engineering Structures*, *26*(7), 917–926. https://doi.org/10.1016/j.engstruct.2004.02.010

Cladera, A., & Mari, A. (2004b). Shear design procedure for reinforced normal and high-strength concrete beams using artificial neural networks. part ii: Beams with stirrups. *Engineering Structures*, *26*(8), 927–936. https://doi.org/10.1016/j.engstruct.2004.02.011

Coenen, G. (2007). *Dwarskrachtcapaciteit van betonconstructies met glasvezelwapening* (Master's thesis). Technische Universiteit Eindhoven, Faculteit Bouwkunde, Afstudeerrichting: Constructief Ontwerpen. https://research.tue.nl/nl/studentTheses/dwarskrachtcapaciteit-van-betonconstructies-met-glasvezelwapening

Collins, M. P. (2001). *Evaluation of shear design procedures for concrete structures* (Report) [Report prepared for the CSA Technical Committee on RC Design]. CSA Technical Committee on RC Design. Canada.

D7205M, A. (2016). Standard test method for tensile properties of fiber reinforced polymer matrix composite bars. *ASTM International*. https://www.astm.org/Standards/D7205.htm

Daniyan, I., Mpofu, K., Adeodu, A., & Adesina, O. (2020). Development of carbon fibre reinforced polymer matrix composites and optimization of the process parameters for railcar applications. *Materials Today: Proceedings*, 1–7. https://doi.org/10.1016/j.matpr.2020.03.480

Davalos, J. F., Chen, Y., & Ray, I. (2012). Long-term durability prediction models for gfrp bars in concrete environment. *Journal of Composite Materials*, *46*(16), 1899–1914. https://doi.org/10.1177/0021998311427777

Elmahdy, A., Feldman, E., & Verleysen, P. (2024). Tensile behavior of basalt fiber reinforced composites at high strain rates. *ECCM18 - 18th European Conference on Composite Materials*, 24–28.

Feng, G. Y., Zhu, D. J., Guo, S. C., Rahman, M. Z., Jin, Z. Q., & Shi, C. J. (2022). A review on mechanical properties and deterioration mechanisms of frp bars under severe environmental and loading conditions. *Cement and Concrete Composites*, *134*, 104758. https://doi.org/10.1016/j.cemconcomp.2022.104758

Fennis, S. (2013). *Ctb2220 - dictaat gewapend beton* (tech. rep.). TU Delft.

Ferguson, P., Breen, J., & Jirsa, J. (1988). *Reinforced concrete fundamentals* (5th ed.). John Wiley; Sons.

fib. (2007). Bulletin 40: Frp reinforcement in rc structures, technical report.

fib Model Code 2010. (2013). *Model code for concrete structures 2010* [Fédération Internationale du Béton - International Federation for Structural Concrete (fib)]. Ernst & Sohn.

Fiore, V., Scalici, T., Di Bella, G., & Valenza, A. (2015). A review on basalt fibre and its composites. *Composites Part B: Engineering*, *74*, 74–94. https://doi.org/10.1016/j.compositesb.2014.12.034

García, J., García, F., Serna, F., & de la Peña, J. (2010). High-performance aromatic polyamides. *Progress in Polymer Science*, *35*, 623.

Grover, M., & Anderson, W. (1996). *Fundamentals of modern manufacturing: Materials, processes, and systems* (1st). Wiley.

Guadagnini, M., Pilakoutas, K., & Waldron, P. (2003). Shear performance of frp reinforced concrete beams. *Journal of Reinforced Plastics and Composites*, *22*(15), 1325–1349. https://doi.org/10.1177/07316844030221501

Guadagnini, M., Pilakoutas, K., & Waldron, P. (2006). Shear resistance of frp rc beams: Experimental study. *Journal of Composites for Construction*, *10*(6), 464–473. https://doi.org/10.1061/(ASCE)1090-0268(2006)10:6(464)

Indraneel R. Chowdhury, J. S., Richard Pemberton. (2022). Developments and industrial applications of basalt fibre reinforced composite materials. *Journal of Composites Science*, *6*(12), 367. https://doi.org/10.3390/jcs6120367

Jamaluddin, N., Hassan, S., Umar, A., Amin, M., Adam, M., & Omar, B. (2018). Compressive behaviour of filament wound steel/carbon hybrid composites tube. *Journal of Mechanical Engineering*, *15*, 135–151. https://www.researchgate.net/publication/325687623_Compressive_behaviour_of_filament_wound_steelcarbon_hybrid_composites_tube

Karbhari, V. M., Murphy, K., & Zhang, S. (2002). Effect of concrete based alkali solutions on short-term durability of e-glass/vinylester composites. *Journal of Composite Materials*, *36*(17), 2101–2121. https://doi.org/10.1177/0021998302036017977

Karunanidhis. (2019). Investigation on spiral stirrups in reinforced concrete beams. *International Journal of Novel Research in Civil Structural Earth Sciences*, *6*(3), 14–28.

Koumoulos, E. P. (2019). Research and development in carbon fibers and advanced high-performance composites supply chain in europe: A roadmap for challenges and the industrial uptake. *Journal of Composites Science*, *3*(3), 86. https://doi.org/10.3390/jcs3030086

Lee, C., Kim, J.-Y., & Heo, S.-Y. (2010). Experimental observation on the effectiveness of fiber sheet strip stirrups in concrete beams. *Journal of Composites for Construction*, *14*(5), 487–497. https://doi.org/10.1061/(ASCE)CC.1943-5614.0000109

Lee, C., Kim, J.-Y., & Heo, S.-Y. (2014). Bend strength of complete closed-type carbon. *Journal of Composites for Construction*, *14*(5), 487–497. https://doi.org/10.1061/(ASCE)CC.1943-5614.0000109

Li, H., Xian, G., Xiao, B., & Wu, J. (2011). Comprehensive characterization of bfrp applied in civil engineering. *Advances in FRP Composites in Civil Engineering*, 157–163. https://doi.org/10.1007/978-3-642-17487-2_11

Lindner, M., Vanselow, K., Gelbrich, S., & Kroll, L. (2018). Fiber-reinforced polymers based rebar and stirrup reinforcing concrete structures. *Journal of Materials Science and Engineering A*, *8*(3-4), 47–54. https://doi.org/10.17265/2161-6213/2018.3-4.001

Lindner, M., Vanselow, K., Gelbrich, S., & Kroll, L. (2019). Fibre-reinforced polymer stirrup for reinforcing concrete structures. *Technologies for Lightweight Structures*, *3*(1), 17–24. https://doi.org/10.21935/tls.v3i1.117

Lingen, K. v. d. (2024). Flexural behaviour of concrete reinforced with basalt fibre reinforcement bars. https://ascelibrary.org/doi/abs/10.1061/%28ASCE%291090-0268%282006%2910%3A6%28464%29

Ma, L., Sun, Y., & Wang, W. (2022). A review on basalt fiber composites and their applications in clean energy sector and power grids. *Polymers*, *14*(12), 2376. https://doi.org/10.3390/polym14122376

Mancini, M. (2023). The production of basalt fiber. *The Basalt Fiber—Material Design Art*. https://doi.org/10.1007/978-3-031-46102-6_2

Marsh, G. (2000). Filament winding: A composite fabrication technique. *Reinforced Plastics*, *44*(5), 38–43. https://doi.org/10.1016/S0034-3617(00)80036-8

Morphy, R., Sheata, E., & Rizkalla, S. (1997). *Bent effect on strength of cfrp stirrups*.

Nanni, A., Luca, A., & Jawaheri Zadeh, H. (2014). *Reinforced concrete with frp bars: Mechanics and design*. https://doi.org/10.1201/b16669

Nanni, A., Okamoto, T., Tanigaki, M., & Osakada, S. (1993). Tensile properties of braided frp rods for concrete reinforcement. *Cement and Concrete Composites*, *15*(2), 121–129.

NEN 6720. (2005). *NEN 6720:2005 nl - Bepaling van de druksterkte van beton uit de drukkromme* (Dutch Standard No. 6720). Nederlands Normalisatie-instituut (NEN).

NEN 8702. (2017). *NEN 8702:2017 nl - Beoordeling van een bestaande constructie bij hergebruik en afkeur - Betonconstructies* (Dutch Standard No. 8702). Nederlands Normalisatie-instituut (NEN).

NEN ISO 527-5. (2009). Plastics - determination of tensile properties - part 5: Test conditions for unidirectional fibre-reinforced plastic composites (iso 527-5:2009).

NEN-EN 12390-3. (2009). *Testing hardened concrete - part 3: Compressive strength of test specimens* (tech. rep.). Dutch Standardization Institute (NEN).

NEN-EN 1992-1-1. (2011). Eurocode 2: Design of concrete structures - part 1-1: General rules and rules for buildings.

Nijssen, R. (2015). *Composite materials: An introduction*. Inholland University of Applied Sciences. https://books.google.nl/books?id=pA2pDAEACAAJ

Paris Agreement. (2015). Paris agreement. *United Nations Framework Convention on Climate Change*. https://unfccc.int/sites/default/files/english_paris_agreement.pdf

Peng, X., Wu, Y., & Wei, Z. (2024). Research progress on the surface modification of carbon fiber. *RSC Advances*, *14*, 4043–4064. https://doi.org/10.1039/D3RA08577E

Protchenko, K., Zayoud, F., Urbański, M., & Szmigiera, E. (2020). Tensile and shear testing of basalt fiber reinforced polymer (bfrp) and hybrid basalt/carbon fiber reinforced polymer (hfrp) bars. *Materials*, *13*(24), 5839. https://doi.org/10.3390/ma13245839

Qureshi, J. (2022). A review of fibre reinforced polymer structures. *Fibers*, *10*(3), 27. https://doi.org/10.3390/fib10030027

Regan, P. E. (1993). Research on shear: A benefit to humanity or a waste of time? *Structural Engineer*, *71*(19), 337–347.

Reinhardt, H. W., & Walraven, J. C. (1982). Cracks in concrete subject to shear. *Journal of the Structural Division*, *108*(1). https://doi.org/10.1061/JSDEAG.0005860

Rijksoverheid. (2022). *Nederland circulair in 2050*. Retrieved June 19, 2023, from https://www.rijksoverheid.nl/onderwerpen/circulaire-economie/nederland-circulair-in-2050

Rue, D., Servaites, J., & Wolf, W. (2017). *Commercial glass fibers*. Springer. https://doi.org/10.1007/978-3-319-48760-1

S806-02, C. (2002). Annex c: Test method for tensile properties of frp reinforcements [Canadian Standard].

Sagar, B., & Sivakumar, M. V. N. (2021). Performance evaluation of basalt fibre-reinforced polymer rebars in structural concrete members–a review. *Innovative Infrastructure Solutions*, *6*(75), 123–456. https://doi.org/https://doi.org/10.1007/s41062-020-00452-2

Schöck Bauteile GmbH. (2022). *Technische informatie schöck combar* (tech. rep.). Schöck Nederland B.V. https://www.schoeck.com/nl/download/eyJwcm9kdWN0IjoiNCJ9

Shehata, E., Morphy, R., & Rizkalla, S. (2000). Fibre reinforced polymer shear reinforcement for concrete members: Behaviour and design guidelines. *Canadian Journal of Civil Engineering*, *27*(5), 859–872.

Singh, R., Verma, S. K., Bhadauria, S. S., & Gupta, R. (2015). Durability of basalt fibers and composites in alkaline environments: A review. *Construction and Building Materials*, *82*, 151–157.

Taylor, R. (1970). *Investigation of the forces carried across cracks in reinforced concrete beams in shear by interlock aggregate* (tech. rep. No. 42.447). Cement and Concrete Association. London, UK.

Veit, D. (2022). Basalt fibers. In *Fibers*. Springer. https://doi.org/10.1007/978-3-031-15309-9_44

Walraven, J. C. (1981). Fundamental analysis of aggregate interlock. *Journal of the Structural Division, Proceedings of the American Society of Civil Engineering*, *107*(ST11), 2245–2269.

Wang, F., Wu, Y., Huang, Y., & Liu, L. (2018). Strong, transparent, and flexible aramid nanofiber/poss hybrid organic/inorganic nanocomposite membranes. *Composites Science and Technology*, *156*, 269.

Wang, J., GangaRao, H., Liang, R., & Liu, W. (2016). Durability and prediction models of fiber-reinforced polymer composites under various environmental conditions: A critical review. *Journal of Reinforced Plastics and Composites*, *35*(3), 179–211. https://doi.org/10.1177/0731684415610920

Yang, H. (2000). Aramid fibers. In A. Kelly & C. Zweben (Eds.), *Comprehensive composite materials* (pp. 199–229). Elsevier.

Yang, Y. (2014). *Shear behaviour of reinforced concrete members without shear reinforcement: A new look at an old problem* (Doctoral dissertation) [Doctoral thesis, Faculty of Civil Engineering and Geosciences, Department of Structural Engineering]. Delft University of Technology. Delft, Netherlands. https://repository.tudelft.nl/record/uuid:ac776cf0-4412-4079-968f-9eacb67e8846

Yang, Y., den Uijl, J., & Walraven, J. (2016). Critical shear displacement theory: On the way to extending the scope of shear design and assessment for members without shear reinforcement. *Structural Concrete*, *17*(5), 790–798. https://doi.org/10.1002/suco.201500135

Yang, Y., Walraven, J., & den Uijl, J. (2017). Shear behavior of reinforced concrete beams without transverse reinforcement based on critical shear displacement [Published online on July 25, 2016]. *Journal of Structural Engineering*, *143*(1), 04016146. https://doi.org/10.1061/(ASCE)ST.1943-541X.0001608

Yuan, Y., Wang, Z., & Wang, D. (2022). Shear behavior of concrete beams reinforced with closed-type winding glass fiber-reinforced polymer stirrups. *Advances in Structural Engineering*, *25*. https://doi.org/10.1177/13694332221104280

A

Corner tensile capacity test design

This chapter describes the corner tensile strength test. In this experiment, the bent FRP sections will be cast into concrete to simulate real-world conditions encountered in structural applications. Along with the results from the uniaxial tensile strength tests, this experiment will offer insights into the relative efficiency of different shapes of BFRP stirrups in corners compared to straight forms of BFRP reinforcement.

A.1. Design of corner tensile strength

FRP reinforcement exhibits reduced tensile strength in corner sections compared to its uniaxial tensile strength due to stress concentrations and kinking. To accurately determine the tensile strength in corner sections of BFRP braided and laminated UD-strip stirrups, a specific experiment is designed. This section outlines the design of such an experiment, aiming to evaluate the relative efficiency of different forms of shear reinforcement in corners compared to their uniaxial strength

For practical considerations, the decision was made to modify ACI 440.3R-12 (2012) test method B.5 to accommodate the use of a Universal Testing Machine (UTM). In this setup, an L-shaped reinforcement sample is cast with the shorter side embedded in the middle of a concrete block, protruding from the top. The concrete block measures 400x200x200 mm (length x width x height) and is securely clamped between two 20 mm thick steel plates using four M24-sized steel threaded rods and nuts. The bottom plate features an additional flange welded perpendicular to it, enabling it to be clamped in the UTM. This flange is reinforced with triangular stiffeners at the location of all four corners. The protruding end of the sample at the top will be bonded in the same circular hollow steel (CHS) anchors used in the uniaxial tensile testing, as described in Section 3.3. The flattened part at the top of the steel anchor is then clamped in the top jaw of the UTM, which moves upwards at a constant rate to apply tensile force to the sample. The FRP samples are debonded from the concrete's top surface up to the corner area to ensure proper stress transfer to the reinforcement at the corner section.

For a BFRP sample with a corner radius of 32 mm, the maximum anchorage length in the concrete is calculated as follows:

$$L_{\text{anchor}} = \text{straight length} \; + \; \text{corner length} = (280 - 32) + 0.25\pi \cdot 32 = 298 \text{ mm} \tag{A.1}$$

.

This anchorage length is expected to be sufficient for all samples. Figure A.1 provides a visual representation of this design. The bonded length of the sample in the CHS-anchor can be determined through trial and error in the uniaxial tensile testing. Since the corner tensile strength is expected to be lower than the uniaxial tensile strength, this length should also suffice for this experiment.

To prevent splitting of the concrete block before rupture of the stirrup, steel splitting reinforcement is applied. Simple calculations indicate that minimal reinforcement is required; however, to ensure that concrete splitting does not dominate the failure mode, the concrete blocks are over-reinforced. Given

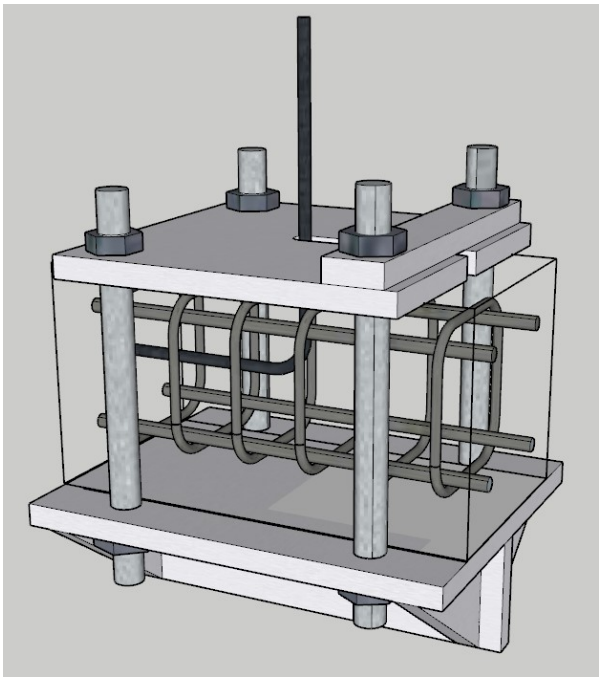

Figure A.1: Design of corner tensile capacity test suitable for universal testing machines.

the block's weight of 0.2 m x 0.2 m x 0.4 m x 2500 kg/m^3 = 40 kg, hoisting stirrups are added at both ends. Figure A.2 provides longitudinal and cross-sections for this design.
The formwork was constructed and the necessary splitting reinforcement cages were prepared, as shown in Figure A.2. Despite all efforts in designing and preparing this experiment to determine the FRP samples corner tensile capacity, it was not conducted due to prioritization of the available time.

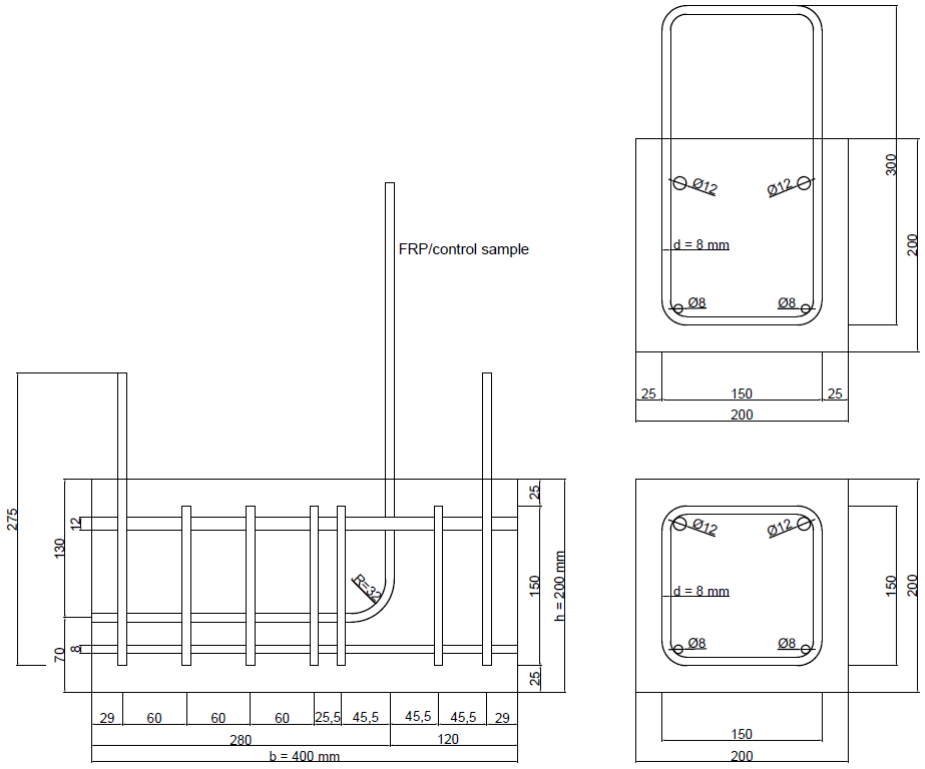

Figure A.2: Cross-sections for corner tensile strength test

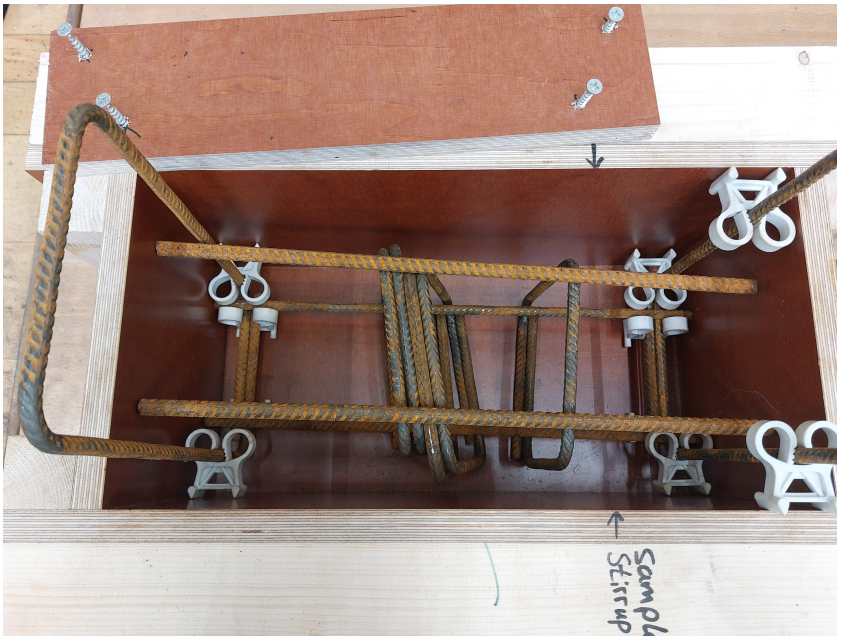

Figure A.3: Cross-sections for corner tensile strength test

B

Cross-sectional properties

	Original sample					From measuring cup			Weighing on the scale				Determining mass% and volume%								
Samples	Length [mm]	Diameter [mm]	Width [mm]	Thickness [mm]	A = b*d OR A=0.25*pi*d^2 [mm^2]	V1 = starting volume of measuring cup (without sample) [ml]	V_2 (with sample) [ml]	V_sample = (V_2-V_1) * 1000 [mm^3]	A [mm^2] = V_sample / length	M_tot = original sample mass [gr]	mass fibres [gr]	mass sand [gr]	▲massa = epoxy mass [gr]	Original sample density [kg/m^3]	Mass fibres [%]	Mass resin [%]	Mass sand [%]	Volume fibres = (Mf * 2670)/1045 [mm^3]	Volume sand (measuring cup) [mm^3]	Volume epoxy = Vsample-Vfibres-Vsand [mm^3]	Volume fibres [%]	Volume resin [%]	Volume sand [%]
Braided Ø8	150.40	6.55								11.25	8.85	-	2.4	1815	79	21	-	3161	0	3039	51	49	0
oude batch	150.30	8.55	N.A.	N.A.	47.58	85	91.20	6200	41.24														
	150.30	7.85																					
avg	**150.33**	**7.78**																					
UD-strip 1	149.70		23.30	2.55																			
	149.65	N.A.	23.35	2.60	59.50	85	93.05	8050	53.77	14.63	11.44	-	3.19	1817	78	22	-	4285	0	3765	53	47	0
	149.75		23.35	2.50																			
avg	**149.70**		**23.33**	**2.55**																			
UD-strip 2	150.35		23.45	2.50																			
	150.40	N.A.	23.55	2.45	57.66	85	93.00	8000	53.21	15.03	11.08	-	3.95	1879	74	26	-	4150	0	3850	52	48	0
	150.30		23.60	2.40																			
avg	**150.35**		**23.53**	**2.45**																			
UD AVG	**150.03**		**23.43**	**2.50**					53.49169684	14.83	11.26	-	3.57	**1848**	75.95736	24.042842	-	4217.228464	0	3807.771536	53	47	0
Sandcoat Ø10	150.10		10.70							25.21	19.53	2.4	3.28	2118	77	13	10	7315	750	3835	61	32	6
	150.10	N.A.	10.50	N.A.	87.69	85	96.90	11900	79.32														
	149.90		10.50																				
avg	**150.03**		**10.57**																				
Braided Ø8																							
nieuwe batch 1			N.A.	N.A.	69.69340559	85	93.8	8800	59.13	15.92	12.61	-	3.31	1809	79	21	-	4723	0	4077	54	46	0
avg	**148.82**	**9.42**																					
braided Ø8																							
nieuwe batch 2				N.A.	59.037516	85	93.5	8500	56.77	15.42	12.50	-	2.92	1814	81	19	-	4682	0	3818	55	45	0
avg	**149.74**	**8.67**	N.A.																				
BRAIDED AVG	149.28	9.045							57.94844828					**1812**	kg/m^3						54	46	0

C

Concrete compressive strength results

Table C.1: Experimental results for concrete compressive strength

Concrete cube batch	Sample no.	Sample age	Force [kN]	Stress [MPa]	AVG [MPa]	STD [MPa]
Ref. beams	1	1 day	96.9	4.31	4.49	0.131
	2		104.0	4.62		
	3		102.2	4.54		
	4	28 days	1101.2	48.94	49.53	0.482
	5		1127.8	50.12		
	6		1114.1	49.52		
UD beams	1	28 days	1021.0	45.38	46.05	0.713
	2		1029.1	45.74		
	3		1058.4	47.04		
Braid beams	1	28 days	1090.4	48.46	47.23	0.868
	2		1049.4	46.64		
	3		1048.5	46.60		

D

MATLAB-script for Critical Shear Displacement Method

The MATLAB script, which is shown on the following pages, is found in Annex I of Y. Yang (2014). The input parameters have been modified to correspond to beam sample NS described in this report.

```
mvd=3.175;
d=157.5;
da=16;
fc=49.53;
bw=150;
rho=0.0416;
Re={[2 25]};
V=CSDM(mvd, da, fc, d, bw, rho, Re)
function [V] = CSDM(mvd, da, fc, d, bw, rho, Re)
%CSDM  Evaluation shear capacity based on Critical Shear Displacement
%
%   V = CSDM(mvd, da, fc, d, bw, rho, Re), is the implementation of the
%   critical shear displacement method proposed in Y.Yang (2014). "Shear
%   behaviour of reinforced concrete 2members without shear reinforcement
%   -A new look and an old problem." The equation numbers in the file is
%   in accordance to the reference.
%   The input variables are explained as follow:
%   mvd is the maximum value of M/Vd in the calculated span in [-];
%   da is the maximum aggregate size in [mm];
%   fc is the compressive strength of concrete in [MPa];
%   d is the effective depth of the beam in [mm];
%   bw is the width of the beam in [mm], here the beam is assumed to be
%   prismatic, the program has not checked for T beams or I beams.
%   rho is the reinforcement ratio of the beam, the percentage is not.
%   needed Re is the rebar configuration. It is a cell, each array stands
%   for the configuration of a beam, which is a two columns matrix. The
%   first column is the number of rebar, the second one is the diameter
%   in [mm].
% Example
%   For two beams with maximum a/d ratio = 3.0, concrete compressive
%   strength 34.2 MPa and 34.8 MPa, effective depth of 420 mm and 720 mm,
%   width of 200 mm, reinforcement ratio of 0.74% and 0.79%, rebar
%   configuration being 1 Ø 14 + 2 Ø 20 and 3 Ø 22(Walraven's A2 and A3
%   beams), the inputs are:


%Last modified by Yuguang Yang on April 04 2014. Copy right reserved.
%

CoreNum = 4; % when parallel calculation is available on the computer,
% determine the number of cores that is available
global Es Ec

Es = 200000; % elastic modules of steel in MPa
Ec = 33000; % elastic modules of concrete in MPa, only effecting the
% crack height calculation, thus a rough estimation is sufficient.
% validation, it is recommended to make Ra = 0.75 for LWA concrete;
% and keep Ra = 1.0, while reduce fc back to 60 MPa for HSC
n = numel(d);       % number of tests
% % d=235;
As = rho.*bw.*d;    % reinforcement area
Ra = ones(n,1);     %reduction factor for special concrete types such as
```

```
% HSC or LWA concrete.
br = zeros(n,1);D = br;
if nargin > 6
    for l = 1:n
        br(l) = sum(Re{l}(:,1).*Re{l}(:,2)); % the part of width occupied
        % by rebar for dowel force Vdw calculation (only applicable when
        % all the rebars are in one layer)
        D(l) = sum(Re{l}(:,1).*Re{l}(:,2).^2)/sum(Re{l}(:,1).*Re{l}(:,2));
        % equivalent rebar diameter Deff, calculated with eq..(4.16)
    end
else
    % When rebar configuration is not available, assuming there are four
    % bars in one layer, calculate the rebar diameter accordingly.
    Re = ones(n,1)*[4 4];
    Re(2) = (As/pi).^.5;
    br = 4*Re(:,2); D = Re(:,2);
end
Vdw = V_dw(bw, br, fc, D);   % calculate the contribution of dowel action
V = zeros(n,1);
%
% %Initialize Matlab Parallel Computing Environment
% if matlabpool('size')<=0 % check parallel computing environment
% matlabpool('open','local',CoreNum);
% % start parallel computing environment
% end

for l = 1:n
    V(l) = Vm(mvd(l), da(l), fc(l), d(l), bw(l), As(l), Vdw(l), ...
    rho(l), D(l), Ra(l));
    % calculation of the maximum shear resistance of each tests
end
% matlabpool close
end
%-------------------------------------------------------------------------
function V = Vm(mvd, da, fc, d, bw, As, Vdw, rho, D, Ra)

global Es Ec

ne = Es/Ec; % ratio between Es and Ec for crack height calculation
delta = min((3.267e-5.*d*25/D+.002204), .025);
scr = (1+rho.*ne-(2*rho.*ne+(rho.*ne).^2).^.5).*d;   % major crack height
lcrm = scr./1.28;       % average crack spacing of major cracks
z = (2*d + scr)/3;      % internal level arm
V1 = 1.5*d*bw;          % first guess of shear resistance
V0 = 0; count = 0;      % initiation of iteration

while abs(V0-V1) > 10
    M0 = V1*d*mvd;      % cross sectional moment
    w = M0/z/As/Es*lcrm;    % estimation of average crack width eq..(4.8)
    V0 = V1;

    Vai = V_ai(delta, w, da, scr, fc, bw);  % aggregate interlock
    Vc = V_c(z,d, V0);          % shear force in compression zone
    V1 = Ra*Vai + Vc + Vdw;     % summation of total shear force
```

```
    V = V1;
    if count == 20  % maximum iteration number is 20
        break
    end
    count = count+1;
end
mvd0 = 2;
if mvd < 2
    V = V*2/mvd0;
end
% fctm = (fc<58).*.3.*(fc-8).^(2/3)+(fc>=58).*2.12.*log(1+(fc/10));
end
%-------------------------------------------------------------------------
function Vai = V_ai(delta, w, da, scr, fc, bw)
% shear resistance contributed by aggregate interlock, based on eq..(4.4)
w0 = 0.01;  % crack width at crack tip
dw = (w0-w)/100;   % increment of crack width in the linear crack profile
CrackProfile = (w: dw: w0);    % crack profile, divided into 100 sections
n = numel(CrackProfile);
L = scr/n;
fc = min(fc,60);    % limitation for high strength concrete
tau = zeros(size(CrackProfile));
parfor l = 1:n
    [~,tau(l)]=AI_walraven(CrackProfile(l), delta, da, fc);
    % Walraven's aggregate interlocking formula eq..(3.30)
end
Vai = -sum(tau.*L )*bw;
% alternative simplified AI formula: eq..(4.7), much faster than
% Walraven's formula:
% Vai = (-978*delta.^2+85*delta-.27).*fc.^.56.*bw.*.03./(w-.01).*scr;
end
%-------------------------------------------------------------------------
function Vdw = V_dw(bw, br, fc, D)
% maximum dowel action force, based on eq..(3.28)
Vdw = 1.64*(bw-br).*D.*(fc).^.333;
end
%-------------------------------------------------------------------------
function Vc = V_c(z, d, V)
% shear force contrition in compression zone, based on eq..(3.26)
Vc = 2*(d-z)/z*V;
end
%=========================================================================
function [sig,tau]=AI_walraven(w0, D0, da, fc)
%AI_Walraven Walraven's formula for aggregate interlock eq..(3.30)
%   [sig,tau]=AI_walraven(w0, D0, da, fc), calculated the shear and
%   normal stresses [MPa] generated due to aggregate interlock when the
%   normal or shear displacement at the crack faces is given. The
%   function only allows the input of single values. If you have an array
%   please do it through iteration. This function has to be a separate
%   file named 'AI_walraven.m'. The inputs of the function are:
%   normal crack opening w0 [mm],
%   shear crack opening D0 [mm],
%   maximum aggregate size da [mm],
```

```
%   concrete compressive strength fc [MPa].
%Exmaple
%   [sig,tau]=AI_walraven(0.01,0.02,16,34.2);

%Last modified by Yuguang Yang on April 04 2014. Copy right researved.

global dm pk u w D
w = w0*(w0>0);  % normal crack opening
D = abs(D0);    % shear crack opening
dm = da;        % maximum aggregate size
% situation when there is no contact between crack faces
if w > dm
    sig = 0;
    tau = 0;
% situation when the shear displacement is larger than Dmax
else if D > dm
    [sig,tau]=AI_walraven_u(w0, da, fc);
    else
% normal situation
pk = 0.75;
u = .4;     % friction coefficient
fcc = fc;
sig_pu = 6.39*fcc^(.56);    % crush strength of the cement matrix
if D > w
    Ay = quad(@ay,2*w,dm);
    Ax = quad(@ax,2*w,dm);
else
    if (w^2+D^2)/D<dm
    Ay = quad(@ay,(w^2+D^2)/D,dm);
    Ax = quad(@ax,(w^2+D^2)/D,dm);
    else
    Ay = 0;
    Ax = 0;
    end
end
sig = sig_pu*(Ax-u*Ay);
tau = sig_pu*(Ay+u*Ax)*(-D/D0);
    end
end
end
function [sig,tau]=AI_walraven_u(w0)
% Walraven's formula when the shear displacement is larger than Dmax
% aggregate size.
global dm pk u w
w = w0;     % crack opening [mm]
dm = 16;    % maximum aggregate size [mm]
pk = 0.75;  % percentage of aggregate
u = .4;     % friction
fcc = 40;   % concrete compressive strength [MPa]
sig_pu = 6.39*fcc^(.56);    % yield strength of concrete under three
% dimensional loading
if w*2 < dm
Ay = quad(@ayu,2*w,dm);
Ax = quad(@axu,2*w,dm);
```

```
sig = sig_pu*(Ax-u*Ay);
tau = sig_pu*(Ay+u*Ax);
else
sig = 0;
tau = 0;
end
end
function [F] = F(d0,dm)
% aggregate size distribution function F(D), see eq..(3.30)
d = d0/dm;
F = .532*d.^.5-.212*d.^4-.072*d.^6-.036*d.^8-.025.^10;
end
function [G1] = G1(d,D,w)
% function G1(n,t,D), see eq..(3.30)
um = UM(w,D,d);
G1 = d.^(-3).*((d.^2-(w^2+D.^2)).^.5.*D./(w^2+D.^2).^.5.*um-w.*um-um.^2);
end
function [G2] = G2(d,D,w)
% function G2(n,t,D), see eq..(3.30)
um = UM(w,D,d);
G2 = d.^(-3).*((D-((d.^2-w^2-D.^2).^.5)*w./(w^2+D.^2).^.5.*um +...
    (um+w).*(d.^2/4-(w+um).^2).^.5 - w*(d.^2/4-w^2).^.5)+...
    d.^2/4.*asin((w+um)./d*2) - d.^2/4.*asin(2*w./d));
end
function [G3] = G3(d,w)
% function G3(n,t,D), see eq..(3.30)
G3 = d.^(-3).*(d/2-w).^2;
end
function [G4] = G4(d,w)
% function G4(n,t,D), see eq..(3.30)
G4 = d.^(-3).*(d.^2*pi/8-w*(d.^2/4-w^2).^.5-d.^2/4.*asin(2*w./d));
end
function um = UM(w,D,d)
% calculation of umax in G1 and G2
um = (-w/2*(w^2+D^2)+(w^2*(w^2+D^2)^2-(w^2+D^2)*((w^2+D^2)^2- ...
D^2*d.^2)).^.5/2)/(w^2+D^2);
end
function [ay] = ay(d)
% projected contact area Ax in x direction in eq..(3.30)
global dm pk w D
if D > w
    if w == 0
        D0 = dm;
    else
        D0 = (w^2+D^2)/w;
    end
d1 = d(d <= D0);
ay1 = pk*4/pi.*F(d1,dm).*G3(d1,w);
d2 = d(d > D0);
ay2 = pk*4/pi.*F(d2,dm).*G1(d2,D,w);
ay = [ay1,ay2];
else
  ay = pk*4/pi.*F(d,dm).*G1(d,D,w);
end
```

```
end
function [ax] = ax(d)
% projected contact area Ax in x direction in eq..(3.30)
global dm pk w D
if D > w
    if w == 0
        D0 = dm;
    else
        D0 = (w^2+D^2)/w;
    end
d1 = d(d <= D0);
ax1 = pk*4/pi.*F(d1,dm).*G4(d1,w);
d2 = d(d > D0);
ax2 = pk*4/pi.*F(d2,dm).*G2(d2,D,w);
ax = [ax1, ax2];
else
  ax = pk*4/pi.*F(d,dm).*G2(d,D,w);
end
end
function [ay] = ayu(d)
% projected contact area Ay in y direction when the shear displacement is
% larger than maximum aggregate size D > dm
global dm pk w
ay = pk*4/pi.*F(d,dm).*G3(d,w);
end
function [ax] = axu(d)
% projected contact area Ax in x direction when the shear displacement is
% larger than maximum aggregate size D > dm
global dm pk w
ax = pk*4/pi.*F(d,dm).*G4(d,w);
end
```

```
V =

   5.3871e+04
```

Published with MATLAB® R2023b